Measuring accretion in young stars: A constraint on the physical processes in protoplanetary disks

Rik A. B. Claes

München 2024

Measuring accretion in young stars: A constraint on the physical processes in protoplanetary disks

Rik A. B. Claes

Dissertation
an der Fakultät für Physik
der Ludwig–Maximilians–Universität
München

vorgelegt von
Rik A. B. Claes
aus Duffel, Belgien

München, den 26 November 2024

Erstgutachter: Prof. Dr. Barbara Ercolano
Zweitgutachter: Prof. Dr. Thomas Preibisch
Tag der mündlichen Prüfung: 5 February 2025

Contents

List of Figures

List of Tables

Zusammenfassung

In den letzten drei Jahrzehnten wurde eine große Anzahl von Exoplaneten entdeckt und charakterisiert. Der Entstehungsprozess dieser Planeten ist jedoch noch immer kaum verstanden. Man geht davon aus, dass die Geburt von Planeten in den zirkumstellaren Scheiben junger Sterne stattfindet. Das Verständnis der in diesen Scheiben ablaufenden physikalischen Prozesse ist daher von entscheidender Bedeutung für unser Verständnis der Planetenentstehung. Ein Aspekt, der noch besser verstanden werden muss, ist die Entwicklung dieser Scheiben selbst. Es ist bekannt, dass sich die Scheiben auf Zeitskalen von einigen Millionen Jahren zerstreuen, aber die physikalischen Prozesse, die zur Umverteilung von Material und Drehimpuls führen und somit für ihre Zerstreuung verantwortlich sind, werden immer noch diskutiert.

Ein wichtiger Anhaltspunkt für die Entwicklung der Scheibe ist die Geschwindigkeit, mit der Materie von der Scheibe auf den Zentralstern akkretiert wird, und wie diese Akkretionsrate mit der Scheibenmasse korreliert. Bei einer bestimmten Scheibenmasse wird eine große Streuung der Akkretionsrate beobachtet. Diese Streuung lässt sich mit einfachen Modellen der Scheibenentwicklung nur schwer erklären, was die Frage aufwirft, ob andere Effekte zu dieser großen beobachteten Streuung beitragen können.

Die Akkretionsraten können mit verschiedenen Methoden untersucht werden. Die direkteste Methode besteht in der Messung der überschüssigen Kontinuumsemission, die durch das einfallende Material beim Aufprall auf die Sternoberfläche freigesetzt wird. Für eine genaue Messung sind Spektren mit einem breiten Wellenlängenbereich erforderlich, die gleichzeitig den ultravioletten und den optischen Wellenlängenbereich abdecken. Das X-Shooter-Instrument am Very Large Telescope (VLT) ermöglicht solche gleichzeitigen Beobachtungen bei ausreichendem Signal-Rausch-Verhältnis in nahen Sternentstehungsgebieten.

In dieser Dissertation stelle ich X-Shooter-Studien junger Sterne vor, die darauf abzielen, unser Verständnis der Akkretionseigenschaften klassischer T-Tauri-Sternpopulationen zu verbessern. Insbesondere habe ich die große Akkretionsvariabilität, die bei XX Cha beobachtet wurde, durch die Verwendung von zwei X-Shooter-Spektren, die im Abstand von etwa 10 Jahren aufgenommen wurden, eingegrenzt. Eine solche Variabilität ist jedoch selten und es ist unwahrscheinlich, dass sie die beobachtete Streuung der Akkretionsraten bei einer bestimmten Scheibenmasse beeinflusst.

Ich habe die bereits existierende Methode zur selbstkonsistenten Ableitung der Akkretionseigenschaften klassischer T-Tauri-Sterne verbessert. Um dies zu erreichen, habe ich die verfügbare Vorlagen zur Darstellung der stellaren Emission erweitert und interpoliert. Die Verwendung einer solchen Interpolation mildert Entartungen und Beobachtungsunsicherheiten, die mit der Verwendung einzelner Vorlagen verbunden sind. Außerdem habe ich die Best-Fit-Metrik geändert, um mehr Informationen aus den Spektren zu berücksichtigen. Dank der interpolierten Vorlagen konnte ich auch eine untere Grenze für die messbare Massenakkretionsrate für jeden Spektraltyp von G8 bis M5,5 angeben.

Mit dieser aktualisierten Methode analysierte ich eine Stichprobe von klassischen T-Tauri-Sternen, von denen bekannt ist, dass sie komplexe Scheibenmorphologien aufweisen, die oft als Substrukturen bezeichnet werden. Die Kombination dieser Stichprobe mit Informationen aus der Literatur ermöglichte eine erste Studie, die die Scheibenmorphologie mit den Akkretionseigenschaften in Beziehung setzt. Die hier vorgestellten Ergebnisse deuten darauf hin, dass

Scheiben mit inneren Staubhohlräumen bei einer gegebenen Scheibenmasse geringere Akkretionsraten aufweisen, als die unaufgelöste Population. Scheiben mit Ringen scheinen sich dagegen nicht von der unaufgelösten Population zu unterscheiden. Dies könnte ein Hinweis darauf sein, dass Quellen, in denen solche Substrukturen beobachtet werden, sich nicht von der unaufgelösten Population unterscheiden und dass die unaufgelöste Population ähnliche Substrukturen aufweisen kann, wenn sie mit einer ausreichend hohen Auflösung beobachtet wird. Ich diskutiere auch, wie die Position einiger interessanter Quellen in den Diagrammen der Massenakkretionsrate gegen die Scheibenmasse mit der beobachteten Morphologie zusammenhängen könnte. Obwohl es Hinweise darauf gibt, dass Substrukturen teilweise zu der beobachteten Streuung der Massenakkretionsraten beitragen, muss ein großer Teil der beobachteten Streuung noch erklärt werden.

Die hier vorgestellte Methodik kann weiter verbessert werden, indem mehr Informationen aus den beobachteten Spektren in die Best-Fit-Bestimmung einbezogen werden, indem ein Modell der Akkretionsemission verwendet wird, das in seinen Parametern kontinuierlich ist und posteriore Wahrscheinlichkeiten liefert. Ein solches Werkzeug wird eine einfachere Analyse größerer Stichprobe von klassischen T-Tauri-Sternen ermöglichen. Solche größeren Stichprobe werden benötigt, um die Beziehungen zwischen Scheibenmorphologien und Akkretionsraten besser zu verstehen. Zu diesem Zweck wäre auch eine homogene Analyse einer größeren Stichprobe von Akkretionsraten für räumlich aufgelöste Scheibenbeobachtungen notwendig.[1]

[1]Translated using `https://www.deepl.com/nl/translator`

Abstract

A large number of exoplanets have been detected and characterised over the last three decades. The formation process that created these planets is, however, still poorly understood. The birth of planets is expected to take place in the circumstellar disks of young stars. Understanding the physical processes active in these disks is therefore crucial to our understanding of planet formation. One aspect that still requires better understanding is the evolution of these disks themselves. It is known that disks dissipate on timescales of a few million years, but the physical processes that lead to the redistribution of material and angular momentum and, therefore, are responsible for their dissipation are still being debated.

A key constraint on disk evolution comes from the rate at which matter is accreted from the disk onto the central star and how this accretion rate correlates with disk mass. A large spread in mass accretion rates is observed at a given disk mass. This spread is hard to explain with simple disk evolution models, which raises the question of whether other effects may contribute to this large observed scatter.

Accretion rates can be probed using several methods, the most direct of which consists of measuring the continuum excess emission released by the infalling material impacting the stellar surface. Doing so in an accurate way requires broad wavelength range spectra that simultaneously cover ultra-violet and optical wavelength ranges. The X-Shooter instrument at the Very Large Telescope (VLT) allows for such simultaneous observations at sufficient signal-to-noise in nearby star-forming regions.

In this thesis, I present X-Shooter studies of young stars, which aim at improving our understanding of the accretion properties of Classical T Tauri Star populations. In particular, I constrained the large accretion variability observed in XX Cha through the use of two X-Shooter spectra that were taken about 10 years apart. Such variability is, however, rare and unlikely to affect the observed scatter in accretion rates at a given disk mass.

Beyond this, I improved on the preexisting method for self-consistently deriving the accretion properties of Classical T Tauri stars. To achieve this I extended and interpolated the library of templates available to represent the stellar emission. The use of such an interpolation mitigates degeneracies and observational uncertainties associated with using individual templates. I also altered the best-fit metric to include more information present in the spectra. Thanks to the interpolated templates I was also able to provide a lower limit on the measurable mass accretion rate for each spectral type ranging from G8 to M5.5.

Using this updated method, I analyzed a sample of Classical T Tauri Stars that are known to have complex disk morphologies, often referred to as substructures. Combining this sample with information from literature allowed for a first study relating disk morphology to accretion properties. The results presented here hint at the fact that disks with inner dust cavities have lower accretion rates at a given disk mass compared to the unresolved population. Disks with annular rings on the other hand do not appear to be distinct from the unresolved population. This may hint that sources, in which such substructures are observed, are not distinct from the unresolved population and that the unresolved population may present similar substructures if observed at a high enough resolution. I also discuss how the position of some interesting sources in the mass accretion rate vs. disk mass diagrams could be related to the observed morphology. While hints are found that substructures partially contribute to the observed spread in mass accretion rates, a

large fraction of the observed scatter has yet to be explained.

The methodology presented here can be further improved by including more information from the observed spectra in the best-fit determination, using an accretion emission model that is continuous in its parameters and providing posterior probabilities. Such a tool will facilitate a more straightforward analysis of larger samples of Classical T Tauri Stars. Such larger samples are needed to better understand the relationships between disk morphologies and accretion rates. For this aim, a homogeneous analysis of a larger sample of accretion rates for spatially resolved disk observations would be necessary.

List of acronyms

YSO	Young Stellar Object
CTTS	Classical T Tauri Star
WTTS	Weak lined T Tauri Star
HRD	Hertzsprung-Russell diagram
SpT	Spectral Type
$T_{\rm eff}$	Effective temperature
$L_\star$	Effective temperature
$M_\star$	Stellar mass
$\dot{M}_{\rm acc}$	Mass accretion rate
$L_{\rm acc}$	Accretion luminosity
$M_{\rm disk,dust}$	Disk dust mass
$M_{\rm disk}$	Disk mass
$M_\odot$	Solar mass
$L_\odot$	Solar luminosity
$L_{\rm acc,noise}$	Noise on the accretion luminosity due to uncertainty on the chromospheric emission
$\dot{M}_{\rm acc,noise}$	Noise on the mass accretion rate due to uncertainty on the chromospheric emission
ADI	Angular Differential Imaging
RDI	Reference Differential Imaging
SDI	Spectral Differential Imaging
EUV	Extreme-ultraviolet
FUV	Far-ultraviolet
HST	Hubble space telescope
DESTINYS	Disk Evolution Study Through Imaging of Nearby Young Stars
VLT	Very Large Telescope
VLTI	Very Large Telescope Interferometer
ALMA	Atacama Large Millimeter/submillimeter Array

1

Introduction

Throughout history, humans have dreamed of what other worlds might be like. An ancient example can be found in Epicurus who wrote "There is an unlimited number of cosmoi (worlds), and some are similar to this one and some are dissimilar" in a letter to Herodotus [1]

In the medieval worldview, the planets in our solar system, the Sun, and stars are interpreted as occupying concentric spheres with the Earth at its center. In Dante's Paradisio, each of these spheres is attributed to a different hierarchy of angels. Each of these heavens is reserved for those who excelled in the associated virtues, making a description of objects in the night sky a description of the afterlife and the virtues valued by society at that time. The shift to the heliocentric model is partially responsible for changing this view afterward.

By the late 19th and early 20th century, the idea of life on Mars became increasingly popular. This resulted in a large number of literary works, such as *"War of the Worlds"* by H.G. Wells and *"Stranger in a Strange Land"* by R. Heinlein, uses the concept of life on the planet to reflect upon our society. This popularity was fueled first by Giovanni Schiaparelli and later by the astronomer Percival Lowell, who mapped out the "canals" he observed on Mars [2]. According to Lowell, these canals were evidence of civilisation on the red planet. However, the astronomical community was sceptical of such canals. Indeed, other observations did not find any evidence for such structures. Schiaparelli and Lowell were in all likelihood drawing either effects of atmospheric perturbations or the veins in his own eyes, made visible on his retina by the large amount of light collected in his large refractor telescope. The later explanation was proposed by Sheehan & Dobbins (2003) to explain the similar structures that Lowell observed on Venus. At the same time, humanity had just undergone a surge in canal construction. Lowell's canals may therefore have been more of a reflection of ourselves than anything else.

As our understanding of the solar system improved, most science fiction moved to more distant planets to tell its stories. The impact of such discoveries on fiction was studied by Puranen et al. (2024), who found planets in fictional works after the discovery and characterization of exoplanets to be less Earth-like, reflecting these discoveries.

It appears that wishing to understand such foreign worlds, be it scientifically or narratively, has been a constant throughout human history. The drive behind this may be both to better understand the universe out there and to better understand our own world, by extension ourselves, and our place in the universe. Regardless of what drives us in this endeavor, astronomers have made great strides in the past decades through the discovery and characterization of thousands of exoplanets. However, one question that, as of yet, remains unsolved is how these planets form.

[1] https://thereader.mitpress.mit.edu/history-speculation-about-aliens/

[2] e.g., https://en.wikipedia.org/wiki/Martian_canals

In this thesis, I hope to contribute to our understanding of planet formation by studying the systems in which they are likely to be formed. These systems consist of young stars surrounded by circumstellar disks in which planets are likely to grow. The focus of this work is on what we can learn about these disks through the rate at which matter accretes from them onto the central star. In this chapter, I present our current understanding of the planet-formation process and some of the observational constraints, thereby providing the context for this thesis. Finally, I outline the current issues that this thesis attempts to address.

1.1 From molecular cloud to stars and planets

Stars are known to have a finite lifespan; they are born, evolve over time, and eventually die. The star formation process and early life of stars are of particular interest since it is during these periods that planets are expected to form.

Star formation begins when a large molecular cloud ($\sim 50 - 100$ pc) begins to fragment due to self-gravity (e.g., Tacconi et al. 2020). Initially, elongated structures, known as *filaments* (widths of ~ 0.1 pc), have been observed to form (André et al. 2010; Kennicutt & Evans 2012). These filaments then collapse into *prestellar cores*, which in turn collapse into one or more stars (André et al. 2010; Gómez et al. 2021). Initially, these protostars will be hidden in their parental cloud, which forms an envelope around the protostar. The gas within the protostellar core will have displayed some degree of turbulent motion; therefore, individual cores will have some angular momentum. As the cores shrink, the rotational velocity of the material will increase. This results in a rotating disk forming around the central protostar (e.g., Lee et al. 2021). This disk is often referred to as a protoplanetary disk since planets are expected to form within this structure. During this process, the envelope gradually dissipates as it accretes onto the central star and disk or is dispersed by outflows (Dunham et al. 2010). Eventually, the disk itself will also disperse. The main mechanism responsible for this dispersal is still debated (see Section 1.2).

In our current understanding, star formation is typically described as occurring in several different stages. The categorization of these stages is based on the spectral energy distribution (SED) of young stars (Lada 1987). This process, along with the corresponding SEDs, is illustrated in Figure 1.1. The classification is quantified using the spectral index $\alpha = d\log(\lambda F_\lambda)/d\log(\lambda)$ in infrared ($\sim 2 - 25\,\mu$m).

Class 0 sources are still highly embedded in their envelope. The mass of the internal protostar is still much lower than that of the envelope. This classification was not part of those originally introduced by Lada (1987), since these sources are not detected in the near infrared (NIR). Instead, they can be detected at longer wavelengths. Class 0 sources are also bright at sub-millimeter wavelengths. This category was introduced by Andre et al. (1993), and describes YSOs with $L_{\rm submm}/L_{\rm Bol.} \gtrsim 1\%$ (André 2015). Here, $L_{\rm submm}$ is the sub-millimeter luminosity measured longwards of $350\,\mu$m and $L_{\rm Bol.}$ is the total bolometric luminosity.

1.1 From molecular cloud to stars and planets

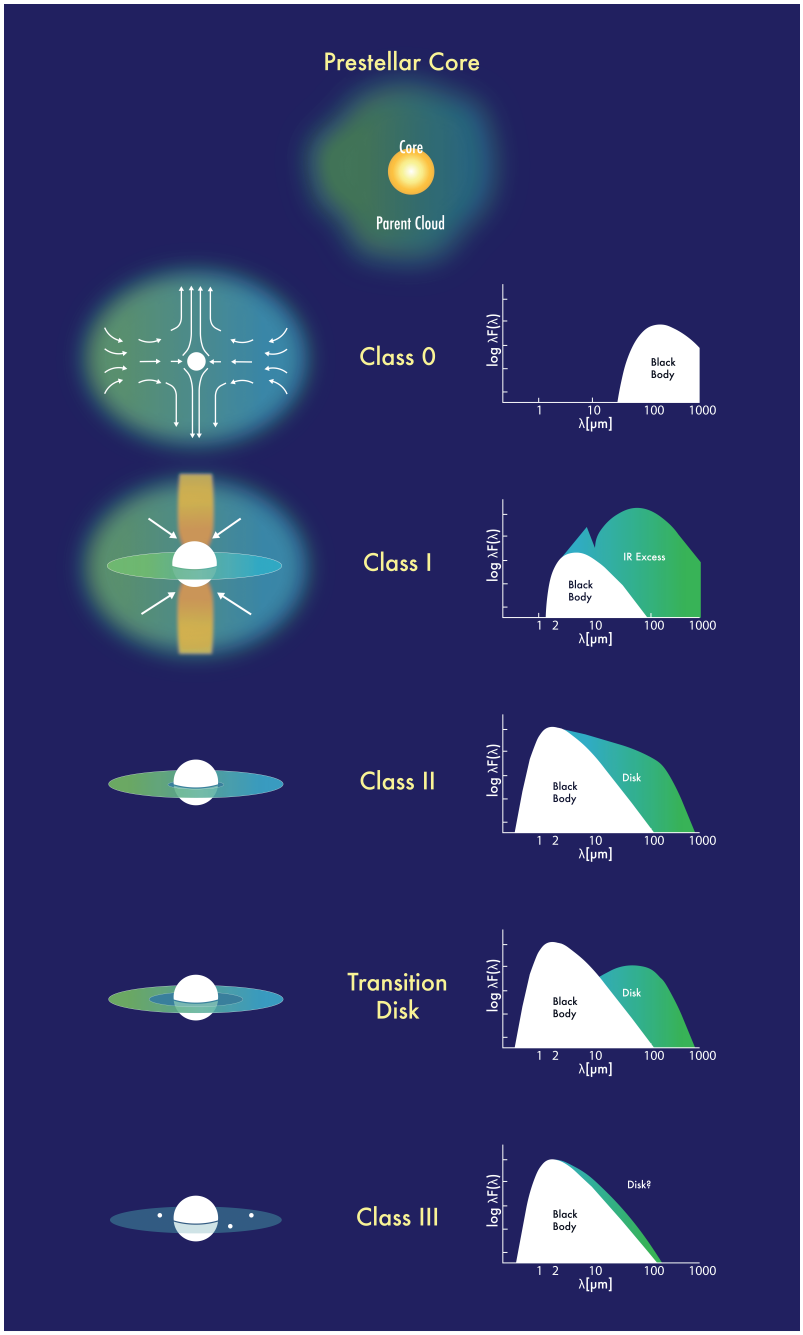

Figure 1.1: Visualization of the different classes of young stars and the corresponding SEDs. Schematics are not on the same scale. Credit: S. Brophy Lee, Based on the images of Persson (2014) and André (2002)

Class I sources are defined to have $0 < \alpha \lesssim 3$. During this stage the envelope has become less massive than the central star. Compared to Class 0 objects the envelope has become more optically thin. The SEDs of Class I objects has been successfully modeled as a star, disk and envelope system with the infalling envelope providing the majority of the emission (e.g.: Kenyon et al. 1993).

Class II stars are sources with $-2 \lesssim \alpha < 0$ and therefore have a decreasing SED slope in the IR. During this stage, the envelope has disappeared and the central star has become visible at optical wavelengths. The presence of a protoplanetary disk is revealed as an infrared excess in the SED.

Transition disks are a subclass of Class II young stars. Like Class II stars their envelope has dissipated and they possess a protoplanetary disk. However, the characteristics of this disk differ from that of traditional Class II disks in that they display a dip in their mid-infrared SED. This has been explained by the presence of a cavity or gap in the inner disk (Calvet et al. 2002). This was later also confirmed by mm observations (e.g., Andrews et al. 2009; Pinilla et al. 2018b). Originally these sources were considered to be in a universal transitional stage between the Class II and III stages, hence the name (e.g. Skrutskie et al. 1990; Calvet et al. 2005). However, more recently this view has changed (Espaillat et al. 2014). Observations of the Atacama Large Millimeter Array ALMA revealed that the transition disk class spans a diverse range of inner gap sizes. Consequently, a number of mechanisms have been proposed to explain this diversity (see van der Marel (2023) for a review).

Class III sources have $-3 < \alpha \lesssim -2$. The SED of Class III sources appears well reproduced by emission solely coming from the central star. Class III sources are therefore thought to have lost their circumstellar disk. Planets and asteroids must therefore already have formed by this stage. However, Lovell et al. (2021) still detected dust emission for 4 out of 31 Class III sources in Lupus using ALMA. This dust emission is consistent with that of debris disks, where small grains are replenished through collisions.

Besides the classification based on the SEDs, young stars are often also classified on the basis of their optical spectroscopic properties. This type of classification can only be performed when optical spectra are available for a source and, therefore, mostly overlap with the Class II and III SED classes. A first distinction exists between high mass ($2M_\odot < M_* < 8M_\odot$) Herbig Ae/Be stars and low mass ($2M_\odot < M_* < 8M_\odot$) T Tauri stars, based on their spectral type (e.g., Bastian et al. 1983). More massive stars ($M_* > 8M_\odot$) are generally believed to remain hidden in their natal cloud during their entire pre-main sequence and disk evolution. Consequently, massive stars have no counterparts to Herbig and T Tauri stars. However, this picture has recently come into question since some optically visible MYSO have been observed and classified as Herbig stars (e.g., Koumpia et al. 2019), making the upper mass range of Herbig stars uncertain.

The focus of this thesis is on T Tauri stars, which are the most abundant and best characterized. T Tauri stars are further subdivided into two different classes: Classical T Tauri stars

(CTTS) and Weak-lined T Tauri Stars (WTTS). This classification is typically based on the strength of the Hα emission line, where CTTS have a Hα equivalent width larger than a threshold depending on the spectral type (White & Basri 2003). Generally, these categories overlap with the SED classification, where CTTS corresponds to Class II YSOs, and WTTS corresponds to Class III YSOs. However, this is not always the case (e.g., Gregorio-Hetem & Hetem 2002). In fact, in chapter 3 of this thesis, I also present a Class III YSO that has a Hα equivalent width corresponding to that of a CTTS.

1.2 Disk evolution

Since main-sequence stars do not show the presence of protoplanetary disks, the disks around young stars must somehow dissipate. This is further supported by the declining fraction of accreting stars and the declining fraction of young stars with IR excess in older regions (e.g. Mamajek 2009; Hernández et al. 2007; Fedele et al. 2010; Ribas et al. 2015). Based on their analysis, both Mamajek (2009), Fedele et al. (2010) concluded that disk lifetimes are typically $\tau_{\rm disk} \sim 2.5 Myr$, where $\tau_{\rm acc.}$ should be interpreted as the mean lifetime in an exponential decay process.

$$f_{disk} = C \cdot \exp\left(-t/\tau_{disk}\right). \tag{1.1}$$

Here, $f_{\rm disk}$ is the disk fraction, C the initial disk fraction, and t the age. More recently, however, Michel et al. (2021) suggested that these disk lifetimes need to be adjusted upwards to $\tau_{\rm acc.} \sim 8 Myr$ although this is still highly debated. Figure 1.2 shows this decay in disk fraction as a function of time. So while the exact timescales are still somewhat contentious, it is clear that protoplanetary disks dissipate on timescales of a few Myr.

For disks to dissipate, most of their material needs to be either ejected from the system or accreted onto the central star. This in turn means that the angular momentum in the disk needs to be removed or redistributed. The physical and chemical processes at play in the disk determine how planet formation will take place. Understanding the evolution of protoplanetary disks is therefore key to understanding both the evolution of young stars and the formation of planets (e.g., Morbidelli & Raymond 2016). Two main mechanisms have been proposed to govern the evolution of protoplanetary disks, with several additional mechanisms potentially contributing at different stages of the disks' life. The two main processes are the viscous evolution paradigm and the MHD wind paradigm. Which of these mechanisms dominates is still a subject of debate in literature. A review on the mechanisms driving disk evolution can be found in Manara et al. (2023), here I describe some of the main attributes of these mechanisms.

1.2.1 Viscous evolution

Viscous evolution was historically the standard model of protoplanetary disk evolution. In this model, the main driver of disk evolution is an 'anomalous' viscosity, which may arise due to turbulence within the disk. Such turbulence could arise due to hydrodynamical instabilities, such

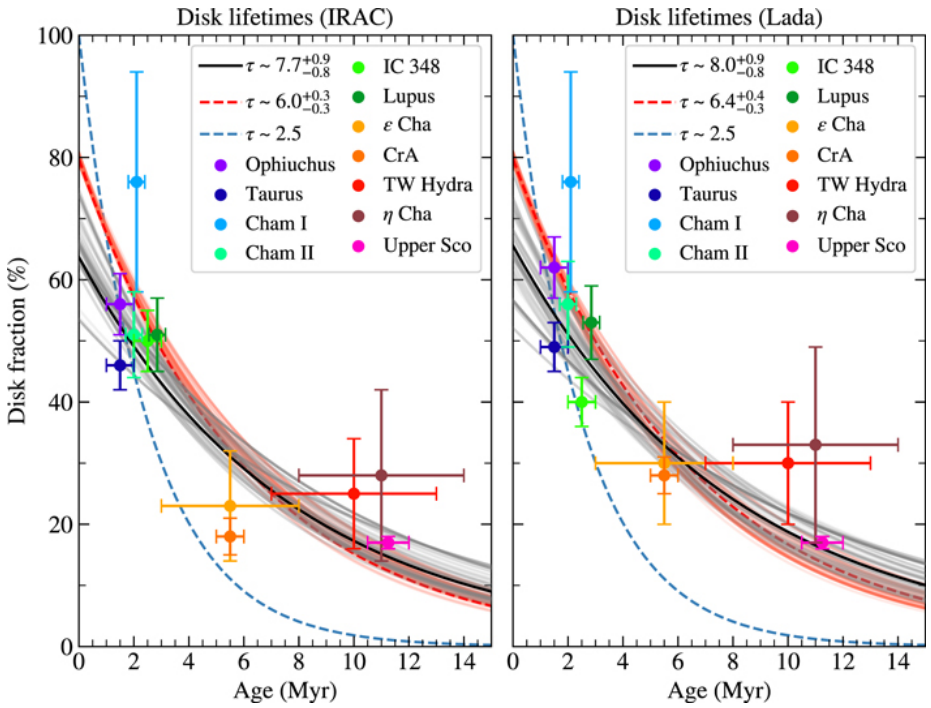

Figure 1.2: Disk fraction of different star-forming regions as a function of age. The solid black line indicates the best fit of equation 1.1. Left: the disk fraction obtained using the classification scheme of Lada (1987) (see section 1.1). Right: the disk fraction obtained using the IRAC classification Lada et al. (2006), an alternative for the Lada (1987) classification based on IRAC and WISE photometry, rather than the K band and Spitzer-MIPS1 or WISE4 photometry used by Lada (1987). The grey lines represent a random sample from the MCMC chain used to obtain the black best fit. The red line indicates the best fit assuming an initial disk fraction of 80%. The dashed blue line indicates the result of Mamajek (2009). Source image: Michel et al. (2021)

as the Vertical Shear Instability (VSI) (e.g., Nelson et al. 2013; Cui & Bai 2022) and gravitational instability (GI) (e.g., Kratter & Lodato 2016) or MHD instabilities such as the Magneto Rotational Instability (MRI) (e.g., Balbus & Hawley 1991; Cui & Bai 2022).

This evolutionary framework is typically expressed using

$$\frac{\partial \Sigma}{\partial t} = \frac{3}{R}\frac{\partial}{\partial R}\left[R^{1/2}\frac{\partial}{\partial R}(\nu \Sigma R^{1/2})\right], \tag{1.2}$$

which expresses the surface density Σ evolution of a Keplerian disk under the influence of viscous forces (Lynden-Bell & Pringle 1974). Here, $\nu = \alpha c_s H$ is the kinematic viscosity, which is parameterized using the dimensionless parameter $\alpha \sim (\delta v_t / c_s)^2$, c_s is the sound speed, and H is the disk scale height following the α viscosity prescription of Shakura & Sunyaev (1973) . The solution of this diffusive partial differential equation depends on how we assume ν to depend on Σ or R. The most widely used solution is the so-called self-similar solution of Lynden-Bell &

Pringle (1974). The self-similar solution is obtained by assuming $\nu = \nu_0(R/R_0)^\gamma$, where γ is a free index, R_c is the initial truncation radius of the disk, and ν_0 the viscosity at R_c.

The solution that Lynden-Bell & Pringle (1974) derived under these assumptions is

$$\Sigma(R,t) = \frac{M_0}{2\pi R_c^2}(2-\gamma)\left(\frac{R}{R_c}\right)^{-\gamma} T^{-\eta} \exp\left(\frac{-(R/R_c)^{(2-\gamma)}}{T}\right),. \tag{1.3}$$

Here,

$$\eta = \frac{5/2-\gamma}{2-\gamma}, \tag{1.4}$$

M_0 is the initial disk mass, and the viscous timescale

$$t_\nu = \frac{R_c^2}{3\nu(R_c)(2-\gamma)^2}, \tag{1.5}$$

and finally

$$T = \frac{t}{t_\nu} + 1, \tag{1.6}$$

describes a dimensionless time. By integrating equation 1.3, one obtains an expression for the total disk mass as a function of time

$$M_d(t) = \int_0^{\inf} \Sigma(R,t)dR = M_0 T^{1-\eta} = M_0(\frac{t}{t_\nu}+1)^{1-\eta} \tag{1.7}$$

(Lodato et al. 2017; Manara et al. 2023). For the disk mass to decrease with time, we need

$$\eta = \frac{5/2-\gamma}{2-\gamma} > 1, \tag{1.8}$$

which in turn implies we require $\gamma < 2$ (Lodato et al. 2017). The mass accretion onto the central star is the mass lost by the disk through its evolution. The mass accretion rate is therefore given by

$$\dot{M}_{\rm acc}(t) = -\frac{dM_{\rm d}}{dt} = \frac{M_0}{t_\nu}(\eta - t)T^{-\eta} = \frac{M_0}{t_\nu}(\eta - t)(\frac{t}{t_\nu}+1)^{-\eta} \tag{1.9}$$

(Lodato et al. 2017; Manara et al. 2023). Using these expressions, we can then also define the accretion timescale

$$t_{\rm acc} = \frac{M_{\rm d}(t)}{\dot{M}(t)} = 2(2-\gamma)(t-t_\nu), \tag{1.10}$$

that is, the time it would take for the disk to be accreted, assuming its current disk mass and mass accretion rate. From equation 1.10 it can be seen that, for a viscously evolving disk, the accretion timescale scale is a measure of the viscous timescale in the case $t \ll t_\nu$, and proportional to the age of the system in the case where $t \gg t_\nu$. This characteristic of viscous evolution was already noted by several authors (Hartmann et al. 1998; Jones et al. 2012; Rosotti et al. 2017).

By eliminating t_ν between equations 1.7 and 1.9, Lodato et al. (2017) obtain isochrones

$$\dot{M} = \frac{M_\mathrm{d}}{2(2-\gamma)t}\left[1 - \left(\frac{M_d}{M_0}\right)^{2-2\gamma}\right] \tag{1.11}$$

describing the relationship between mass accretion rate and disk mass for viscous disks with an initial disk mass of M_0 and age t. An interesting property of these isochrones is that for evolved disks ($t \gg t_\nu$), there is a linear dependence of $\dot{M}_\mathrm{acc}$ on M_disk. Another interesting property of viscous evolution is found by considering the time evolution of the disk's truncation radius, that is, the exponential cutoff radius. This radius evolves in time as

$$R_{trunc.}(t) = R_\mathrm{c} T^{1/(2-\gamma)} = R_\mathrm{c}\left(\frac{t}{t_\nu} + 1\right)^{1/(2-\gamma)} \tag{1.12}$$

(Hartmann et al. 1998). Considering $\gamma < 2$, it becomes evident that the truncation radius of the disk is expected to grow over time. A viscously evolving disk can therefore be described as a disk in which the angular momentum gets redistributed through the disk, resulting in viscous spreading. Most of the material will be accreted onto the central star, while most of the angular momentum will get carried outwards, to increasing radii.

1.2.2 MHD wind-driven evolution

More recently, the viscous framework has been challenged by the Magnetho-Hydrodynamical (MHD) wind-driven evolution (see Lesur (2021a) for a recent review). In this scenario, angular momentum is removed from the disk rather than redistributed as in the viscous case. The culprit for this removal of angular momentum is a wind launched by the interaction between the ambient magnetic field and the disk. A seminal work developing this idea was performed by Blandford & Payne (1982a), who also introduced the magnetic lever arm parameter $\lambda = L/(R\Omega(R)$. In this expression, L is the specific angular momentum carried away with the disk wind launched at radius R, where the disk rotates at an angular (Keplerian) velocity $\Omega(R)$. The magnetic lever arm can therefore be interpreted as the ratio between the angular momentum carried away by the wind and the angular momentum in the disk. For the angular momentum to be extracted, the lever arm must satisfy ($\lambda > 1$).

The lever arm parameter can be used to write the master equation

$$\frac{\partial \Sigma}{\partial t} = \frac{2}{R}\frac{\partial}{\partial R}\left[(\lambda - 1)R^2\dot{\Sigma}_w\right] - \dot{\Sigma}_w \tag{1.13}$$

of MHD wind-driven evolution (e.g., Bai 2016; Manara et al. 2023). In equation 1.13 $\dot{\Sigma}_\mathrm{w}$ is the rate at which the disk loses mass in the wind, and viscosity is completely neglected. In order to solve this equation, a parameterization for $\dot{\Sigma}_\mathrm{w}$ and λ needs to be adopted. Unlike the viscous model, where the α characterization has become the standard, there is no commonly used parameterization for MHD wind-driven evolution. A variety of 1d global evolutionary

models have been presented in the literature (e.g., Armitage et al. 2013; Bai 2016; Suzuki et al. 2016; Chambers 2019), most of which adopted different parameterizations for $\dot{\Sigma}_{\rm w}$ and λ and lacked simple analytical solutions. Such simple analytical solutions were only recently provided by Tabone et al. (2022a). Tabone et al. (2022a) achieved this by introducing the parameter $\alpha_{\rm DW}$ such that

$$\dot{\Sigma}_{\rm w} = \Sigma \frac{3\alpha_{\rm DW} c_{\rm s}^2}{4(\lambda-1)\Omega R^2} \tag{1.14}$$

becomes the expression for the mass loss rate. Here, the definition of α_{DW} was chosen to have a similar physical meaning as the viscous alpha (torque normalized by midplane thermal pressure). Using this parameterization, the master equation reads as

$$\frac{\partial \Sigma}{\partial t} = \frac{3}{2R}\frac{\partial}{\partial R}\left(\frac{\alpha_{DW}\Sigma c_{\rm s}^2}{\Omega}\right) - \frac{3\alpha_{\rm DW}\Sigma c_{\rm s}^2}{4(\lambda-1)r^2\Omega}, \tag{1.15}$$

which also admits a self-similar solution as in the viscous case. Tabone et al. (2022a) presents two classes of solutions to this equation: A fiducial case in which $\alpha_{\rm DW}$ is constant and a time-dependent case where $\alpha_{\rm DW}$ is constant throughout the disk but decreases in time according to $\alpha_{\rm DW} \propto \Sigma_{\rm c}(t)^{\omega}$, where $0 < \omega \leqslant 1$. $\Sigma_c(t)$ is defined using the ansatz solution

$$\Sigma(R,t) = \Sigma_{\rm c}(t)\left(\frac{R}{R_{\rm c}(t)}\right)^{\xi-1} \exp\left(\frac{-R}{R_{\rm c}(t)}\right), \tag{1.16}$$

to be $\sigma_{\rm c}(t) = \Sigma(R = R_{\rm c}, t)$where $\xi = 1/[2(\lambda-1)]$ and $R_{\rm c}(t)$ the characteristic radius. The first interesting property of both of these solutions is that $R_{\rm c}$ is constant over time. This is in contrast to the viscous scenario in which the disk expands according to equation 1.12.

What follows is a brief discussion of the evolution of the global disk properties of the time-dependent case of Tabone et al. (2022a). The disk mass evolves in time following [3]

$$M_{\rm d}(t) = M_0\left(1 - \frac{\omega}{2t_i}t\right)^{1/\omega}. \tag{1.17}$$

where $t_{\rm i}$ is the initial accretion timescale given by $t_{\rm i} = R_{\rm c}(t=0)/3\epsilon_c c_{\rm s,c}\alpha_{\rm DW}(t=0)$, with $\epsilon_{\rm c}$ the disc aspect ratio and $c_{\rm s,c}$ the sound speed at $r = r_{\rm c}(t=0)$. The accretion rate onto the star in this case is not simply the derivative of the disk mass with respect to time since mass is also lost in the wind. To account for this, Tabone et al. (2022a) use the mass ejection to accretion ratio $f_{\rm M}$. Using this parameter, the mass accretion rate reads

$$\dot{M}_{\rm acc,\star}(t) = \frac{1}{(1+f_{\rm M})}\dot{M}_{\rm d}(t) = \frac{M_0}{2t_{\rm i}(1+f_{\rm M})}\left(1 - \frac{\omega}{2t_{\rm i}}t\right)^{-1+1/\omega}. \tag{1.18}$$

[3]Here we use t_i to refer to the initial accretion timescale rather than $t_{acc,0}$ as used by Tabone et al. (2022a), to prevent confusion with the accretion timescale $t_{\rm acc} = M_d/\dot{M}_{\rm acc}$

Using equations 1.17 and 1.18, one can then find the accretion timescale to evolve following

$$t_{\rm acc} = \frac{M_{\rm d}(t)}{\dot{M}_{\rm acc}} = 2t_{\rm i}(1+f_M)\left(1-\frac{\omega}{2t_{\rm i}}t\right). \tag{1.19}$$

Similar to the viscous case, one can eliminate t_i between equations 1.17 and 1.18 to obtain the isochrones, which are given by

$$\dot{M} = \frac{M_{\rm d}}{\omega(1+f_{\rm M})t}\left[\left(\frac{M_{\rm d}}{M_0}\right)^{-\omega} - 1\right]. \tag{1.20}$$

Which implies that at low disk masses, assuming the same initial conditions, disks fall on a $\dot{M}_{\rm acc,\star} \propto M_{\rm d}^{1-\omega}$ slope. Considering these global properties, three main differences from the viscous case are of interest. Firstly, the critical radius stays constant in time in the MHD case, whereas it increases in time in the viscous case. Secondly, the disk mass becomes equal to 0 and the disk stops accreting within a finite time $t = 2t_i/\omega$, whereas in the viscous case they both go to zero for $t \longrightarrow \infty$. This is not the case in the fiducial solution of Tabone et al. (2022a), where an exponential decrease is found in both the mass of the disk and the mass accretion rate, which still implies faster clearing of the disk compared to the viscous case. Finally, the isochrones for the MHD wind case depend on the initial conditions through $f_{\rm M}$, which implies that the position of an evolving disk in the $\dot{M}_{\rm acc}$-$M_{\rm disk}$ diagram will always be influenced by its initial conditions. This is not the case for evolved disks in the viscous scenario, where when $M_d \ll M_0$, disks of the same age and viscosity prescription fall on the same line $\dot{M}_{\rm acc} \sim M_{\rm disk}$, thus forgetting their initial conditions. An illustration of the isochrones for the different models can be found in Figure 1.3.

1.2.3 Hybrid model

It is important to note that viscosity and MHD winds are not mutually exclusive. To this end, Tabone et al. (2022a) introduced a master equation that includes both effects. In this master equation

$$\frac{\partial \Sigma}{\partial t} = \frac{3}{R}\frac{\partial}{\partial R}\left[R^{1/2}\frac{\partial}{\partial R}(\alpha_{\rm SS}c_{\rm s}H\Sigma R^{1/2})\right] + \frac{3}{2R}\frac{\partial}{\partial R}\left(\frac{\alpha_{\rm DW}\Sigma c_{\rm s}^2}{\Omega}\right) - \frac{3\alpha_{\rm DW}\Sigma c_{\rm s}^2}{4(\lambda-1)r^2\Omega} \tag{1.21}$$

the two right-hand side terms of equations 1.2 (with application of $\nu = \alpha_{\rm SS}c_{\rm s}H$) and 1.15 can be recognized. Here, $\alpha_{\rm SS}$ represents the viscous alpha of Shakura & Sunyaev (1973). This equation is constructed in such a way that it facilitates an easy identification of the main driver of accretion, as the ratio of the accretion driven by the wind compared to that driven by viscosity is given by

$$\frac{\dot{M}_{\rm acc}^{\rm DW}}{\dot{M}_{\rm acc}^{\rm visc}} \simeq \frac{\alpha_{\rm DW}}{\alpha_{\rm SS}} \tag{1.22}$$

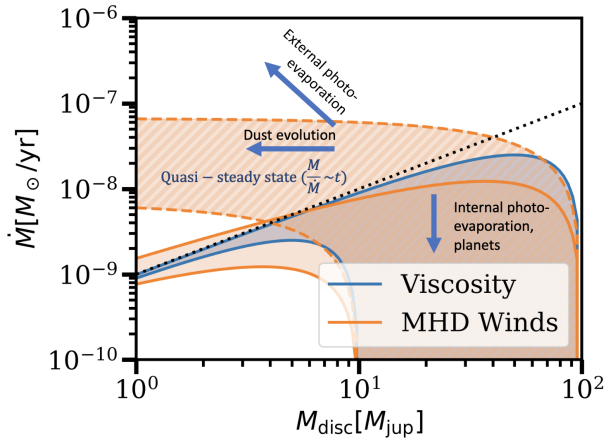

Figure 1.3: Isochrones of the viscous and MHD wind models in the $\dot{M}_{\mathrm{acc}}$ -M_{disk} diagram. The blue lines are isochrones for initial disk masses of 0.1 and 0.01 $M_\odot$. The orange dashed lines indicate the MHD Wind model isochrones for $\omega = 1$ at the same initial disk masses. The solid orange lines indicate the isochrones for the fiducial case of Tabone et al. (2022a), where α_{DW} is constant. The black dotted line indicates the $M_{\mathrm{disk}}/\dot{M}_{\mathrm{acc}} = 1$ Myr relationship. The colored areas indicate regions that are covered by each model for initial disk masses between 0.1 and 0.01 $M_\odot$. Source image: Manara et al. (2023)

(Tabone et al. 2022b). Here, this hybrid model will not be discussed in detail, as most studies focus on MHD wind or viscosity-dominated models (E.g., Somigliana et al. 2023; Yap & Batygin 2024; Tabone et al. 2022b). Tabone et al. (2022a) provided self-similar solutions to this equation under the assumption of constant α_{DW} and α_{SS}. In this solution, the properties of viscously evolving disks are recovered, such as a growing critical radius, a disk mass and accretion rate for $t \longrightarrow \infty$, and a tendency for most evolved disks to fall into the $\dot{M}_{\mathrm{acc}} \sim M_{\mathrm{disk}}$ relation, although with a somewhat increased scatter due to initial conditions when compared to the purely viscous case.

1.2.4 internal photoevaporation

An additional process that affects the evolution of protoplanetary disks is known as internal photoevaporation. Internal photoevaporation is the process in which high-energy radiation from the central star heats the gas on the surface of the disk sufficiently to reach escape velocities (e.g., Owen et al. 2012; Alexander et al. 2014). There are currently three main models of internal photoevaporation, defined by the type of radiation that dominates this mechanism, namely FUV, EUV, and X-ray. It is currently still unclear which of these dominates, although the study of low-accreting Class II stars appears to point to X-ray photoevaporation as the preferred mechanism (Ercolano et al. 2023). The evolution of a disk under the effect of internal photoevaporation can be described by adding an additional term to one of the aforementioned evolution equations (equations 1.2 , 1.13, and 1.21). In the case of the hybrid model, the master equation then

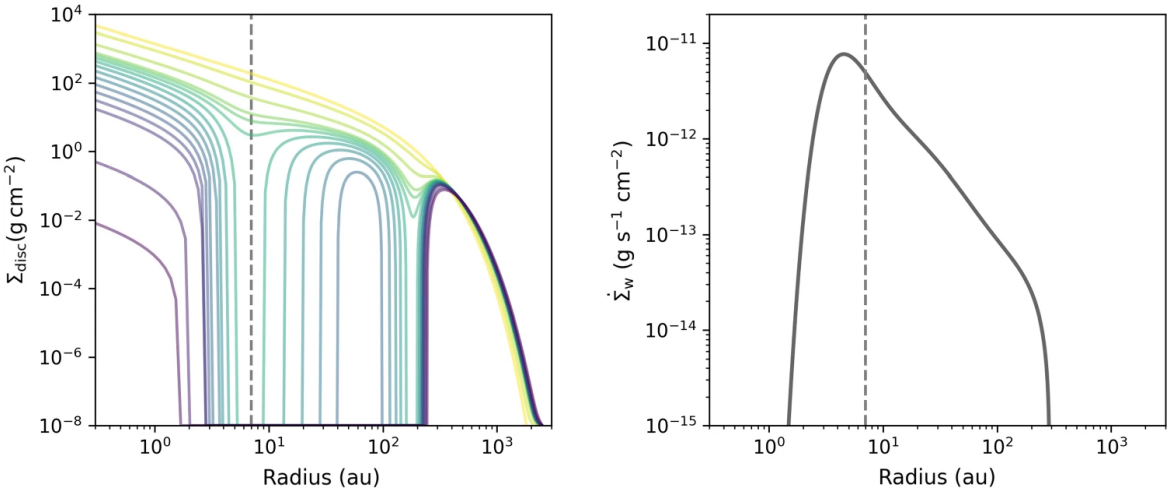

Figure 1.4: Left: Model of the evolution of the surface density of a viscous disk experiencing internal photoevaporation. The mass of the central star is taken to be 1 $M_\odot$, the disk mass is $M_{\rm d} = 0.1\,M_\odot$, and the x-ray luminosity is 2.04×10^{30} erg/s. The lines correspond to 0, 25, 50, 60, 62, 64, 66, 68, 70, 72, 74, 76, 78, 80, 90, and 99 % of the disk lifetime, with lighter colors indicating earlier stages. Right: The corresponding mass loss rate as a function of radius. The dashed line indicates the position of the gap opening in both panels. Source figure: Ercolano & Picogna (2022)

becomes

$$\frac{\partial \Sigma}{\partial t} = \frac{3}{R}\frac{\partial}{\partial R}\left[R^{1/2}\frac{\partial}{\partial R}(\alpha_{SS} c_s H \Sigma R^{1/2})\right] + \frac{3}{2R}\frac{\partial}{\partial R}\left(\frac{\alpha_{DW}\Sigma c_s^2}{\Omega}\right) - \frac{3\alpha_{DW}\Sigma c_s^2}{4(\lambda-1)r^2\Omega} + \dot{\Sigma}_{PhotWind}(R,t). \tag{1.23}$$

The exact form of $\dot{\Sigma}_{\rm PhotWind}(R,t)$ depends on the chosen model (FUV, EUV, or X-ray). Photoevaporation is commonly included in population synthesis models considering viscous evolution (E.g., Benz et al. 2014; Emsenhuber et al. 2023; Alexander et al. 2023) The reason for this is that pure viscous disks have infinite lifetimes, with $M_{\rm d}$ moving asymptotically to 0. Including internal photoevaporation overcomes this issue, providing finite lifetimes. In the MHD wind scenario, on the other hand, disk dispersal is an intrinsic feature. Here we provide a qualitative description of the effect of internal photoevaporation on a disk. This effect is illustrated in figure 1.4. The right panel of figure 1.4 shows the mass loss rate due to a photoevaporative wind. Here, it can be seen that this mass loss rate is the strongest at radii of a few AU. This profile is set by two effects. On the one hand, the gravitational potential due to the star is weaker at large radii, making it easier for the gas to be heated sufficiently to reach escape velocities. On the other hand, the flux onto the disk becomes weaker at large radii, resulting in less heating.

In the initial phase of disk evolution, the effect of photoevaporation is negligible. At early times, the accretion flow through the disk is too large compared to the mass loss rate of the wind ($\dot{M}_{\rm acc} \gg \dot{M}_{\rm wind}$). The mass lost at the radius where photoevaporation is the most effective is therefore readily replenished. In both the viscous and MHD wind-driven cases with $\omega < 1$,

the mass accretion rate is expected to decrease with time, so eventually the wind mass loss rate becomes comparable to the accretion rate. The material carried off in the wind will therefore no longer be replenished, and an annular gap will open up near the radii where the wind is the most effective. All of the material that continues to flow inward will start to be diverted into the wind at this point, cutting off the inner disk from the outer disk. The inner disk will continue to accrete until it is eventually dissipated. During this dissipation of the inner disk, the mass accretion rate is expected to drop sharply. After this has happened, the outer disk wall will be directly exposed to the high-energy radiation, thereby increasing its mass-loss rate due to the wind and resulting in the dissipation of the outer disk.

This was the classical explanation for the existence of transition disks, which led to their name. Transition disks were considered to be a transition stage between a full Class II disk and a diskless Class III object (see Section 1.1). However, this picture is increasingly uncertain. Pinilla et al. (2018b), for example, found that photoevaporation is unlikely to explain both the cavity sizes of resolved transition disks and the flat relationship between disk mass and stellar mass for their sample of transition disks. It is therefore unlikely that internal photoevaporation is responsible for all of the observed cavities, and an increasing number of additional mechanisms have been proposed to explain the existence of such cavities (see Chapter 4.1 or Andrews (2020); Bae et al. (2023) for reviews). It is likely that internal photoevaporation coexists with these mechanisms.

1.3 Disk evolution and planet formation

As mentioned in Section 1.1, protoplanetary disks are the birthplace of planets. A large sample of exoplanets has been detected and constrained through various observational techniques. At the time of writing, the NASA exoplanet archive[4] lists 5743 detected exoplanets. Figure 1.5 shows the mass and orbital semi-major axis observed population of exoplanets, as well as the sensitivity curves of different observing techniques. So, while it is clear that planets are abundant, the formation process of these planets is still poorly understood. A recent review of our understanding of planet formation is given by Drążkowska et al. (2023). Here, I focus on the link between planet formation and disk evolution.

A first constraint on the planet formation process comes from the timescale on which protoplanetary disks disappear. Planet formation must happen on timescales of a few Myr, although the exact timescale of disk dissipation is still debated (see section 1.2). The evolution of the disk mass itself also provides an important time constraint. It has been found that the dust- inferred disk masses of Class II stars are too low to form the typically observed systems (Najita & Kenyon 2014; Manara et al. 2018). One potential explanation for this is that planets must acquire most of their mass during the earlier Class 0/I stages of evolution (Tychoniec et al. 2020). This would support the idea that the substructures observed in Class II disks are the result of early- formed planets (see section 1.5). Another explanation could come from the uncertainties on dust based disk mass estimates discussed in section 1.5.1 (Mulders et al. 2021). A last explanation could

[4] https://exoplanetarchive.ipac.caltech.edu/

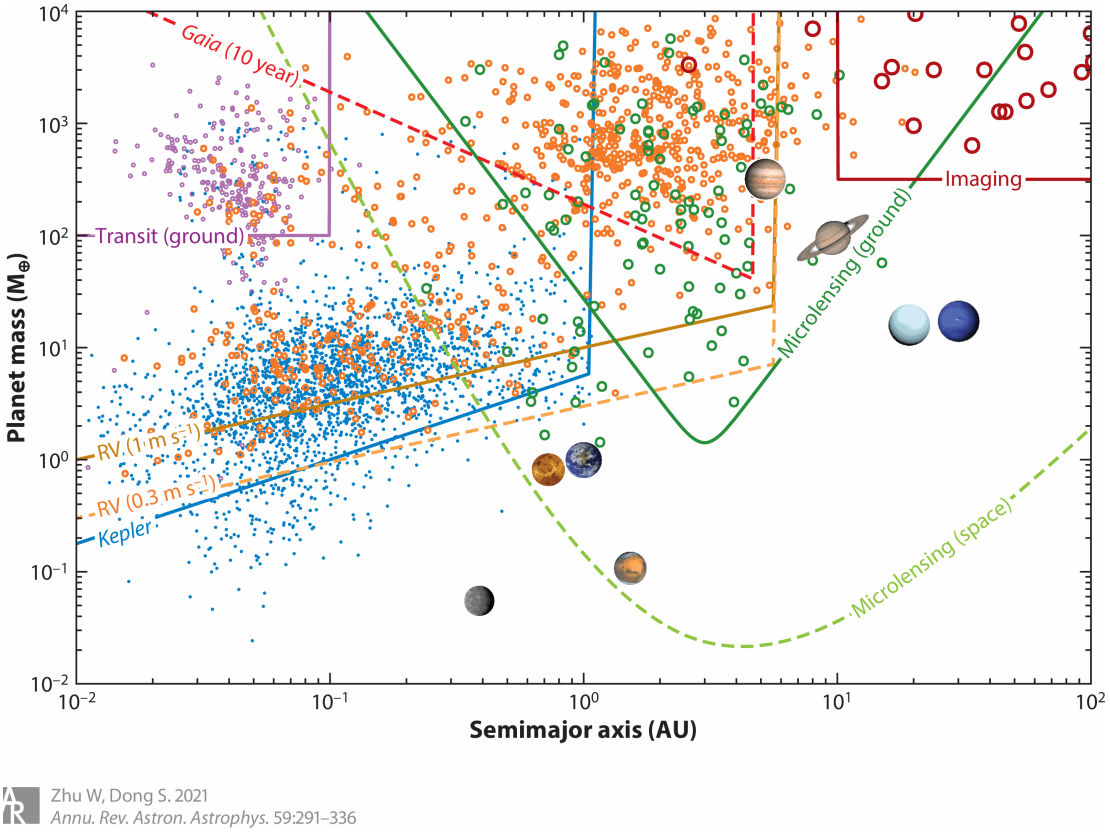

Zhu W, Dong S. 2021
Annu. Rev. Astron. Astrophys. 59:291–336

Figure 1.5: Top: Mass vs. orbital semimajor axis for the observed population of exoplanets using different observing methods and their respective approximate observational biases. The colors used for the detected exoplanets correspond to the colors of the curves indicating the observational biases. source image: Zhu & Dong (2021)

be that disks are frequently replenished by material from their surrounding clouds (Manara et al. 2018; Gupta et al. 2023). The timescale at which protoplanets acquire the majority of their mass is therefore still uncertain.

For planets to form, the dust in the disk must aggregate to larger and larger sizes. This process can get divided into the growth from dust into pebble-sized objects (from μm to mm and cm sizes), to the formation of planetesimals (m to km sizes), and ending with Moon- and planet-sized objects ($\gg$ km). During the growth into pebble- sized objects, the interaction between the dust and gas in the disk is an important factor regulating the dust distribution and therefore its growth. Small grains are well coupled to the gas and therefore move along with it on a slightly sub-Keplerian orbit supported by the gas pressure. When the particles exceed a certain size, they will no longer be supported by the gas pressure. Instead, larger grains will experience a headwind from the subkeplerian gas, causing them to slow down and drift inwards towards the central star. This effect is expected to remove dust from the disk and is therefore often referred to as the radial drift barrier (e.g., Laibe et al. 2012; Testi et al. 2014).

One way of overcoming the radial drift barrier is through the existence of dust traps in the

disk. These dust traps consist of local overdensities and pressure maxima in gas, strong enough to prevent the radial drift of larger grains. Such dust traps can form due to a variety of effects and can be either symmetric or asymmetric. A first potential cause of symmetric dust traps is the existence of dead zones in the disk (e.g., Ueda et al. 2019). These dead zones are areas in the disk where the MRI is suppressed and therefore have very low turbulent viscosity. Other symmetric options include snow lines (e.g., Vericel & Gonzalez 2020), zonal flows (see section 1.5.1) and the edges of planetary gaps (e.g., Stammler et al. 2023), although in the latter case planets must already have formed in some way. Such dust accumulations may result in a drag of the dust on the gas, called a back reaction (e.g., Lesur et al. 2023). Non-axissymmetric traps can come in the form of vortices and spirals induced by a companion (e.g., Bae et al. 2023). Modeling such mechanisms requires assumptions regarding the viscosity or efficiency of MHD winds in creating gaps. Constraining disk evolution is therefore crucial to understanding these processes.

There are, however, other barriers to dust growth that stem from interactions between dust grains. These are referred to as growth barriers (Testi et al. 2014; Lesur et al. 2023). For dust grains of sizes $\gtrsim$1 cm, it has been found that on average collisions tend to be erosive, destructive, or nonadhesive (Blum 2018). They are therefore also separately referred to as the erosion, fragmentation, and bouncing barrier. Several mechanisms have been proposed to overcome these barriers. The first is the occurrence of very low velocity collisions (e.g., Windmark et al. 2012; Garaud et al. 2013; Booth et al. 2018). However, Schräpler et al. (2018) find that the timescales for such slow collisions to significantly grow dust are too long compared to the radial drift and erosion timescales. In addition to this, porous aggregates covered with a monolayer of ice have been proposed as ways to facilitate dust growth (Potapov et al. 2020) .

A third way to overcome these barriers avoids collisional growth and instead proposes a gentle collection of solids into a dust overdensity, resulting in a local gravitational collapse. Such an overdensity could form in several ways. The first consists of secular gravitational instabilities, that is, the further gravitational collapse of clumps formed in a gravitationally unstable disk (Goldreich & Ward 1973; Youdin & Shu 2002; Chiang & Youdin 2010). Another option consists of dust grains that concentrate in turbulent vortices (Cuzzi et al. 2001). The third way to explain the formation of such clumps is through the so-called streaming instability (e.g., Lesur et al. 2023, and references therein). The efficiency of the streaming instability is dependent on the turbulence of a disk and therefore the viscosity (Chen & Lin 2020), once again highlighting the need to constrain the viscosity of the disk. The formation of planetesimals through the collapse of the local dust over-density appears to be supported by measurements of the structure and tensile strength of solar system comets, which is too low to be the result of collisional growth but consistent with such a gravitational collapse (Blum et al. 2017). The predominantly prograde rotation of planetesimal binaries in the Kuiper Belt also appears to support formation through streaming instabilities (Nesvorný et al. 2019).

Once planetesimal- sized objects exist, they continue to grow, be it through planetesimal accretion (Wetherill & Stewart 1989; Lissauer 1993) or, at higher masses, pebble accretion (Lambrechts & Johansen 2012). Once the object has grown to a sufficient mass, it will also start accreting the gas inside of its Bondi radius ($r_{\mathrm{B}} = 2GM/c_{\mathrm{s}}^2$). The eventual planet-sized bodies will also start to have gravitational interactions with the disk in which they are embedded. How these interactions take place depends on the mass of the planet as well as the evolutionary char-

acteristics of the disk. A comprehensive recent review of planet- disk interactions is given by Paardekooper et al. (2023). Planet migration is typically divided into three different types for viscous disks.

Type I migration applies to planets whose mass is too low to clear a gap in the disk. Such a planet feels the effect of two types of torque: a wave torque and a co-rotational torque. The wave, or Lindblad torque, occurs as the planet excites spiral density waves in the disk inward and exterior of its orbit. These spiral waves cause the outer disk to gain angular momentum at the expense of the planet's angular momentum, while the inner disk loses angular momentum to the planet (Goldreich & Tremaine 1980; Artymowicz 1993). The torque on the outer disk is generally expected to dominate, resulting in a loss of angular momentum and inwards migration (Ward 1997; Lubow & Ida 2010). The corotation torque is also known as horseshoe drag and occurs as gas that is close to the planet will be deflected by the planet's gravity. The material ahead of the planet's orbit is deflected inwards, thereby imparting angular momentum onto the planet, whereas material outwards, gains angular momentum (Masset & Casoli 2009). These deflections are typically referred to as horseshoe turns, due to their shape; hence the name horseshoe drag. The torque this will exert on the planet is dependent on the viscosity, density profile, and entropy profile of the disk and can drive the planet outward in case of a sufficient entropy gradient (e.g., Masset & Casoli 2009; Paardekooper et al. 2010). The angular momentum that can be imparted by the material orbiting at a radius similar to the planet is, in principle, finite, but given sufficient turbulence (and therefore viscosity), this angular momentum can be replenished (e.g., Masset 2001; Ward 2007; Paardekooper et al. 2011).

In type II migration, the planet's mass is large enough to carve a gap in the disk. This gap emerges as the previously mentioned wave torques increase the angular momentum of the disk outwards of the planet's orbit and decrease that of the disk inwards sufficiently to overcome the viscous spreading of the disk. In the traditional picture of type II migration, the gap is completely empty, and the planet will follow the viscous motion of the disk, which can result in slow inward migration in the inner disk and outward migration in the outer disk (Lin & Papaloizou 1986). However, nowadays it has become understood through simulations that gas can continue to flow across the gap (e.g., Bryden et al. 1999; Kley 1999; Masset & Snellgrove 2001), implying that type II migration is subject to the same torques as type I migration, but modified to account for the lower density in the gap (Paardekooper et al. 2023).

Type III migration, or runaway migration (Lubow & Ida 2010), occurs for already migrating planets. In this scenario, the motion of the planet will induce an additional asymmetry between the inbound horseshoe turn, which will migrate with the planet, and the trailing horseshoe turn, which will not. This effect modifies the torque on the planet due to the density gradient in the disk. If the horseshoe libration timescale is larger than the migration timescale, this can result in a runaway process for outward migration (Pepliński et al. 2008). It can also modify the torque exerted on the planet if the planet is capable of partially clearing its surroundings, even when there are no other gradients present (Masset & Papaloizou 2003).

The interaction between planets and MHD wind- driven disks has not been investigated as much due to the recent resurgence of this evolutionary framework. However, so far McNally et al. (2020), found the co-rotation torque to be negative. This happens since in their 3D MHD wind- driven models, accretion happens in surface layers with gas densities too low to influence

the migration of embedded planets near the mid-plane. There therefore appears to be a strong inward migration. Kimmig et al. (2020) used 2D simulations to study the migration of massive (Saturn to Jupiter mass) planets in MHD driven disks and found that the migration process differs significantly from the viscous case and can result in a strong outward type III migration under the right conditions.

Given the large implications of the different evolutionary frameworks on the different stages of planet formation, it is clear that disk evolution is an essential component of any theory of planet formation. In order to obtain such constraints, observational studies of disk populations are necessary.

1.4 Accretion onto young stars

Young Class I and II stars are known to grow as a result of material that is accreted from their circumstellar disk (see Hartmann et al. 2016, for a review). While the previously described evolutionary mechanisms explain how matter from the disk is driven towards the central star, they do not describe what happens once this material starts to interact with the central star. A first description was provided by Lynden-Bell & Pringle (1974) and is referred to as *boundary layer accretion*. In this paradigm, the inner disk extends down onto the stellar surface. Particles accreting across this boundary layer must slow down from the disk's rotational velocity to the rotational velocity of the star. The energy released in this process is emitted in the form of UV radiation.

Although this paradigm may still hold for more massive stars (Wichittanakom et al. 2020) and accreting protoplanets (Owen & Menou 2016), it cannot explain observations of classical T Tauri stars, which are the main subject of this thesis. The accretion process in CTTS is known to be variable (e.g., Costigan et al. 2012, 2014; Zsidi et al. 2022; Fischer et al. 2023) and nonaxis symmetric hotspots have been shown to be present on the stellar surface (e.g., Bouvier et al. 2007). Several emission lines (higher Balmer lines, Paβ, Brγ, He I, and NaD) in CTTS spectra display red-shifted absorption features, indicative of in-falling matter in between the line of sight and emitting regions (e.g., Appenzeller et al. 1988; Edwards et al. 1994; Folha et al. 1997). These absorption profiles show high velocity ($\gtrsim 200\,\mathrm{km/s}$) in falling material, consistent with free fall velocities (Bonnell et al. 1998). These emission lines also show complex variable profiles that cannot be explained with a simple emitting boundary layer (e.g., Hartmann et al. 1994). Such observations have given rise to the currently accepted paradigm in which the disk transfers mass to the star through *magnetospheric accretion*. Here I provide a short overview of our current understanding of the accretion process in young stars; a more in-depth review can be found in Hartmann et al. (2016)

1.4.1 Magnethosperic accretion

In this section, I detail what happens to material moving inward through the disk in the magnetospheric accretion paradigm, which represents our current understanding of accretion in CTTS. Material moving close to the star, to radii of about $\sim$ 0.1 AU, is strongly heated by stellar ra-

diation to temperatures of about $\sim$ 1500 K , causing the dust to sublimate (e.g, Bans & Königl 2012). As a result, a dust wall appears at this radius, which re-emits the stellar radiation that it absorbs and is therefore responsible for most of the NIR excess observed in Class II young stars (Dullemond & Monnier 2010; Hartmann et al. 2016).

The gaseous material continues on its inward trajectory until it is truncated by the magnetic field of the central star. Here, I present a similar argument for the size of the truncation radius as given by Bouvier et al. (2007) and Hartmann et al. (2016). The disk will be truncated at the radius where the gas ram pressure is balanced by the magnetic pressure $\rho v^2 \approx B^2/8\pi$, where v is approximately the Keplerian velocity ($v = (GM_\star/R)^{1/2}$). This can be rewritten in terms of the mass accretion rate as $\dot{M}_{acc} v/r^2 = B^2$, under the assumption of spherical infall. The magnetic field is then assumed to be a dipole, which means that the magnetic field scales with radius as $B(r) \simeq B_\star(R_\star/r)$. With these, the truncation radius $r_{\text{trunc.}}$ becomes

$$r_{\text{trunc.}} \approx \frac{B_\star^{4/7} R_\star^{12/7}}{(GM_\star)^{1/7} \dot{M}_{\text{acc}}^{2/7}} \approx 7.8 \left(\frac{B_\star}{1kG}\right)^{4/7} \left(\frac{M_\star}{0.5M_\odot}\right)^{-1/7} \left(\frac{\dot{M}_{\text{acc}}}{10^{-8} M_\odot/yr}\right)^{-2/7} \left(\frac{R_\star}{2R_\odot}\right)^{5/7} R_\star. \tag{1.24}$$

From this it can be seen that, using the fiducial values of $B = 1\,\text{kG}$, $M_\star = 0.5M_\odot$, $M_\star = 10^{-8}M_\odot/\text{yr}$, and $R_\star = 2R_\odot$, one finds a truncation radius of 7.8 stellar radii. In the case where the infall is not spherically symmetric, the coefficient (7.8) above is changed. If all the matter is concentrated in the inner edge of the disk, the density will be higher than in the spherical assumption made here; therefore the radius at which the ram and magnetic pressure are balanced will move inwards (Bouvier et al. 2007). The above result can therefore be seen as an upper limit on the truncation radius. Indeed, in literature a truncation radius of $r_{\text{trunc.}} = 5R_\star$ is often assumed (E.g., Gullbring et al. 1998; Shu et al. 1994).

Once material has passed this truncation radius, it is expected to follow the magnetic field lines at free-fall velocities towards the central star, forming into concentrated accretion columns. During this infall, the gas is heated to temperatures of a $\sim$ 8000 K, and starts to produce strong line emission. The exact process responsible for this heating is poorly understood, but it is likely magnetic in nature (Hartmann et al. 2016). This process is variable, both due to stellar rotation (on a different axis compared to the star) and potential unstable interactions between the magnetic field and the disk (e.g., Romanova et al. 2008). This variability is well illustrated in figure 1.6, where the morphology of accretion streamers in three-dimensional magnetohydrodynamics simulations at different phases of stellar rotation are shown. This change in morphology is reflected in the line profiles of the emission lines originating in the accretion streamers.

Due to being funnelled into accretion streamers, the material will impact the stellar surface at non-axissymmetric regions. In these regions the material in the accretion streamers will shock with that of the stellar surface. The energy contained in the accretion flow will be thermalized, heating the shock to temperatures on the order of $10^5 - 10^6$ K and therefore producing soft X-ray emission (Hartmann et al. 2016). Most of this emission is not observed because it is absorbed by the surrounding material and re-emitted at longer wavelengths. This results in an observable UV continuum excess emission originating at a hotspot on the stellar surface.

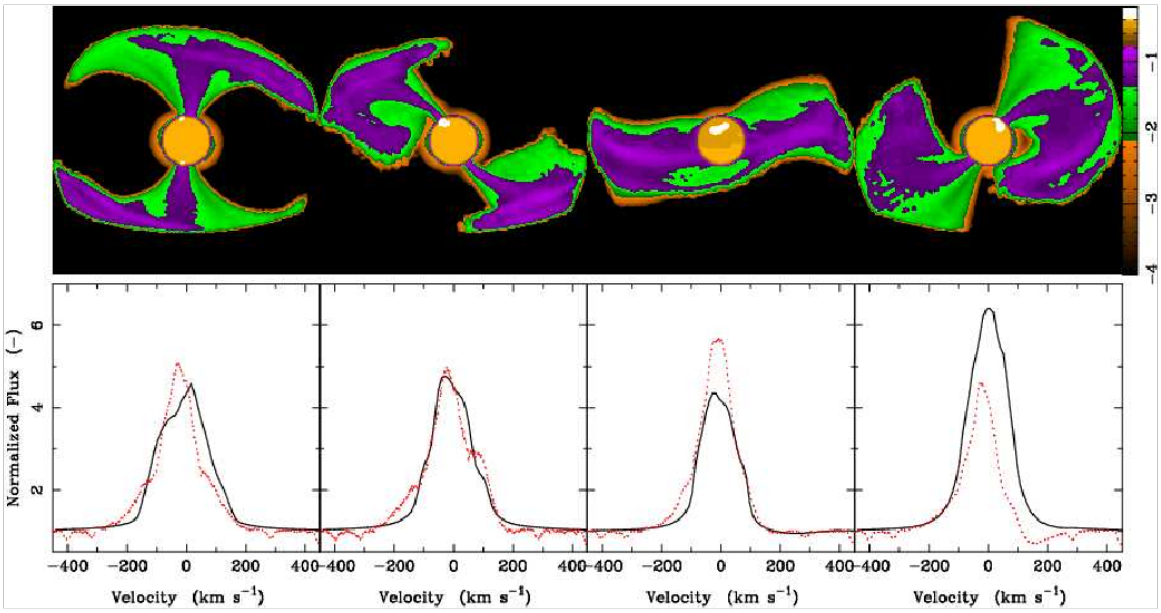

Figure 1.6: Top: Hα intensity maps for three-dimensional magnetohydrodynamics simulations assuming a dipolar magnetic field. The intensity scale is logarithmic with arbitrary units and represents the plane perpendicular to the line of sight. Bottom: corresponding model line profiles and observed line profiles of V2129 Oph. Source figure: Alencar et al. (2012a)

1.4.2 Measuring $\dot{M}_{acc}$

As mentioned in the previous section, the accretion hotspot on the stellar surface will release most of the energy obtained by accreting material during its free fall in the form of UV continuum emission. The kinetic energy obtained by a mass parcel m under free fall from the truncation radius to the stellar surface is

$$E_{\rm kin} = \frac{1}{2}mV_{\rm ff}^2 = \frac{2GmM_\star}{R_\star} - \frac{2GmM_\star}{r_{\rm trunc.}}, \tag{1.25}$$

where V_{ff} is the free fall velocity at the stellar surface. The accretion luminosity is the energy released per unit time, that is, $L_{\rm acc} = (1/2)\dot{M}_{\rm acc}V_{ff}^2$ if we assume all of the kinetic energy gets emitted. By applying the free fall velocity obtained from the equation 1.25 we find that the mass accretion rate can be expressed in terms of the accretion luminosity as

$$\dot{M}_{\rm acc} = \left(1 - \frac{R_\star}{r_{\rm trunc.}}\right)\frac{L_{\rm acc}R_\star}{GM_\star}. \tag{1.26}$$

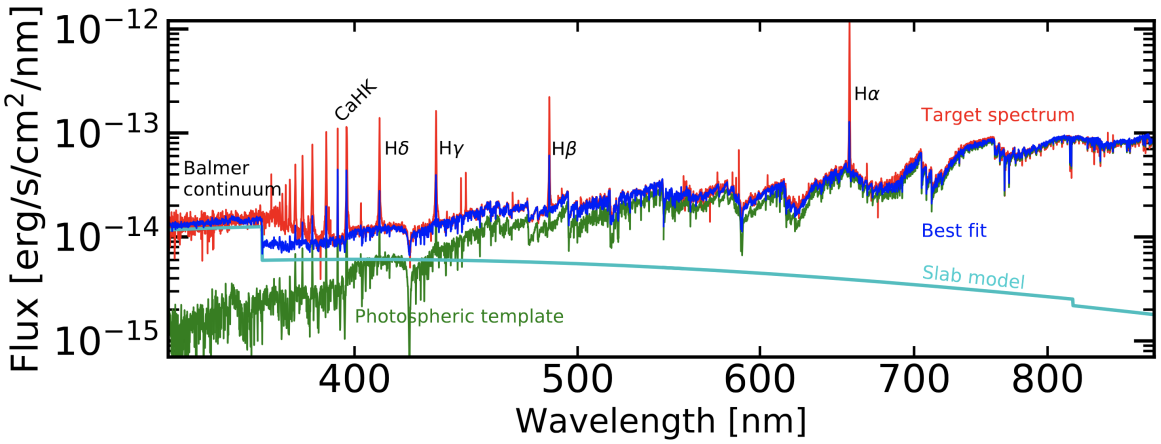

Figure 1.7: UV excess modeling of Ass Cha T 2-10. The extinction corrected target spectrum is shown in red. The best- fit photospheric template and slab model are shown in green and cyan, respectively. The best fit to the continuum emission consists of the sum of the photospheric template and the slab model and is shown in dark blue. Source image: Manara (2017)

If we then make the typical assumption for the truncation radius $r_{\rm trunc.} \sim 5R_\star$ (E.g., Gullbring et al. 1998; Shu et al. 1994), we obtain

$$\dot{M}_{\rm acc} = 0.8\frac{L_{\rm acc}R_\star}{GM_\star}. \tag{1.27}$$

Therefore, in order to measure the mass accretion rate of a CTTS we need to measure the accretion luminosity, stellar mass, and radius.

There are several ways to estimate the accretion luminosity of a CTTS. The first, most direct, way of estimating the accretion luminosity consists of modeling broad wavelength range spectra covering the Balmer jump. Figure 1.7 shows an example of such a modeling. It can be seen that both a photospheric template and a model of the accretion shock emission are used to reproduce a target spectrum. An additional aspect to such a modeling is not indicated in the figure. In order to model an observed CTTS, spectrum one needs to take into account the reddening due to the interstellar medium and adopt an extinction law such as the one from Cardelli et al. (1989). To represent the stellar contribution, spectra of non- accreting young stars are best used because of the chromospherically active nature of young stars. These active chromospheres produce emission in both the UV continuum and in a number of emission lines (Ingleby et al. 2011; Manara et al. 2017a). Model spectra do not include emission originating in the chromosphere, and the spectra of main sequence stars are chromospherically less active. Therefore, both lack the stellar UV emission present in young stars (Houdebine et al. 1996; Franchini et al. 1998). In fact, Ingleby et al. (2011) showed that the use of a field dwarf spectrum to measure accretion luminosity results in an overestimation of 0.05 $L_\odot$ for an M3 CTTS, which can significantly affect the accretion rates measured in low- accreting CTTS. An important constraint in such modeling of observed spectra is the veiling of the absorption lines present in CTTS spectra. Veiling refers

to the decrease in equivalent width of photospheric lines due to the continuum excess emission and is computed using

$$r_\lambda = \frac{EW(\text{phot.}, \text{Line}_\lambda)}{EW(\text{obs.}, \text{Line}_\lambda)} - 1 = \frac{F_{\text{acc.},\lambda}}{F_{\text{phot.},\lambda}}, \tag{1.28}$$

where r_λ is the veiling at a given wavelength, $F_{\text{acc.},\lambda}$ and $F_{\text{phot.},\lambda}$ are the flux from the accretion shock and photosphere, respectively, and $EW(phot., Line_\lambda)$ and $EW(obs., Line_\lambda)$ are the equivalent widths of absorption lines in the stellar photosphere and observed spectrum. The equivalent width is defined as:

$$EW(\lambda) = \int \frac{F_\text{c} - F_\text{s}(\lambda)}{F_\text{s}} d\lambda, \tag{1.29}$$

where the integral is computed across the wavelength range of a spectral line, F_c represents the continuum flux density, and F_s the flux density of the spectrum.

Several methods for modeling CTTS spectra have been used over the years (e.g., Ingleby et al. 2013; Manara et al. 2013a; Pittman et al. 2022). One such method that was particularly successful was the method of Manara et al. (2013a), which was used in a large number of accretion rate surveys (e.g., Alcalá et al. 2014, 2017; Manara et al. 2016a). This method is tailored for X-Shooter spectra and employs a grid of non- accreting Class III templates to represent the stellar emission. Its main benefit is that it provides a self-consistent method to constrain the stellar properties, extinction, and accretion luminosities simultaneously. For the emission coming from the accretion hotspot, Manara et al. (2013a) use a grid of hydrogen slab models (Valenti et al. 1993; Herczeg & Hillenbrand 2008; Manara 2014). Such models do not take into account the complex physics happening around the accretion shock but are computationally cheap and produce good agreement with the observations and more detailed models of the accretion shock. The accretion luminosity is obtained by integrating the accretion slab models. The choice of model is therefore critical, as the slab model extends beyond the observed X-Shooter range into the UV part of the spectrum, where a significant part of the accretion luminosities is emitted.

The method of Pittman et al. (2022) uses the more complicated shock models that take into account the fact that the shock is a consequence of material impacting the stellar surface and therefore is inhomogeneous. In particular, Pittman et al. (2022) uses the models of Calvet & Gullbring (1998), updated to include three components of different temperatures and mass flux, as was done by Espaillat et al. (2021) and Espaillat et al. (2022). This method is, however, more focused on constraining detailed characteristics of the accretion flow rather than surveying accretion properties, as they rely on prior constraints on the SpT (often adopting SpT's obtained with the method of Manara et al. (2013a)) and veiling and the three- component accretion column fit is only well constrained when spectra covering deeper into the UV (to 200 nm) are available. Such spectra can only be observed with space- based observatories and are therefore less available. So far it appears that the accretion luminosities found by Pittman et al. (2022) are higher in 7 out of 8 sources, by a factor of $\sim$ 1.5 to 8, than those found with the method of Manara et al. (2013a). Fiorellino in prep. compare a larger sample studied with both methods to reveal that there is a large scatter between the results obtained with both methods rather than a systematic offset. It therefore remains to be seen whether any adjustments need to be made to the slab models used by Manara et al. (2013a).

Both methods are largely reliant on the same set of Class III templates, with only 11 additional HST/STIS templates available. In both cases, however, the use of these templates introduces additional uncertainties, as the non- accreting stars may have different levels of chromospheric activity and the templates have their own observational uncertainties.

Even ground based spectra obtained with instruments such as X-Shooter are still observationally expensive. A less expensive alternative can be found in the use of photometry. In particular, the combination of U-Band photometry with other longer wavelength bands has often been used to first obtained a *U-band excess* which can then be converted into accretion luminosities (e.g., Gullbring et al. 1998; Rigliaco et al. 2011; Venuti et al. 2024). Alternatively, one could also use Hα photometry instead of the U-band (e.g., De Marchi et al. 2013; Venuti et al. 2014; Beccari et al. 2015). This method is naturally less accurate because of the large assumptions made on the relationship between the color excess and the actual accretion luminosity, as well as stellar properties and extinction.

A third method for constraining the accretion luminosity is also indicated in figure 1.7. This method consists of measuring the line luminosities of one or more emission lines present in the spectra of CTTS. Examples of such lines include the Balmer series, Ca II and He I lines. It therefore stands to reason that these lines correlate with the accretion luminosity. Several works have constrained these empirical correlations (e.g., Herczeg & Hillenbrand 2008; Rigliaco et al. 2012; Alcalá et al. 2014, 2017). The empirical relationships constrained by these works can be used to convert the line luminosities to accretion luminosities. However, to compute the line luminosities, the extinction needs to be taken into account. The extinction value used is ideally obtained through other means. Mass accretion rates can also only be computed if estimates of the stellar properties obtained through other means are available. This method is particularly useful to determine the accretion properties in regions with high interstellar extinction or of Class I young stars, as for such targets the UV part of the spectrum is hard to detect. Fiorellino et al. (2023) for example, were able to use the Brγ lines to constrain the accretion rates of Class I targets, although here the uncertainties remain high due to the poor constraints on the stellar properties.

Yet another method consists of the modeling of emission lines using magnetohydrodynamics simulations, as shown in figure 1.6 (e.g., Muzerolle et al. 1998, 2003). This method is not often preferred because of the high computational cost to compute such simulations and the assumptions that need to be made, such as the morphology of the magnetic field. Nevertheless, this method may still be of use to characterize low accretors, since for such targets the emission line luminosities will be dominated by chromospheric emission and the continuum excess method will be too uncertain due to both the chromospheric noise and uncertainties on the used non- accreting templates. Due to these reasons, Thanathibodee et al. (2023) used magnetospheric flow models to constrain the accretion properties of low accretors. Thanathibodee et al. (2023) took care to account for the contribution of the chromosphere.

1.4.3 Accretion variability

As previously mentioned, the accretion process in CTTS has long been known to be intrinsically variable. This variability comes in several different flavors, an overview of which is given in

1.4 Accretion onto young stars

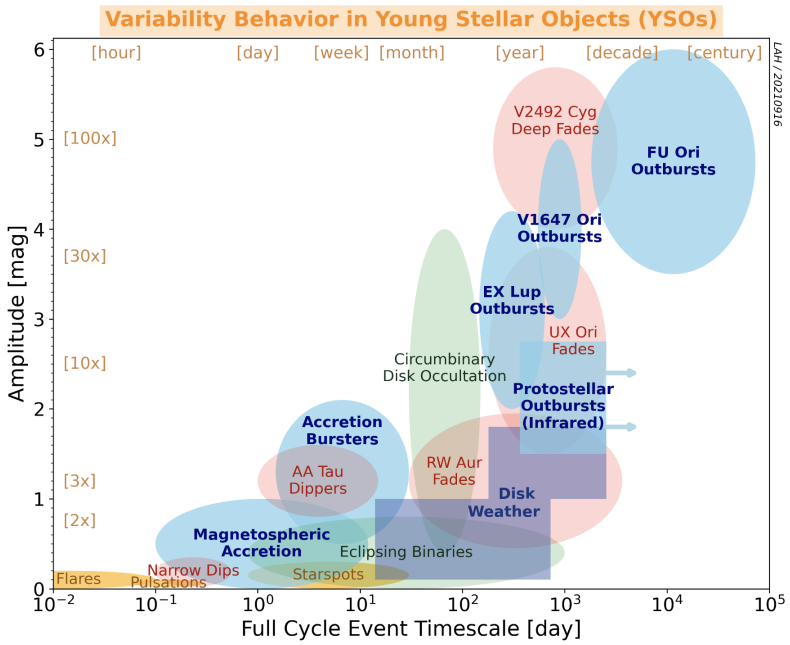

Figure 1.8: Timescale and amplitude for different types of variability observed in YSO. The routine variability originating from the disk and observed at NIR and longer wavelengths is colored purple under the name "disk weather". The accretion-related types of variability is indicated in blue. Extinction-related variability is indicated in red. Yellow indicates stellar phenomena, and variability related to binarity is indicated in green. The boundaries indicate typical ranges rather than precise delineations. source image: Fischer et al. (2023)

figure 1.8. Figure 1.8 also shows other sources of CTTS variability. Here, I will only focus on the accretion-related sources of variability that affect Class II YSOs. A more detailed review on the subject of variability in young stars can be found in Fischer et al. (2023).

magnetosphericaccretion variability is the most common form of variability and is present to some extent in all CTTS. This type of variability is driven by the interactions between the stellar magnetic field and the disk. The stellar magnetic field rotates around a different axis and on a different timescale than the disk. This will affect how much mass is loaded onto the accretion streamers. The timescale of this variability, therefore, often coincides with the rotational timescale of the central star (days to a week), with short duration flares (timescale of hours) (Hartmann et al. 2016; Fischer et al. 2023). The periodicity of this type of variability can differ significantly, with some targets displaying a clear quasiperiodicity linked to the rotational period of the star, while others appear to display more stochastic lightcurves. This is a likely consequence of different regimes for the interaction between the stellar magnetosphere and the disk, depending on where the magnetosphere perturbs the disk, magnetic field morphology, and the inclination of the stellar magnetic field with respect to the disk (e.g., Romanova et al. 2008, 2012; Blinova et al. 2016; Robinson et al. 2021). This type of accretion variability has a typical

amplitude of $\lesssim 0.5\,dex$ (e.g., Costigan et al. 2014; Biazzo et al. 2012; Frasca et al. 2015). This variability is accompanied by variability in the emission line profiles of the accretion tracing lines (e.g., Alencar et al. 2012b; Campbell-White et al. 2021).

Bursters display frequent accretion bursts. These bursts are observed as a sudden brightening in the light curve that can last 1 to 10 days (Stauffer et al. 2014; Cody et al. 2017). The time between such outbursts can vary greatly for different sources, as can the regularity. The amplitude of such bursts typically corresponds to a flux increase of 10 to 700% (Cody et al. 2017). These bursts can be observed in some CTTSs on top of the regular rotational magnetospheric accretion variability. Cody et al. (2017) found that $\sim$ 9% of the targets observed in ρ Ophiuchus and Upper Sco are bursters. These types of bursts are likely another form of stochastic behavior that can occur in magnetospheric accretion (Robinson et al. 2021).

EX Lup/EXor outbursts are named after the prototypical outbursts of EX Lup and have since been typically misnamed as EXor outbursts. These types of outbursts have amplitudes of several magnitudes and are interpreted as an increase in mass accretion rate by a factor of 10 to 100, that is, to accretion rates up to $10^{-7}\,M_{\odot}$/yr (e.g., Aspin et al. 2010; Audard et al. 2014). The duration of the outbursts can last from one to several months with a quiescent period between outbursts that lasts up to several years (Audard et al. 2014). During quiescence, the spectra and accretion rates of the EXor variables resemble those of normal CTTS. However, during an outburst, metallic lines such as Na, Ca, Fe, Si, Ti, and K, as well as the CO bandheads, which all originate from the disk, can be seen in emission (Lorenzetti et al. 2009; Rigliaco et al. 2020). The accretion tracing emission lines also become significantly stronger. EXor-type objects are rare, with only about 30 objects/candidates known as of 2016 (Hartmann et al. 2016). The mechanism responsible for such outbursts is still somewhat uncertain. A likely explanation proposed by D'Angelo & Spruit (2010, 2012) is that during the quiescence the accretion streamers perturb the disk beyond the co-rotation radius, which reduces accretion and results in a mass build-up in the inner disk. As this mass continues to build up, the truncation radius will shift inwards until pushing beyond it, resulting in the outburst. This idea is supported by the observations of Banzatti et al. (2015), who noticed a significant change in the CO emission of EX Lup after a burst compared to before. This is a possible result of a decrease in the mass in the inner disk. An alternative explanation was suggested by Zhang et al. (2015), and this scenario sees a large parcel of gas lifted up from the disk through the magnetic buoyancy instability, after which it accretes.

FU Ori outbursts represent the most extreme type of accretion outbursts, resulting in accretion rates as high as $\sim 10^{-4}\,M_{\odot}/yr$ (Hartmann & Kenyon 1996). These accretion rates are likely high enough to overcome the magnetic pressure and directly reach the stellar surface, resulting in boundary layer accretion (Hartmann et al. 2016). These types of outbursts are characterized by a sudden onset followed by a long-lasting, slowly decaying high accretion rate phase on the order of decades. Only very few true FU Ori bursters are known as they are photometrically hard to distinguish from other variables (Fischer et al. 2023). The rate of FU Ori outbursts was estimated

to be 10^{-4} outbursts per accretor per year (Hillenbrand & Findeisen 2015), although this number is still highly uncertain (see section 5.2 of Fischer et al. (2023); **?**). The outburst spectra of FU Ori stars lack features associated with magnetospheric accretion, such as red-shifted absorption components in the emission line profiles. Their spectra are dominated by their hot disk, rather than the stellar photosphere. Broad blue-shifted absorption lines are present in their spectra, indicating the presence of strong winds. The Hα line appears either fully in absorption or as a P Cygni type line profile. The Li line at 670 nm also appears stronger in absorption with regard to normal T Tauri stars (Hartmann & Kenyon 1996). The mechanism responsible for such large outbursts is still unknown. One proposed explanation suggests that the amplitude of the outburst can be explained by the disk being perturbed by a stellar fly-by (Vorobyov et al. 2021; Borchert et al. 2022). Borchert et al. (2022) find that the perturbing star itself also needs a disk to explain the long outburst lifetime.

V1647 Ori outbursts form a hybrid category between both FU Ori outbursts and EXor bursts. The amplitudes of these types of bursts fall between those typical of either category (Fischer et al. 2023). Spectroscopically, they may also display features of both categories. V1647 Ori, for example, showed a strong Paβ line and CO overtone bandheads in emission, typical of EXors and water, and He I absorption typical of FU Ori bursts (Briceño et al. 2004; Acosta-Pulido et al. 2007). There are also examples of stars that spectroscopically resemble EXors but have outburst durations more comparable to FU Ori's such as ASAS13b (Sicilia-Aguilar et al. 2017). The reverse situation has also been observed in VVV-v721, where the burst timescale appears to be short, but the spectrum is FU Ori-like (Guo et al. 2020). It therefore appears that there exists a sort of continuum between the FU Ori and EXor categories.

1.5 The high angular resolution revolution

The first images of protoplanetary disks were obtained with the Hubble Space Telescope (HST) (O'Dell et al. 1993; O'Dell & Wen 1994). These images, taken in photometric bands corresponding to strong emission lines (Hα, [OIII], [NII] 658.3 nm, [OI] + [SIII], and [SII]) revealed the outline of externally photoevaporated disks (proplyds) in the Orion nebula. Since then, observational techniques have made remarkable progress, allowing us to trace the continuum and emission scattered by or directly coming from the disk at much greater angular resolutions. Here, I briefly discuss these techniques as well as some of the recent breakthroughs they have provided for our understanding of protoplanetary disks. An in-depth review on this subject can be found in Andrews (2020).

1.5.1 mm Observations

The advent of (sub)millimeter interferometers, such as the SubMillimeter Array (SMA), Very Large Array (VLA), The NOrthern Extended Millimeter Array (NOEMA), and the Attacama Large sub-Millimeter Array (ALMA), has revolutionized our understanding of protoplanetary disks. Such interferometers are capable of obtaining higher angular resolution than single-dish

telescopes by combining multiple antennas. The light of pairs of receivers is combined in order to measure the interference produced between the two apertures. From the resulting interference pattern, one can measure the phase and amplitude of the so-called complex visibility $\mathcal{V}(u,v)$. Here u and v are, respectively, the distances x and y between the two receivers in units of wavelength. The interference is related to the observed brightness distribution through the van Cittert–Zernike theorem

$$\mathcal{V}'(u,v) = \int_{-\infty}^{\infty}\int_{-\infty}^{\infty} I_\nu(x,y)e^{-2i\pi(ux+vy)}dxdy \tag{1.30}$$

(e.g., Thompson et al. 2017). In other words, the complex visibility between the two antennas is equal to the Fourier transform of the sky brightness distribution at a position set by the baseline between the two antennas and the wavelength. Therefore, a large number of antennas need to be combined to fill the u,v plane and to more clearly recover the sky brightness distribution. Often observations are also conducted over several hours to allow for the rotation of the Earth to shift the baselines with respect to the sky brightness distribution. By nature of the Fourier transform, the smallest spatial resolution to which a set of interferometric observations of a source is sensitive is set by $\theta \sim \lambda/B_{\rm max}$ and the minimum is set by $\theta \sim \lambda/B_{\rm min}$ (Millour 2014). The angular resolution is therefore often given as $\theta \sim \lambda/B_{\rm max}$, although given the typically uneven sampling of the UV plane, the resolving power is non-circular and is often better described using the beam. Here I will, however, not further discuss these details. (Sub)millimeter interferometers are capable of both observing the continuum in different wavelength ranges and spectrally resolving molecular emission lines originating from the disk. This has proven to be revolutionary for our understanding of protoplanetary disks. Here, I will first focus on what this technique has provided for our understanding of disk masses, as this is one of the most important properties for this thesis.

Disk masses

The continuum (sub)mm emission of a protoplanetary disk originates from dust present in the disk. The continuum emission originating from a protoplanetary disk can therefore provide us with crucial information about the surface density distribution of the dust, dust mass, and dust properties. Doing so is, however, not straightforward, as many assumptions are often made (see (Miotello et al. 2023) and (Testi et al. 2014) for reviews). To illustrate this, I will follow the example of Miotello et al. (2023) to show how continuum emission is often used to derive the dust mass.

When neglecting scattering, the outgoing intensity of an isothermal plane-parallel layer of dust with homogeneous opacity is given by

$$I_\nu = (1 - e^{-\tau_\nu})B_\nu(T_{dust}), \tag{1.31}$$

where τ_ν is the optical depth at frequency ν and B_ν a black body spectrum at temperature $T_{\rm dust}$. In the optically thick limit, on the other hand, the intensity becomes that of a black body radiator $I_\nu = B_\nu(T_{\rm dust})$ and therefore only traces the temperature. However, the submm emission orig-

inating from the disk is often assumed to be optically thin ($\tau \ll 1$). In this limit, the outgoing intensity can be approximated as

$$I_\nu = \tau_\nu B_\nu(T_{\rm dust}) = \kappa_{\rm abs}\Sigma_{\rm dust}B_\nu(T_{\rm dust}), \tag{1.32}$$

where on the right hand the optical depth is expressed in terms of the surface density $\Sigma_{\rm dust}$ and opacity $\kappa_{\rm abs}$. If one assumes the temperature and opacity of the dust all throughout the disk to be well approximated by their averages $\bar{T}_{\rm dust}$ and $\bar{\kappa}$, then we can find an expression that relates the disk mass to the observed flux. For a source at distance d the flux is given by

$$\begin{aligned} F_\nu &= \frac{1}{d^2}\int 2\pi r I_\nu(r) dr \\ &= \frac{1}{d^2}B_\nu(\bar{T}_{\rm dust})\int 2\pi r \Sigma_d(r) r dr \\ &= \frac{B_\nu(\bar{T}_{\rm dust})\bar{\kappa}}{d^2}M_{\rm dust}. \end{aligned} \tag{1.33}$$

The above expression can be written in terms of $M_{\rm dust}$ to give the commonly used flux-to-mass conversion of Hildebrand (1983)

$$M_{\rm dust} = \frac{F_\nu d^2}{B_\tau(T_{\rm dust})\kappa_\nu}. \tag{1.34}$$

In order to apply this expression, one needs to constrain the average temperature and opacity of the disk. Typical values assumed in literature are $T_{\rm dust} = 20\,{\rm K}$ and $\kappa_\nu = 2.3(\nu/230\,{\rm GHz}){\rm cm}^2/{\rm g}$ (e.g., Ansdell et al. 2016; Manara et al. 2023; Bae et al. 2023). This temperature is justified by the fact that the majority of the mm emission originates from the cool, nearly isothermal outer regions of the disk (Tazzari et al. 2021). Dust mass estimates are therefore based on an assumed uniform temperature and opacity and the assumption that the dust is optically thin. The influence of scattering is also neglected. Particularly the assumption that disks are optically thin in the most commonly used wavelength ranges in disk surveys (e.g., ALMA Band 7 $\lambda \sim 0.95\,{\rm mm}$ (Ansdell et al. 2016) ALMA Band 6 $\lambda \sim 1.3\,{\rm mm}$ (Ansdell et al. 2018)) has recently come under scrutiny (e.g., Ribas et al. 2020; Macías et al. 2021). The recently introduced ALMA Bands 1 and 2 as well as the currently under construction ngVLA will allow for disks to be observed at longer wavelengths, where the disk is less optically thick, and could alleviate this issue (Tazzari et al. 2021). Despite these drawbacks, dust masses have been the most common way to estimate disk masses. Converting dust masses to disk masses is typically done by assuming a gas-to-dust ratio of 100, consistent with ISM values (e.g., Manara et al. 2023; Bae et al. 2023). The validity of this assumption is, however, uncertain, as the dust in protoplanetary disks is expected to evolve significantly (Birnstiel et al. 2012; Rosotti et al. 2019). Since the gas comprises the majority of the mass in the disk it may therefore provide a better tracer for the bulk of the disk mass.

The ability of (sub)mm interferometers to spectrally resolve emission lines present in the gaseous component of protoplanetary disks allows the gas mass of the disk to be constrained. Most of this gas is made up of hydrogen (atomic and molecular $\sim 70\%$) and helium ($\sim 28\%$)(Bae et al. 2023). At the densities and temperatures in most of the disk, atomic lines from hydrogen

are hardly observable. The emission of H_2 is also faint due to its lack of dipole moment, weak quadrupole moment, and the large difference in the energy levels of its ground-state transition requiring high temperatures to be exited (Field et al. 1966; Miotello et al. 2023). Constraints on the gas properties of disks must therefore come from less abundant tracers. A detailed review on the various molecular tracers used to constrain the gas properties of protoplanetary disks can be found in Miotello et al. (2023). Here I will briefly mention some of the most important tracers.

Due to its dipole moment, the less abundant H_2 isotopologue HD has a rotational emission line at 112 μm. Despite the low relative abundance with respect to H_2 and the fact that HD does not directly trace the bulk of H_2, HD can still be used to constrain the disk gass mass by using physical-chemical models (e.g., Kama et al. 2016; Trapman et al. 2017). No current or planned facilities are capable of detecting the 112 μm HD line.

A commonly used gas tracer is CO, which is the second most abundant molecule after H_2. Its chemistry is also well understood, allowing it to have been implemented in physical-chemical models. The most abundant isotopologues ^{12}CO tend to be optically thick and can therefore be used to study the kinematics and temperature of disks. Less abundant CO isotopologues, such as ^{13}CO, C^{18}O and ^{13}C^{17}O are optically thin and therefore trace the column density and could be used to estimate disk masses (e.g., Miotello et al. 2016; Ruaud et al. 2022; Booth et al. 2019). To estimate the bulk disk mass from such tracers, physical-chemical models are needed to extrapolate the bulk disk mass. A significant uncertainty in these models stems from the poor constraints on the C/H ratio. A potential solution to this was proposed by Trapman et al. (2021), who showed that the $N_2H^+(3-2)/C^{18}O(2-1)$ line ratio is proportional to the *CO*-to H_2 abundance. An additional constraint on these models can be found in the [OI] 63.2 μm line, which constrains the surface temperature of the disk (Kamp et al. 2010, 2011). The downside of CO mass estimates with respect to dust mass estimates is that longer integration times are needed to detect CO. The sample of disk masses constrained with CO is therefore much smaller than the available dust mass estimates.

Disk morphology

One of the most significant breakthroughs provided by mm interferometry came when ALMA was able to observe the iconic image of HL Tau shown in figure 1.9 (ALMA Partnership et al. 2015). This image revealed that HL Tau possesses complex annular substructures in its continuum, with gaps as narrow as 3.5 au being revealed. The continuum emission is expected to trace the distribution of the dust in the disk. Since then, a large number of disks have been observed at high angular resolutions, revealing that such substructures are more common than initially expected (e.g., Andrews et al. 2016; Isella et al. 2016; Long et al. 2018; Huang et al. 2018a). Such substructures have also been observed in Class I disks, suggesting that they form early during the lifetime of a disk (Ohashi et al. 2023). Similar substructures have also been observed in the molecular emission of these disks and do not necessarily overlap with the structures seen in the dust (e.g., Law et al. 2021). In addition to annular rings and gaps, spirals, asymmetries, and cavities have also been detected. The latter of these substructures was already theorized based on the typical transition disk SEDs (Strom et al. 1989).

Substructures are most commonly identified in massive disks around massive stars. This is

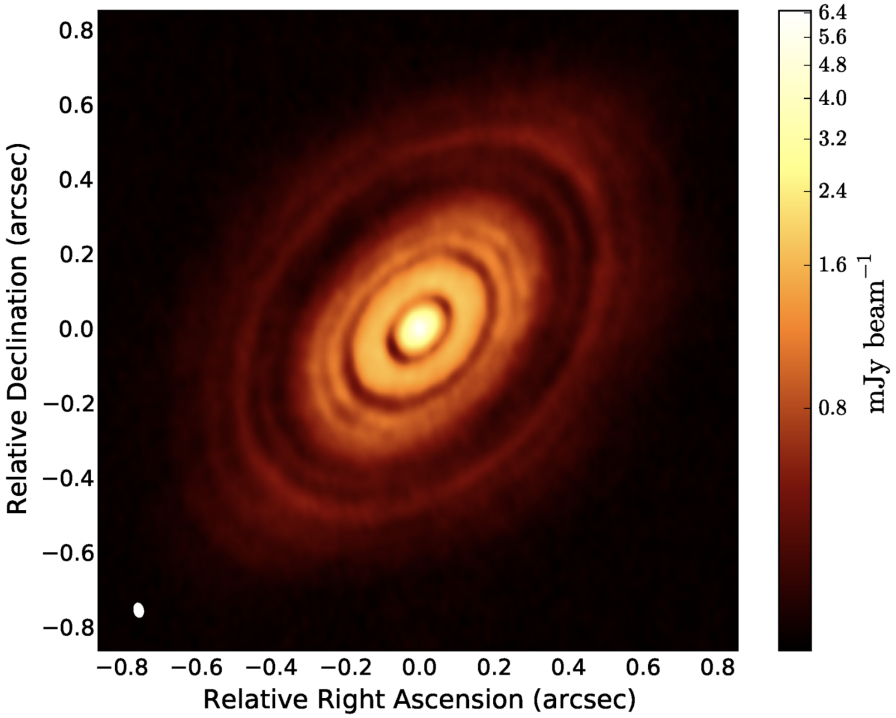

Figure 1.9: Left:Alma band 6 image of HL tauri first presented by ALMA Partnership et al. (2015).

most likely due to observational bias (see section 4.2.1). Parker et al. (2022) studied the complete sample of disks observed with ALMA from the ALMA archive and found that about $\sim$ 27% of their sample of 798 observations display substructures. This fraction increases when excluding sources observed at lower angular resolution. As it stands, it remains plausible that the majority of protoplanetary disks display some form of substructure.

The detection of these substructures has resulted in a large number of mechanisms being proposed in order to explain them. A detailed and complete explanation of each of these is beyond the scope of this chapter, but a comprehensive review can be found in Bae et al. (2023). Here I will briefly discuss two of the most intriguing possibilities; other potential causes are discussed in the introduction of chapter 4.

One potential mechanism that could explain a large variety of substructure morphologies is the presence of embedded protoplanets in the disk. Such an embedded planet could be responsible for carving gaps and cavities, inducing a spiral wake and creating a vortex, resulting in an over-density that shows as an asymmetry in the disk. The embedded planet hypothesis was already proposed by ALMA Partnership et al. (2015), who presented the first image of HL Tau. Since then, several works have attempted to estimate the masses of these hypothetical embedded planets based on the observed substructures (e.g., Rosotti et al. 2016; Lodato et al. 2019; Toci et al. 2020; Wang et al. 2021; Ruzza et al. 2024). However, very little of these hypothetical planets has been confirmed through other means. So far protoplanets have only been directly ob-

served in one system: PDS70 (Keppler et al. 2019; Müller et al. 2018; Mesa et al. 2019; Benisty et al. 2021) There are also two additional candidate direct detections that lack follow-up confirmations: AS209 (Bae et al. 2022) and AB Auriga (Currie et al. 2022). Less direct confirmation of embedded planets can come from the gas kinematics of the disk. This was, for example, done by Pinte et al. (2019), who found a velocity perturbation in the CO moment maps of HD 97048, at a position consistent with a gap in the continuum image. In an earlier work, Pinte et al. (2018) detected a planet with the same method, although the position of this planet is located at an orbit outside the range where continuum flux is detected. Only one other gap-carving planet has been confirmed through kinematics and is located in HD 163296 (Izquierdo et al. 2022). In addition to this, a potential planet was detected kinematically in the inner cavity of 2MASS J16042165-2130284 (Stadler et al. 2023). It therefore remains very uncertain whether all of the observed gaps and cavities have been carved by embedded protoplanets.

A second explanation for the observed annular substructures comes in the form of the same MHD winds that may be driving disk evolution. Several works (e.g., Béthune et al. 2016; Riols et al. 2020) found that the MHD wind naturally leads to the development of annular gaps in simulations. This occurs because the vertical magnetic field lines tend to concentrate in regions with a surface density minimum. This enhances the MHD winds in these localized regions, resulting in the so-called zonal flows. If the MHD winds deplete the material in these regions faster (both through the wind itself and by removing angular momentum) than it gets replenished from the outer disk, a gas gap is formed (Suzuki et al. 2016). Rings with higher gas density will form pressure maxima that are capable of trapping dust particles. This will only result in dust rings if the radial drift timescale is shorter than the depletion timescale, since without drifting inwards, the dust particles will remain in their initial distribution (Takahashi & Muto 2018). A complete overview of MHD simulations in protoplanetary disks and how substructures may arise as a consequence of MHD effects can be found in Lesur et al. (2023).

1.5.2 IR and optical high resolution observations

The advent of adaptive optics has allowed instruments such as VLT/SPHERE, Gemini/GPI, and SUBARU/HiCIAO to obtain diffraction rather than seeing limited observations at NIR and visible wavelengths. A description of this imaging technique and a detailed review of what it has meant for our understanding of protoplanetary disks can be found in Benisty et al. (2023). For the currently largest class of telescopes ($d \sim 8$ m), this implies that we can observe things on a scale of ~ 4 au at 100 pc. It is therefore possible to characterize protoplanetary disks in the visible and NIR at scales as obtainable with ALMA in the mm regime. At these wavelengths, however, the emission from the central star tends to be larger than that of the disk, resulting in contrast issues. In order to prevent this, a chronograph is employed to block the light from the central star. This is typically not sufficient, and a speckle halo will remain in the captured image. Three different post-processing techniques can be employed to remove the remaining part of the central star's point spread function (PSF): Angular Differential Imaging (ADI), Reference star Differential Imaging, Polarization Differential Imaging (PDI) and Spectral Differential Imaging (SDI).

In the ADI technique, several images are taken during a night of observing (Benisty et al. 2023). During these observations, the de-rotator of the instrument is turned off. This allows

the field of view to rotate with respect to the instrument due to the Earth's rotation, while the instrumental PSF will remain stable. This allows for the real signal resulting from the stellar environment to be distinguished from that of the PSF. The main advantage of ADI with respect to DI is that the stellar contribution is mitigated using information from the science star itself. However, ADI is not ideal for observing sources with a large spatial extension. Such an extended structure may overlap with itself in the images observed at different angles. This leads to so-called *self-subtraction*, where the real signal will be suppressed. For protoplanetary disks, this effect will affect the signal mainly along the minor axis (e.g., Milli et al. 2012; Ginski et al. 2016).

The RDI technique, as the name suggests, requires simultaneous observation of a reference star (Boccaletti et al. 2021; Benisty et al. 2023). The reference star should have similar brightness and spectral properties as the science target and ideally be observed shortly after or before the science observations. This reference star observation allows one to recover the instrumental and sky PSF of the central star, under the assumption that the sky conditions remain the same. The stellar PSF can then be subtracted from the science observations.

The PDI technique relies on polarization filters or a polarizing beam splitter implemented in the instrument (Kuhn et al. 2001; Benisty et al. 2023). This allows for the linearly polarized light in two different directions to be measured. That is, such instruments typically measure the terms I, Q, and U of the Stokes vector ($S = [I, Q, U, V]$, where I is the total intensity, Q the vertical and horizontal linear polarized light, U the linear polarized light, and V the circular polarized light) for each position on the detector. To account for the low level of polarization and instrumental polarization, the total intensity and polarized intensity are measured in an area of the image where the contribution of both is expected to be dominant. The contribution of both to the polarized intensity is then assumed to scale with the total intensity of the stellar light. Under this assumption, one can subtract the contribution of the stellar and instrumental polarization from the polarized images (Canovas et al. 2011). The corrected polarized components are then typically combined in either the polarized image $PI = \sqrt{Q^2 + U^2}$ or azimuthal images

$$\begin{aligned} Q_\phi &= -Q\cos 2\phi - U\sin 2\phi \\ U_\phi &= Q\sin 2\phi - U\cos 2\phi \end{aligned} \tag{1.35}$$

where ϕ is the azimuthal angle (Benisty et al. 2023). PDI has been particularly successful when it comes to imaging circumstellar disks, with the majority of recent observations using this technique (Benisty et al. 2023). The light from the central star will be scattered by large dust grains in the disk, which polarizes the light. The amount at which light gets polarized depends on the scattering angle. The highest amount of polarized light is seen when the light is scattered at a 90 deg angle.

Finally, SDI requires the implementation of an integral field spectrograph, allowing images at different wavelengths to be simultaneously recorded Benisty et al. (2023). The size of stellar PSF scales with wavelength, whereas the size of any resolved continuum source in the image remains constant. By rescaling the images taken at different wavelengths, one can subtract the stellar spectrum. The benefit of this technique with respect to ADI and RDI is that the PSF subtraction relies on simultaneous observations of the science source.

More than 100 sources have been observed using the PDI technique (Benisty et al. 2023), and this number is increasing drastically due to the recent DESTINYS survey (e.g., Ginski et al. 2024; Garufi et al. 2024). This has revealed the same categories of substructures as in (sub)mm imaging. However, the substructures observed in optical and NIR wavelengths do not always coincide with those observed at millimeter wavelengths. Some disks that display rings at millimeter wavelengths may display spirals at NIR wavelengths (e.g., WW Cha (Kanagawa et al. 2021; Benisty et al. 2023)) and for others that display rings at both wavelengths, there may be no correspondence between the location and sizes of the rings (e.g., TW Hya (van Boekel et al. 2017; Andrews et al. 2016)). This is possible since both types of observation trace different materials. NIR and visible light trace the upper layer of small dust grains. This is the case because the dust is optically thick at these wavelengths. The dust grains in this layer should be small or porous, as they need to be well coupled to the gas to reach their elevation above the midplane, allowing efficient vertical mixing processes to elevate them above the midplane to heights several times the pressure scale height (Lagage et al. 2006). The mechanisms proposed to explain these substructures generally overlap with those observed at millimeter wavelengths. Of the more than 100 observed disks, the $\sim$ 80 disks have been well resolved and detected. About 45 of these disks show clear detections of substructures, with the remaining disk only having a small radial extent, potentially explaining their lack of substructures (Benisty et al. 2023). The currently available sample is biased towards brighter, more massive stars. This bias comes from the minimum brightness needed for the AO systems of the telescope to function properly.

In addition to the substructures also observed at millimeter wavelengths, one additional structure has been revealed using adaptive optics: azimuthal shadows. The currently accepted explanation is a misalignment or warp in the inner disk. This explanation was first proposed to explain the shadows observed in HD142527 by Canovas et al. (2013). This was first reproduced using radiative transfer models (Marino et al. 2015) and then possibly imaged by Avenhaus et al. (2017). SU Aur is one example of a source that shows similar features (Ginski et al. 2021), and where the existence of a misaligned inner disk was directly confirmed using the CHARA array (Labdon et al. 2019). Such perturbations to the inner disk can potentially be formed by late-time interaction with material from the environment (Dullemond et al. 2019), an inner binary (Pinilla et al. 2015, 2018a), a massive planet in the inner disk (Benisty et al. 2018) or a vortex (Varga et al. 2021).

One of the most significant discoveries made through the use of adaptive optic imaging consists of the first direct detection of forming protoplanets in PDS70. A first exoplanet, PDS70b, was detected using polarized light images obtained with the VLT/SPHERE instrument by Keppler et al. (2018). By applying the SDI technique to VLT/MUSE observations, Haffert et al. (2019) managed to obtain Hα images of the system, confirming the detection of PDS70b and detecting a second giant planet, PDS70c. Benisty et al. (2021) detected a circumplanetary disk around PDS70c using ALMA continuum observations. Images showing direct detections of PDS70b and circumplanetary disk around PDS70c are shown in figure 1.10.

A completely different technique to obtain high angular resolution observations of YSOs comes in the form of optical and IR interferometers (O/IR interferometers). These instruments make use of the same principles as mm interferometers, combining the light obtained in multiple apertures to obtain higher angular resolutions. However, optical and IR interferometers are

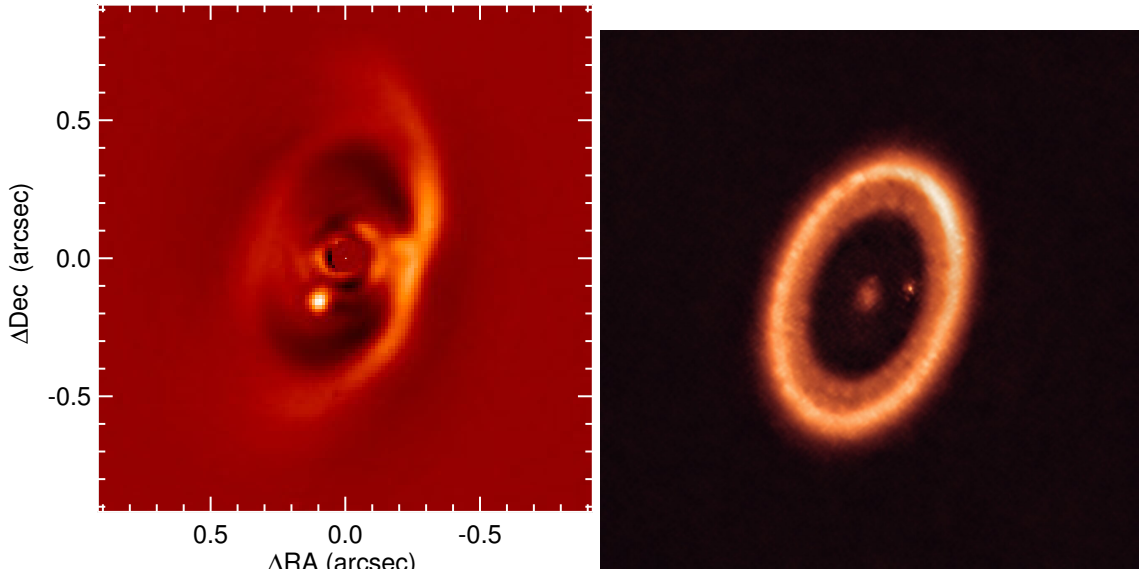

Figure 1.10: VLT/IRDIS image of PDS70 obtained using the ADI technique showing PDS70b inside the gap of the disk. The center of the image has been masked out for display purposes. source image: Müller et al. (2018). Right: The disk of PDS70 as observed with ALMA. The small point inside the inner cavity is the circumplanetary disk around PDS70c Image credit: ALMA (ESO/NAOJ/NRAO)/Benisty et al. (2021)

more limited due to the lower number of apertures that are typically combined and atmospheric turbulence affecting the phases of the observed visibilities (e.g., Renard et al. 2011; Thiébaut & Young 2017; Eisenhauer et al. 2023). Current interferometers such as VLTI and CHARA have baselines of $\sim$ 200 m [5] and $\sim$ 300 m[6] respectively, resulting in angular resolutions on the order of a few mas (Eisenhauer et al. 2023). At this resolution, O/IR interferometers are capable of resolving features at scales of 0.1 au in nearby star-forming regions.

In the NIR continuum, interferometry traces the dust sublimation front in the inner disk. This allowed a correlation between the size of the dust sublimation front and stellar luminosity to be established, showing the dust sublimation temperatures to be somewhere between 100 and 200 k (e.g., Monnier & Millan-Gabet 2002; Kluska et al. 2020). O/IR interferometers are also capable of resolving the Brγ line. This has enabled GRAVITY Collaboration et al. (2024) to show that this emission line most likely originates from an MHD disk wind that is launched very closely to the star, within the dust sublimation radius. These are but a few examples of how O/IR interferometers is providing insights into the very inner disks of young stars.

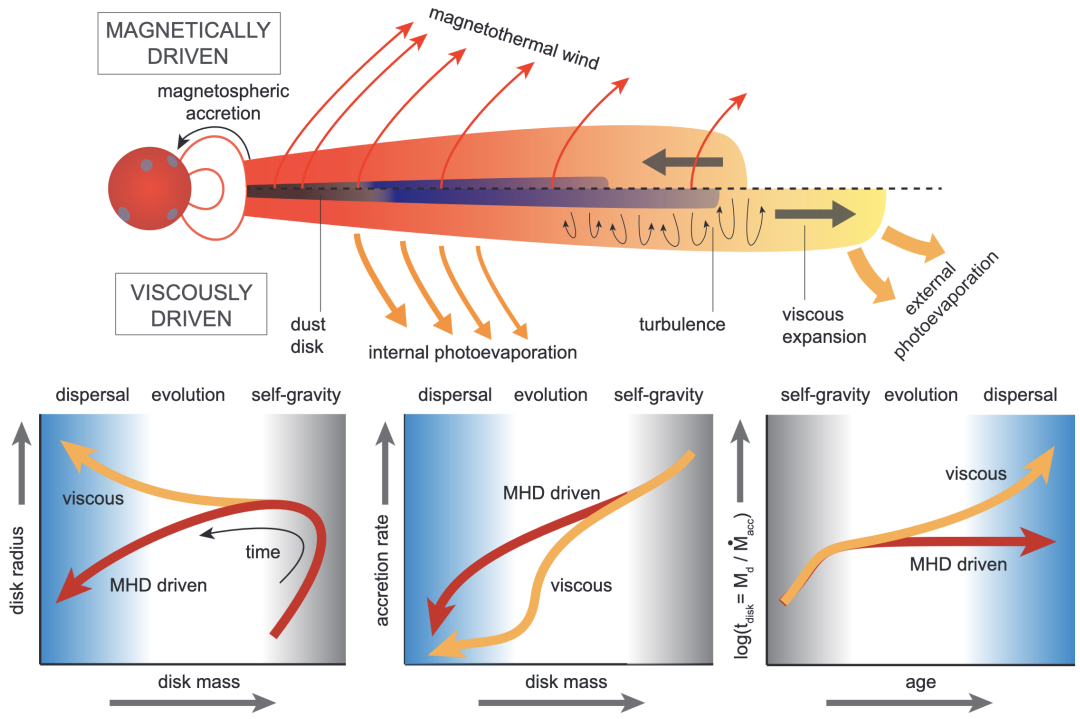

Figure 1.11: Illustration of the two main paradigms of disk evolution. The upper half of the disk in the top panel shows the MHD-wind driven paradigm in which angular momentum is lost in the wind. The bottom half of the disk shows the viscous model in which angular momentum is redistributed due to turbulence. The potential for internal photoevaporation to contribute to the disk's dispersal is also highlighted. The three bottom panels illustrate potential observational diagnostics. Source Image: Manara et al. (2023)

1.6 Observational constraints on disk evolution

In sections 1.2 we described how the predictions of the viscous and MHD wind disk evolution paradigms differ. These predictions are summarized in figure 1.11. An in-depth review discussing the observational constraints on disk evolution is provided by Manara et al. (2023). Here, I provide some of the key points presented in the review of Manara et al. (2023).

1.6.1 Disk Radius

On the bottom left-hand panel of figure 1.11, it can be seen that the disk radii are expected to evolve differently in both observational scenarios. Measuring the radii of disks at different ages could therefore provide a useful constraint on the evolutionary paradigm. To measure disk radii, one ideally needs spatially resolved observations tracing the surface density profile of molecular

[5] https://www.eso.org/public/teles-instr/paranal-observatory/vlt/vlti/
[6] https://www.chara.gsu.edu/instrumentation/chara-array

hydrogen, since it comprises most of the disk mass. However, as mentioned in section 1.5.1, the emission of molecular hydrogen is too faint. The first, most easily accessible tracer consists of the dust continuum emission, which is traced by the millimeter wavelength flux. Such a study was, for example, carried out by Hendler et al. (2020), who found a decrease in median disk radii with age for the Ophiuchus, Lupus, Taurus, Chamaleon I, and Upper Scorpius star-forming regions. This work confirmed the previously obtained result obtained by Barenfeld et al. (2017), who found that the disks in the older Upper Scorpius region are smaller than those in the younger Taurus, Ophiuchus, and Lupus regions. Tazzari et al. (2017) on the other hand, found that the disks in the Lupus region have larger radii than those in the younger Taurus and Ophiuchus regions.

However, the findings of Hendler et al. (2020) do not rule out the possibility that viscous spreading takes place in protoplanetary disks. Dust is affected by both grain growth and radial drift; the latter describes the spiraling in of the dust towards the central star as a consequence of the headwind the dust experiences with respect to the gas.

Rosotti et al. (2019) modeled the dust surface density evolution in viscous disks and found that although radial drift plays a significant role initially, the dust radii are still expected to increase. Rosotti et al. (2019), however, point out that in order to observe this expansion, one needs to use a definition of the outer radius based on a high fraction of the total flux. A definition based on a lower percentage of the flux will result in the disk appearing to shrink, due to both the surface density in the inner disk decreasing and such a radius being a measure of where the grain sizes are larger than a threshold set by the opacities. This effect is illustrated by figure 1.12, where it can be seen that while the surface brightness distribution extends further and further, the 95% radius increases and the 68% radius shrinks. The precise percentage of the flux that needs to be used to measure viscous spreading is determined by the disk's viscosity α. To trace such a large percentage of the flux, higher sensitivity observations than currently available are needed. Zagaria et al. (2022b) performed a similar study, comparing the evolution of disk radii in both the viscous and MHD wind-driven cases, confirming the findings of Rosotti et al. (2019) and showing that in the MHD wind case dust radius stay constant or decrease with time. Zagaria et al. (2022b) compared these results with available ALMA band 7 observations in Lupus, Chamaeleon I, and Upper Scorpius and found the disk radius to be compatible in both cases.

Potential other tracers of the disk size can be found in the line emission of various other types of molecules in the disk. In particular, disk radii have been measured using the emission of ^{12}CO, ^{13}CO, C^{18}O, and CN. Barenfeld et al. (2017) measured the CO radii in their sample of ALMA observation in Upper Scorpius. Here, the CO radii of only 7 disks out of a sample of 57 could be well constrained, due to a lack of detection in most targets, highlighting the difficulty of measuring CO radii. Najita & Bergin (2018) combined literature gas disk radii obtained from different tracers and saw indication that the disks around Class II sources are larger than those of Class I/0 sources. This result appears to support the viscous model but is contradicted by the small disk radii found by Barenfeld et al. (2017) in Upper Scorpius. The study of Najita & Bergin (2018) was also limited by the low number of targets, inhomogeneity of the tracers used to measure the radius, and bias towards brighter objects. Thermo-chemical modeling is needed to interpret observations of different tracers, as the depletion of certain molecules may affect our interpretation (Miotello et al. 2023). Trapman et al. (2020) and Trapman et al. (2022) performed

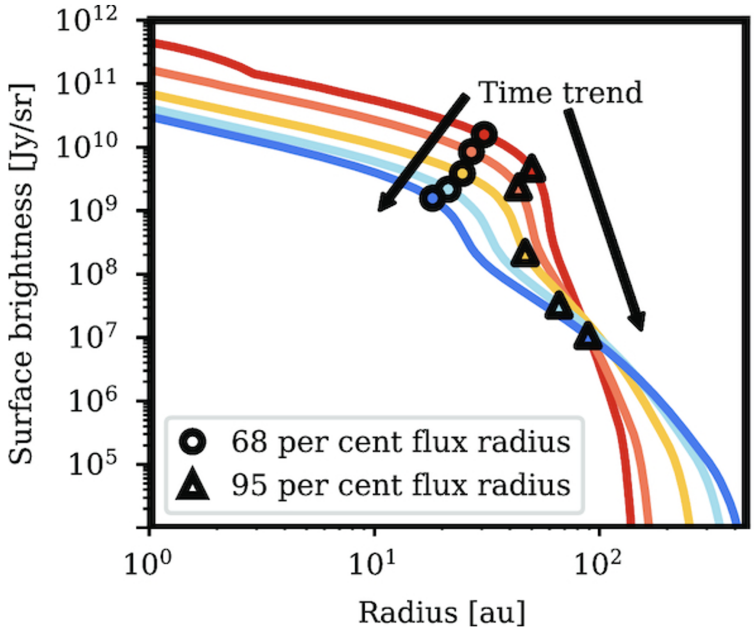

Figure 1.12: Surface brightness as a function of radius for different evolutionary ages of a viciously evolving disk (0.1, 0.3, 1 ,2 , and 3 Myr). As time passes, the 68% radius can appear to shrink, while the 95% radius grows. Figure adapted from Rosotti et al. (2019)

such simulations for the viscous and MHD cases, respectively, and found the expected effect of an expanding CO radii in the viscous scenario and a contracting CO radii in the MHD case. However, both models are unable to explain the observed small CO radii in Upper Scorpius.

Observations at sufficient depth and angular resolution are time-consuming and, therefore, limit sample sizes. To overcome this hurdle, Zagaria et al. (2023) proposed using ^{12}CO fluxes instead of radii, as they showed that these scale with the disk surface area. Doing so drastically increases the sample that can be used, although this has still proved to be insufficient as a result of uncertainties on the carbon depletion process and initial conditions. Future surveys have the potential to provide both the needed larger sample of ^{12}CO fluxes and reduce the uncertainties on carbon depletion. More systematic studies of gas disk radii are thus needed to constrain the mechanism driving interplanetary disk evolution.

1.6.2 Constraints from accretion properties

The central and rightmost panels in the bottom Figure 1.11 highlight some of the different expectations regarding the evolution of the disk mass and mass accretion rate in the viscous and MHD wind-driven scenario. Figure 1.13 shows the measurements of $\dot{M}_{\rm acc}$, as a function of $M_{\rm disk}$. Here, it can be seen that there indeed appears to be a correlation between both quantities, but the scatter on this correlation is large.

The first hints that such a correlation indeed exists were found when Mendigutía et al. (2013) studied the accretion rates and disk masses in both CTTS and Herbig Ae/Be stars. Since then,

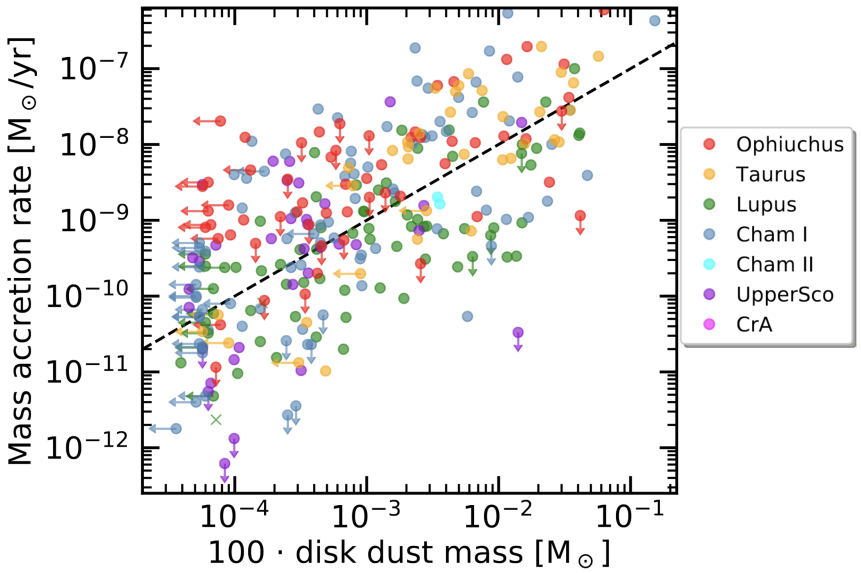

Figure 1.13: Mass accretion rate as a function of disk mass for the sample collected by Manara et al. (2023). The disk mass here is taken to be 100 (based on the typical ISM gas-to-dust ratio) times the dust mass. The dashed line indicates an accretion timescale of $t_{\rm acc} = M_{\rm disk}/\dot{M}_{\rm acc} = 1$ Myr and does not represent a fit to the data. Figure adapted from: Manara et al. (2023)

near-complete spectroscopic accretion rate surveys in the Chamaeleon I (Manara et al. 2016a, 2017b) and Lupus (Alcalá et al. 2014, 2017) regions have allowed for the confirmation and thorough characterization of the empirical correlation between $\dot{M}_{\rm acc}$ and $M_{\rm disk}$ (Manara et al. 2016b; Mulders et al. 2017). These studies could be performed due to the larger samples of disk masses obtained through large ALMA surveys in Chamaeleon I (Pascucci et al. 2016) and Lupus (Ansdell et al. 2016). Similar studies have also been performed in the younger L1688 region of Ophiuchus (Testi et al. 2022) and the older Upper Scorpius region (Manara et al. 2020). Testi et al. (2022) found that the overall relation between $\dot{M}_{\rm acc}$, and $M_{\rm disk}$ in L1688 is similar to that of Lupus and Chamaeleon I. However, the survey of Manara et al. (2020) is incomplete, preventing a thorough characterization of $\dot{M}_{\rm acc}$ and $M_{\rm disk}$ in Upper Sco. Despite this caveat, Manara et al. (2020) found that the relationship between $\dot{M}_{\rm acc}$ and $M_{\rm disk}$ has a similar distribution along the $M_{\rm disk}/\dot{M}_{\rm acc}$= 1 Myr line, although the disk masses typically fall in the lower half of the distributions of Lupus and Chamaeleon I (see figure 1.13). The mass accretion rates found in Upper Scorpius, as well as the large scatter at a comparable disk mass, are hard to explain using viscous evolution.

As discussed in section 1.2, a correlation between $\dot{M}_{\rm acc}$ and $M_{\rm disk}$ is one of the fundamental predictions of the viscous evolution model for disks much older than the viscous timescale. The slope of this correlation is expected to be approximately linear, as is the case for the observed correlation. The correlation is expected to shift to lower $\dot{M}_{\rm acc}$, and to tighten with age as the effect of initial conditions (M_0) fades. It is important to note that the choice of viscosity affects only the timescales on which this correlation evolves. This allowed Lodato et al. (2017) to use

the observed scatter in Lupus to constrain the viscous timescale in Lupus, assuming a purely viscous model. The large scatter points towards a viscous timescale on the order of $\sim$ 1 Myr, corresponding to low viscosities and a disk lifetime much longer than expected from studies of the disk fractions in different regions (see the beginning of section 1.2). Such a viscosity can also not simultaneously explain the large scatter observed in the significantly older Upper Scorpius region, as mentioned before.

In the MHD wind-driven scenario, there is no immediate expectation of a correlation between $\dot{M}_{\rm acc}$ and $M_{\rm disk}$. Equation 1.20 shows that the isochrones for this particular solution are dependent on the initial conditions at all times through the parameter $f_{\rm M}$. In the case where $\omega = 1$, the isochrones even become flat. In order to reproduce the observed correlation, one therefore needs to adopt the right initial conditions. Initial studies by (Mulders et al. 2017; Shadmehri & Ghoreyshi 2019; Tabone et al. 2022b) have shown that it is possible to reproduce the correlation observed in lupus with MHD wind-driven disk population models. The model used by Tabone et al. (2022b) could also reproduce the disk dispersal time scale of Fedele et al. (2010) (see the beginning of Section 1.2), but it remains to be seen whether the longer timescales suggested by Michel et al. (2021) (see Section 1.2) can also be reproduced simultaneously. Somigliana et al. (2023) compared the time evolution of the disk population synthesis models in both viscous and MHD cases, adopting the same models as Tabone et al. (2022b) for the latter, and found that in both cases the scatter in the $\dot{M}_{\rm acc}$ -$M_{\rm disk}$ correlation is expected to decrease over time. This evolution is illustrated in figure 1.14. Although some authors (e.g., Rosotti et al. 2017) suggest that internal photoevaporation is able to increase the scatter in the viscous case, making it better able to match the observation, Somigliana et al. (2023) only find insignificant differences when including it in their simulations. The MHD wind-driven scenario therefore appears to be better able to reproduce the observations in older regions.

One caveat to these studies is the high uncertainties on the measured disk masses due to the assumptions regarding the optical depth and gas-to-dust ratio discussed in Section 1.5.1. Therefore, better constraints on disk masses are needed to draw solid conclusions from the relationship between $\dot{M}_{\rm acc}$ and $M_{\rm disk}$. The introduction of ALMA band 1 and ngVLA will allow observations of disks at longer wavelengths, therefore probing lower optical depths and improving dust mass measurements (Tazzari et al. 2021). Ideally, one should also include dust evolution models when using dust disk masses (Sellek et al. 2020). Alternative mass estimates, such as dynamical estimates and estimates obtained through molecular gas mass tracers such as HD, CN, and CO, could also improve the strength of these methods but are currently unavailable for large enough samples (see Section 1.5.1 or Miotello et al. (2023) for a review).

To avoid the issue of disk masses altogether, Alexander et al. (2023) proposed that the distribution of $\dot{M}_{\rm acc}$ itself can be used to distinguish between a MHD wind-driven model and a viscous+photoevaporative model, since in the former it should be more weighted towards high mass accretion rates. However, in order to constrain this effect observationally, a larger sample ($\sim$ 300 homogeneous observations in the $0.5-1.0\ M_{\odot}$ range) than currently available is needed.

Another potential difficulty in constraining the mechanism driving disk evolution through mass accretion rates is the influence of other mechanisms on a disk's mass accretion rate. An example of this is the influence of binarity. An external binary companion has the potential to tidally truncate a disk and increase the mass accretion rate. This was shown by Zagaria et al.

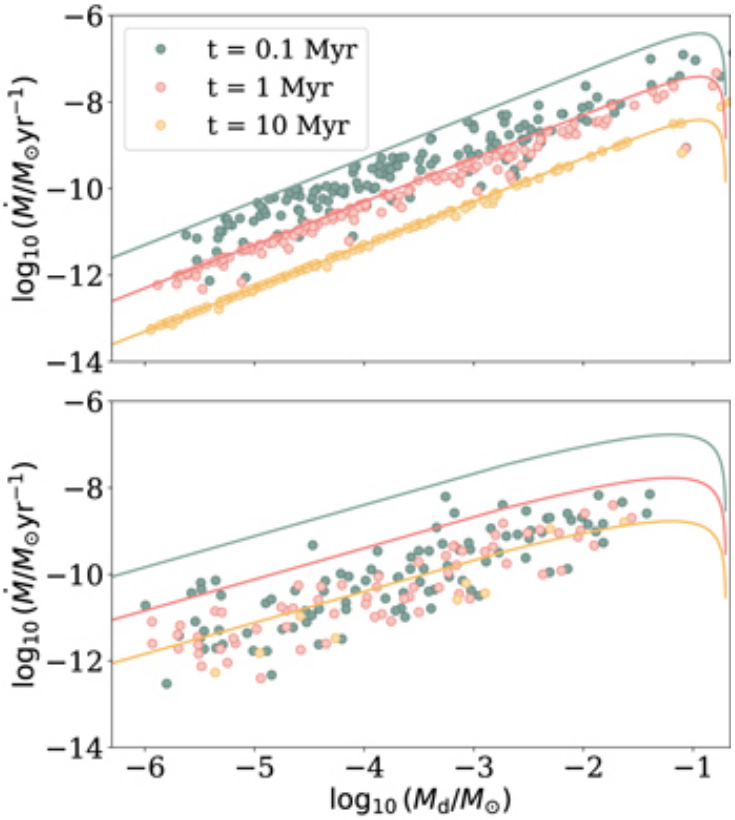

Figure 1.14: $\dot{M}_{\rm acc}$ As a function of $M_{\rm disk}$ for two synthetic populations at different ages. Top: A population of disks evolved through viscosity. Bottom: a synthetic population evolved through MHD disk winds. The theoretical isochrones are shown using the solid lines using the same color scheme. The MHD wind-driven disk shows a large dispersion, while the viscous disks converge over time to fall on the isochrone. Source figure: Somigliana et al. (2023)

(2022a), who showed this through the use of 1D evolutionary models and found observational evidence to support this. Figure 1.15 shows a comparison between the sample of binary stars collected by Zagaria et al. (2022a) and isolated disks in the $\dot{M}_{\rm acc}$ - $M_{\rm disk}$ diagram. The binary disks appear to mostly fall in the upper part of the distribution.

The protoplanetary disks are expected to be the birthplace of planets (see Section 1.3). The influence of potential growing planets embedded in the disk therefore needs to be taken into account when studying disk evolution. One-dimensional models of viscous disks with embedded massive ($\sim$ 1 $M_{\rm j}$) planets have shown that the accretion flow is drastically reduced by the presence of the planet (Lubow & D'Angelo 2006; Manara et al. 2019). However, this is not necessarily the case for MHD wind-driven disks, where 3D global non-ideal MHD simulations have shown that the accretion flow across a planet-induced gap is not significantly affected (Wafflard-Fernandez & Lesur 2023). Najita et al. (2015) have argued that transition disks have lower mass accretion rates than full disks with a comparable disk mass and that this is consistent with embedded massive planets decreasing the accretion flow. Therefore, to test the hypothesis that these

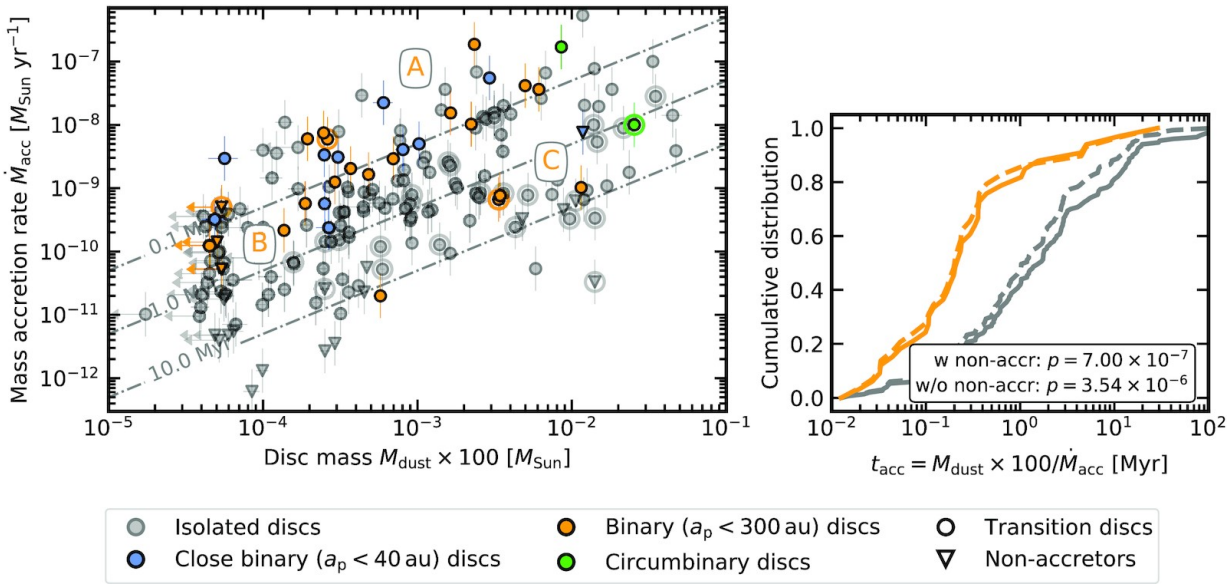

Figure 1.15: Left: Mass accretion rate as a function of disk mass for Chamaeleon I, Lupus, and Upper Scorpius class II sources. Orange and blue dots indicate binaries ($a_p < 300$ au) and close ($a_p < 40$ au) binaries, respectively. Green dots indicate circumbinary disks. Grey dots mark isolated stars. Non-accretors are marked using downwards-pointing triangles, and transition disks are marked with an additional circle. The dash-dotted lines mark constant accretion timescales of t_{acc} =0.1, 1, and 10 Myr. The letter A highlights the bulk of the binary population, which has $t_{acc} \approx 0.1$ Myr. B marks binaries with a faint disk, which is often undetected in the submillimeter, providing a disk mass limit of $M_{Disk} \lesssim 2 \cdot 10^{-4}\ M_{\odot}$. C marks binaries with massive disks $M_{Disk} \gtrsim 2 \cdot 10^{-3}\ M_{\odot}$. Right: Cumulative distributions of the accretion timescales for binary (orange) and single star (grey) disks. The solid lines mark the full sample, and the dashed lines mark the sample without non-accretors. The respective p-values for the null hypothesis that binaries and single stars are drawn from the same accretion timescale distribution are indicated in the caption. Source figure: Zagaria et al. (2022a)

cavities may (in part) be carved by giant planets, Manara et al. (2019) compared observations of transition disks and full disks to population synthesis models of viscous disks with and without embedded giant planets (see Figure 1.16). This revealed that the mass accretion rates observed in transition disks are mostly higher than that expected from the models containing planets. Population synthesis studies of MHD-driven disks with embedded planets have yet to be performed.

The influence of a disk's environment may also affect its evolution. External photoevaporation is one of the ways in which the environment affects protoplanetary disks (E.g., Johnstone et al. 1998; Winter & Haworth 2022). External photoevaporation is the process in which high-energy radiation of nearby massive OB stars heats and disperses material of protoplanetary disks. This process is expected to decrease the disk mass while minimally affecting the mass accretion rate, resulting in a lower $t_{acc} = M_{disk}/\dot{M}_{acc}$ (Rosotti et al. 2017). Indeed, Maucó et al. (2023)

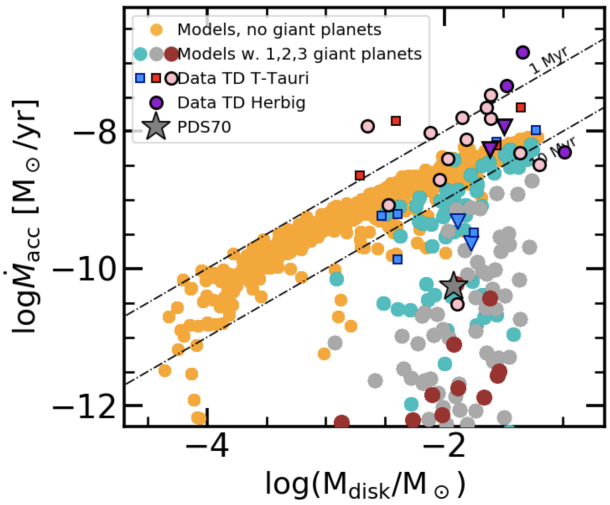

Figure 1.16: $\dot{M}_{\rm acc}$ -$M_{\rm disk}$ Diagram for population synthesis models, with and without giant planets. Transition disks with resolved cavities are also shown. The gray symbol indicates PDS 70, one of the only systems with directly detected protoplanets inside the disk cavity (see section 1.5.2). Source image: Manara et al. (2019)

observed hints that the disks in the σ-Orions cluster that are closer to the massive O9.5V star σ-Ori display different accretion timescales, compared to those further away. However, this effect should not significantly influence the well-characterized nearby star-forming regions such as Lupus and Taurus (Winter et al. 2018; Winter & Haworth 2022).

Yet another effect of the environment comes in the form of stellar flybys. Such close encounters with other stars are expected to truncate the disk similarly to binary companions. Such a flyby has even been proposed to explain the extreme outburst observed in FU Orionis (Borchert et al. 2022). Finally, the environment may influence the evolution of disks through late infall of material, which has indeed been observed (Gupta et al. 2024), although its overall prevalence is still uncertain. Such a late infall is expected to increase the mass accretion rate and increase the disk mass of the affected disk (Kuffmeier et al. 2023).

Figure 1.17 shows the relationship between the observed mass accretion rates and stellar masses for the sample of Manara et al. (2023). It can be seen that there appears to be a correlation between both quantities. This correlation was first shown to exist by Hillenbrand et al. (1992). Whether this correlation is physical has been a source of discussion in the literature. Several authors have suggested that the correlation may have been shaped by selection biases, lower and upper limits (e.g., Clarke & Pringle 2006; Tilling et al. 2008; Mendigutía et al. 2015). Several works since then have studied close to complete samples and have shown that the relationship is not the result of observational biases (e.g., Hartmann et al. 2016; Manara et al. 2017b; Alcalá et al. 2017). It has become clear that there is a physical correlation between $\dot{M}_{\rm acc}$ and $M_\star$, with slopes of $\sim 1.6-2$ and a scatter of $\sim 1-2$ dex depending on the region (Manara et al. 2023). However, some authors have argued that this relationship is more complex in older regions. In particular, Manara et al. (2017b) and Alcalá et al. (2017) argued that a double power law fit

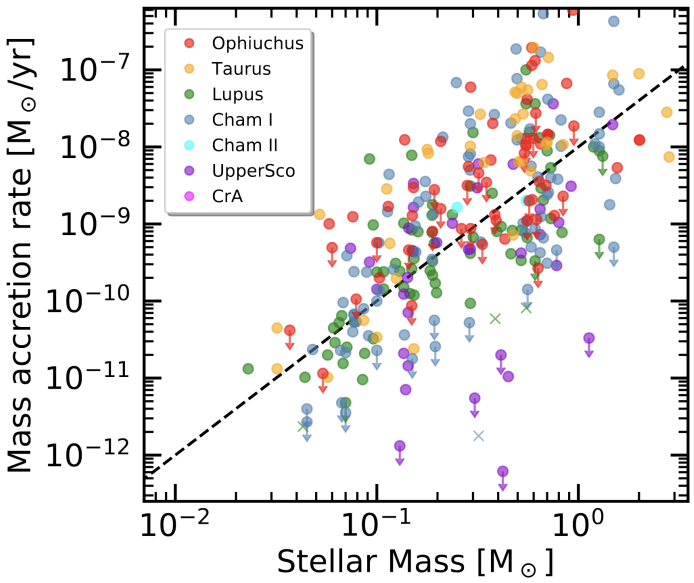

Figure 1.17: Mass accretion rate as a function of disk mass for the sample collected by Manara et al. (2023). The dashed line shows the $\dot{M}_{\rm acc} \propto M_\star^2$ relationship. Source image: Manara et al. (2023)

better represents the observed relation in Lupus and Chamaeleon I, respectively. This was further studied by Almendros-Abad et al. (2024), who analyzed expanded samples in ρ Ophiuchus, Lupus, Chamaeleon I, and Upper Scorpius. Here, they concluded that both double and single power law models reproduce the relation at similar statistical significance.

How the relationship between $\dot{M}_{\rm acc}$ and $M_\star$ comes about and relates to the evolution of protoplanetary disks is not immediately evident. The equations describing disk evolution presented in Sections 1.2.1 and 1.2.2 do not have any immediate dependency on $M_\star$. There are two possible ways to obtain such a correlation. The first option is that this correlation is the result of internal photoevaporation (e.g., Clarke & Pringle 2006; Ercolano et al. 2014). An alternative explanation could be that the observed correlation is a result of the initial conditions (e.g., Dullemond et al. 2006; Alexander et al. 2006; Somigliana et al. 2022). These works, however, only considered viscous evolving disks. Somigliana et al. (2022) studied the evolution of the $\dot{M}_{\rm acc}$ - $M_\star$ relation using population synthesis models in the case of viscous + photevaporative evolution and MHD wind-driven evolution. In this case it was found that in the viscous case the power law shape of the correlation is preserved but the slope evolves, whereas in the MHD driven case the relationship bends. The latter, however, still appears as an evolving power law correlation thanks to the spread in initial conditions. Finally, Somigliana et al. (2022) find that the evolution of both slopes differs between both models when given the same initial conditions, but that the current sample in Upper Scorpius is too small to distinguish between both models.

1.7 This thesis

The main goal of this thesis is to further our understanding of the mechanisms that dominate disk evolution. The approach taken here focuses on the observational relationship between the mass accretion rate and the disk or stellar mass. In particular, the thesis attempts to constrain various other influences that may affect the measured mass accretion rates. As previously mentioned in Section 1.4.2, the most direct approach to obtain mass accretion rates is through the modeling of broad wavelength range flux calibrated spectra. For this purpose, the VLT/X-Shooter spectrograph is particularly useful, since it provides such spectra in the wavelength range of $\lambda\lambda \sim 300 - 2500$ nm at a medium resolution (up to $\sim$ 9700 in the UVB arm, although here we mostly use lower resolutions of $\sim$ 5400, $\sim$ 18400 in the VIS arm, and $\sim$ 11600 in the NIR arm (Vernet et al. 2011)). This wavelength coverage allows X-Shooter to obtain simultaneous observations of the Balmer jump at 330 nm, which is a good tracer of the UV excess emission and molecular bands present in the spectra at longer (e.g., $\sim$ 710 nm). It also provides sufficient spectral resolution to obtain constraints from the veiling of atomic absorption lines in the spectra. It is because of this reason that X-Shooter spectra are the main tool used in this thesis.

This thesis attempts to address three open questions using an observational approach.

What is the impact of variability on the observed spread in mass accretion rates at a given stellar or disk mass? CTTS are known to display a large range of accretion variability amplitudes and timescales (see section 1.4.3). This raises the question to which extent such variability contributes to the scatter in mass accretion rates observed at a given disk or stellar mass. The majority of sources appear to present an accretion variability of $\lesssim 0.5$ dex, which is much smaller than the observed scatter. Rare outliers can be found in the categories of FU Orionis and EXor bursters. However, only a small number of surveys cover a timescale of decades or longer. Most surveys are also limited to single-band photometry, which has a hard time distinguishing between accretion and other sources of variability. In this thesis, I present X-Shooter observations of the CTTS XX Cha, which displays an unusually large accretion variability of $\sim$ 1.5 dex on a timescale of $\sim$ 10 years. The implications of such large variability on the observed scatter in mass accretion rates are also discussed. This work is presented in chapter 2.

What uncertainties and limits are associated with the use of observed templates to model the spectra of CTTS, and how do we mitigate them? The most direct way to measure mass accretion rates is by modeling broad wavelength range spectra (see section 1.4.2). Observed spectra of non-accreting young stars need to be used to represent the stellar contribution to the observed emission of an accretor. Young stars are, however, known to be chromospherically active, which may result in different levels of emission at short wavelengths for templates of the same SpT. In addition to this, the templates themselves come with observational uncertainties. In this thesis I attempted to improve our understanding and use of Class III templates. To do so, I first expanded and verified the currently available grid of templates. I then proposed a method to interpolate between the templates as a function of spectral type. Finally, I use the uncertainties on this interpolated grid to obtain a lower limit for the mass accretion rates that

we can confidently measure by modeling broad wavelength range spectra using the interpolated templates and discuss the implications on the $\dot{M}_{\rm acc}$ -$M_{\star}$ relationship. This is described in Section 3.

Is there any relation between the accretion properties of a disk and its observed substructures? Protoplanetary disks have been observed to display a large variety of substructures such as rings, cavities, spirals, and asymmetries observed in both IR and millimeter wavelengths. This raises the question of whether the evolutionary models presented in Section 1.2.1 are too simplistic to explain the observed mass accretion rates. Indeed, it could very well be the case that the mechanisms responsible for these substructures also affect the mass accretion rate of the disk. Finding a relationship between the accretion properties and substructures of disks could therefore help explain the observed scatter in mass accretion rates and put constraints on the mechanism responsible for the creation of these substructures. In order to address this question, I obtained new X-Shooter spectra of sources with known substructures as part of my own PI program and collected arrival spectra. These spectra are then analyzed using the modeling technique developed in chapter 3. This sample was then combined with literature accretion rate measurements to provide a sample of 61 sources with known substructures. Using literature disk masses allowed this sample to be situated in the $\dot{M}_{\rm acc}$ -$M_{\rm disk}$ diagram and for the accretion timescales to be computed. This allows for the accretion timescale distribution of sources with different types of substructures as well as the non-resolved population, to be compared. Finally, we look at the relationship between the accretion timescale and the properties of hypothetical planetary systems, deduced from the observed substructures. Therefore, this thesis provides the first study of the relationship between substructures and accretion properties. This work is contained in Chapter 4 Finally, I summarize the implications of these studies for our understanding of the observed $\dot{M}_{\rm acc}$ -$M_{\rm disk}$ and $\dot{M}_{\rm acc}$ -$M_{\star}$ relationships and discuss the implications this has for our understanding of disk evolution. I also provide a future perspective detailing how the measurements of mass accretion rates may be further improved and how an improved understanding of disk evolution through the study of accretion properties may be reached. This is provided in chapter 5.

2

The peculiar accretion variability of XX Cha and its impact on the observed spread of accretion rates

This chapter was published as The peculiar accretion variability of XX Cha and its impact on the observed spread of accretion rates ***Claes, R.A.B.****; Manara, C. F.; Garcia-Lopez, R.; Natta, A.; Fang, M.; Fockter, Z. P.; ábrahám, P.; Alcalá, J.M.; Campbell-White, J.; Caratti o Garatti, A.; Covino, E.; Fedele, D.; Frasca, A.; Gameiro, J. F.; Herczeg, G. J.; Kóspál, Á.; Petr Gotzens, M. G.; Rosotti, G.; Venuti, L.; Zsidi, G. A&A, 2021, 664, L7; PENELLOPE. III.*

This chapter depends on a collaborative work, in which had the opportunity to take the lead. In particular I was responsible for verifying the data reduction, including the flux calibration and telluric correction, the analysis and interpretation. Finally, I composed the manuscript.

Abstract

The processes regulating protoplanetary disk evolution are constrained by studying how mass accretion rates scale with stellar and disk properties. The spread in these relations can be used as a constraint to the models of disk evolution, but only if the impact of accretion variability is correctly accounted for. While the effect of variability might be substantial in the embedded phases of star formation, it is often considered limited at later stages. Here we report on the observed large variation in the accretion rate for one target, XX Cha, and we discuss the impact on population studies of classical T Tauri stars. The mass accretion rate determined by fitting the UV-to-near-infrared spectrum in recent X-Shooter observations is compared with the one measured with the same instrument 11 years before. XX Cha displays an accretion variability of almost 2 dex between 2010 and 2021. Although the timescales on which this variability happens are uncertain, XX Cha displays an extreme accretion variability for a classical T Tauri star. If such behavior is common among classical T Tauri stars, possibly on longer timescales than previously probed, it could be relevant for discussing the disk evolution models constrained by the observed spread in accretion rates. Finally, we remark that previous studies of accretion variability based on spectral lines may have underestimated the variability of some targets.

2.1 Introduction

While planets are forming, the protoplanetary disks they are born in evolve under the effect of several processes. Of particular relevance is how the material is transported through the disk and how it is accreted onto the central star (Hartmann et al. 2016). Accretion regulates the final stellar mass, and it is commonly used in combination with the stellar and disk mass to constrain the models driving the global evolution of disks (Manara et al. 2023).

The accretion process is intrinsically highly variable (e.g., Stauffer et al. 2014) on timescales of minutes to years (e.g., Fang et al. 2013; Costigan et al. 2014), with different magnitudes of variability (e.g., Hillenbrand & Findeisen 2015; Fischer et al. 2023). It has often been questioned whether accretion variability can explain the spread of $\sim$2-3 dex observed in the relations between accretion rates and stellar or disk masses (e.g., Manara et al. 2020, 2023). If not dominated by accretion variability, this spread is a way to test and constrain disk evolution models, in particular to highlight the limits of the viscous evolution scenario (e.g., Mulders et al. 2017; Lodato et al. 2017; Manara et al. 2020, 2023). Independently from each other, several works have shown that, typically, accretion variability peaks at $\lesssim$0.5 dex on timescales of a few weeks (Costigan et al. 2012, 2014; Biazzo et al. 2012, 2014; Venuti et al. 2014; Frasca et al. 2015; Zsidi et al. 2022). Such variability is too small to explain the observed scatter. However, little data exist probing longer timescales of decades, and this is usually limited to single band photometric studies, which would hardly distinguish between variations in the stellar photosphere or accretion variability. Finally, a tiny fraction of young stars, named FU Orionis and EXor, have been identified to show a strong ($\sim$2-3 dex) increase in their accretion rates lasting years (e.g., Audard et al. 2014; Fischer et al. 2023). Since they are rare, they are not considered to have a significant impact on the observed relations.

Here we present and analyze the case of the highly variable young stellar object (YSO) XX Cha, observed with the same spectrograph in 2010 (Manara et al. 2016a, 2017b) and then in 2021. We then discuss the implications on studies of disk evolution based on accretion and stellar or disk masses.

2.2 Target, observations, and data reduction

The target of this study is XX Cha (2MASS J11113965-7620152, Ass Cha T 2-49), a classical T Tauri star (CTTS) in the Chamaeleon I region, at a distance of 192 pc (Gaia Collaboration et al. 2021). This star is part of a very wide binary system with CHX 18N (Kraus & Hillenbrand 2007), with an angular separation of 24.38 $''\sim$4,600 au.

XX Cha hosts a disk that was detected with Atacama Large Millimeter Array (ALMA) in the Band 7 continuum (Pascucci et al. 2016), but it was not detected in the ^{13}CO gas emission (Long et al. 2017). The corresponding disk dust mass is 8.12 $M_{\oplus}$ (Manara et al. 2023).

XX Cha is known to have a significant mid-infrared variability. Kóspál et al. (2012) compared the ISO/ISOPHOT-S and Spitzer IRS spectra of this target, and found a strong decadal change in the 5-12 μm range, with a peculiar wavelength dependence. XX Cha is one of the only sources where an anti-correlation was found in the silicate emission feature at 10μm with the continuum

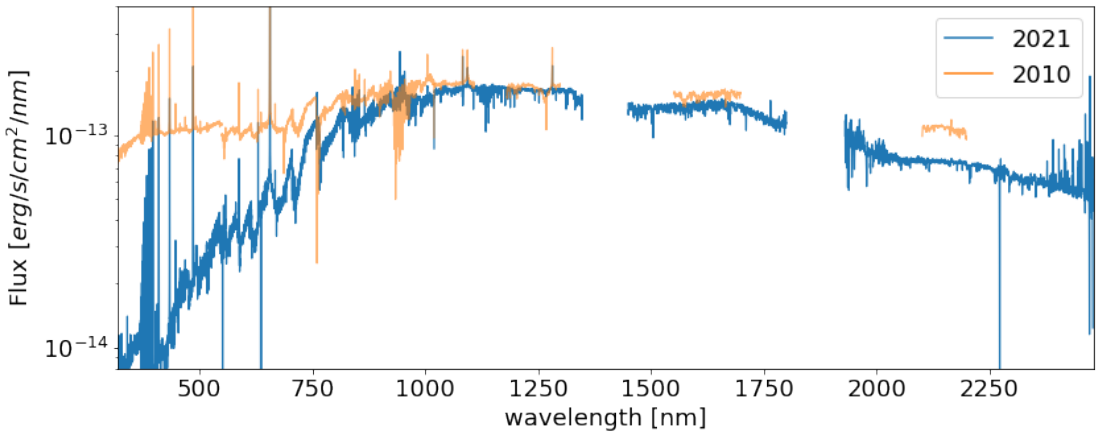

Figure 2.1: Comparison between the spectra of XX Cha as observed with X-Shooter in January 2010 (orange) and June 2021 (blue). For the sake of clarity of the figure, the spectra were convolved by a Gaussian with a standard deviation of three times the spectral resolution.

flux between $6-8\mu$m, as opposed to a correlation. Such a variability may be caused by variable shadowing of the silicate emitting region (Kóspál et al. 2012).

2.2.1 Spectroscopic observations

XX Cha was observed from the ESO Very Large Telescope (VLT) with the X-Shooter instrument. It is a medium-resolution spectrograph simultaneously observing in three wavelength ranges, called the UV-Blue (UVB) (∼300–560 nm), Visible (VIS) (∼560–1024 nm), and Near-IR (NIR) (∼1020–2480 nm) arms (Vernet et al. 2011).

The first observation was taken on 19 January 2010 (UT 07:39:06) in visitor mode, and it was analyzed by Manara et al. (2016a). The target was observed a second time on 5 June 2021 (UT 03:45:18) as a part of the PENELLOPE Large Program (Manara et al. 2021). The latter observation is presented here for the first time. Both observations used a combination of a short exposure with a wide set of slits - 5.0″ wide, except for the NIR arm in 2010 when a 1.5″ slit was used to measure absolute fluxes, followed by a long nod-on-slit integration with a narrower set of slits - 1.0″-0.4″-0.4″ in the UVB, VIS, and NIR arms, so as to achieve a spectral resolution $R \sim 5400$, 18400, and 11600 in the three arms, respectively.

The reduction of the spectra taken was performed using the ESO X-Shooter pipeline (Modigliani et al. 2010) v1.3.2 and v3.5.0 for the 2010 and 2021 epochs, respectively. The final flux calibration was performed by rescaling the narrow slit spectrum to the wide slit one as described by Manara et al. (2016a, 2021). The flux calibration accuracy for the 2010 epoch of XX Cha was found by Rugel et al. (2018) to be $\sim 4\%$. We expect a similar value for the 2021 epoch. In 2010, the low signal to noise of the flux standard star in the NIR arm did not allow for a proper flux calibration of most of this arm, and telluric correction could also not be performed. Telluric lines were removed from the VIS and NIR parts of the 2021 spectrum using the molecfit tool (Smette

et al. 2015).

2.2.2 Photometric data

The American Association of Variable Star Observers (AAVSO) obtained photometric data for XX Cha to complement the TESS and Hubble Space Telescope (HST) ULLYSES (Roman-Duval et al. 2020; Espaillat et al. 2022) observations[1] from April to August 2021. We collected this dataset, covering *B*, *V*, *R*, and *I* band photometry, from the AAVSO website [2] (Kafka 2020).

Optical photometry in the *V*, *R*, and *I* band is also available for periods spanning from April 2010 to May 2010 and January 2013. The 2010 photometry contains ten observations obtained with the REM telescope (Pr.Id. 21703, PI: Michel Curé). The 2013 photometry contains four epochs obtained with the ANDICAM instrument on the CTIO 1.3m telescope (Project ID: ESA-12B-0001, PI: Ágnes Kóspál). The light curve and additional information is reported in Appendix 2.A.1.

2.3 Analysis

2.3.1 Continuum variations

A comparison between the two X-Shooter spectra can be seen in Fig. 2.1. The spectrum obtained in 2010 is significantly brighter than the one taken in 2021 at wavelengths shorter than $\sim$800 nm, suggestive of either a higher accretion rate in 2010 or different extinction. The two spectra look quite similar at longer wavelengths; although, the *K*-band spectrum in the 2010 epoch is, on average, $\sim$ 1.4 times brighter than in the 2021 epoch, hinting at a difference in the inner disk properties.

Synthetic photometry was performed on both X-Shooter spectra using the PYPHOT package[3] in the Johnson-Cousins *B*, *V*, *R* and *I* bands. The obtained values are listed in Table 2.2. A good agreement between the 2021 spectrum and almost simultaneous photometry can be seen in Fig. 2.4. The 2021 X-Shooter observation was obtained when the star was at a minimum of the short-term light curve. No simultaneous photometry is available for the 2010 epoch. However, the synthetic photometry of the 2010 spectrum appears to fall close to the maximum brightness observed in the available photometry. We conclude that the X-Shooter observations are taken close to the extremes of the known photometric variability of XX Cha.

Variations in the circumstellar extinction can explain dippers and dimming events of peculiar stars (e.g., Schisano et al. 2009; Bouvier et al. 2013; Facchini et al. 2016; Schneider et al. 2018; Koutoulaki et al. 2019). To exclude this possibility, Fig. 2.5-2.6 show the color-magnitude diagram of XX Cha, and they indicate that the variations between the two epochs are incompatible with just extinction variations. Similarly, flux ratios between the two spectra are compared with

[1] https://www.aavso.org/
hst-ulyssessouthern-t-tauri-campaign-01
[2] https://www.aavso.org/data-download
[3] https://mfouesneau.github.io/docs/pyphot/index.html

Table 2.1: Stellar and accretion parameters obtained for both epochs

	Epoch of observation		
Property	2010	2021	2010*
SpT	M3.5	M3	M3*
$T_{\rm eff}$ (K)	3300	3410	3410*
A_v (mag)	1.0	0.3	0.3*
$L_\star$ ($L_\odot$)	0.42	0.30	0.39
log $L_{\rm acc}$($L_\odot$)	-0.65	-2.34	-1.06
$M_\star$ ($M_\odot$)	0.24	0.30	0.30
log $\dot{M}_{\rm acc}$($M_\odot$/yr)	-7.14	-9.06	-7.69

Notes: The values listed under "2010*" report the results obtained fitting the 2010 epoch with the same photospheric template and A_V as the values obtained fitting the 2021 epoch. Typical uncertainties are the following: 0.1 for A_v , 0.2 dex for $L_\star$, 0.1 dex for $M_\star$, 0.25 for $L_{\rm acc}$ (Manara et al. 2017b), and 0.35 for $\dot{M}_{\rm acc}$ (Manara et al. 2023).

typical reddening laws for increasing values of A_V and R_V in Fig. 2.7, showing that the observed variations cannot be fully explained by a difference in extinction.

Finally, the lithium line at 670.78 nm is found to have a lower equivalent width in 2010 (~ 0.150) when compared to 2021 (~ 0.550) (Fig. 2.8). This is due to an increase in the veiling in 2010, which is related to an increase in the accretion rate. The analysis of the spectra with ROTFIT (Frasca et al. 2017) indeed leads to a measured veiling at 620 nm of 6.4 in 2010 and of 0.6 in 2021.

2.3.2 Stellar and accretion properties

The stellar and accretion parameters were derived by fitting the UV excess in the X-Shooter spectra with the procedure described by Manara et al. (2013a) (see Appendix 2.B.2). The 2010 data were analyzed with this method by Manara et al. (2016a). Here, for 2010, we use the values reported by Manara et al. (2023), which were computed by rescaling the distance to 192 pc, assuming the relation between spectral type and temperature by Herczeg & Hillenbrand (2014), and the non-magnetic evolutionary tracks by Feiden (2016) to obtain the stellar mass. These values are reported in Table 2.1.

With the same method and the same assumptions, we fit the 2021 spectrum, and we derived a spectral type consistent with the 2010 result within half of a subclass, but we obtain significant differences in the other parameters. In particular, the mass accretion rate ($\dot{M}_{\rm acc}$) is found to be smaller by $\sim$2 dex than in 2010, and A_V is found to be smaller by 0.7 mag. Since veiling can make the determination of the stellar parameters more uncertain (e.g., Calvet & Gullbring 1998), we repeated the fit of the 2010 spectrum, using the same photospheric template and extinction as derived in the 2021 epoch. We obtain a lower $\dot{M}_{\rm acc}$ than previously reported (see Table 2.1, column 2010*), leading to a difference in $\dot{M}_{\rm acc}$ of $\sim$ 1.4 dex compared to the 2021 observations.

2.3.3 Accretion properties from the emission lines

Starting from the relations between the line luminosity ($L_{\rm line}$) and the accretion luminosity ($L_{\rm acc}$) by Alcalá et al. (2017), we calculated $L_{\rm acc}$ using different emission lines and assuming $A_V = 0.3$ mag for both observations. The mean values of $L_{\rm acc}$ measured from the line luminosity agree within the uncertainties with the corresponding value from the UV-excess fitting at each epoch (Fig. 2.12 for 2010*, $\log(\langle L_{\rm acc,lines}/L_\odot \rangle) = -1.50 \pm 0.35$; Fig. 2.13 for 2021, $\log(\langle L_{\rm acc,lines}/L_\odot \rangle) = -1.98 \pm 0.35$). On the other hand, the difference between the two values of $L_{\rm acc}$ from the line luminosity is smaller than when computed from the UV excess.

We note that the line profiles are very different between the two epochs (Fig. 2.16-2.15). In particular, the 2010 observations show a stronger red-shifted absorption and a wider blueshifted emission in the hydrogen emission lines. Both aspects are in line with the stronger accretion rate measured in 2010.

We also considered additional estimates of $L_{\rm acc}$ from line emission available from an observation of XX Cha in 2009 by Antoniucci et al. (2011). We scaled the luminosity of the Hα, Paβ, and Brγ lines, accounting for the different distance and extinction adopted here. We find an average accretion luminosity of $\log(\langle L_{\rm acc,lines}/L_\odot \rangle) = -1.3 \pm 0.5$ dex, which is slightly higher but compatible with the one measured in 2010 from the line luminosity. We derived an accretion rate of $\log \dot{M}_{\rm acc}(M_\odot/{\rm yr}) = -8.0 \pm 0.7$ dex, assuming the stellar mass obtained for the 2010* epoch. This value is consistent with the accretion properties found in 2010*.

2.4 Discussion

2.4.1 Variability of XX Cha in context

The $\gtrsim$1.4 dex variations in accretion rates measured in XX Cha poses the question of whether this target could be part of either the FU Orionis or EXor variable classes (e.g., Fischer et al. 2023). We exclude the former, since FU Orionis stars experience sudden jumps in accretion rate to about $\dot{M}_{\rm acc} \sim 10^{-4} M_\odot$/yr (Kóspál 2011) which last for timescale of decades to centuries. Both the value of $\dot{M}_{\rm acc}$ and the timescales of the photometric evolution (Fig. 2.4) are very different than typical FU Orionis outbursts. During an outburst, several spectral features in the spectra of FU Orionis stars are the opposite of what we observe in XX Cha, for example in FU Orionis stars the Paβ line is observed in absorption and the CaII infrared triplet is not detected (Connelley & Reipurth 2018).

EXor stars, on the other hand, display an increase in $\dot{M}_{\rm acc}$ of $\sim 1-2$ dex, similar to XX Cha. These variations occur in an outburst that typically lasts several months to a year. In EXor-type outbursts, a large number of emission lines can be detected in the near-infrared (e.g., Kóspál et al. 2011). Such lines are not evident in the 2010 spectrum of XX Cha, but Antoniucci et al. (2011) in 2009 observed ro-vibrational CO transitions at $\lambda > 2300$ nm in emission, which is a typical feature of EXor outbursts (Fischer et al. 2023). As discussed in Sect. 2.3.3, XX Cha was accreting at a similar $\dot{M}_{\rm acc}$, both in our 2010 observations and in 2009. Both the high accretion luminosity and CO emission found by Antoniucci et al. (2011) suggest that XX Cha may have

experienced an EXor-type outburst in 2009, with our 2010 observations being taken at a later stage during this outburst. However, the lack of data between the two epochs does not allow us to confirm or exclude this possibility.

Even if it is unclear whether XX Cha is an EXor variable star, it is instructive to compare its extreme accretion variability to previous samples of CTTS. We show in Fig. 2.2 the extent of its variability in comparison with literature results (Biazzo et al. 2012; Costigan et al. 2014; Zsidi et al. 2022) and with the preliminary analysis of 11 other targets from the PENELLOPE survey (Manara et al. 2021, Garcia-Lopez et al. in prep.). The data for XX Cha are displayed using the interval between the observations, and both of the values measured from UV excess and line luminosity. Based on our data, we cannot distinguish between a timescale for the observed variability of 11 years or of $\sim$ 22 days, an indication of which could be determined in reviewing the observed light curve in 2021 (Fig. 2.4). Either way, the accretion variability of XX Cha measured from the UV excess is more extreme than literature results for CTTS, including the similarly analyzed PENELLOPE targets. Among other possible objects showing a potentially similar variability as XX Cha, we can cite V347 Aur, since it has periodic V band variations with an amplitude of $\sim$ 2 mag on timescales $\sim$ 160 days. However, other effects, such as a variable extinction, could significantly contribute to the photometric variability.

The accretion variability measured from the line luminosity ($\sim$0.5 dex) is instead in line with literature results. We strongly advocate that studies of accretion variability should be performed with flux-calibrated broad wavelength range spectra. A possible explanation for the different results obtained from the UV excess and emission lines could be a partial occultation due to an inner disk warp. In this case, similar to AA-Tau (Bouvier et al. 2013; Schneider et al. 2015), the UV radiation from the shock region on the stellar surface is obscured by the disk, whereas the line emission coming from the accretion columns would be less obscured. In turn, this would result in comparatively higher line emission in the epoch with lower UV excess, and vice versa. If such a differential extinction could explain the discrepancy between a line and UV excess, this would affect the measurements of $\dot{M}_{\rm acc}$ in population studies based on a single value of A_V and on UV-excess measurements. Therefore, when we discuss the impact of this accretion variability on the observed spreads in the next section, the difference measured from the UV excess is the relevant one.

2.4.2 Impact on accretion rates spread

The observed distributions on the $\dot{M}_{\rm acc}$ - $M_{\rm disk}$ and $\dot{M}_{\rm acc}$ - $M_\star$ planes are a useful test bench of the mechanisms driving protoplanetary disk evolution (Manara et al. 2023). To understand how a significantly variable object such as XX Cha impacts these relations, we plotted in Fig. 2.3 and Fig. 2.17 the data taken from Manara et al. (2023) for the Chamaeleon I and Lupus star-forming regions, as well as the two measured values for XX Cha. This target does not appear to be an outlier in the distribution of $\dot{M}_{\rm acc}$ values in either 2010 or 2021, since its variability is still smaller than the observed spread, and the measured values of $\dot{M}_{\rm acc}$ are well in line with typical measurements for similarly massive stars or disks. In this specific case, the measured variability therefore has no impact on the observed spread. The effect would be significant if a

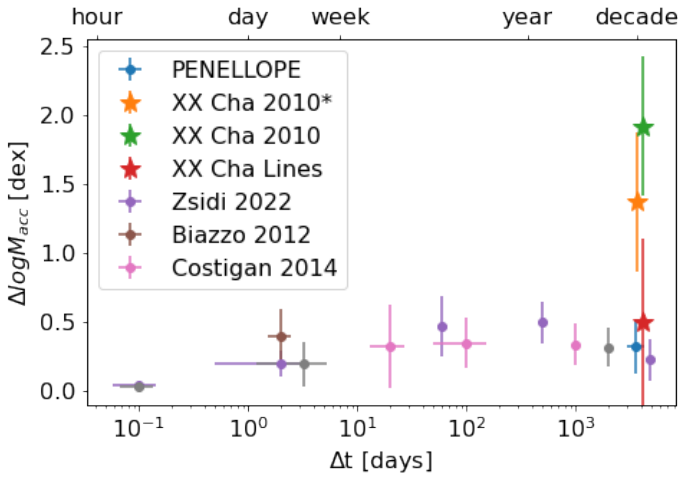

Figure 2.2: Relative accretion rate variations as a function of the time difference between observations. The points indicate the mean variability and the errorbars mark their standard deviations. We note that literature values, with the exeption of those from Zsidi et al. (2022), are drawn from measurements in several stars.

larger number of targets would undergo similarly significant variability, or even a stronger one.

Based on currently available information, XX Cha seems still to be a rare outlier. Indeed, the preliminary analysis of other PENELLOPE data points to the fact that, even looking at the UV excess, typical variability is $\lesssim$0.5 dex (see both Fig. 2.2 and 2.3). Also literature exploration of both short- and long-term variability seems to converge on this result. Venuti et al. (2014, 2015) used photometrically derived UV-excess measurements to determine that, overall, variations on UV excess over timescales of years are statistically consistent with those on timescales lasting for weeks, with a typical variation of 0.4 ± 0.3 dex when considering all CTTS, and 0.6 ± 0.5 dex when considering only CTTS with $\dot{M}_{\rm acc}$ variations $>$1 dex over $\sim$2 week timescales. Only about 14% of stars in their sample show additional long-term variations in UV excess beyond 0.5 dex. If these results are confirmed, we can assume that the majority of the spread of accretion rates is intrinsic, and not related to accretion variability.

However, we cannot base our estimates purely on line equivalent width or luminosity estimates since we have shown that these could lead to an underestimation of the extent of the variability. Further monitoring with broad wavelength range spectra is needed to constrain the fraction of sources showing large variability, so as to better constrain the effect of accretion variability on the observed relations, making them a more powerful tool to study protoplanetary disk evolution.

Finally, we note that the large variability in the accretion rate of XX Cha would have an effect on the measured value of $t_{\rm acc}$=$M_{\rm disk}/\dot{M}_{\rm acc}$ anyways. This quantity is used, for example, to discriminate between targets whose evolution is regulated by viscous evolution (e.g., Lodato et al. 2017; Mulders et al. 2017), magnetohydrodynamic wind-driven evolution (e.g., Mulders et al. 2017; Tabone et al. 2022b), or even by other internal or external disk evolution processes (e.g.,

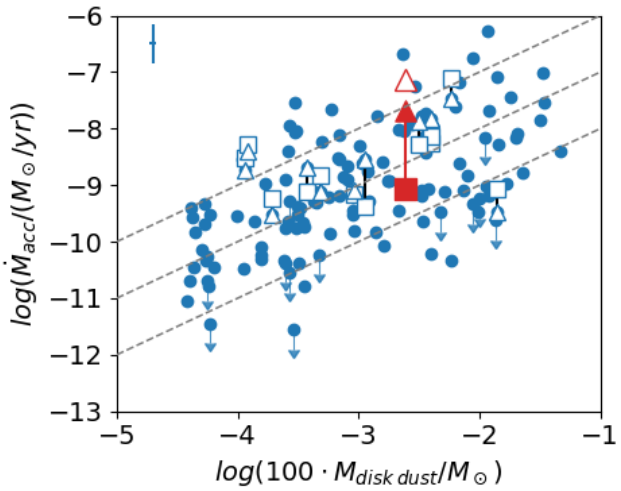

Figure 2.3: Measured $\dot{M}_{\rm acc}$ and $M_{\rm disk}$ for targets in the Lupus and Chamaeleon I star-forming regions (blue filled dots). The red filled (empty) triangle and square indicate the 2010* (2010) and 2021 mass accretion rates of XX Cha, respectively. The dashed lines display the $M_{\rm disk}/\dot{M}_{\rm acc}$ ratio of 0.1, 1, and 10 Myr, respectively. The white empty squares and triangles indicate targets observed in 2021 in the PENELLOPE program (Manara et al. 2021) and around 2010, respectively.

Rosotti et al. 2017). While population studies are unaffected, since the spread is not sensitive to this magnitude of variability, results on individual targets must consider this additional cause of uncertainty due to variability before firmly assessing whether the displacement of a target on the $\dot{M}_{\rm acc}$-$M_{\rm disk}$ plane is due to one or another disk evolution mechanism. The interpretation of individual values should be confirmed with multiple epochs of observation, when possible.

2.5 Conclusions

We report a variability in accretion rates for XX Cha of $\gtrsim$1.4 dex between 2010 and 2021, when measured from the UV excess. This change in accretion rate is much larger than the typical accretion variability of $\lesssim$0.5 dex found in other CTTS. However, a smaller $\sim$0.5 dex variability is obtained for XX Cha when measured from the luminosity of emission lines. This result highlights the need to monitor accretion using flux-calibrated broad wavelength range spectra. Although large, the measured variability of XX Cha has no impact on the observed spread of $\dot{M}_{\rm acc}$ in the relations with $M_{\rm disk}$ or $M_\star$. Since the variability of XX Cha seems rare to date, this confirms that the spread of $\dot{M}_{\rm acc}$ is related to disk evolution. However, we suggest that more extensive exploration of accretion variability on longer timescales than previously probed must be performed, so as to firmly asses its importance.

Aknowledgements: We thank M. Benisty and J. Bouvier for discussions on this target. R. Claes acknowledges the PhD fellowship of the International Max-Planck-Research School (IMPRS) funded

by ESO. This work benefited from discussions with the ODYSSEUS team (HST AR-16129), https://sites.bu.edu/odysseus/. Funded by the European Union under the European Union's Horizon Europe Research & Innovation Programme 101039452 (WANDA). Views and opinions expressed are however those of the author(s) only and do not necessarily reflect those of the European Union or the European Research Council. Neither the European Union nor the granting authority can be held responsible for them. This project has received funding from the European Union's Horizon 2020 research and innovation programme under grant agreement No 716155 (SACCRED) and under the Marie Sklodowska-Curie grant agreement No 823823 (DUSTBUSTERS). This work was partly funded by the Deutsche Forschungsgemeinschaft (DFG, German Research Foundation) - 325594231. This research received financial support from the project PRIN-INAF 2019 "Spectroscopically Tracing the Disk Dispersal Evolution". R.G.Lopez acknowledges support by Science Foundation Ireland under Grant no. 18/SIRG/5597. J.F.Gameiro was supported by fundacao para a Ciência e Tecnologia (FCT) through the research grants UIDB/04434/2020 and UIDP/04434/2020. G. Rosotti acknowledges support from an STFC Ernest Rutherford Fellowship (grant number ST/T003855/1)

2.A Broadband variability

2.A.1 Photometric variability

The available photometric data presented in Sect. 2.2.2 is shown in Fig. 2.2 as a function of the time of the observations. On the same plot, the synthetic photometry derived from the X-Shooter spectra (see Sect. 2.3.1 for the procedure and Table 2.2 for the values) is also included for comparison. The synthetic photometry measured on the 2021 spectrum agrees with the photometry taken close in time. When looking at the light curve around the 2021 observations, the brightness of the target at the time of the 2021 X-Shooter observations is close to the local variability minimum. Indeed, there seems to be a quasi-periodic variability pattern with timescales of $\sim$22 days which, however, is only hinted at in the periodogram analysis we carried out, possibly due to the short time coverage with respect to the length of this putative period. The 2010 synthetic data fall on the high side, but within the range of variability for all epochs of observation.

The variability amplitude observed in the photometry is larger for bluer bands. Such a trend is expected in the case of a variable accretion rate or reddening. To further explore this effect, we show in Fig. 2.5 the V versus $V-R$ and in Fig. 2.6 the B versus $B-V$ color-magnitude diagram (CMD), respectively, and a reddening vector with R_V=3.1. The reddening vector is well aligned with the AAVSO data in the $V-R$ CMD, and less so in the $B-V$ one. In either case, the reddening vector cannot reproduce the variability between the 2010 and 2021 spectra analyzed here. The variability, or at least a part of it, must be ascribed to accretion variability.

2.A.2 Continuum variability

We computed the flux ratio between the 2010 and 2021 spectra as F_{2021}/F_{2010} using the median flux in an interval of 4 nm around a number of wavelengths in the spectra, chosen to sample the continuum in the spectra and avoiding emission lines. The errors were then computed from the

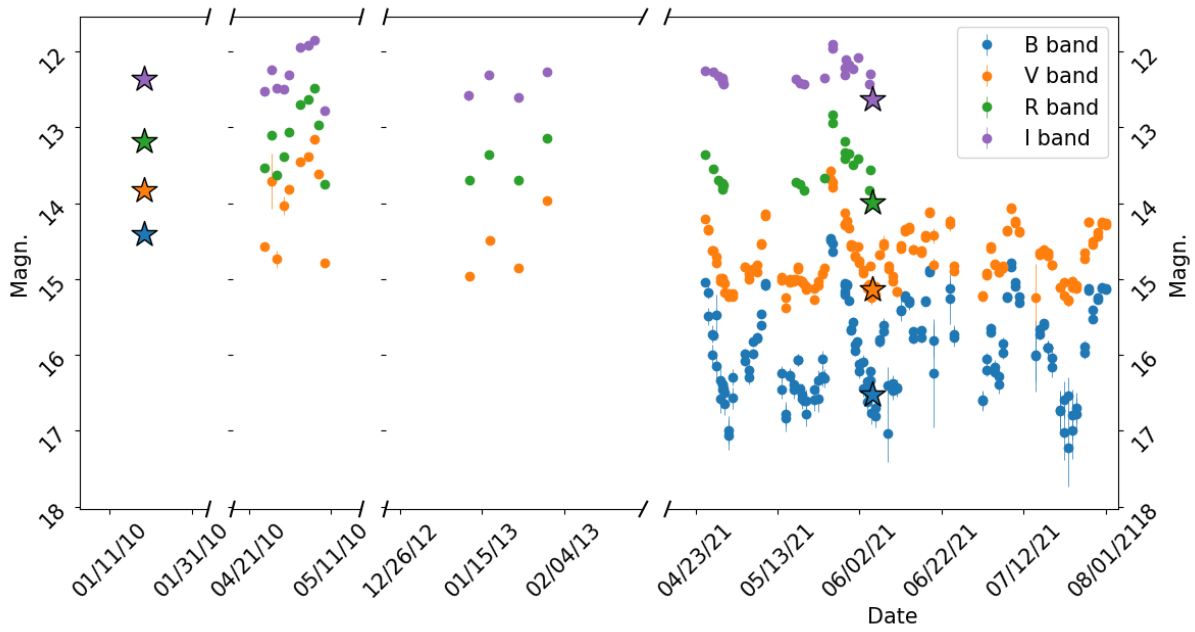

Figure 2.4: Comparison between the synthetic photometry and the available photometric data. The stars indicate synthetic photometry measured on the X-Shooter data in 2010 and 2021. The colors correspond to the same band as the photometric data.

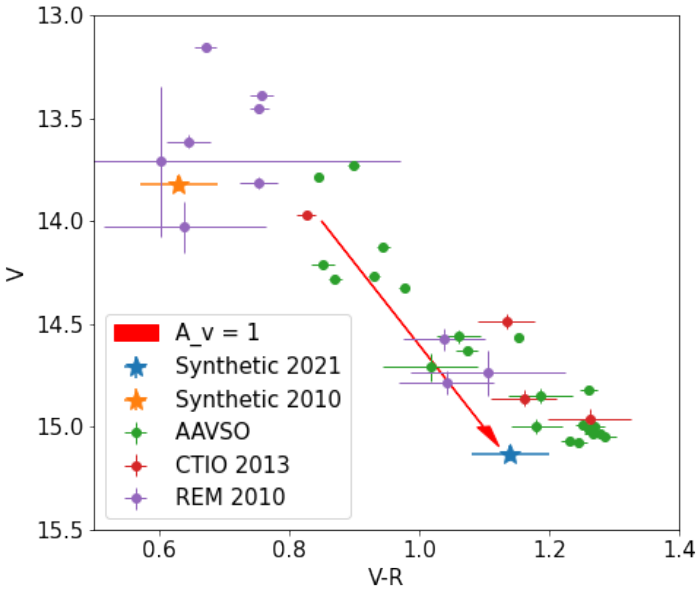

Figure 2.5: $V - R$ Color-magnitude diagram for the AAVSO photometric bands. The blue dots show the AAVSO photometry. The color was computed by combining the closest in time observations during the same nights. The red arrow displays the reddening vector for $A_V = 1$ mag and $R_V = 3.1$ using the extinction law by Cardelli et al. (1989). Synthetic photometry data obtained on the X-Shooter spectra and REM photometry is also shown.

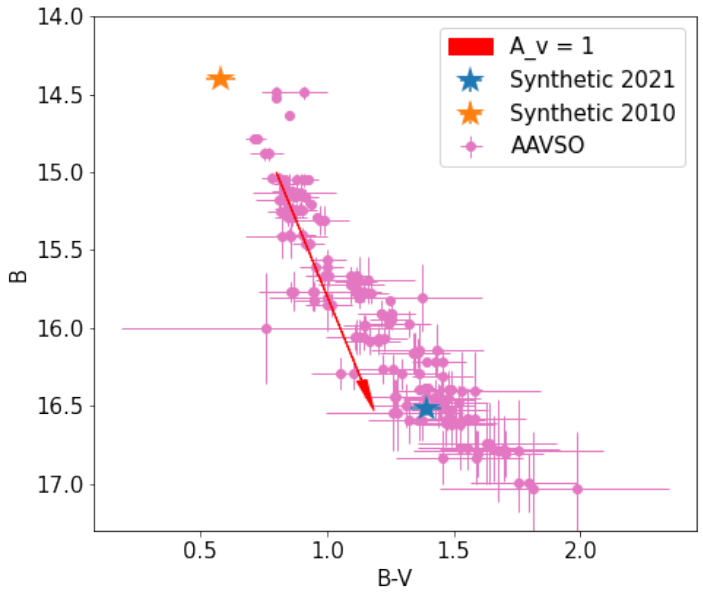

Figure 2.6: Same as Fig. 2.5, but for the $B - V$ color.

Table 2.2: Synthetic photometry on the X-Shooter spectra

Band	2010	2021
B	14.40	16.52
V	13.82	15.13
R	13.19	13.99
I	12.36	12.64

standard deviation of the ratios within these intervals. Fig. 2.7 displays the measured flux ratio of the two spectra along with the ratio expected from a difference in extinction (ΔA_V) following the Cardelli et al. (1989) reddening law.

The measured flux ratio between the spectra is steeper than any reasonable extinction difference and reddening law. This confirms that the difference in both spectra cannot be attributed to a variation in extinction between the two epochs, as described in Sect. 2.A.1.

2.B Additional analysis of the spectra

2.B.1 Variations in the lithium absorption

The lithium absorption line at $\lambda = 670.78$ nm is one of the strongest absorption lines in low-mass CTTS. The depth of this line solely depends on the stellar temperature and on the age of the target. For this reason, this is a key feature to constrain whether the variations seen in the spectra are due to accretion, which would result in a higher veiling of this line, or extinction, which would leave the line depth unaffected.

We decided to compare the depth of this line, not only between the 2010 and 2021 epochs of the X-Shooter observations, but to also include the spectra of XX Cha taken with the UVES instrument on the VLT within ± 2 days from the 2021 observations with X-Shooter. The UVES data were reduced with the ESO Reflex pipeline as described in Manara et al. (2021).

The continuum normalized lithium absorption line is shown in Fig. 2.8. The four spectra obtained in 2021 all show very similar depths, with differences mainly being due to the lower resolution of the X-Shooter observations with respect to the UVES ones. On the other hand, the spectrum obtained in 2010 shows a significantly shallower depth in this line, which is a clear signature of an increased veiling in this epoch. This should thus be ascribed to a stronger accretion rate in 2010.

2.B.2 Fitting of the X-Shooter spectra

To derive the stellar and accretion properties, we used the method by Manara et al. (2013a). This method consists of fitting three components to the observed spectra: a Class III template to reproduce the stellar photosphere, a slab model for the continuum excess emission due to accretion, and the reddening law by Cardelli et al. (1989) to account for interstellar extinction. The slab model and Class III template were scaled to match the observed flux at 360 and at 710 nm.

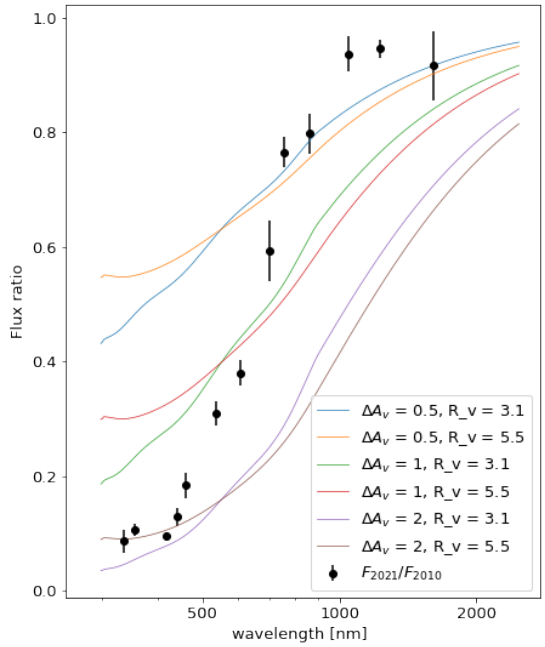

Figure 2.7: Comparison of the flux ratio of the observed spectra with the ratio expected from a difference in reddening ΔA_V applied to the two spectra. The black points indicate the average ratio of the observed spectra in wavelength windows of 4nm. The colored lines indicate the expected ratio from the Cardelli reddening law (Cardelli et al. 1989).

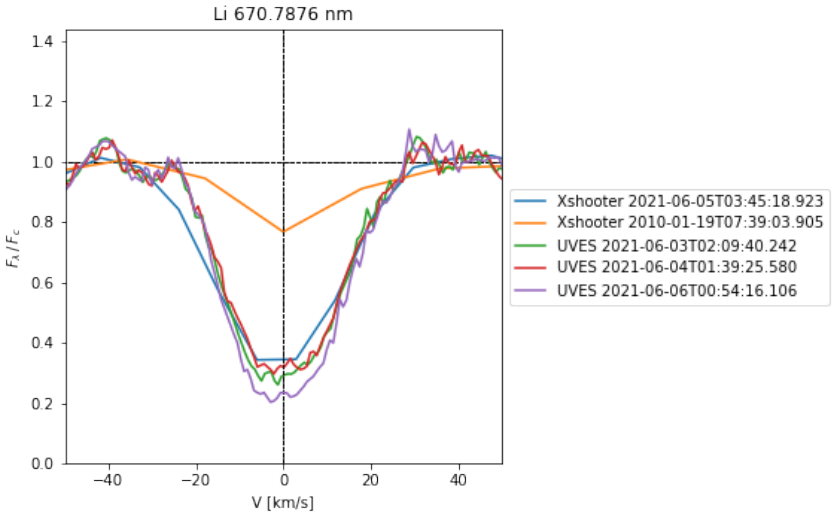

Figure 2.8: Lithium 670.78 nm line is shown normalized to the local continuum and as a function of velocity, after correcting for barycentric and radial velocity. The dates of the observations are reported in the legend.

A $\chi^2_{\rm like}$ function was computed for a grid of parameters considering different extinction values, slab model parameters and normalization, and Class III templates and their normalizations. This $\chi^2_{\rm like}$ was computed in some key spectral features, such as the Balmer jump, Balmer continuum, Paschen continuum, and a number of molecular bands that are indicative of the spectral type of the target.

Figures 2.9, 2.10 and 2.11 display the best-fit components around the Balmer jump. Comparing both figures highlights the significant differences in the accretion spectrum between the epochs.

2.B.3 Accretion luminosity from emission lines

The accretion luminosities obtained from individual lines (see Sect. 2.3.3) in both epochs are listed in table 2.3. These values are also plotted in Figs. 2.12 and 2.13, where they are compared to the results obtained from the UV excess in the corresponding epochs. The lines are ordered with increasing wavelengths, allowing one to discern possible trends with wavelength, which would indicate a wrong correction for extinction. Such a trend is not observed when using the value $A_V = 0.3$ mag for the 2010 epoch, whereas a slight dependence with wavelength is present at higher values of $A_V = 1$ mag (see Fig. 2.12). The accretion luminosity obtained from the CaK line is lower than that found from the other lines in both epochs. This difference is more pronounced in 2010. The accretion luminosity derived from this line is even lower in 2010 than in 2021. In Fig. 2.15 we show the profile of this line in the two X-Shooter observations, and we observe an inverse P-Cygni profile in the 2010 observation, with an otherwise similar profile and intensity. The additional absorption seen here is a likely cause for the low accretion luminosity

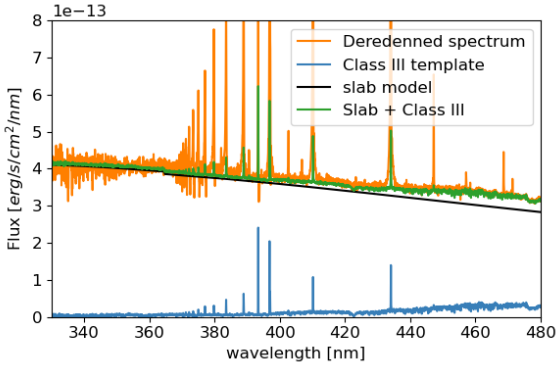

Figure 2.9: Best fit of the 2010 X-Shooter spectrum of XX Cha, with the best-fit parameters reported by Manara et al. (2016a).

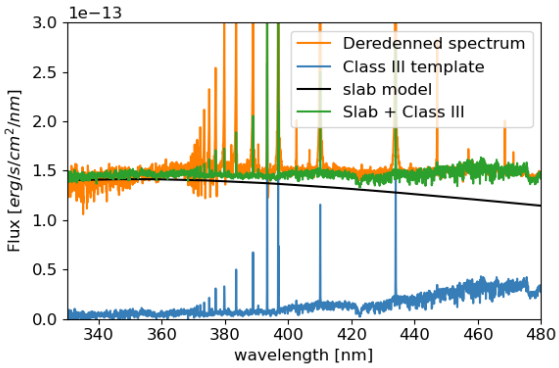

Figure 2.10: Best fit of the 2010 X-Shooter spectrum of XX Cha, assuming A_V = 0.3 mag, referred to as 2010* in the text.

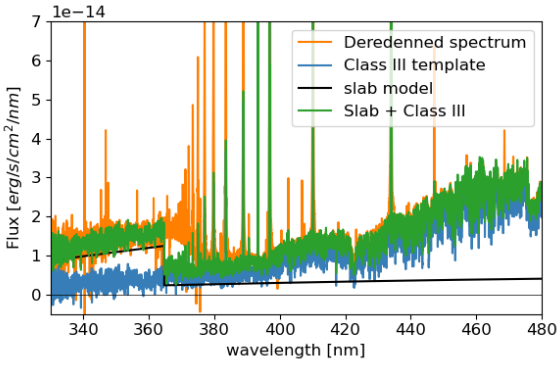

Figure 2.11: Best fit of the 2021 X-Shooter spectrum of XX Cha.

Table 2.3: Accretion parameters derived from the emission lines.

Epoch of observation	2010*	2021
	$\log(L_{\rm acc}/L_\odot)$	$\log(L_{\rm acc}/L_\odot)$
Hα	-1.43	-1.91
Hβ	-1.45	-2.02
Hγ	-1.43	-1.91
Hδ	-1.45	-1.90
CaK	-2.22	-2.23
$\rm HeI_{587}$	-1.42	-1.93
$\rm HeI_{667}$	-1.34	-1.91
Pa β	-1.52	-2.00
Pa γ	-1.66	-2.07
mean	-1.50 ± 0.35	-1.98 ± 0.35
$\log(\dot{M}_{\rm acc}/(M_\odot/{\rm yr}))$	-8.1 ± 0.4	-8.7 ± 0.4

Notes: The error on the mean $\log(L_{\rm acc}/L_\odot)$ is the standard deviation of the values obtained for the lines.

obtained. However, the Paβ, Paγ, and HeI line at 667.82 nm also display a similar absorption feature in 2010, but the derived $L_{\rm acc}$ are larger than in 2021.

The Hβ, Hγ, and Hδ lines profiles also change between both epochs. In 2021 they appear almost symmetrical, whereas in 2010 they are more extended on the blueshifted side. This is illustrated in figure 2.16, and further discussed in Sect. 2.3.3.

2.C $\dot{M}_{\rm acc}$-$M_\star$relation

Figure 2.17 displays the measured $\dot{M}_{\rm acc}$ and $M_\star$ for the targets in the Lupus and Chamaeleon I star-forming regions observed with X-Shooter. The data are taken from Manara et al. (2023), as in Fig. 2.3. XX Cha, reported with red symbols, is observed to be within the observed scatter in both epochs.

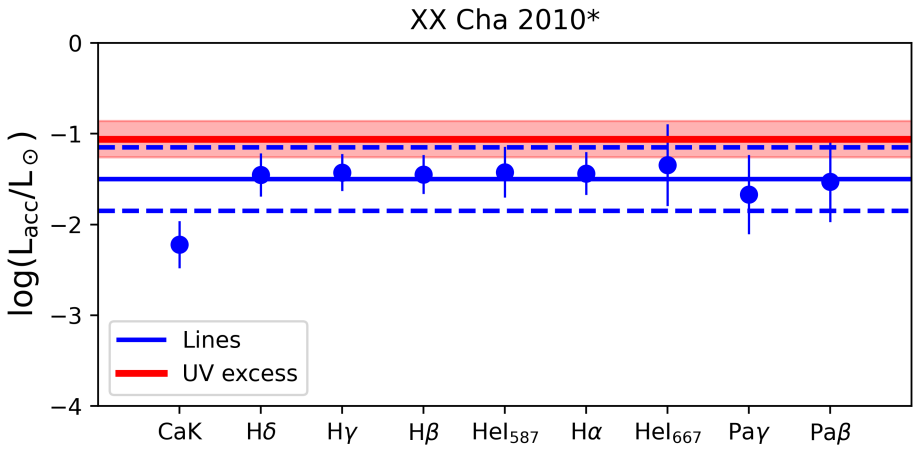

Figure 2.12: Comparison of the accretion luminosity derived from emission lines in the 2010* epoch with that derived from the UV excess. The mean accretion luminosity obtained from the lines is indicated with the solid blue line. The dashed lines indicates the error on the mean value. The accretion luminosity obtained from the UV excess is displayed with the solid red line and its error is shown via the shaded area.

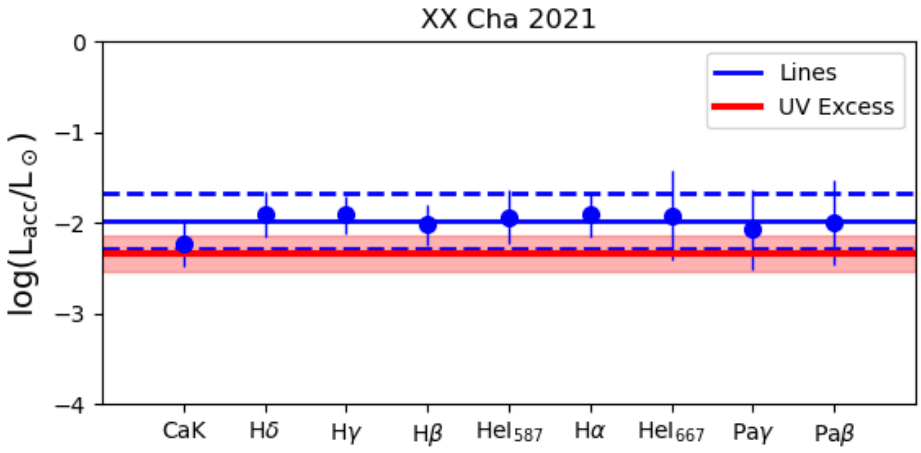

Figure 2.13: Comparison of the accretion luminosity derived from emission lines in the 2021 epoch with that derived from the UV excess. The mean accretion luminosity obtained from the lines is indicated with the solid blue line. The dashed lines indicates the error on the mean value. The accretion luminosity obtained from the UV excess is displayed with the red solid line and its error is shown via the shaded area.

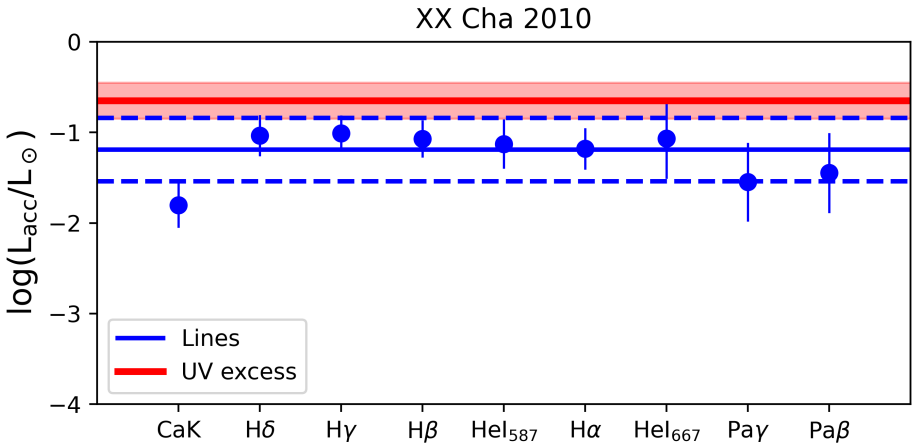

Figure 2.14: Comparison of the accretion luminosity derived from emission lines in the 2010 epoch with that derived from the UV excess. The mean accretion luminosity obtained from the lines is indicated with the solid blue line. The dashed lines indicates the error on the mean value. The accretion luminosity obtained from the UV excess is displayed with the red solid line and its error is shown via the shaded area.

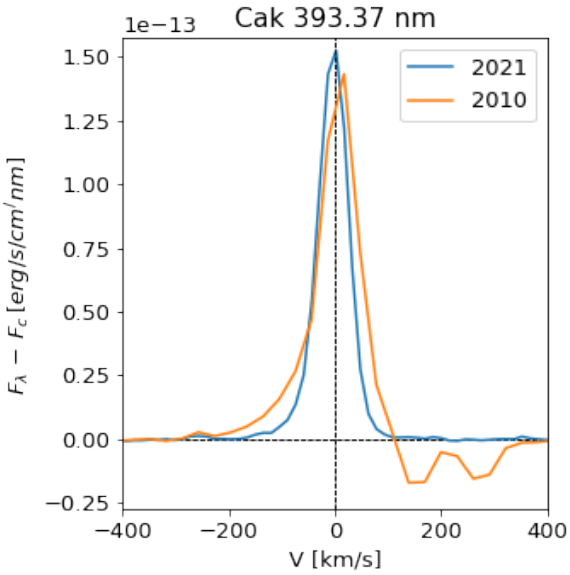

Figure 2.15: Profile of the CaK 393.37 nm line in the two X-Shooter observations.

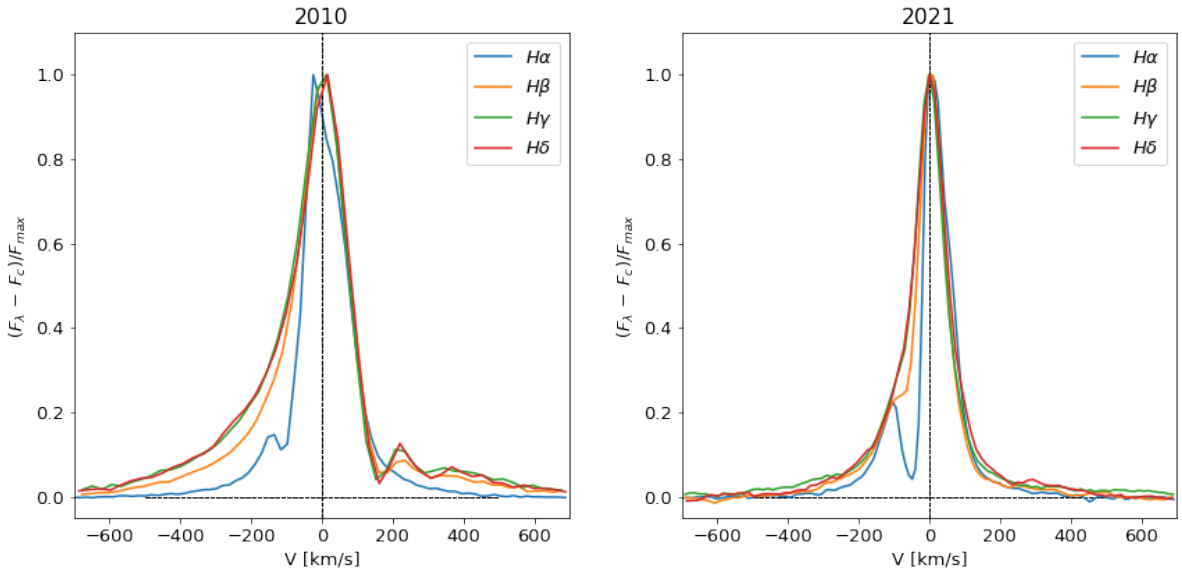

Figure 2.16: Comparison of the Balmer line profiles for the 2010 and 2021 X-Shooter spectra.

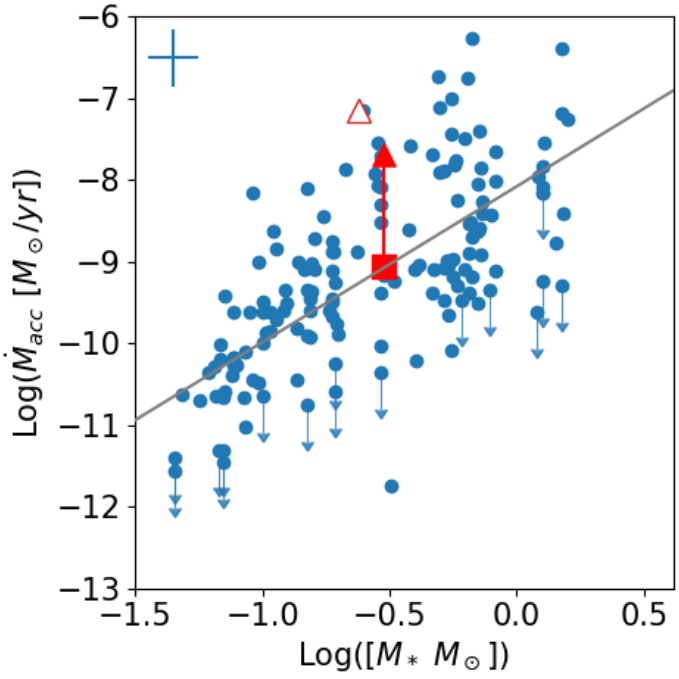

Figure 2.17: Measured $\dot{M}_{\rm acc}$ and $M_{\star}$ for the targets in the Lupus and Chamaeleon I star-forming regions observed with X-Shooter. The red-filled (empty) triangle and square indicate the 2010* (2010) and 2021 observations of XX Cha, respectively. The assumed errors for each data point is displayed on the top left-hand side. The gray line indicates the best-fit linear regression to the data.

3

A new approach to use class III spectra to derive stellar and accretion properties

This chapter was published as FitteR for Accretion ProPErties of T Tauri stars (FRAPPE): A new approach to use class III spectra to derive stellar and accretion properties ***Claes, R.A.B.****; J. Campbell-White, C. F. Manara, A. Frasca; A.Natta, J.M. Alcalá, A. Armeni; M. Fang; J.B. Lovell; B. Stelzer; L. Venuti; M. Wyatt; A. Queitsch; A&A 2024 Volume 690, id.A122, 26 pp*

This chapter depends on a collaborative work, in which had the opportunity to take the lead. In particular I was responsible for the data reduction, including the flux calibration and telluric correction, the analysis with exception of that performed with ROTFIT, code and interpretation. Finally, I composed the manuscript.

Abstract

Studies of the stellar and accretion properties of classical T Tauri stars (CTTS) require photospheric spectral templates to be compared with. The use of low-activity, slowly rotating field dwarfs or model spectra can be advantageous for the determination of stellar parameters, but it can lead to an overestimate of the mass accretion rate, since both classes of templates do not include the emission of the active chromosphere present in young stars. Observed spectra of non-accreting young stars are best suited to this purpose. Using such templates comes with the downside of a limited number of available templates and observational uncertainties on the properties of the templates.

For this work, we aimed to expand the currently available grid of wide-wavelength coverage observed spectra of non-accreting stars with additional new spectra and an interpolation method that allowed us to obtain a continuous grid of low resolution spectra ranging from spectral type G8 to M9.5, while also mitigating observational uncertainties. This interpolated grid was then implemented in the self-consistent method to derive stellar and accretion properties of CTTS. With the new templates, we aimed to estimate a lower limit on the accretion luminosities that can be obtained through a study of the UV excess emission using observed templates.

We analyzed the molecular photospheric features present in the VLT/X-shooter spectra of the targets to perform a spectral classification, including estimates of their extinction.

We applied a non-parametric fitting method to the full grid of observed templates to obtain an interpolated grid of templates. Both the individual templates and interpolated grid are provided to the community. We implemented this grid to improve the method to self-consistently derive stellar and accretion properties of accreting stars. We used the uncertainties on our interpolated grid to estimate a lower limit on the accretion luminosity that we can measure with this method.

Our new method, which uses a continuous grid of templates, provides results that are consistent with using individual templates but it significantly improves the reliability of the results in the case of degeneracies associated with the peculiarities of individual observed templates. We find that the measurable accretion luminosities range from $\sim$ 2.7 dex lower than the stellar luminosity in M5.5 stars to $\sim$ 1.3 dex lower for G8 stars. For young stars with masses of $\sim 1 M_{\odot}$ and ages of 3-6 Myr this limit translates into an observational limit of the mass accretion rate on the order of $10^{-10} M_{\odot}/\mathrm{yr}$. This limit is higher than the lower limit on the measurable mass accretion rate when using the various emission lines present in the spectra of young stars to estimate the accretion rate. An analysis of these emission lines allows us to probe lower accretion rates, pending a revised calibration of the relationships between line and accretion luminosities at low accretion rates The implementation of an interpolated grid of observed templates allows us to better disentangle degenerate solutions, leading to a more reliable estimate of accretion rates in young accreting stars. [1]

3.1 Introduction

Young stars are surrounded by circumstellar disks in which planets form (e.g., Williams & Cieza 2011). These disks dissipate in a few million years (e.g., Fedele et al. 2010). The processes governing their evolution and dispersal, and their impact on planet formation remain open questions (e.g., Manara et al. 2023, for a review). The first proposed mechanism involves the gradual spread of the disk due to viscosity, resulting in most of the material accreting onto the central star, with a small fraction of material carrying the angular momentum outward (Lynden-Bell & Pringle 1974; Hartmann et al. 1998). An alternative scenario sees the evolution dominated by the ejection of angular momentum from the disk in magnetohydrodynamic (MHD) winds (Blandford & Payne 1982b; Lesur 2021b,a; Tabone et al. 2022b). At the same time, high-energy radiation from the star, such as far-ultraviolet (FUV), extreme ultraviolet (EUV), or X-ray radiation, removes material from the inner disk in the form of photoevaporative winds. This process may potentially create a gap in the inner disk and ultimately lead to the dissipation of the disk (e.g., Clarke et al. 2001; Alexander et al. 2014; Ercolano & Pascucci 2017). Understanding the impact of viscosity, MHD winds, and internal photoevaporation is critical for our understanding planet formation. Indeed, while these processes are ongoing, the dust grains present in the disks are expected to grow from small grains into planetesimals (e.g., Johansen et al. 2007; Booth & Clarke 2016; Carrera et al. 2017, 2021). These planetesimals can further grow into planetary systems (e.g., Alibert et al. 2005; Liu et al. 2019; Lyra et al. 2023), or may be revealed in the form of collisionally active debris disks once the gas in the disk has dissipated (e.g., Wyatt 2008; Hughes et al. 2018; Lovell et al. 2021).

Each of these disk evolution mechanisms makes specific predictions about the time evolution of accretion rates through the disk, and thus on the central star. Determining the mass accretion rate of young stars is therefore a key parameter to shed light on whether viscous or MHD-wind

[1] Based on observations collected at the European Southern Observatory under ESO programmes 085.C-0764(A), 093.C-0506(A), 106.20Z8.004, 106.20Z8.006, 106.20Z8.008, 109.23D4.001, 110.23P2.001

driven evolution dominates disk evolution and which role photevaporation plays in dissipating the disk (e.g., Mulders et al. 2017; Lodato et al. 2017; Somigliana et al. 2020, 2023).

Numerous studies attempted to constrain disk evolution by analyzing theoretically expected and observed relationships between the mass accretion rate and stellar or disk properties, such as the disk and stellar mass (e.g., Dullemond et al. 2006; Hartmann et al. 2006; Alexander et al. 2006; Ercolano et al. 2014; Mulders et al. 2017; Rosotti et al. 2017; Manara et al. 2020). Currently no definitive conclusions have been drawn in favor of either model.

Recently, Alexander et al. (2023) showed that the distribution of $\gtrsim 300$ homogeneous accretion rate measurements of young stars in the $0.5 - 1.0\ M_{\odot}$ range should suffice to distinguish between a viscous+photoevaporation and a MHD-wind driven disk evolution scenario. Currently, only ~ 100 accretion rate measurements are available in this mass range, and this sample lacks homogeneous upper limits for the non-detections. Providing such upper limits could enable even stronger statistical approaches to further constrain model parameters. Ercolano et al. (2023) used the accretion rate distribution of a sample of potential extreme low accretors presented by Thanathibodee et al. (2022, 2023) to discern between different types of photoevaporation that could dissipate the disk at the end of a viscously driven evolution scenario. This sample was limited as it only contained 24 sources. A thorough characterization of more low accretors can therefore provide valuable constraints on disk evolution processes.

Tracers of the accretion and outflow processes can be found in the spectra of young stars. The current paradigm for accretion in young, low-mass ($\lesssim 1\ M_{\odot}$) stars is known as magnetospheric accretion (Hartmann et al. 2016, for a review). In this scenario, accreting material is funneled by the star's magnetosphere onto its surface, creating hotspots that emit excess continuum radiation in the ultraviolet and optical spectra (Calvet & Gullbring 1998). The hot gas associated with the accretion streamers leads to the appearance of various prominent emission lines (e.g., Hα, Hβ Ca K, and Paβ) in the spectra (e.g., Muzerolle et al. 2001; Campbell-White et al. 2021).

The spectroscopic study of young stars can, therefore, provide vital constraints on the physics governing disk evolution. Accurately representing the emission from the central star is crucial in these investigations. Several methods are employed to estimate accretion rates in young stars. As a first option one can fit the line profile using magnetospheric accretion flow models (Muzerolle et al. 2001; Thanathibodee et al. 2023). The downside of these models is that they assume the stellar magnetic field to be both dipolar, aligned with the stellar rotation axis and disk, which is not necessarily accurate (e.g., Donati et al. 2008; Alencar et al. 2012b; Singh et al. 2024). In a second method, the line luminosity of various emission lines is converted into an accretion luminosity using empirical relations (e.g., Herczeg & Hillenbrand 2008; Alcalá et al. 2014, 2017). These relations are calibrated using the third method which is the only one that directly probes the energy released at the accretion shock. This method consists of measuring the UV continuum excess emission (e.g., Valenti et al. 1993; Calvet et al. 2004; Herczeg & Hillenbrand 2008; Rigliaco et al. 2012; Ingleby et al. 2013; Pittman et al. 2022; Robinson et al. 2022). In order to self-consistently determine both the stellar and accretion parameters, the UV-excess and the spectral features in the optical part of medium-resolution flux-calibrated spectra must be fit simultaneously (Manara et al. 2013a). For this aim, both the photospheric and chromospheric emission in the UV part of the spectrum must be correctly accounted for (Ingleby et al. 2011; Manara et al. 2013b).

3.1 Introduction

Available synthetic spectra (e.g., Allard et al. 2011) do not fully reproduce the observed spectra of chromospherically active low gravity objects, such as pre-main sequence low-mass stars. In particular, none of the current models contain emission originating in the chromospheres of young stars, since only the stellar photospheres are modeled, which dominate only at wavelengths longer than the Balmer Jump. At shorter wavelengths, bound free and free free emission originating in the chromosphere starts to dominate the continuum (Houdebine et al. 1996; Franchini et al. 1998). The chromosphere also emits in several spectral lines that are used to constrain accretion properties of accreting young stellar objects (YSOs, Stelzer et al. 2013). The spectra of field dwarfs will also poorly represent those of young stars as the former have a significantly higher $\log g$. The best solution appears to use spectra of non-accreting young stars. Class III stars (Greene et al. 1994), which are defined according to their infrared classification where they display a lack of infrared excess emission $d\log(\nu F_\nu)/d\log(\nu) < -1.6$ (Williams & Cieza 2011), make ideal candidates for such templates, as this category often overlaps with Weak lined T Tauri Stars (WTTS), which present much fainter emission lines than CTTS.

A grid of class III templates with broad wavelength coverage medium-resolution spectra obtained with the X-shooter spectrograph on the ESO Very Large Telescope (VLT) was previously provided to the community by Manara et al. (2013b) (hereafter MTR13) and further expanded by Manara et al. (2017a) (hereafter MFA17). This grid includes 41 spectra and contains spectral types ranging from G4 to M8. Both MTR13 and MFA17 used these spectra to estimate the contribution of chromospheric emission to the emission lines that are commonly used for the determination of mass accretion rates. To study the contribution of the chromosphere to the UV continuum emission, Ingleby et al. (2011) compared the spectrum of the M0 class III RECX-1 to the photospheric spectrum of a standard dwarf star. Here it was found that attributing this excess to accretion would result in an estimated accretion luminosity of $\log(L_{\rm acc}/L_\star) = -1.3$. The chromospheres of young stars can therefore significantly affect measured accretion rates in low accretors. Moreover, the Balmer continuum excess emission and the Balmer Jump are more difficult to detect in the spectra of early-type (<K3) YSOs than in the later types due to the lower contrast between photospheric emission and accretion induced continuum excess emission (Herczeg & Hillenbrand 2008). Constraints on the influence of the chromospheric emission in the UV on measurements of (low) accretion rates is still lacking. A better understanding of the chromospheres of young stars is therefore needed to characterize the lowest accretors to better understand the late phases of disk dispersal and hence, provide constraints on disk evolution models.

Here we expand the library of X-shooter class III templates previously provided by MTR13 and MFA17 by an additional 18 templates and present a method for interpolating between them. We also aim to constrain the influence of the UV continuum chromospheric emission on determination of mass accretion rates. The paper is structured as follows. The sample selection, observations and data reduction are described in Sect. 3.2. The analysis of the stellar properties of our sample is described in Sect. 3.3. In Sect. 3.4 the final grid and our method for interpolating it are discussed. Sect. 3.5 discusses an application of this interpolated grid using a self consistent method to derive the mass accretion rates and validate this method on a set spectra of accreting young stars in the Chamaeleon I star-forming region. In Sect. 3.6.1 we obtain a lower limit on the mass accretion rates that we can measure from the UV excess, taking into account

uncertainties on the chromospheric emission and discuss the implications for studies of mass accretion rate ($\dot{M}_{\rm acc}$) in CTTS. Finally, we summarize our conclusions in Sect. 3.7.

3.2 Sample, observations, and data reduction

The new targets considered in this work come mainly from the sample of Lovell et al. (2021), who studied 30 class III stars (age $\lesssim$10 Myr) using the Atacama Large Millimeter Array (ALMA). Lovell et al. (2021) reaffirmed that these sources are class III YSO through a comparison of the K-band (2MASS) and either 12μm (WISE) or 24μm (*Spitzer*) fluxes. In addition to this Lovell et al. (2021) fitted the SEDs of these targets and found no significant NIR excess emission. These stars are likely members of of the Lupus star forming region, although their membership still needs to be confirmed (Lovell et al. 2021; Michel et al. 2021). A total of 19 objects of this sample were recently observed using X-shooter (Pr.ID. 109.23D4.001, 110.23P2.001, PI Manara), a broad-band, medium-resolution, high-sensitivity spectrograph mounted on the ESO/VLT. The two components of a binary system, THA15-36A and THA15-36B, were observed simultaneously in the slit. Three additional archival X-shooter spectra were available for the targets MT Lup and NO Lup (Pr.ID. 093.C-0506(A), PI Caceres) and MV Lup (Pr.ID. 085.C-0764(A), PI Günther). Other targets in the sample of Lovell et al. (2021) were already included in the grid of MTR13 and MFA17. In addition to this, we use in this work two targets observed with VLT/X-shooter in the PENELLOPE Large Program (Pr.ID. 106.20Z8, Manara et al. 2021), namely RECX-6 and RXJ0438.6+1546. RECX-6 was identified as a class III YSO by Sicilia-Aguilar et al. (2009) based on a fit of its SED. RXJ0438.6+1546 was already included in the grid of MFA17, who selected their targets based on available *Spitzer* data. The latter was already observed with X-shooter and included in the sample of MFA17, but the new observations are used here. In total the targets considered in the analysis in this work are 24, observed in 23 observations.

The wavelength range covered with X-shooter is divided into three arms, the UVB arm ($\lambda\lambda \sim 300 - 550$nm), the VIS arm ($\lambda\lambda \sim 500 - 1050$nm), and the NIR arm ($\lambda\lambda \sim 1000 - 2500$nm). Different slit widths were used for the different arms and for fainter or brighter targets. For brighter sources, we used 1.″0, 0.″4, 0.″4 wide slits in the UVB, VIS and NIR arm respectively. These slit widths provide typical spectral resolutions of $R \sim$ 5400, 18400 and 11600 in the three arms. Fainter, later spectral type objects were observed using 1.″0, 0.″9, 0.″9 in the three arms, providing resolutions of $R \sim$ 5400, 8900 and 5600. For MV lup, RXJ0438.6+1546, MT Lup and NO Lup, the 0.″5 wide slits were used in the UVB arm, resulting in spectra with resolution $R \sim$ 9700. The observations with the slits with the aforementioned widths were preceded by short exposures with a slit with the significantly larger width of 5.″0 in all arms to obtain spectra not affected by slit losses to be used for absolute flux calibration. The only exception of the use of the wide slits were MV Lup, MT Lup, and NO Lup.

Appendix 3.A contains a log of the observations presented here. In the observing log, several targets are highlighted as spatially unresolved binaries. We exclude these spectra from our sample since they can not be used as templates to represent the stellar emission of individual targets and an analysis of these spectra is outside the scope of this paper. In particular, we exclude

CD-39 10292, THA15-38, CD-35 10498, V1097 Sco and NN Lup. NN Lup was discovered to be SB2 binaries in our analysis with the ROTFIT tool (see Sect. 3.3.2). CD-39 10292 is an SB2 binary first identified by Melo et al. (2001). V1097 Sco and CD-35 10498 were identified as binaries by Zurlo et al. (2021) and were not spatially resolved in the X-shooter slit. THA15-38 was resolved as a binary in the acquisition image of ESPRESSO observations that are part of the PENELLOPE program. This was possible due to the excellent seeing conditions ($\lesssim 0\farcs6$) during the night of the ESPRESSO observations.

The data reduction was performed using the ESO X-shooter pipeline v.4.2.2 (Modigliani et al. 2010) in the Reflex workflow (Freudling et al. 2013). The pipeline executes the standard reduction steps: flat fielding, bias subtraction, extraction and combination of orders, rectification, wavelength calibration, flux calibration using a standard star observed during the same night and the final extraction of the 1D spectrum. The telluric lines were removed from the narrow slit observations using the molecfit tool (Smette et al. 2015). This was done by fitting the telluric features on the spectra themselves, rather than by using a telluric standard star. As a final step, the narrow slit observations were rescaled to the continuum flux of the wide slit spectra to get flux-calibrated spectra, using the procedure developed for the PENELLOPE program (see Manara et al. 2021). For the UVB arm this was done using a correction factor constant with wavelength. The VIS and NIR arms were rescaled using a factor with a linear dependency on wavelength. To test the flux calibration of our spectra they were compared to archival photometry. The overall agreement between the spectra and photometry is excellent (Δmag < 0.2 mag) with the exception of 2MASSJ16090850-3903430 and THA15-36. This is however within the typical variation range at optical wavelength which is mostly due to starspots rotational modulation. A description of how we flux calibrated targets with Δmag > 0.2 mag can be found in Appendix 3.A. Appendix 3.A also contains a description of how we obtained an accurate flux calibration for the apparent visual binary THA15-36, which was spatially resolved in the X-shooter slit. Zurlo et al. (2021) resolved this system using VLT/NACO, and argued that both components are unbound given their different *Gaia* distances (146.5 ± 0.8 pc for the primary and 154.3 ± 1.8 pc for the secondary).

3.3 Stellar parameters of the new class III spectra

In this section, we derive the stellar parameters for all the 19 resolved stars whose spectra are presented here for the first time. This was done by first determining the spectral type from atomic and molecular features present in the spectra, then comparing these estimates with results from the fitting of individual absorption lines, and finally determining the stellar luminosity to place the targets on the Hertzsprung-Russel Diagram (HRD) to derive their stellar masses.

3.3.1 Spectral type and extinction determination

Determining spectral types (SpT) for (non-accreting) young stellar objects is a complex process that is best performed by comparison with other targets of well known SpT. In this case, we consider the grid of non-accreting class III young stellar object of MTR13 and MFA17 as a starting point, and later also check and refine their grids using the new spectra presented here.

Table 3.1: Spectral types and extinction obtained in this work.

Name	A_V	SpT	Uncertainty	literature	HH14	TiO	Riddick et al.
CD-31_12522	0.0	K0.5	$\pm$1	K2[a]	K0.7	K4.7	...
RXJ1608.9-3905	0.0	K2.0	$\pm$1	K2[b]	K1.7	K4.5	...
MV Lup	0.0	K2.0	$\pm$1	K2[c]	K2.0	K4.5	...
RXJ0438.6+1546	0.0	K2.0	$\pm$1	K2[d]	K1.3	K4.6	...
2MASSJ15552621-3338232	0.1	K6.0	$\pm$1	K5[e]	K8	K5.6	...
MT Lup	0.1	K5.5	$\pm$1	K5[f]	K8.7	K4.9	...
MX Lup	0.0	K6.0	$\pm$0.5	K6[c]	K9.0	K5.2	...
RXJ1607.2-3839	0.35	K7.5	$\pm$0.5	K7[c]	K9.0	K7.7	...
MW Lup	0.0	K7.5	$\pm$0.5	K7[c]	K11.9	K7.4	...
NO Lup	0.35	K7.5	$\pm$0.5	K7[c,g]	K9.9	K7.5	...
THA15-43	0.0	K7.5	$\pm$0.5	M0[h]	M3.6	K7.7	...
THA15-36A	0.0	M0.5	$\pm$1	...	M1.1	M0.8	...
THA15-36B	0.5	M2.0	$\pm$1	...	M2.7	M2.0	...
RECX-6	0.0	M3.0	$\pm$0.5	M3[i]	M3.6	M3.4	M3.6
Sz67	0.0	M3.0	$\pm$0.5	M4[c]	M3.8	M3.7	M3.8
2MASSJ16090850-3903430	0.3	M5.0	$\pm$0.5	M5[c]	M5.3	M5.4	M5.3
2MASSJ16075888-3924347	0.25	M4.5	$\pm$0.5	M5[c]	M5.0	M4.8	M5.1
2MASSJ16091713-3927096	0.75	M5.5	$\pm$0.5	M5[c]	M5.8	M6.0	M5.7
V1191 Sco	0.4	M5.5	$\pm$0.5	M5[c]	M6.2	M5.8	M5.9

Notes: The spectral types and extinction obtained in this work from comparing to available templates are reported in column 2 and 3, with the uncertainty on the SpT reported in column 4. The other columns report previous literature SpT values, and those obtained using the spectral indices from HH14, Jeffries et al. (2007), and Riddick et al. (2007). The uncertainty on the SpT is given in subclasses. Refrences: a: Torres et al. (2006), b: Galli et al. (2015),c: Padgett et al. (2006), d: MFA17,e: Köhler et al. (2000),f: Krautter et al. (1997),g: Hardy et al. (2015),h: Merín et al. (2008),i: Rugel et al. (2018)

3.3 Stellar parameters of the new class III spectra

The first estimate of the SpT of our targets was obtained applying to the new spectra the same spectral indices used by MTR13 and MFA17, namely the spectral indices presented by Riddick et al. (2007), the TiO index of Jeffries et al. (2007) and the indices presented by Herczeg & Hillenbrand (2014, hereafter HH14). The indices of Riddick et al. (2007) are accurate for spectral types later than M3. The indices by Jeffries et al. (2007) hold for spectral types later than K6, since the used TiO feature disappears for earlier SpTs. The indices of HH14 are accurate for SpTs from early K to late M stars. The results for these different methods are listed in Table 3.1. Spectral indices are less reliable estimates of the SpT in cases in which the extinction is substantial since they are based on ratios of features at different wavelength ranges. In general, extinction is low for our targets, but it can still introduce additional uncertainty to the SpT estimates obtained from the spectral indices.

Therefore, to obtain a simultaneous extinction and SpT estimate, we performed a comparison of the spectra in our sample with the spectra of MTR13 and MFA17, which have negligible extinction. We obtained the first estimates of SpT and A_V using a simple χ^2-like comparison. The final values of both the spectral type and extinction are derived through a visual comparison between the spectra presented here and those presented by MTR13 and MFA17. The main indicators used in this comparison are the depths of various molecular bands. The K6 to M9.5 spectra include a variety of molecular features whose depth increases almost monotonically for later SpTs in the spectral region between 580 and 900 nm. This includes various absorption bands from TiO ($\lambda\lambda$ 584.7-605.8, 608-639, 655.1-685.2, 705.3-727, 765-785, 820.6- 856.9, 885.9-895 nm), CaH ($\lambda\lambda$ 675-705 nm) and VO ($\lambda\lambda$ 735-755, 785-795, 850-865 nm). Fig. 3.1 displays spectra with SpTs ranging from M1 to K7.5. Similar figures for the other spectra with SpT later than K5 can be found on ZENODO [2]. The previously mentioned molecular features can be seen to increase in depth for later spectral types.

For SpT earlier than K6 a MgH and Mg b absorption feature ($\lambda\lambda$ 505-515 nm) was used to assess the spectral type. The use of this feature was first discussed by HH14 who present it in the context of a spectral index. The depth of this absorption feature is best determined by comparing the flux at 510nm to the flux expected at the same wavelength from a linear fit between the median flux of the spectral regions of $\lambda\lambda$ 460-470 nm and $\lambda\lambda$540-550nm. Fig. 3.2 displays this feature for spectral types from K1 to K6. Here the linear fit between $\lambda\lambda$ 460-470 nm and $\lambda\lambda$540-550 nm is also indicated. Additionally, a linear fit for the regions of $\lambda\lambda$ 488-492 nm and $\lambda\lambda$514-516 nm was included in this figure to highlight the increasing depth of this feature with SpT. We perform this comparison at different values of extinction to estimate it simultaneously. The results are listed in Table 3.1, where we have rounded the SpT to half a subclass.

Our estimates are typically consistent within at most 1.5 subclass of the literature values. The TiO spectral indices agrees within 1 subclass for targets later than K5. The spectral indices of HH14 agree within a subclass at all spectral types except for the K5 to M0 range. Finally the indices of Riddick et al. (2007) have a similar agreement for the targets later than M3. We note that the use of features in the NIR region ($\lambda\lambda > 1000$ nm) can give rise to significantly different spectral types. On top of the fact that the NIR indices are based on features covering a larger wavelength range and thus are more affected by extinction and by imperfect telluric removal

[2] https://zenodo.org/doi/10.5281/zenodo.12686015

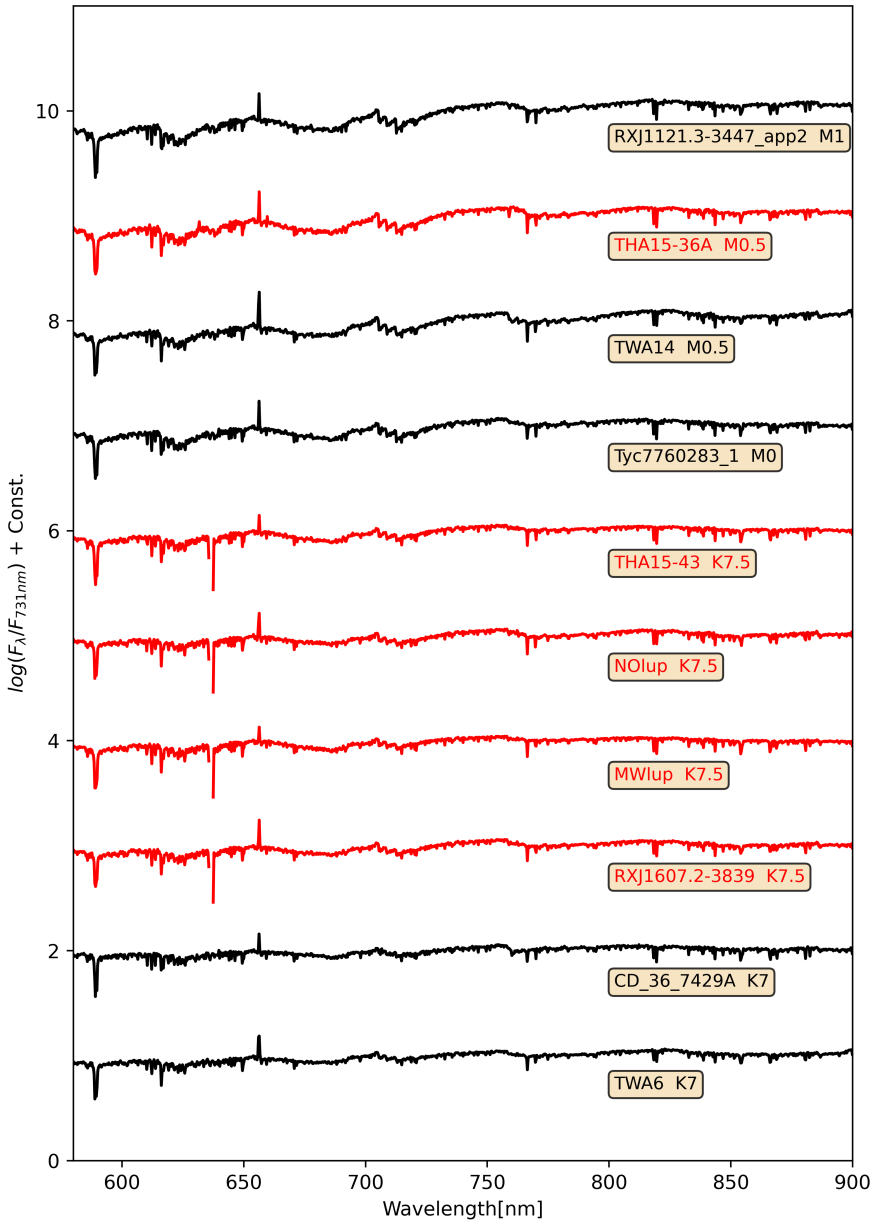

Figure 3.1: X-shooter spectra of class III YSOs with spectral type ranging from M1 to K7. All the spectra are normalized at 731 nm and offset in the vertical direction for clarity. The spectra are also smoothed to the resolution of 2500 at 750 nm to make easier the identification of the molecular features. The black colors indicate spectra presented by MTR13 and MFA17. The red color is used for spectra presented for the first time here.

and or flux calibration in that wavelength range (e.g., MTR13), the likely explanation for this deviation is the presence of cold spots on the stellar surface (e.g., Stauffer et al. 2003; Vacca & Sandell 2011; Pecaut 2016; Gully-Santiago et al. 2017; Gangi et al. 2022).

We adopted similar uncertainties on the SpT as MFA17. For objects later than K6 we estimate the uncertainties to be 0.5 subclass. For objects earlier than K6 we estimate the uncertainties to be 1 subclass. For the binary components of THA15-36 we assumed larger uncertainties of 1 subclass due to the less certain flux calibration of the spectra. We estimate the uncertainty on the extinction to be 0.2 mag. A description of how we confirmed the uncertainties on the SpT and estimated those on the extinction follows in Sect. 3.4 and Appendix 3.B.

3.3.2 Photospheric properties from ROTFIT

A large number of absorption lines are resolved in the spectra, allowing us to obtain photospheric properties. We analyzed the absorption lines in the VIS arm of the X-shooter spectra using the ROTFIT tool (e.g., Frasca et al. 2015, 2017) to derive the effective temperature ($T_{\rm eff}$), surface gravity ($\log g$), projected rotational velocity ($v \sin i$), radial velocities (RV), and veiling at three wavelengths ($\lambda\,620$ nm, $\lambda\,710$ nm and $\lambda\,970$ nm). The veiling is given by $r = EW(template)/EW(observation) - 1$, where EW is the equivalent width of absorption lines near the wavelength of interest. ROTFIT searches, within a grid of templates, for the spectrum that minimizes the χ^2 to the target spectrum in different spectral regions. The templates consist of a grid of BT-Settl model spectra (Allard et al. 2011) of solar metallicity, $\log g$ ranging from 0.5 to 5.5 dex and an effective temperature ranging from 2000 to 6000 K. ROTFIT achieves this by first deriving the radial velocity of the star cross-correlating the target and template spectrum and uses this information to shift the observed spectrum to the rest frame. ROTFIT then convolves the templates with both a Gaussian to match the X-shooter resolution. Then the templates are iteratively broadened by convolution with a rotational profile with increasing $v \sin i$ until a minimum χ^2 is attained. ROTFIT analyzes spectral intervals that contain features sensitive to $\log g$ and/or the $T_{\rm eff}$ such as the KI doublet at $\lambda \approx 766 - 770$ nm and the NaI doublet at $\lambda \approx 819$ nm. An additional continuum emission component is added to the template in order to estimate the veiling. As for the $v \sin i$, per each template, the veiling is also a free parameter in the fit.

We did not set this continuum component and therefore the veiling to 0 despite most of our targets being non-accretors. We preferred to let the veiling vary for our class III stars as a check. As expected, we always found zero or low veiling values, which could be the result of small residuals in the scattered light subtraction or the effect of the interplay between different parameters. The largest value of r=0.4 is found at 620 nm for three K-type stars. A possible explanation could be the effect of starspots on the spectra. Another possible explanation is that of an undetected companion. Apart from these extreme values, we do not consider veiling values as small as 0.2 to be significant. The photospheric parameters, $v \sin i$, veiling measurements, and RV derived with ROTFIT can be found in Table 3.2. As stated in Sect. 3.2, during this analysis, we found two targets to be double lined spectroscopic binaries, namely NN Lup and CD-39 10292. We excluded these from our analysis. Fig. 3.3 shows the comparison between the $T_{\rm eff}$ derived using ROTFIT and obtained using different SpT -$T_{\rm eff}$ conversions. Here it can be seen that the effective temperature obtained from the SpT agrees best with ROTFIT when using

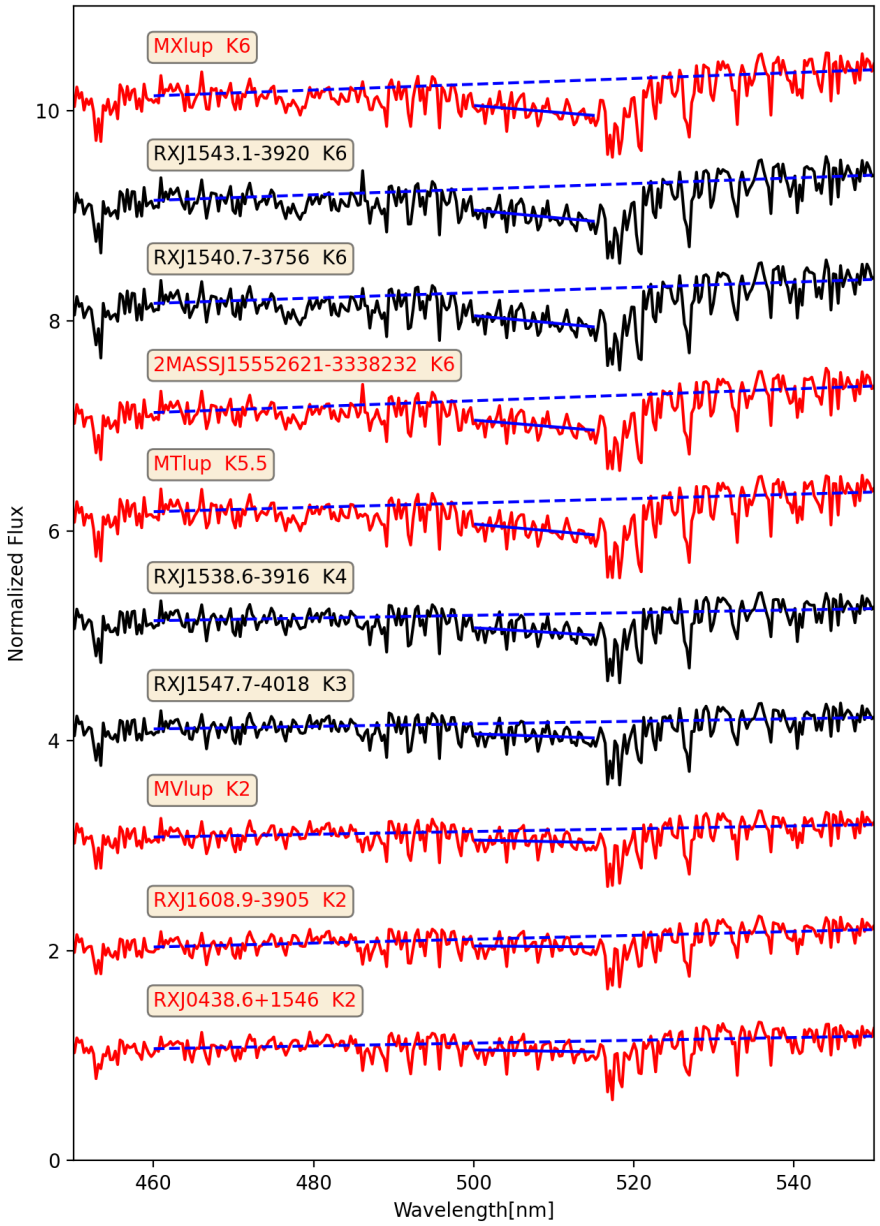

Figure 3.2: X-shooter spectra of class III YSOs with a SpT ranging from K6 to K2. The spectra have been normalized at 460 nm and an offset has been added for clarity. The spectra have been smoothed to have a resolution of ∼2500 at 750nm. The observations presented here are displayed in red, while the spectra of MTR13 and MFA17 are indicated in black. We highlight the R510 spectral index feature using the solid blue line. The dashed blue line indicates the slope of the surrounding continuum.

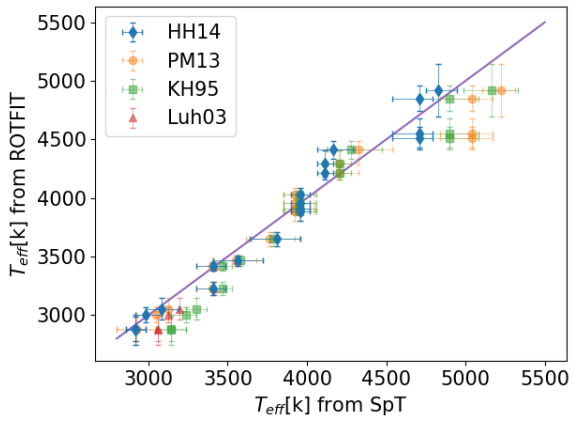

Figure 3.3: Comparison between the temperatures obtained with ROTFIT and from the spectral type for the targets presented here. The relation of Herczeg & Hillenbrand (2014) is labeled as HH14, the one by Pecaut & Mamajek (2013) as PM13, that of Kenyon & Hartmann (1995) asn KH95 and the relationship of Luhman et al. (2003) as Luh03. The relations are only applied to spectral type ranges where they are valid. The solid line represents the one-to-one relation.

the SpT -$T_{\rm eff}$ relation by HH14. The low $\log g$ found are mostly compatible with that of young objects ($\lesssim$10 Myr).

3.3.3 Luminosity determination

The stellar luminosities were obtained using a method similar to that used by MTR13. In this method, the dereddened spectra are extrapolated to wavelengths not covered by the spectra and integrated to compute the bolometric flux.

The X-shooter spectra were extrapolated using a BT-Settl (Allard et al. 2011) synthetic spectrum appropriate for the target. We used the effective temperature obtained from the SpT$-T_{\rm eff}$ relation of HH14. We prefer this $T_{\rm eff}$, since in Sect. 3.5.1 we will use the obtained SpT to compute the luminosity. For the metallicity of the synthetic spectra we assumed solar values, typical for targets in the Lupus region (Biazzo et al. 2017), and for the surface gravity we chose $\log g = 4.0$ in all cases. This parameter has very limited impact on the global luminosity estimate, since most of the stellar emission is covered by the X-shooter spectra and the synthetic spectra are used to measure a minor fraction of the global emission. The synthetic spectra were then matched to the spectra at 400.5 nm and 2300 nm and used to represent the flux at wavelengths shorter and longer than these respective values. The wavelengths chosen here differ from those used by MTR13. We chose these wavelengths in order to avoid the high noise level at short wavelengths and poor flux calibration at the end of the K-band present in some spectra. Due to this difference, we also reapplied this method to the sample of MTR13 and MFA17. We also performed a linear interpolation across the strong telluric absorption features between the J,H, and K band ($\lambda\lambda$ 1330-1550 nm, $\lambda\lambda$ 1780-2080 nm) in order to account for the stellar flux in these regions. An example of a prolonged spectrum created in this way is shown in Appendix

3.C. The bolometric flux was then computed by integrating over the prolonged spectrum.

We used the photogeometric distances of Bailer-Jones et al. (2021) to convert the fluxes to luminosities for all targets with exception of TWA 26. For this star we used the geometric distance of the same authors since a photogeometric distance is unavailable. The distances provided by Bailer-Jones et al. (2021) are based on the *Gaia* DR3 (Gaia Collaboration et al. 2016, 2023) parallaxes but include a photometric and geometric prior to improve the distance estimate. The inclusion of these priors significantly improves the uncertainties for the most distant targets (namely those in σ Orionis). For more nearby targets the distance estimate and its uncertainty do not change significantly from the inverse *Gaia* parallaxes.

The uncertainties on these estimates are computed by propagating the uncertainties of matching the BT-Settl models to the observations, the distance, the extinction, and the photometric flux. We adopt an extinction uncertainty of $\sigma_{A_V} = 0.2mag$. For the targets calibrated using wide slit spectra, we assumed the uncertainties on the photometric flux 5% of the total flux, which is slightly more conservative than the 4% of Rugel et al. (2018). For the spectra calibrated using the available photometry we assumed an uncertainty of 0.2 dex on the luminosity, the same as that of MTR13.

We also computed the luminosities of the grid using the bolometric correction of HH14. This correction uses the flux measured at 751 nm to estimate the total flux of the star. We noticed a small but systematic discrepancy between the luminosities derived from the two methods at effective temperatures lower than 4500K. We therefore propose a correction to the relationship provided by HH14 which is further discussed in Appendix 3.C. This new relation is assumed in this work.

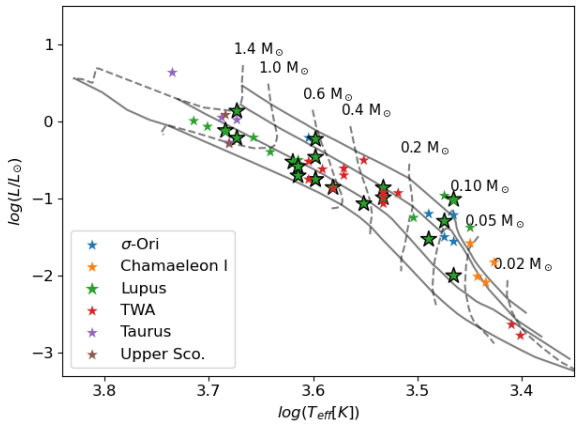

Figure 3.4: HR Diagram of the objects analyzed here (highlighted with larger black outlined star symbols) and those analyzed by MTR13 and MFA17. The model isochrones and evolutionary tracks by Baraffe et al. (2015) are also shown. The isochrones are the 1.2, 3, 10 and 30 Myr ones.

Fig. 3.4 shows our sample in a Hertzsprung-Russell diagram together with the samples of MTR13 and MFA17. Here, we used the luminosities obtained by integrating the extended spectrum and the effective temperature is obtained from the spectral type using the relationship of

HH14. The isochrones and evolutionary tracks of Baraffe et al. (2015) are also plotted. The isochronal age of the targets in our sample appears to be dependent on the stellar mass. Targets with $M_\star \gtrsim 0.7 M_\odot$ tend to be $\sim$ 10 to 30 Myrs old according to the isochrones, whereas those with lower mass have ages of $\sim$ 1 to 10 Myrs, despite all except one target being members of the Lupus star forming region. This trend is also present in the samples of MTR13 and MFA17 as well as other star samples such as those of Bell et al. (2014), Herczeg & Hillenbrand (2015), and Pecaut (2016). Stelzer et al. (2013) see a similar trend when comparing their sample to isochrones in the $\log g - T_{\rm eff}$ diagram. It is unclear what causes this discrepancy but possible origins include the presence of starspots affecting the position in the HRD (e.g., Gangi et al. 2022; Pérez Paolino et al. 2024) or affecting overall evolution (Somers & Pinsonneault 2015), the effect of accretion during earlier stages of the star's evolution (Baraffe et al. 2017) or the effect of the stellar magnetic field on the subphotospheric convective motions in the stars (Feiden 2016). The evolutionary tracks by Feiden (2016) include the later effect and are similar to the models of Baraffe et al. (2015) in the nonmagnetic case. The SPOTS models of Somers et al. (2020) includes the influence of starspots at different filling factors on the isochrones. An analysis of the spot coverage of our sample and comparison with the SPOTS isochrones is beyond the scope of this work and deferred to a future work.

3.4 New combined grid

The first goal of this work is to improve upon the grid of template spectra of YSOs presented by MTR13 and MFA17 by adding new templates to the grid and interpolating the spectra to generate a continuous grid. This is discussed in this section.

3.4.1 Description of the new grid

We combined the observations presented here with those of MTR13 and MFA17 to create an enhanced library of spectral templates that is made available to the community. We add one additional spectrum presented by Manara et al. (2016a), that of the K0 star HBC407. The sources selected by MTR13 and MFA17 were classified to be class III YSOs and using *Spitzer* data (e.g., Evans et al. 2009). Manara et al. (2014) presented additional X-shooter observations of class III targets, namely IC348-127, T21, CrA75. These targets were highly extincted, with $A_V \sim$ 6 mag, $A_V = 3.2$ mag and $A_V = 1.5$ mag, respectively. This high extinction causes additional uncertainties in the dereddened spectra due to the uncertainties in the assumed extinction law. Therefore we do not include these spectra in our grid.

There are 6 stars from our new observations that are not included in the grid. The 5 unresolved binaries previously mentioned in Sect. 3.2 are excluded from our grid since they cannot be used to represent the stellar emission of individual stars. To avoid potential accretors in our sample we we used the $H\alpha$ equivalent width criterion of White & Hillenbrand (2004) and Barrado y Navascués & Martín (2003), among others. The spectrum of 2MASSJ16075888-3924347 shows evidence of ongoing accretion, therefore we excluded it from our grid. This is further discussed in Appendix 3.E.

From the grid of MTR13, Sz121 and Sz122 were excluded since they are likely spectroscopic binaries or ultrafast rotators (MTR13, Stelzer et al. 2013). For RXJ0438.6+1546 a spectrum was presented by MFA17. This target was also observed as a part of the PENELLOPE VLT Large Program (Manara et al. 2021). We only use the more recent PENELLOPE spectrum since the observations were performed with better sky transparency conditions.

We confirmed the spectral types of all except for one target of MTR13 and MFA17 through visual inter-comparison. The TiO absorption bands of CD 36-7429A appear to best match that of the K7 templates. We reassigned the spectral type of CD 36-7429A from K5 (MTR13) to K7. This spectral type was further confirmed by the TiO index of Jeffries et al. (2007) which yields a spectral type of K7.0 and the analysis of Fang et al. (2017, 2021) who also adopted a SpT of K7 for this target. Pecaut & Mamajek (2013) also adopt a SpT of K7 for this source. Interestingly, the estimate of $T_{\rm eff}$ from the ROTFIT analysis of the absorption lines lead to a result more consistent with a SpT of K5 (Stelzer et al. 2013). It is possible that spots covering the stellar surface lead to this discrepancy (e.g., Stauffer et al. 2003; Vacca & Sandell 2011; Pecaut 2016; Gully-Santiago et al. 2017; Gangi et al. 2022). We however assumed K7 as the SpT for this target based on the molecular features. The spectra first presented in this work have been dereddened using the values listed in Table 3.1 to provide an extinction-less grid. This grid can be found on GitHub[3].

The uncertainties on both A_V and SpT were estimated by fitting the spectra of targets within 1 spectral type subclass of other targets in the combined grid. In this procedure, we search for the best fitting template spectrum in the remainder of the grid at different values of extinction. The best fit template and extinction are found by searching for the minimum of a χ^2-like metric that includes the spectral features discussed in Sect. 3.3.1.

For both the difference in spectral type and extinction we find a distribution with a median value of 0 and standard deviations of $\sim$ 0.5 subclasses and $\sim$ 0.25 mag respectively. We note that the standard deviation is larger for spectra earlier than K6, in part due to the lack of spectra of similar spectral type. We therefore estimated the uncertainties on SpT's earlier than K6 to be $\sim$ 1 subclasses, those at later SpT to be $\sim$ 0.5 subclasses. For the extinction we adopt an uncertainty of 0.2 mag. THA15-36B appears as a strong outlier with ΔSpT $= -1.5$ and $\Delta A_V = 0.8$. This supports our decision to provide higher uncertainties on both THA15-36A and THA15-36B. Because of this we also excluded THA15-36A and THA15-36B when constructing our interpolated grid in Sect. 3.4.2.

The final grid of templates is reported in Table 3.12. Fig. 3.5 shows the spectral type distribution of all the spectra in our final grid. Our final grid of templates includes 57 targets and spans a range of spectral types from G5 to M9.5. The spectral types later than K6 appear to be well represented. The earlier spectral types appear less well sampled, with the most prominent gaps between G5 to G8 and K4 to K5.5.

[3] https://github.com/RikClaes/FRAPPE

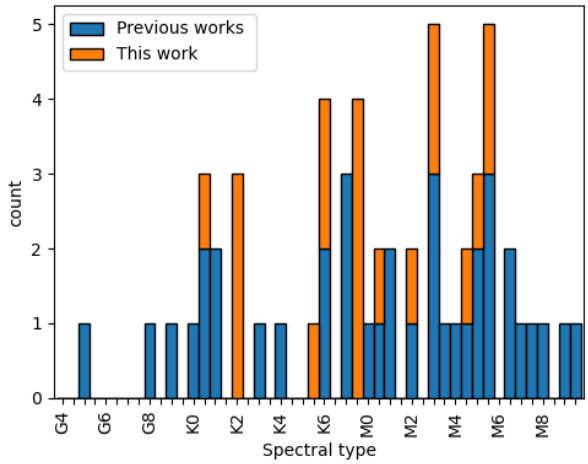

Figure 3.5: Histogram of SpT for the grid of class III templates.

3.4.2 Interpolation

The grid presented in Sect. 3.4.1 is limited in two key ways. First, the grid is sparse and possesses gaps at a number of spectral types. Secondly, individual spectra have intrinsic uncertainties. Directly applying one of these spectra to represent the photosphere of a class II star or to analyze other class III targets may therefore bias the results. In order to mitigate these downsides we interpolated the grid of template spectra for the characterization of young stellar photospheres.

We first started by normalizing the dereddened spectra to the flux measured at 731 nm in order to remove the dependency of individual target's distance and luminosity. We chose 731 nm as our reference region, since it is free of strong telluric features, avoids features dependent on $\log g$ and the photospheric emission dominates at this wavelength. Median normalized fluxes were then computed in a wavelength interval of choice for each of the spectra. To compute the uncertainty on this flux, we propagated the uncertainties on the flux in the normalization range ($\sim$ 731 nm) and the flux in the wavelength range. We also propagated the uncertainties on the extinction. The spectra of some of the later spectral type stars in our sample have a signal to noise of $\sim$ 0 at the shortest wavelengths in the UVB arm. In this case, we excluded these normalized fluxes from the procedure. This procedure results in a set containing a normalized flux $f_\lambda/f_{731\mathrm{nm}}$ and associated uncertainty for each template in our library.

We used a non-parametric local polynomial fit (Cleveland 1979) to interpolate between these fluxes as a function of SpT. In this type of interpolation, the value at a given position (spectral type in our case) is obtained by fitting a polynomial to a weighted version of the data points, this is expressed in Eq. 3.1.. The polynomial at a given x, representing SpT subclass, is defined by the parameters $\hat{a}_1(x), ..., \hat{a}_n(x)$ as

$$\hat{a}_1(x), ..., \hat{a}_n(x) = argmin_{a_0,...,a_n} \sum_i K\left(\frac{x - x_i}{h}\right)\left(y_i - \sum_{k=0}^{n} a_n \cdot x_i^k\right)^2 . \tag{3.1}$$

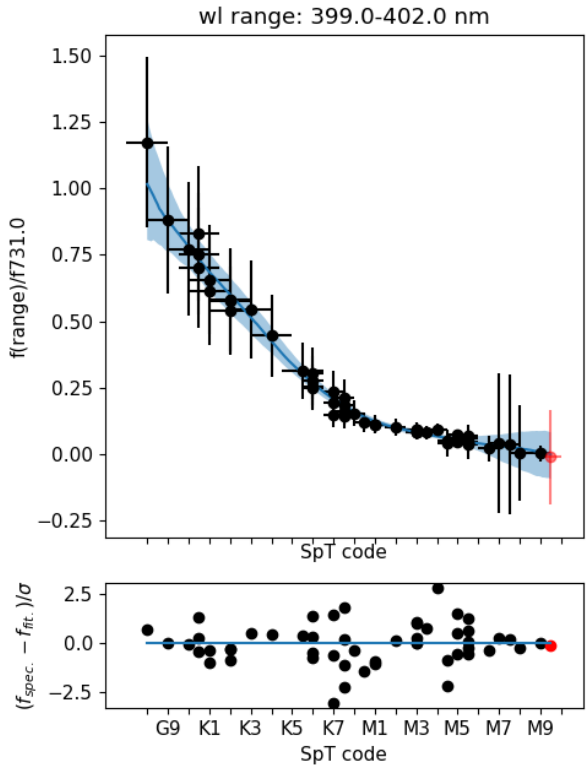

Figure 3.6: Example of a local polynomial fit to the normalized fluxes (black points) extracted in the wavelength range of 399 to 402 nm. The red point have been excluded from the fit due to the low S/R of this spectrum. The blue line indicates the median fit resulting from the Monte Carlo simulation. The transparent blue region indicates the 1-σ uncertainty interval. The residuals are computed using only the uncertainties on the non-parametric fit.

Here x_i represents the SpTs of our set of median fluxes in a given wavelength range and y_i is the values of the normalized fluxes themselves. K is a chosen kernel used for weighting the values that are fitted and h is the selected bandwidth. We used a polynomial of degree 2, a bandwidth of 2.5 SpT subclasses, and a Gaussian kernel.

To obtain the value of the local polynomial fit (y) at spectral type position (x), the expression

$$y = \sum_{k=0}^{n} \hat{a}_n \cdot x \tag{3.2}$$

is evaluated. This procedure is repeated at several equally spaced x values representing spectral types from G8 to M9.5, allowing us to retrieve the interpolated value at any SpT within this range. We limited our interpolation to range from G8 to M9.5 because of the large gap between our only G5 spectrum and the rest of our grid. We made use of the implementation provided by

the localreg PYTHON package [4].

To account for the heteroscedastic uncertainties we used a Monte-Carlo simulation of 1000 iterations. In each iteration, we resampled the normalized flux and SpT of each data point by adding a value sampled from a Gaussian distribution with a standard deviation equal to the respective error and a mean of zero. The non-parametric fit was computed for each iteration. At each of the spectral type points we adoped the median values of these fits as the final interpolated model spectrum and for the error we adopt the 1-σ interval around this median. Fig. 3.6 shows an example of this procedure for one wavelength range.

We repeated this procedure for multiple wavelength ranges. An interpolated spectrum is then obtained by evaluating the values of these multiple non-parametric fits at a given spectral type. We applied it to wavelength ranges of 1 nm width over the entire UVB and VIS arms. A comparison between our interpolated spectra and class III templates of the same spectral type is shown in Fig. 3.7. Here it can be seen that individual templates can have a flux that is lower (PZ99J160843.4-260216) or higher (Par Lup 2) than that of the interpolated templates at short wavelengths. This effect could be a consequence of the uncertainties on the SpT and/or A_V of the spectra and/or differing levels of chromospheric activity. We find that roughly half of the class III spectra have a Balmer continuum flux higher than that of the interpolated templates while the other half have a lower flux. Fig. 3.7 also shows that the interpolation can deviate significantly from the observed spectra in the region around 950 nm. This is a consequence of a poor telluric correction in several template spectra. This extinction-less interpolated grid can be found on GitHub [5] along with the Python script used to generate it and obtain the interpolated templates.

3.5 Interpolated spectra for spectral fitting

In this section, we apply the new class III interpolated grid to the classic problem of deriving in a self-consistent way the stellar (SpT, A_V, $L_\star$) and accretion properties ($L_{\rm acc}$) of an actively accreting TTS. In particular, we compare our results to those obtained using a method in which the individual template spectra (those listed in Table 3.12) are used to account for the stellar contribution.

Determining accretion and stellar properties in YSOs is not trivial. Excess continuum emission due to accretion and extinction alters the observed spectrum in opposite ways, although with a different wavelength dependence. A self consistent method for deriving stellar properties, accretion luminosity, and extinction simultaneously was previously presented by Manara et al. (2013a). The method presented here is a further development of this prescription, but with a different approach to the way the stellar photosphere is accounted for when modeling an observed spectrum. This also implies changes in how the stellar luminosity is calculated. We refer to this method as FRAPPE: FitteR for Accretion ProPErties. Here, we apply this method to the 14 accreting T Tauri stars in the Chamaeleon I star-forming region observed with X-shooter during the VLT/PENELLOPE Large Program (Manara et al. 2021).

[4] https://github.com/sigvaldm/localreg/tree/master

[5] `https://github.com/RikClaes/FRAPPE`

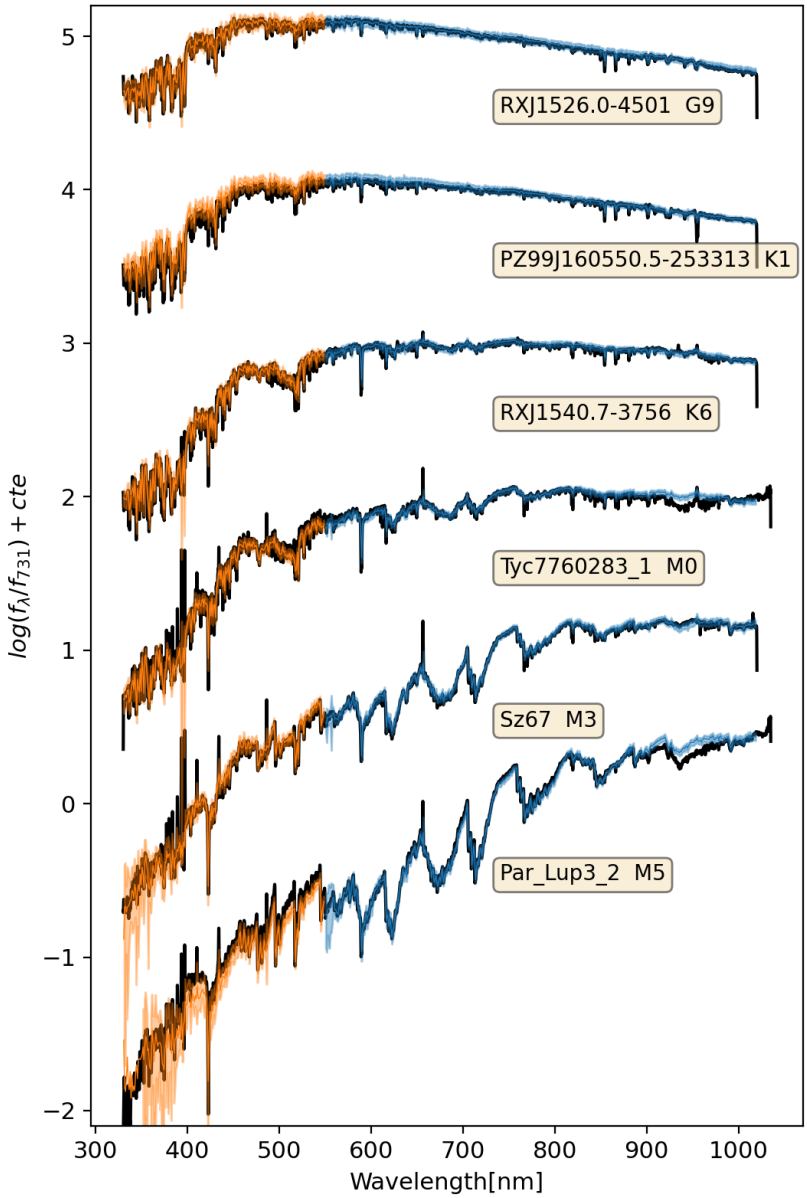

Figure 3.7: Comparison between individual class III templates and the interpolated spectra of the same spectral type. The templates are plotted in black and the interpolated spectra in blue and orange. The transparent blue/orange regions represent the 1-σ uncertainties in the interpolated spectra. The blue and orange colors correspond to the wavelength ranges of the X-shooter VIS and UVB arms respectively. The templates have been convolved with a Gaussian kernel for clarity.

3.5.1 Fitting the UV excess

The fitting procedure used here combines three components to fit an observed spectrum: 1) A continuum slab model is used to represent the emission from the accretion shock; 2) a reddening law to account for extinction; 3) our interpolated templates are used to represent the stellar contribution. Our fitting procedure consists of a Python code that searches in a grid of parameters the combination that best reproduces the observed spectrum of the input accreting YSO.

For the continuum excess emission we used the grid of isothermal hydrogen slab models developed by Rigliaco et al. (2012) and Manara et al. (2013a), the details of which details are described in Manara (2014). Prior to these works, such an approach was used by Valenti et al. (1993) and Herczeg & Hillenbrand (2008). Here we describe the key parts of the model. The models assume local thermodynamic equilibrium (LTE) and include emission from both H and H^-. A given models are described by an electron density (n_e), electron temperature (T_{e^-}), and the optical depth at 300 nm (τ). The grid contains slab models for n_e ranging from 10^{-11}cm^{-3} to 10^{-16}cm^{-3}, T_{e^-} ranging from 5000 to 11000 K and τ from 0.01 to 5. The slab models are matched to the observed, dereddened spectrum of an accreting YSO using a scaling factor ($H_{\rm slab}$). The models extend below the minimum wavelength of X-shooter ($\lesssim$ 330nm), allowing us to compute $L_{\rm acc}$ from the total flux of the slab model when scaled to match the observed spectrum during the fitting procedure.

We used the Cardelli extinction law (Cardelli et al. 1989) to account for extinction in our procedure. We fixed the total-to-selective extinction value R_V to the average interstellar value of $R_V = 3.1$ for all of the fits performed in this work. To find the best fitting A_V value we let the extinction free to vary from 0.0 to 2.0 mag in steps of 0.1 mag. When an extinction value is found at the upper edge of this range, we reran the procedure for larger A_V.

The main difference with respect to the method presented by Manara et al. (2013a) is the use of an interpolated grid of templates created with the method described in Sect. 3.4.2., while Manara et al. (2013a) used the individual spectra in the grid of class III templates from MTR13 (and later MFA17) to represent the photospheric and chromospheric contribution of the central star. During the fitting procedure, this grid is sampled at specific SpT values. We ran our procedure for SpTs at steps of 0.5 subclasses. The interpolated spectra were scaled to the observed, dereddened spectrum of the accreting YSO using a scaling factor ($K_{\rm cl3}$) which sets the stellar luminosity.

The best fit is found by minimizing the likelihood function given by

$$\chi^2_{like} = \sum_{W.L.ranges} \frac{(f_{mod.} - f_{obs,dered})^2}{\sigma^2_{obs,dered} + \sigma^2_{mod.}}. \tag{3.3}$$

Here $f_{mod.}$ is the flux density of the model spectrum, which comprises the sum of the scaled slab model and scaled interpolated class III template, within one of the selected wavelength range. $f_{obs,dered}$ is the flux of the observed spectrum in the corresponding range after dereddening, σ_{obs} is the noise of the dereddened observation in the same range. This expression is different than that from Manara et al. (2013a) in that it includes $\sigma_{mod.}$, the uncertainties on the interpolated grid, taking into account the scaling applied to match the observations (i.e., $\sigma_{mod.} = K_{\rm cl3} \cdot \sigma_{interp.}$

). At the edges of the interpolations SpT range its uncertainties become larger in all wavelength ranges. This will bias the results toward the edges of our spectral type range. To prevent this, we set the errors at SpT's earlier than K0 equal to those obtained at K0.

We selected a limited number of wavelength ranges to create an interpolated grid of templates using the method presented in Sect. 3.4.2. These wavelength ranges were selected starting from those used by Manara et al. (2013a), but with some additions, as they carry information about the SpT and about the excess emission due to accretion. Wavelength ranges not considered by Manara et al. (2013a) are highlighted in Table 3.3. We note that the way Manara et al. (2013a) used the information in these ranges differs from ours. In the best fit determination of Manara et al. (2013a) the slopes of the observed Balmer and Paschen continuum and the flux ratio at both sides of the Balmer jump are matched to the model. We, however, chose to directly match the flux within these wavelength ranges. We also modified some of the regions adopted from Manara et al. (2013a) to prevent an overlap in wavelength. We included a number of TiO bandheads around $\sim$ 710 nm to constrain the spectral type of targets ranging from K6 to M9.5. To constrain targets with SpT from G5 to K6 we included wavelength ranges around $\sim$ 465, $\sim$ 510, and $\sim$ 540 nm. These are based on the ones used in the R515 index presented by HH14 with slight adjustments being made to avoid the sharp edges of features which are present in the spectra of later type stars.

To constrain the accretion spectrum we included two wavelength ranges that carry information about the size of the Balmer jump to be constrained ($\sim$ 361 nm and $\sim$ 400.5 nm), three additional ranges to further constrain the Balmer continuum ($\sim$ 335 nm, $\sim$ 340 nm and $\sim$ 355 nm) and three more to constrain the Paschen continuum ($\sim$ 414.5 nm, $\sim$ 450 nm, and $\sim$ 475 nm). At longer wavelengths, the inner disk of class II YSO can contribute to the observed flux (e.g., Pittman et al. 2022). Since our models do not include such a component, we omitted the use of wavelength ranges in the NIR arm. Suboptimal telluric correction of both the templates and spectra being analyzed can affect the analysis when included. Wavelength regions that include telluric lines were therefore also omitted. The exact wavelength ranges can be found in Table 3.3.

The accretion emission is known to veil photospheric absorption features in the observed YSO spectrum. Therefore we compared the Ca I line at $\sim$ 420nm in the observed spectrum with that of a veiled class III template to verify the goodness of our fits. We used a random class III template with the SpT nearest to the best fit solution and the best fitting slab model for this test.

Fig. 3.8 shows how the normalized TiO 710 nm features vary as a function of SpT in our interpolated grid. Here it can be seen that the different wavelength rages disperse at late spectral types, showing the usefulness of this feature to classify M stars.

The procedure works as follows. For each spectral type we dereddened the observed spectrum for each value of A_V. Then for each of these combinations, we considered all of the slab models. The scaling factor for each combination was obtained by having the combined model match the dereddened observation at $\sim$ 355 nm and $\sim$ 731 nm. We note that the latter wavelength range is the same one as used to normalize our grid of interpolated spectra. K_{clIII} therefore corresponds to the stellar flux at 731 nm. In other words, we solved the following system of equations

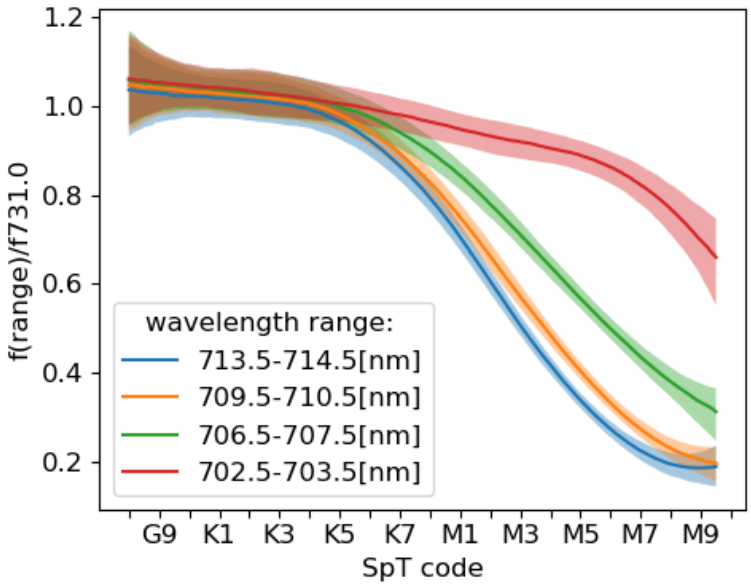

Figure 3.8: Example of several interpolated normalized fluxes and their associated uncertainties. The values of the fluxes in the TiO 710 nm absorption band can be seen to diverge at late spectral types, indicating its usefulness to constrain the spectral type of these later than K5. The shaded areas indicate the respective 1 sigma uncertainties.

numerically for $K_{\rm cl3}$ and $H_{\rm slab}$.

$$\begin{cases} f_{355} &= K_{\rm cl3} \cdot f_{clIII,355} + H_{\rm slab} \cdot f_{slab,355} \\ f_{731} &= K_{\rm cl3} \cdot f_{clIII,731} + H_{\rm slab} \cdot f_{slab,731} \\ &= K_{\rm cl3} \cdot 1 + H_{\rm slab} \cdot f_{slab,731} \end{cases} \tag{3.4}$$

We then used the parameters to calculate χ^2_{like}. This was done for every point in the grid. When this is done for the entire grid of parameters we select the model with the lowest χ^2_{like} as the best fit. This optimization procedure is the same as that used by Manara et al. (2013a).

From this procedure, we directly obtained SpT and A_V. The accretion luminosity was calculated by first integrating the scaled slab model over its entire wavelength range ($\lambda\lambda$ = 50 nm to 2500 nm). This results in the total accretion flux F_{acc} which can then be converted to L_{acc} using $L_{acc} = 4\pi d^2 F_{acc}$, with d being the distance to the target. $T_{\rm eff}$ was obtained from the SpT using the relationship by HH14.

Due to our use of interpolated spectra, our stellar luminosity calculation differs from that of Manara et al. (2013a). To obtain the stellar luminosity we first computed the stellar flux at 751 nm, the reference wavelength of our bolometric correction. We obtained f_{751} by first computing the flux at this wavelength in the dereddened observed spectrum and then subtracting the scaled slab model flux at the same wavelength. For sources with $T_{\rm eff} < 3500$K we applied the same

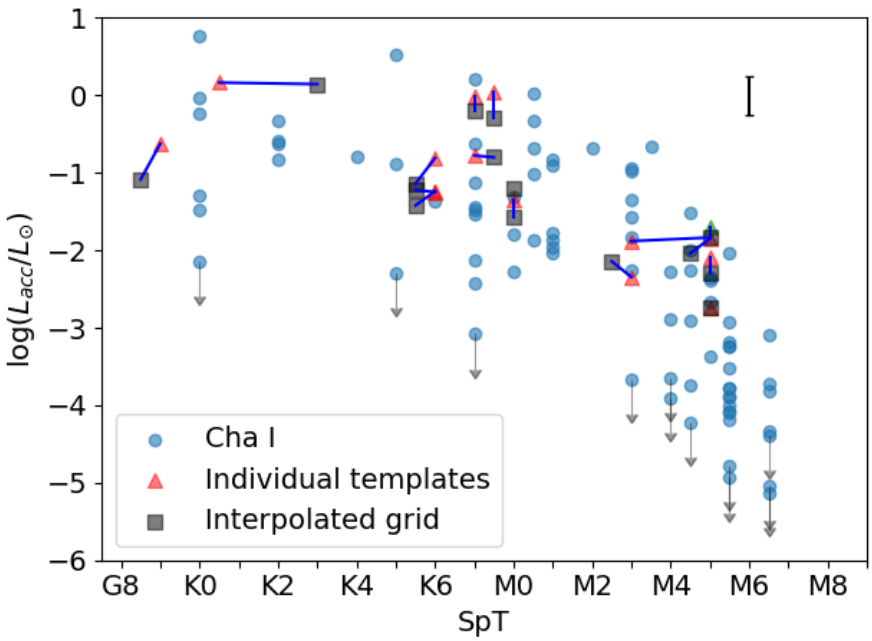

Figure 3.9: Accretion luminosities vs. spectral type as obtained using FRAPPE (gray squares) and obtained using the method of Manara et al. (2013b) (red triangles). Results obtained for the same target with the two methods are connected with a blue line. The green triangle indicates the M5 solution of WZ Cha. The light blue circles are the nearly complete Chamaeleon I sample presented by Manara et al. (2013a). The black errorbars indicate the uncertainties on the accretion luminosity. The gray arrows indicate sources listed as upper limits by Manara et al. (2023).

interpolation over the VO feature as discussed in Appendix 3.C. The bolometric flux $F_{bol.}$ is then computed using our adjusted relationship of HH14 and converted to $L_\star$ using $L_\star = 4\pi d^2 F_{\rm bol}$.

The stellar radius was computed from $T_{\rm eff}$ and $L_\star$ using $R_\star = L_\star/(4\pi\sigma_{\rm Boltz}T_{\rm eff}^4)$. The stellar mass ($M_\star$) and age are derived by placing the target on the HRD and interpolating evolutionary tracks at its position. We preferred to use to more recent models of Baraffe et al. (2015). However, for 5 targets the $T_{\rm eff}$ and/or $L_\star$range of the Baraffe et al. (2015) models did not extend to the found values, in these cases we used the tracks of Siess et al. (2000) instead. Finally, we can obtain the mass accretion rate $\dot{M}_{\rm acc}$ using

$$\dot{M}_{acc} = \frac{L_{acc}R_\star}{GM_\star}\left(1-\frac{R_\star}{R_{in}}\right)^{-1}, \tag{3.5}$$

where we use the typical assumption for the inner disk radius of $R_{in} = 5R_\star$ (Gullbring et al. 1998).

3.5.2 Accretion rates in accreting young stars in the Chamaeleon I region

To test our method we applied it to the sample of 14 Chamaeleon I targets observed with the VLT/X-shooter spectrograph as part of the VLT/PENELLOPE Large Programme (see Manara et al. 2021, for details on the survey). The results are listed in Table 3.4, and are presented here for the first time. A comparisons between the dereddened observations and best fit models can be found on ZENODO [6]. For the purpose of comparison, we applied the procedure of Manara et al. (2013a) to the same sample and list the results in Table 3.5. In Fig. 3.9 the results of both methods are plotted on a $L_{\rm acc}$-SpT diagram. Fig. 3.10 displays both the obtained stellar luminosity and accretion luminosity. Results obtained for the same target are connected with a blue line to make the comparison easier. The values for the nearly complete sample of accreting young stars in the Chamaeleon I star-forming region presented by Manara et al. (2017a), using the values from Manara et al. (2023), is also shown with blue circles.

It can be seen that the results obtained here are generally in agreement within the typical uncertainties for the fitting procedure of Manara et al. (2013a) ($\sigma_{A_V} \approx 0.2$ mag, $\sigma_{L_{\rm acc}} \approx 0.25$ dex and $\sigma_{\dot{M}_{\rm acc}} \approx 0.35$ dex, Manara et al. 2023). For the SpT we expect typical uncertainties of half a subclass for SpTs later than K6, for earlier SpTs we expect uncertainties of about 1 subclass. For 3 targets we find differences larger than the typical uncertainties. These targets are WZ Cha, CV Cha and VZ Cha. We describe the results for these targets in Appendix 3.D.

The derived accretion luminosities of all targets agree within the aforementioned uncertainties. The obtained stellar luminosities are also in good agreement.

Fig. 3.11 displays the resulting $\dot{M}_{\rm acc}$- $M_\star$ diagram. For WZ Cha we obtained two degenerate solutions using the method of Manara et al. (2013a) one at SpT M3 (indicated in red) and one at SpT M5 (indicated in green). We prefer the M5 solution as the class III template to which the M3 solution was fitted appears to be an outlier (see Appendix 3.D). Here it can be seen that, with exception of the M3 solution of WZ Cha, our results are within the typical uncertainties.

The result obtained for WZ Cha and VZ Cha illustrates the benefits of our method (see Appendix 3.D). For WZ Cha, FRAPPE breaks a degeneracy between spectral types and in the case of VZ Cha the Paschen continuum appears better reproduced. The analysis for CV Cha highlights the need for improved constraints when fitting late G to early K stars. Such constraints can not only be obtained from the inclusion of class III spectra around these spectral types in our grid but also from additional information on the emission and absorption lines present in the spectra of the class II YSOs.

3.6 Limits on the derived accretion properties

3.6.1 Limits on accretion luminosity measurements from the UV excess

The study of the class III spectra is important not just because they are used as templates of the photospheres of accreting stars, but also because they provide essential information on the

[6] https://zenodo.org/doi/10.5281/zenodo.12686015

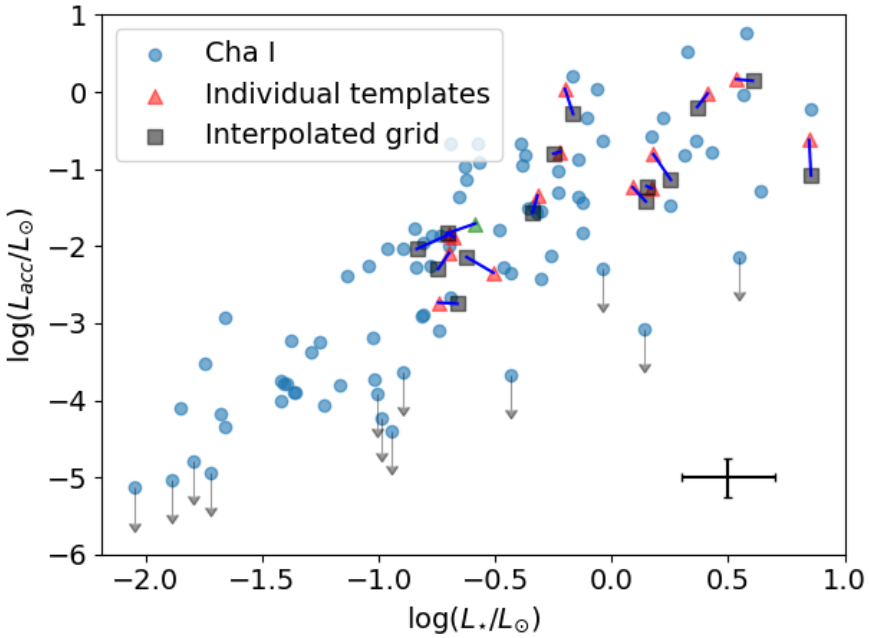

Figure 3.10: Accretion luminosities vs. stellar luminosity as obtained using FRAPPE (red triangles) and obtained using the method of Manara et al. (2013b) (gray squares). Results obtained for the same target with the two methods are connected with a blue line. The green triangle indicates the M5 solution of WZ Cha. The light blue dots is the nearly complete Chamaeleon I sample presented by Manara et al. (2013a). The black errorbars indicate the uncertainties on the stellar luminosity and accretion luminosity. The gray arrows indicate sources listed as upper limits by Manara et al. (2023).

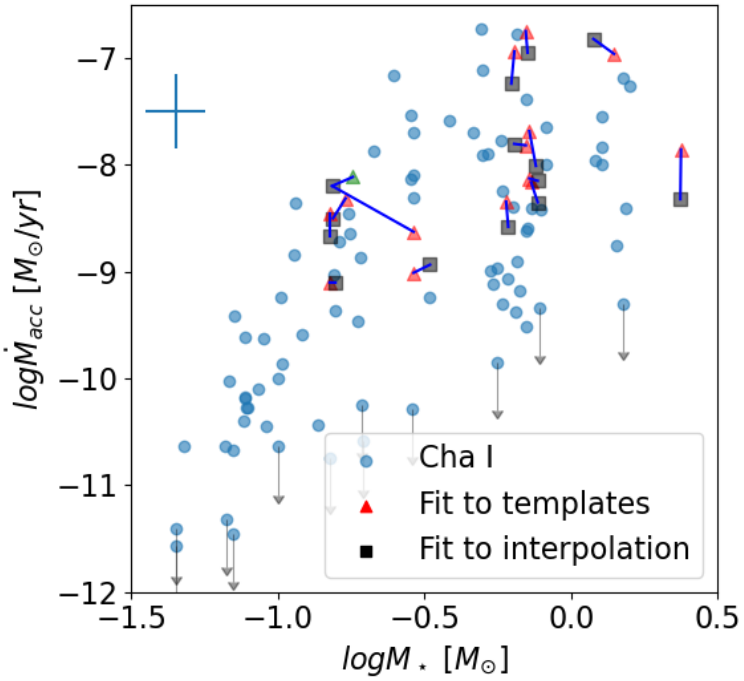

Figure 3.11: Mass accretion rate vs. stellar mass as obtained using FRAPPE (red triangles) and obtained using the method of Manara et al. (2013b) (gray squares). Results obtained for the same target with the two methods are connected with a blue line. The green triangle indicates the M5 solution of WZ Cha. The light blue dots are the nearly complete Chamaeleon I sample presented by Manara et al. (2013a). The blue errorbars indicate the uncertainties on the stellar mass and mass accretion rate. The gray arrows indicate sources listed as upper limits by Manara et al. (2023).

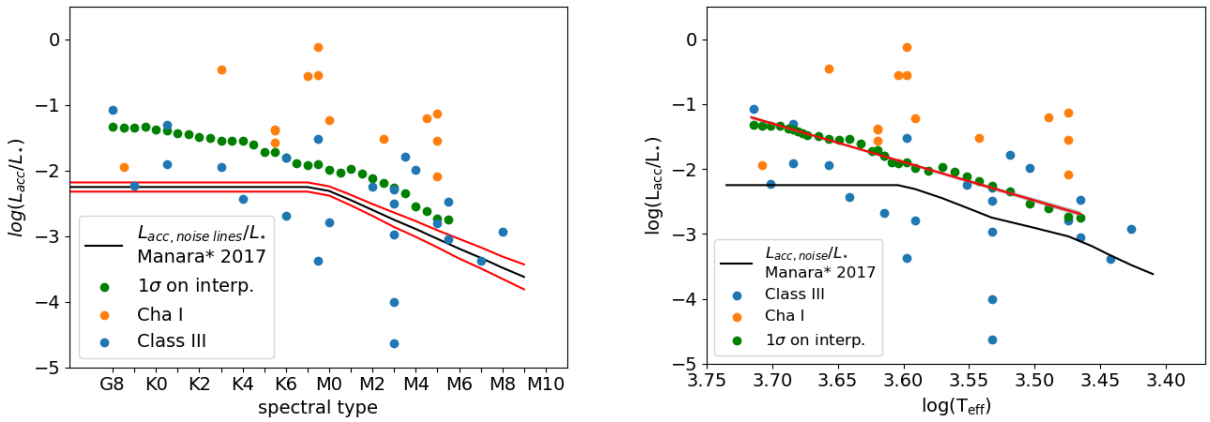

Figure 3.12: SpT and $T_{\rm eff}$ depedency of the accretion noise $\log(L_{acc,noise}/L_\star)$ values obtained from interpreting the uncertainties in the Balmer and Paschen continuum ($<$ 500 nm) on our model class III spectra as accretion (green dots). The blue dots illustrate the $\log(L_{acc,noise}/L_\star)$ values obtained when fitting the class III spectra with an accretion slab model. The results obtained for the PENELLOPE Chamaeleon I sample is indicated with orange dots. The black line shows the $L_{\rm acc,noise}$ relationship measured from the emission lines by MFA17 and the red lines on the left show the uncertainty thereon. On the right, the red line illustrates the best fit to the $\log(L_{acc,noise}/L_\star)$ values.

limitations introduced by the stellar chromospheric activity to the measurements of low accretion luminosities. MTR13 and MFA17 discussed how chromospheric activity in the form of line emission defines the lower boundaries to $L_{\rm acc}$ derived from the well-established correlation between line emission and accretion luminosity, and named this $L_{\rm acc,noise}$. Here we examined how the noise in the Balmer continuum emission in class III objects sets an upper boundary to the values of $L_{\rm acc}$ derived from the Balmer excess.

A variety of factors such as the uncertainties on the spectral type, extinction, and levels of chromospheric activity may contribute to the uncertainties on our interpolated model spectra. While such uncertainties may only cause minor contributions to the accretion luminosity measured in strong accretors, in weakly accreting objects such noise may have an important impact. Therefore, to characterize the limitations of our method we derived the accretion luminosities that correspond to the 1 σ uncertainties on our interpolated spectra, and we refer to this value as $L_{\rm acc,noise}$. To do this, we create a set of artificial spectra that include a UV excess equivalent to the 1 σ uncertainties and fit these with FRAPPE.

Templates later than SpT M5.5 have a S/N < 1 in the Balmer and Paschen continuum. Therefore, including these templates in our analysis would strongly affect the uncertainty of the continuum UV flux. We therefore limited the analysis presented here to spectral types ranging from G8 to M5.5. We generate another interpolated grid based on our templates but excluding templates later than M5.5. We used this grid to create a set of blue enhanced artificial spectra. For wavelength ranges in the Balmer and Paschen continuum (< 500nm) we set the value of the artificial spectrum equal to the interpolation spectra plus 1σ of the uncertainty thereon. The 1σ uncertainty is obtained from the Monte Carlo simulation discussed in Sect 3.4.2. For longer wavelengths, we simply adopt the values of the interpolated spectrum. The artificial spectra are unitless since our interpolation is normalized to have the flux at 731 nm equal to 1. We therefore multiply the artificial spectra with a random value on the order of 0.1×10^{-14} to 100×10^{-14} erg nm^{-1}s^{-1}cm^{-2} so that they have a "realistic" flux. We created such artificial spectra for each half subclass ranging from G8 to M5.5.

During this fitting procedure, we kept the SpT fixed to the value used for constructing the spectrum. The extinction was fixed to $A_V = 0$ mag. In doing so we obtained the accretion luminosities corresponding to spectra whose Balmer and Paschen continuum are 1σ interval above the interpolation. Here we assumed that the uncertainties in the Balmer and Paschen continuum are fully correlated.

The $L_{\rm acc,noise}$ and $L_\star$ obtained with this method are arbitrary as they scale with the multiplicative factor used to create the artificial spectra. Therefore we do not report the obtained values of $L_{\rm acc,noise}$ and $L_\star$. Instead, we report the ratio $L_{\rm acc,noise}/L_\star$ which is independent of this scaling and representative of the contrast down to which we can accurately measure a UV excess. The results are listed in Table 3.6. The dependence of $L_{acc,noise}/L_\star$ as a function of SpT is shown in Fig. 3.12. Assuming the SpT-$T_{\rm eff}$ relation of HH14, we also plot $L_{acc,noise}/L_\star$ as a function of $T_{\rm eff}$ in Fig. 3.12. Here it can be seen that the trend as a function of $T_{\rm eff}$ can be well approximated as a simple linear relation. This relationship is be expressed as

$$\log(L_{\rm acc,noise}/L_\star) = (5.9 \pm 0.2) \cdot \log(\mathrm{T_{eff}[K]}) - (23.3 \pm 0.7). \quad (3.6)$$

The relationships in Eq. 3.6 and Table 3.6 can be seen as a criterion for the lowest measurable accretion luminosities. If the $\log(L_{\rm acc,noise}/L_\star)$ measured for a CTTS is of a similar order of magnitude or falls below it, then we can not conclude if a target is accreting based on the UV excess measurement. Several relations between the effective temperature and spectral type have been presented in the literature (e.g., HH14, Pecaut & Mamajek 2013; Kenyon & Hartmann 1995; Luhman et al. 2003). Due to this lack of uniformity, we recommend to directly use the values of $L_{\rm acc,noise}$ at each SpT reported in Table 3.6.

Figure 3.12 also includes results obtained by fitting the class III templates themselves with FRAPPE. Here we once again kept the SpT fixed to the SpT of the respective class III and kept $A_V = 0$ mag. In this way, we obtain a similar $L_{\rm acc,noise}$ measurements. Only half of the class III templates provide a $L_{\rm acc,noise}$ measurement since half have a Balmer continuum below the interpolation. The $L_{\rm acc,noise}$ values obtained from the class III templates display a large scatter, this is a natural consequence of the scatter in the residuals between the templates and the interpolation in the Balmer and Paschen continuum. These results demonstrate how different the Balmer continua, and therefore the inferred UV-excess, of the various templates are. Using individual templates one may derive accretion luminosity that can change by fractions of the stellar luminosity of up to 10% relative to that found by using the interpolated spectra. The most extreme case is for late G SpT targets. This uncertainty is significantly weaker at later SpTs and in most cases it is only on the order of 1% of the stellar luminosity or lower.

We also plot the results for the class II targets presented in Sect. 3.5.2. One target, Sz19, clearly falls below the relationship in Eq. 3.6. Its measured mass accretion rate can therefore be highly affected by uncertainties on the chromospheric emission. Finally, for comparison, we also plot a similar relationship derived by MFA17 for the lowest accretion luminosities that one can measure by studying the emission lines. MFA17 measured the luminosities of several chromospheric emission lines in class III stars and converted them to accretion luminosities using the relations of Alcalá et al. (2014). We converted their results obtained as a function of spectral type to effective temperature using the SpT-$T_{\rm eff}$ of HH14 for consistency. It can be seen that the 1σ threshold that we derive for the UV continuum excess is higher in the entire SpT/$T_{\rm eff}$ range than the threshold obtained from the line luminosities. This implies that an analysis of accretion tracing emission lines allows us to measure lower accretion luminosities than the UV excess. However, the empirical relationships used to convert line luminosities to accretion luminosities (Alcalá et al. 2014, 2017) have been calibrated using measurements of the UV excess. It is therefore uncertain whether these relationships can be extrapolated to accretion luminosities below the threshold on the measurable UV excess. A more detailed modeling of the Hα emission lines, such as performed by Thanathibodee et al. (2023) may yet allow for the characterization of accretion properties of stars with low accretion rates, even well below the threshold of MFA17. Here we need to add the caveat that new work is currently being done on the influence of chromospheric emission lines on accretion rate measurements (Stelzer et al. in prep.), which will update the limit of MFA17 using the relationship between line and accretion luminosity of Alcalá et al. (2017).

We note that our criterion for measurable accretion luminosities and that of MFA17 are different in nature. The criterion of MFA17 represents typical chromospheric line luminosities, whereas ours represents the 1 sigma uncertainty on the stellar and chromospheric UV continuum

emission in our interpolated class III model spectrum. The interpretation of both therefore differs. If the line luminosity measured in a CTTS is of a similar order of magnitude to the criterion of MFA17, then the chomospheric emission likely provides a dominant contribution to the measured $L_{\rm acc}$. On the other hand, if a $L_{\rm acc}$ obtained from the UV excess is smaller than the limit presented here, then the uncertainties on this $L_{\rm acc}$ is dominated by the uncertainties on the stellar emission.

3.6.2 Implications for mass accretion rate estimates.

The limitations on measuring $L_{\rm acc}$ through the UV excess in turn reflects on the $\dot{M}_{\rm acc}$ values that we can reliably measure. It is of particular interest to investigate how these limitations affect the $\dot{M}_{\rm acc} - M_\star$ relation. We used the values of $L_{\rm acc,noise}$ from Eq. 3.6 to compute the lower limit of $\dot{M}_{\rm acc}$ as a function of stellar mass using the nonmagnetic isochrones of Feiden (2016) at 1, 2, 3, and 6 Myr. The results are shown in Fig. 3.13. We use these isochrones since they extend to higher masses than those of Baraffe et al. (2015) and therefore better cover the spectral types in Table 3.6. The isochrones of Feiden (2016) are mostly consistent with those of Baraffe et al. (2015).

We also applied the relationship of Eq. 3.6 directly to the measured $L_{\rm acc}$ and $L_\star$ of the Chamaeleon I sample from Manara et al. (2023) and the sample presented in Sect. 3.5.2. The results are also plotted in Fig. 3.13. The majority of class II targets fall well above the UV excess measurement limit. However, a considerable fraction appears to fall below the limit. The measured accretion rates of these targets are therefore dominated by the uncertainties on the stellar UV-continuum emission. More detailed analyzes are needed to disentangle the possible low accretion rate in these targets from the stronger chromospheric emission.

Manara et al. (2017b) used the Chamaeleon I sample shown here in combination with a sample of targets in Lupus (from Alcalá et al. 2017) to discuss whether the correlation between $\dot{M}_{\rm acc}$ and $M_\star$ is driven by the detection limits and if the observed scatter in $\dot{M}_{\rm acc}$ fills the observable range. Only 3 sources from the sample of Manara et al. (2023) that fall below our detection limit were previously not indicated as upper limits. These targets all fall in a locus were upper limits were already present. Our limit on the measurable mass accretion rate therefore does not change the conclusion reached by Manara et al. (2017b). Namely, that this correlation is real and not a consequence of detection limits.

3.7 Summary and conclusions

We presented the analysis of 24 new VLT/X-shooter spectra of class III young stars for their use as photospheric templates to complement the previous samples of MTR13 and MFA17. All spectra are available in reduced and dereddened form on GitHub [7]. We obtained the spectral type through the use of spectral indices and by comparing the relative strength of photospheric features to the samples of MTR13 and MFA17.

[7] https://github.com/RikClaes/FRAPPE

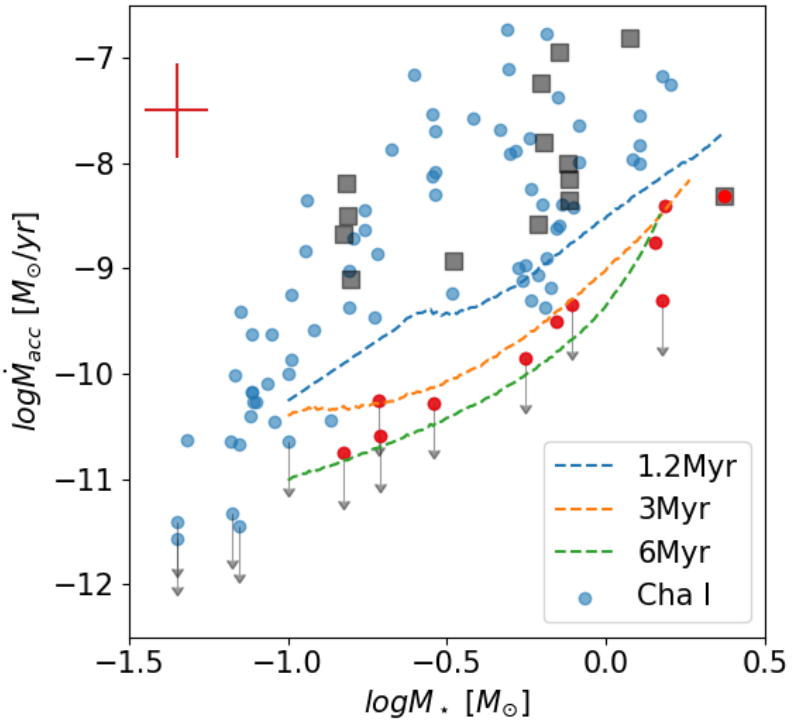

Figure 3.13: Mass accretion rate vs. stellar mass for the Chamaeleon I sample presented by Manara et al. (2023) (blue dots) and the Chamaeleon I sample analyzed in this work. Objects that have an accretion luminosity lower than the criterion given in equation 3.6 are marked with a red dot. The limits we derived based on the uncertainties on the chromospheric emission are shown with the blue, orange, and green lines for 1.2, 3, and 6 Myr old objects respectively. The red errorbars indicate the uncertainties on the stellar mass and mass accretion rate. The gray arrows indicate sources listed as upper limits by Manara et al. (2023).

3.7 Summary and conclusions

We employed ROTFIT to derive the photospheric properties ($\log g$, $T_{\rm eff}$, $v \sin i$, RV) of the sample. The results of both methods are generally in agreement with each other and the photospheric properties confirm the young nature of these targets. As previously noted in the literature (e.g., Bell et al. 2014; Herczeg & Hillenbrand 2015; Manara et al. 2017a; Pecaut 2016), we see a mass dependent trend of the derived isochronal ages for targets in the same star forming region. We compared the stellar luminosities obtained through extending and integrating the X-shooter spectra in our sample with luminosities obtained by applying the bolometric correction of HH14. We found a small but systematic difference between the results of both methods for effective temperatures lower than about 4500 K, leading us to propose an adjustment to the bolometric correction of HH14.

To remove the nonuniform SpT sampling of the templates and mitigate the uncertainties associated with their use, we proposed a method of interpolating between the templates. We applied this type of interpolation to the entire wavelength range covered by the spectra in 1nm wide bins and made the results publicly available on GitHub[7]. We also applied the method to specific regions in the spectra that are useful to obtain the stellar and accretion properties of class II targets. This empirical method has been implemented in a code that self consistently measures the extinction, stellar, and accretion properties. We verified this framework by analysing the Chamaeleon I sample observed as part of the PENELLOPE program and compared the results to those obtained using the method presented by Manara et al. (2013a) on the same spectra. We found good agreement in the results obtained with the two methods. Several future improvements, such as additional class III templates at early SpTs or the inclusion of veiling measurements in the best fit determination, can still be made to FRAPPE. Such improvements are particularly useful to constrain the stellar properties of stars with a spectral type earlier than K6 and will make FRAPPE more user friendly.

We measured the typical accretion to stellar luminosity ratios that would be obtained if the 1 σ uncertainties in our model spectra were interpreted as excess emission due to accretion. This ratio is representative of the typical lower limit on the measurable mass accretion rates in young stars when using continuum UV excess. The value has a strong dependency on the spectral type. This trend is likely a consequence of the worse constraints on earlier SpT stellar emission within our sample of class III sources, as well as of a worse contrast with the UV excess due to earlier stars having the peak of the photospheric emission at bluer wavelengths, hampering the detection of an excess for contrast reasons. This limit is higher than the lower limit presented for accretion rates derived from emission lines presented by MFA17. We, therefore, conclude that an in-depth analysis of emission lines is needed to obtain accurate measurements of mass accretion rates in low accreting objects. We applied our lower limit to the Chamaeleon I sample of Manara et al. (2023). The majority of objects in this region were found to have accretion rates well above our lower limit.

This shows that the uncertainties associated with the use of class III templates do not significantly affect the observed correlations between mass accretion rate and disk mass or stellar mass (see Manara et al. 2023 for a review). Our improved methodology for self consistently deriving accretion properties will facilitate further studies into these relations.

We thank the anonymous referee for the useful comments to our submitted manuscript. R. Claes acknowledges the PhD fellowship of the International Max-Planck-Research School (IMPRS) funded by

ESO. This work was partly funded by the Deutsche Forschungsgemeinschaft (DFG, German Research Foundation) in the framework of the YTTHACA Project 469334657 under the project code MA 8447/1-1. Funded by the European Union (ERC, WANDA, 101039452). Views and opinions expressed are however those of the author(s) only and do not necessarily reflect those of the European Union or the European Research Council Executive Agency. Neither the European Union nor the granting authority can be held responsible for them. J. B. Lovell acknowledges the Smithsonian Institute for funding via a Submillimeter Array (SMA) Fellowship. J.M. Alcalá acknowledges financial support from PRIN-MUR 2022 20228JPA3A "The path to star and planet formation in the JWST era (PATH)" funded by NextGeneration EU and by INAF-GoG 2022 "NIR-dark Accretion Outbursts in Massive Young stellar objects (NAOMY)". J.M. Alcalá and A. Frasca acknowledge financial support from Large Grant INAF 2022 "YSOs Outflows, Disks and Accretion: towards a global framework for the evolution of planet forming systems (YODA)". This work benefited from discussions with the ODYSSEUS team (HST AR-16129), `https://sites.bu.edu/odysseus/`*. This work has made use of data from the European Space Agency (ESA) mission Gaia (*`https://www.cosmos.esa.int/gaia`*), processed by the Gaia Data Processing and Analysis Consortium (DPAC,* `https://www.cosmos.esa.int/web/gaia/dpac/consortium`*). Funding for the DPAC has been provided by national institutions, in particular the institutions participating in the Gaia Multilateral Agreement. This research has made use of the SIMBAD database, operated at CDS, Strasbourg, France.*

Table 3.2: Photospheric parameters derived using ROTFIT.

Name	$T_{\rm eff}$ $[K]$	$\sigma(T_{\rm eff})$ $[K]$	$\log g$ $[cgs]$	$\sigma(\log g)$ $[cgs]$	$v \sin i$ $[km/s]$	$\sigma(v \sin i)$ $[km/s]$	RV $[km/s]$	$\sigma(RV)$ $[km/s]$	$r_{\rm 970nm}$	$r_{\rm 710nm}$	$r_{\rm 620nm}$
CD-31_12522	4920	223	4.04	0.12	30.2	1.0	2.2	0.8	0.00	0.00	0.00
RXJ0438.6+1546	4851	111	4.08	0.23	21.0	1.0	18.9	0.7	0.30	0.00	0.40
RXJ1608.9-3905	4552	124	4.27	0.14	43.6	1.0	-0.7	0.9	0.00	0.00	0.40
MV Lup	4513	96	4.83	0.25	1.0	6.0	2.4	0.7	0.00	0.00	0.00
MT Lup	4411	77	4.41	0.12	7.9	1.4	2.7	0.6	0.40	0.20	0.30
J15552621-3338232	4295	112	4.88	0.24	1.0	11.0	0.8	0.6	0.10	0.00	0.20
MX Lup	4216	61	4.45	0.21	10.0	1.0	2.4	0.6	0.00	0.00	0.20
MW Lup	4032	54	5.03	0.29	15.2	3.2	3.4	0.6	0.00	0.00	0.00
RXJ1607.2-3839	3954	86	4.53	0.11	32.8	2.0	-0.4	1.0	0.00	0.00	0.40
NO Lup	3907	98	4.43	0.11	11.2	1.0	-2.3	0.8	0.10	0.20	0.30
THA15-43	3885	23	5.19	0.18	9.4	2.0	1.6	0.7	0.10	0.00	0.30
THA15-36A	3650	60	4.57	0.12	19.2	1.0	2.2	0.8	0.10	0.20	0.30
THA15-36B	3465	43	4.92	0.11	21.1	1.0	1.8	0.7	0.10	0.20	0.30
RECX-6	3419	36	4.68	0.12	23.4	1.9	16.3	0.7	0.00	0.00	0.00
Sz67	3226	57	4.53	0.20	70.3	1.0	-0.6	3.6	0.00	0.00	0.10
J16075888-3924347	3054	93	4.24	0.15	25.0	11.0	2.4	0.9	0.00	0.00	0.00
J16090850-3903430	3000	64	4.25	0.13	4.1	10.2	-1.6	1.0	0.20	0.00	0.10
V1191Sco	2883	105	3.59	0.11	33.5	9.7	-0.2	1.0	0.00	0.00	0.00
J16091713-3927096	2876	130	4.73	0.13	69.0	13.0	2.8	4.3	0.00	0.00	0.00

Notes: $r_{\rm 970nm}$, $r_{\rm 710nm}$, and $r_{\rm 620nm}$ is the veiling measured around 970nm ,710 nm, and 620 nm, respectively.

Table 3.3: Wavelength ranges included in the interpolated grid used in our fitting procedure.

Name	wavelength ranges
Balmer jump	359-362 [b]
	399-402 [b]
Balmer continuum	337.5-342.5
	352-358 [b]
Paschen continuum	414-415 [a]
	448-452
	474-476
TiO 710 nm	702.5-703.5
	706.5-707.5
	709.5-710.5
	713.5-714.5
R515	464-466 [b]
	510-515 [a]
	539-544 [a]

Notes: Wavelength ranges that are newly introduced with respect to Manara et al. (2013a) are indicated with *a*. Wavelength ranges that have been modified with respect to Manara et al. (2013a) are reported with *b*.

Table 3.4: Accretion properties of the Chameleon I PENELLOPE targets obtained with FRAPPE.

Name	Dist [pc]	SpT	$T_{\rm eff}$ [K]	A_V [mag]	$L_\star$ [$L_\odot$]	$\log(L_{acc}/L_\odot)$	$M_\star$_B15 [$M\odot$]	M_{acc}_B15 [$M_\odot$/yr]	$M_\star$_S00 [$M\odot$]	M_{acc}_S00 [$M_\odot$/yr]
CHX18N	192.0	K5.5	4164	0.70	1.40	-1.42	0.77	$4.48 \cdot 10^{-9}$	0.85	$4.06 \cdot 10^{-9}$
CHX18N_ep2	192.0	K5.5	4164	0.70	1.41	-1.22	0.77	$7.11 \cdot 10^{-9}$	0.86	$6.40 \cdot 10^{-9}$
CSCha	190.0	K5.5	4164	0.40	1.79	-1.13	0.76	$9.81 \cdot 10^{-9}$	0.85	$8.75 \cdot 10^{-9}$
CVCha	192.0	K3.0	4540	1.10	4.03	0.14	1.19	$1.52 \cdot 10^{-7}$	1.47	$1.23 \cdot 10^{-7}$
Hn5	195.0	M5.0	2980	0.80	$1.79 \cdot 10^{-1}$	-2.30	...	...	0.15	$2.14 \cdot 10^{-9}$
INCha	193.0	M5.0	2980	0.00	$2.18 \cdot 10^{-1}$	-2.75	...	...	0.16	$7.91 \cdot 10^{10}$
IPTau	129.4	M0.0	3900	1.10	$3.96 \cdot 10^{-1}$	-1.21	0.63	$5.43 \cdot 10^{-9}$	0.64	$5.31 \cdot 10^{-9}$
SYCha	181.0	K7.5	3960	0.70	$5.63 \cdot 10^{-1}$	-0.80	0.63	$1.58 \cdot 10^{-8}$	0.67	$1.52 \cdot 10^{-8}$
Sz10	184.0	M4.5	3084	0.70	$1.46 \cdot 10^{-1}$	-2.04	0.15	$3.17 \cdot 10^{-9}$	0.17	$2.87 \cdot 10^{-9}$
Sz19	189.0	G8.5	5104	1.50	7.17	-1.083	...	...	2.36	$4.79 \cdot 10^{-9}$
Sz45	192.0	M0.0	3900	0.50	$4.57 \cdot 10^{-1}$	-1.56	0.61	$2.64 \cdot 10^{-9}$	0.61	$2.62 \cdot 10^{-9}$
VWCha	190.0	K7.0	4020	2.10	2.32	-0.194	...	...	0.71	$1.13 \cdot 10^{-7}$
VZCha	191.0	K7.5	3960	1.20	$6.83 \cdot 10^{-1}$	-0.29	0.63	$5.79 \cdot 10^{-8}$	0.67	$5.40 \cdot 10^{-8}$
WZCha	193.0	M5.0	2980	0.60	$1.97 \cdot 10^{-1}$	-1.83	...	...	0.15	$6.37 \cdot 10^{-9}$
XXCha	192.0	M2.5	3484	0.50	$2.38 \cdot 10^{-1}$	-2.14	0.33	$1.16 \cdot 10^{-9}$	0.35	$1.11 \cdot 10^{-9}$

Notes: The stellar mass and mass accretion rates are computed with both the isochrones of Baraffe et al. (2015) (marked as B15) and Siess et al. (2000) (marked as S00). CV Cha and CS Cha are binaries (Reipurth et al. 2002; Guenther et al. 2007, respectively). We do not report values that are outside of the ranges of the Baraffe et al. (2015) isochrones.

Table 3.5: Accretion properties of the Chameleon I PENELLOPE targets obtained with the method presented by Manara et al. (2013a).

Name	Dist. [pc]	SpT	$T_{\rm eff}$ [K]	A_V [mag]	$L_\star$ [$L_\odot$]	$\log(L_{\rm acc}/L_\odot)$	$M_\star$	$\dot{M}_{\rm acc}$ [$M_\odot$/yr]	Model
CHX18N	192	K6	4115	0.7	1.23	-1.236	0.73	$6.90 \cdot 10^{-9}$	B15
CHX18N_ep2	192	K6	4115	0.8	1.48	-1.248	0.72	$7.49 \cdot 10^{-9}$	B15
CSCha	190	K6	4115	0.4	1.51	-0.808	0.72	$2.08 \cdot 10^{-8}$	B15
CVCha	192	K0.5	4830	1.1	3.43	0.166	1.40	$1.10 \cdot 10^{-7}$	B15
Hn5	195	M5	2980	1.1	0.20	-2.093	0.15	$3.55 \cdot 10^{-9}$	S00
INCha	193	M5	2980	0.2	0.18	-2.732	0.15	$7.93 \cdot 10^{-10}$	S00
SYCha	181	K7	4020	0.8	0.60	-0.775	0.70	$1.53 \cdot 10^{-8}$	B15
Sz10	184	M5	3125	1.0	0.20	-1.849	0.17	$4.87 \cdot 10^{-9}$	B15
Sz19	189	G9	5025	1.5	7.04	-0.623	2.37	$1.40 \cdot 10^{-8}$	S00
Sz45	189	M0	3900	0.7	0.48	-1.344	0.60	$4.54 \cdot 10^{-9}$	B15
VWCha	190	K7	4020	2.3	2.58	-0.019	0.70	$1.80 \cdot 10^{-7}$	S00
VZCha	191	K7.5	3960	1.7	0.63	0.040	0.64	$1.16 \cdot 10^{-7}$	B15
WZCha	193	M3	3410	1.0	0.21	-1.881	0.29	$2.37 \cdot 10^{-9}$	B15
*WZCha	193	M5	3060	0.8	0.26	-1.706	0.18	$7.73 \cdot 10^{-9}$	S00
XXCha	192	M3	3410	0.3	0.31	-2.344	0.29	$9.78 \cdot 10^{-10}$	B15

Notes: The degenerate solution of WZ Cha is marked as *WZ Cha.

Table 3.6: Accretion noise values as a function of SpT and $T_{\rm eff}$.

SpT	$T_{\rm eff}$[K]	$\log(L_{\rm acc,noise}/L_\star)$
G8.0	5180	-1.3
G8.5	5102	-1.3
G9.0	5025	-1.3
G9.5	4947	-1.3
K0.0	4870	-1.4
K0.5	4830	-1.4
K1.0	4790	-1.4
K1.5	4750	-1.5
K2.0	4710	-1.5
K2.5	4625	-1.5
K3.0	4540	-1.5
K3.5	4457	-1.5
K4.0	4375	-1.5
K4.5	4292	-1.6
K5.0	4210	-1.7
K5.5	4162	-1.7
K6.0	4115	-1.8
K6.5	4067	-1.9
K7.0	4020	-1.9
K7.5	3960	-1.9
M0.0	3900	-2.0
M0.5	3810	-2.0
M1.0	3720	-2.0
M1.5	3640	-2.0
M2.0	3560	-2.1
M2.5	3485	-2.2
M3.0	3410	-2.3
M3.5	3300	-2.3
M4.0	3190	-2.5
M4.5	3085	-2.6
M5.0	2980	-2.7
M5.5	2920	-2.7

Notes: The accretion noise values are obtained from interpreting the 1σ level of uncertainty on the Balmer and Paschen continua ($<$ 500 nm) on our interpolated class III spectra at a given spectral type as accretion luminosity. $T_{\rm eff}$ obtained from the relationship from HH14 are also listed for convenience.

Table 3.7: Stellar and accretion luminosities obtained for the class III templates when fitted with FRAPPE using $A_V = 0$ and the spectral type of the respective class III template.

Name	$\log L_\star$	$\log L_{acc}$	$\log(L_{\rm acc}/L_\star)$
RXJ1508.6-4423	-0.06	-1.09	-1.07
RXJ1526.0-4501	-0.03	-2.293	-2.23
PZ99J160843.4-260216	0.09	-1.817	-1.91
CD-31_12522	-0.14	-1.449	-1.31
RXJ1547.7-4018	-0.18	-2.128	-1.94
RXJ1538.6-3916	-0.36	-2.795	-2.43
2MASSJ15552621-3338232	-0.69	-2.485	-1.80
RXJ1543.1-3920	-0.48	-3.165	-2.68
RXJ1607.2-3839	-0.21	-3.586	-3.38
NOlup	-0.45	-1.968	-1.52
Tyc7760283_1	-0.61	-3.401	-2.79
THA15-36B	-1.11	-3.352	-2.24
Sz67	-1.16	-4.837	-2.97
RECX-6	-1.05	-3.237	-2.50
CD_36_7429B	-0.99	-4.134	-4.63
TWA7	-0.84	-5.616	-4.00
TWA15_app2	-0.95	-3.553	-2.29
TWA15_app1	-1.01	-2.786	-1.78
Sz94	-1.23	-3.225	-1.99
Par_Lup3_2	-0.96	-3.753	-2.79
2MASSJ16091713-3927096	-1.83	-4.887	-3.05
Sz107	-1.06	-3.538	-2.48
J11195652-7504529	-2.07	-5.451	-3.38
CHSM17173	-1.86	-4.790	-2.93

3.A Observations and data reduction

The sources MV Lup, NO Lup, and MT Lup were not observed using slits of 5.0". The narrow slit spectra were therefore flux calibrated by using the available photometry (see Table 3.9). This was done by converting the photometry in a given band to a corresponding flux density. The flux density in the same bands is also computed for the narrow-slit spectra by integrating them after being multiplied to the filter bandpass. The ratio of these fluxes allows us to rescale the spectra in absolute units correcting for slit losses. For MV Lup and NO Lup the spectrum in the UVB arm is matched to the photometric flux using a factor constant with wavelength. whereas VIS and NIR arm spectra are rescaled using a factor with a linear dependency on wavelength. This was done because variation of the seeing disk with wavelengths in the wide ranges of VIS and NIR arms and atmospheric refraction can produce a wavelength dependent light loss. For MT Lup a constant factor was used for the entire spectrum to preserve continuity between the UVB and VIS arms.

2MASSJ16090850-3903430 and THA15-36 were both observed consecutively during the night of 23/24-Jun 2022. Both are about ~ 0.7 mag less bright than the archival photometry. The spectrum of 2MASSJ16090850-3903430 whas therefore rescaled with a constant factor to match the photometry (see Table 3.9).

THA15-36 is a binary system with a separation of $\sim 2''$ that was aligned-with and resolved-in the X-shooter slits. The traces were fitted with two Gaussians at a number of wavelengths. This customized spectra extraction allowed us to estimate the flux ratio between both components as a function of wavelength. The latter enabled us to calculate the total flux in the broad-slit spectra for both components. In the narrow slit observations components were extracted from the rectified, flux calibrated 2d spectra using an extraction window with a width of $0.8''$ in all arms in order to avoid contamination from its companion. The extracted narrow slit spectra were then rescaled to their respective flux contributions to correct for wavelength dependent flux loss in the same way as mentioned before. The spectra were then multiplied by the same constant factor such that the sum of both components matches the available photometry (see Table 3.9).

For RXJ1607.2-3839 we noticed noticed that the continuum in the NIR arm bent upward at shorter wavelengths and was less bright than the archival photometry. The bend in the continuum is likely caused by an issue with the used flux standard. The flux standard taken later that night was therefore used instead. This mitigated the upward bend of the VIS arm. After this correction, the overall flux density in the arm was still lower compared to the VIS arm and the NIR photometry. This was rectified by scaling the NIR to the VIS arm such that their overlapping regions have the same median flux density. This also improved the match between the NIR arm and the available 2MASS photometry.

The NIR arm of RECX-6 displayed a similar upward bend as RXJ1607.2-3839. To mitigate this issue the flux standard of the night before was used for the reduction of the NIR arm spectrum of RECX-6.

CD-31_12522 was observed in poor seeing conditions. This caused the slit losses in the UVB narrow slit observation to become wavelength depended. We, therefore, used a linear relation rather than the mean flux ratio to rescale the UVB narrow slit to the broad slit observation.

Table 3.8: Night log of the observations.

Name	Date of observation [UT]	Slit width [" × 11"] UVB	VIS	NIR	Exp. Time[N_{exp} × s] UVBexpT	VISexpT	Exp. time [N_{exp} × $NDIT$ × s] NIRexpT
CD-31_12522	2022-06-03T00:41:42.9278	1.0	0.4	0.4	2 × 250	2 × 160	2 × 2 × 150
RXJ1608.9-3905	2022-05-03T08:35:32.8475	1.0	0.4	0.4	2 × 180	2 × 90	2 × 2 × 100
MV Lup	2010-05-05T08:30:21.1291	0.5	0.4	0.4	4 × 150	8 × 60	12 × 1 × 100
RXJ0438.6+1546	2021-12-08T02:10:32.3906	0.5	0.4	0.4	2 × 110	2 × 20	2 × 4 × 30
J15552621-3338232	2022-05-03T06:04:01.0328	1.0	0.4	0.4	4 × 180	4 × 90	4 × 2 × 100
MT Lup	2014-04-28T05:33:01.1666	0.5	0.4	0.4	4 × 179	4 × 80	4 × 20 × 10
MX Lup	2022-06-03T02:34:14.6760	1.0	0.4	0.4	4 × 180	4 × 90	4 × 2 × 100
RXJ1607.2-3839	2022-06-24T04:15:05.3699	1.0	0.4	0.4	4 × 180	4 × 90	4 × 2 × 100
MW Lup	2022-06-03T01:52:44.9932	1.0	0.4	0.4	4 × 200	4 × 110	4 × 2 × 100
NO Lup	2014-04-28T08:07:12.0366	0.5	0.4	0.4	4 × 219	4 × 120	4 × 20 × 12
THA15-43	2022-07-19T03:13:14.3819	1.0	0.4	0.4	4 × 200	4 × 110	4 × 2 × 100
THA15-36A	2022-06-24T05:03:13.4256	1.0	0.4	0.4	4 × 210	4 × 120	4 × 3 × 80
THA15-36B	2022-06-24T05:03:13.4256	1.0	0.4	0.4	4 × 210	4 × 120	4 × 3 × 80
RECX-6	2022-03-02T03:22:05.3962	1.0	0.4	0.4	2 × 440	2 × 350	2 × 5 × 100
Sz67	2022-06-16T03:55:17.2951	1.0	0.4	0.4	2 × 280	2 × 190	2 × 3 × 100
J16090850-3903430	2022-06-24T05:34:42.3279	1.0	0.9	0.9	4 × 600	4 × 510	4 × 3 × 200
16075888-3924347	2022-07-13T23:46:15.8273	1.0	0.9	0.9	4 × 600	4 × 510	4 × 3 × 200
J16091713-3927096	2022-06-03T04:01:34.0592	1.0	0.9	0.9	4 × 700	4 × 610	4 × 3 × 250
V1191Sco	2022-06-02T07:50:32.4620	1.0	0.9	0.9	4 × 550	4 × 460	4 × 3 × 200
Binaries							
CD-39_10292	2022-07-25T01:02:17.1203	1.0	0.4	0.4	2 × 250	2 × 160	2 × 3 × 100
THA15-38	2022-07-22T02:23:20.5225	1.0	0.4	0.4	4 × 210	4 × 120	4 × 3 × 80
CD-35_10498	2023-03-06T07:52:55.5080	1.0	0.4	0.4	2 × 200	2 × 110	2 × 2 × 100
V1097Sco	2022-06-05T00:47:31.7504	1.0	0.4	0.4	4 × 210	4 × 120	4 × 3 × 80
NN Lup	2022-06-16T04:16:09.4443	1.0	0.4	0.4	4 × 200	4 × 110	4 × 2 × 100

Table 3.9: Photometry available for our targets.

Band	MVlup	NOlup	MTlup	THA15-36	2MASSJ16090850
U	11.98 (2)	15.13 (2)	...	...	...
B	12.59 (3)	14.65(2)	...	15.30 (6)	18.00 (8)
V	11.28(3)	12.86 (5)	12.32 (6)	13.89 (6)	16.60 (8)
R	10.02 (2)	12.14 (2)	12.10 (6)	13.57 (6)	16.43 (8)
G	11.04 (1)	12.21 (1)	11.99(1)	...	15.66 (1)
I	9.5210.02 (4)	11.15 (5)	11.01 (5)	11.68 (7)	14.16 (8)
J	9.56 (4)	9.90 (4)	10.11 (4)	10.47 (4)	12.20 (4)
H	9.02 (4)	9.29 (4)	9.57 (4)	9.77(4)	11.64 (4)
Ks	8.88 (4)	9.12 (4)	9.38 (4)	9.53 (4)	11.36 (4)
SDSS_g	...	...	12.90 (6)	14.61 (6)	...
SDSS_r	...	...	11.86 (6)	13.29 (6)	...
SDSS_i	...	...	11.42 (6)	12.26 (6)	...

Notes: (1): Gaia Collaboration et al. (2021), (2): Makarov (2007), (3): Høg et al. (2000), (4): Cutri et al. (2003) (5): Kiraga (2012) (6): Zacharias et al. (2012) (7): Cieza et al. (2007) (8): Merín et al. (2008)

Table 3.10: Signal-to-noise ratios at different wavelengths.

name	416 nm	448 nm	490 nm	701 nm	750 nm	801nm	1217.5 nm	1600 nm	2214 nm
RXJ0445.8+1556	15.93	12.99	14.77	56.26	53.54	115.46	48.87	14.27	273.74
RXJ1508.6-4423	16.24	14.61	16.63	69.86	50.61	136.19	50.14	30.65	88.64
RXJ1526.0-4501	6.60	8.07	7.86	24.60	21.29	116.23	106.00	16.40	131.51
HBC407	6.06	7.47	7.57	19.43	16.57	104.87	84.71	14.47	160.83
PZ99J160843.4-260216	7.63	8.95	8.65	28.02	24.43	135.80	109.30	19.15	150.05
CD-31_12522	7.67	9.09	8.26	24.71	21.82	74.21	123.74	16.71	367.12
RXJ1515.8-3331	6.24	7.26	7.15	22.46	18.48	109.48	72.32	20.20	239.62
PZ99J160550.5-253313	5.73	6.83	6.73	19.68	16.02	91.52	94.63	11.15	124.80
RXJ0457.5+2014	6.75	7.53	7.41	25.51	22.08	105.95	101.53	13.02	172.28
RXJ0438.6+1546	6.15	7.26	7.07	20.07	19.44	61.56	95.07	16.04	252.33
RXJ1608.9-3905	7.97	8.52	7.83	25.72	24.26	96.94	147.80	15.28	409.61
MV Lup	5.28	6.05	6.33	17.62	15.12	72.69	113.82	13.89	237.25
RXJ1547.7-4018	5.50	6.03	6.20	18.46	15.93	84.74	96.32	11.79	189.26
RXJ1538.6-3916	5.45	5.69	6.04	18.39	14.74	76.15	103.16	15.17	209.29
MTlup	5.41	5.55	6.06	19.81	16.27	86.89	101.78	12.81	150.80
2MASSJ15552621-3338232	6.73	6.37	6.72	18.14	15.27	71.02	141.01	15.20	229.93
RXJ1540.7-3756	5.65	5.54	6.24	20.54	16.85	87.05	200.39	16.13	271.96
RXJ1543.1-3920	5.61	5.57	6.17	19.65	16.16	85.94	166.84	17.40	204.82
MX Lup	6.41	6.38	6.69	18.25	15.91	71.51	152.44	14.45	287.35
SO879	6.77	6.87	7.57	23.79	19.75	33.73	67.35	18.16	115.75
TWA6	8.59	7.95	8.20	40.78	30.25	56.04	80.51	18.99	161.06
CD -36 7429A	5.77	5.56	6.36	18.44	15.67	68.95	49.40	13.86	94.58
RXJ1607.2-3839	7.56	7.23	7.70	24.94	22.70	62.65	158.47	19.88	230.31
MW Lup	7.15	7.02	7.75	18.97	18.36	69.86	198.35	17.78	228.41
NOlup	6.21	5.67	6.77	18.57	18.27	66.65	118.13	16.40	156.53
Tyc7760283_1	6.97	6.55	7.76	16.85	17.27	61.08	98.96	16.05	100.23
TWA14	8.51	7.49	8.99	28.03	26.01	60.53	79.91	22.04	143.18
THA15-36A	8.39	7.51	8.59	15.02	19.72	52.67	102.13	24.23	167.92
RXJ1121.3-3447_app2	7.39	6.92	8.24	15.38	18.34	59.87	61.83	19.41	62.27
RXJ1121.3-3447_app1	7.57	6.88	8.13	14.52	18.62	50.31	88.64	14.27	52.72
THA15-36B	9.08	8.21	9.49	14.36	20.78	42.33	79.87	34.78	108.86
CD -29 8887A	9.39	8.53	10.00	15.82	20.39	57.08	63.04	20.19	122.24
CD -36 7429B	14.08	10.62	10.78	9.69	19.74	34.59	59.83	31.37	91.81
TWA15_app2	9.73	7.95	9.99	12.17	20.60	42.61	80.82	23.36	82.30
TWA7	11.32	9.45	10.25	9.82	20.29	33.24	85.80	22.48	103.95
Sz67	15.69	13.26	14.02	26.27	34.31	56.15	154.49	49.16	185.14
RECX-6	14.06	11.61	11.95	12.88	24.79	39.64	132.75	34.53	161.71
TWA15_app1	10.47	7.19	10.73	16.40	23.91	39.71	66.87	24.27	106.87
Sz94	14.37	12.51	12.55	16.18	27.21	53.03	82.15	38.01	101.69
SO797	7.47	8.30	11.13	17.07	29.16	33.55	40.57	15.84	45.29
Par_Lup3_2	12.00	12.77	9.96	13.89	23.39	26.01	85.31	35.86	58.28
2MASSJ16090850-3903430	2.75	4.80	4.02	9.46	21.75	23.83	87.33	60.66	75.65
SO925	2.48	4.84	6.99	11.99	21.53	23.61	55.29	14.36	7.40
SO999	4.13	6.82	8.69	12.86	22.97	24.16	43.29	36.90	10.63
SO641	7.66	7.24	9.12	11.82	22.64	26.69	52.31	41.93	43.13
V1191Sco	6.73	8.55	8.03	12.52	22.06	20.13	102.46	49.53	86.91
2MASSJ16091713-3927096	0.73	1.87	4.68	13.13	21.43	23.64	68.44	54.13	49.19
Sz107	8.35	10.41	10.47	21.05	30.13	34.14	87.44	39.34	71.01
Par_Lup3_1	0.41	0.97	1.59	4.83	14.26	12.26	54.47	31.02	56.42
LM717	0.55	1.06	2.94	7.90	16.36	11.87	63.38	38.59	58.48
J11195652-7504529	0.17	0.13	0.45	4.13	13.42	6.24	52.85	39.90	38.90
LM601	0.00	0.19	0.54	5.10	11.83	5.44	48.58	42.03	46.00
CHSM17173	0.22	0.10	0.97	8.49	12.82	6.17	42.83	33.14	48.77
TWA26	0.23	0.60	2.50	10.46	11.32	9.03	41.68	41.30	57.69
DENIS1245	0.20	0.12	0.41	6.25	8.96	8.13	35.15	46.19	40.09

3.B Uncertainties on extinction.

An independent confirmation of the extinction can be found through the ratio $F_{\rm red} = F(833.0nm)/F(634.8nm)$, as first suggested by HH14. This ratio is sensitive to both extinction and spectral type. Here we adopt the relationship of MFA17, who recalibrated the relations of HH14 using observations of class III YSO's. MFA17 adjusted the relationships of HH14 to account for differences in observed M-type spectra and the corresponding synthetic and dwarf spectra on which (HH14) based their relations. Fig. 3.14 shows these ratios for our observations after dereddening. Here it can be seen that our sample has a similar agreement with $A_V = 0$ as the samples of MTR13 and MFA17.

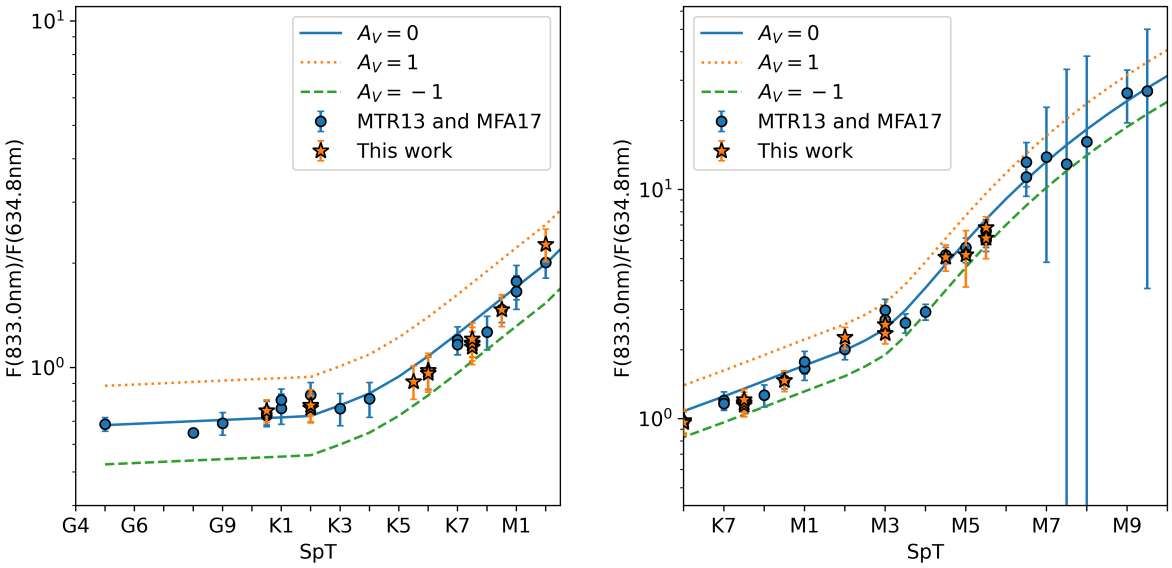

Figure 3.14: $F_{red} = F(833nm)/F(634.8nm)$ ratio calculated for the class III templates analyzed here (orange stars) as well as for the samples presented by MTR13 and MFA17 (blue circles). The error bars represent the uncertainties due to the noise in the spectra and do not include the uncertainty on the extinction correction. The blue line shows the value of F_{red} for $A_V = 0$ as a function of spectral type as derived by MFA17. The green and orange lines are obtained by deredening and reddening the relationship of MFA17 by 1 mag respectively.

3.C Luminosity calculation

Fig. 3.15 shows an example of an extrapolated X-shooter spectrum used in our luminosity calculation. We notice a small but systematic discrepancy between the luminosities obtained by integrating our extrapolated X-shooter spectra and the values found by using the bolometric correction of HH14. Fig. 3.16 shows that the ratio between the two luminosity estimates increases for later spectral types. The correction of HH14 was based on the same BT-Settl models that we used to extrapolate our X-shooter spectra. HH14 mention that for targets with $T_{\rm eff} < 3500$ K they interpolate over a VO feature that is stronger in the BT-Settl models compared to their observations. We apply the same interpolation when using the bolometric correction.

The reason for the discrepancy appears to be due to additional flux in the NIR part of the observed spectra compared to the BT-Settl models. A likely cause for this could be the presence of cold spots on the stellar surface, which was discussed in Sect. 3.3.1. We therefore propose a correction to the relationship provided by HH14, which we expect to account for the typical contribution of stellar spots to the total luminosity. We compute this temperature dependent correction factor by using the non-parametric fit displayed on Fig. 3.16. During this fitting procedure, we excluded Par Lup3 1, since it is an extreme outlier, with an extremely bright NIR flux for its SpT, which affects the resulting best fit. The adjusted bolometric correction can be found is illustrated in Fig. 3.17 and its values are listed in Table 3.11.

Table 3.11: Bolometric correction of HH14 and our adjustment to it.

T_{eff}	$F_{751}/F_{bol}[Å^{-1}]$ HH14	$F_{751}/F_{bol}[Å^{-1}]$ Adjusted
2400	$8.98 \cdot 10^{-6}$	$5.60 \cdot 10^{-6}$
2500	$1.49 \cdot 10^{-5}$	$9.76 \cdot 10^{-6}$
2600	$2.35 \cdot 10^{-5}$	$1.60 \cdot 10^{-5}$
2700	$3.37 \cdot 10^{-5}$	$2.38 \cdot 10^{-5}$
2800	$4.26 \cdot 10^{-5}$	$3.10 \cdot 10^{-5}$
2900	$5.30 \cdot 10^{-5}$	$3.95 \cdot 10^{-5}$
3000	$5.80 \cdot 10^{-5}$	$4.41 \cdot 10^{-5}$
3100	$6.41 \cdot 10^{-5}$	$4.97 \cdot 10^{-5}$
3200	$6.98 \cdot 10^{-5}$	$5.51 \cdot 10^{-5}$
3300	$7.52 \cdot 10^{-5}$	$6.04 \cdot 10^{-5}$
3400	$7.93 \cdot 10^{-5}$	$6.48 \cdot 10^{-5}$
3500	$8.20 \cdot 10^{-5}$	$6.82 \cdot 10^{-5}$
3600	$8.43 \cdot 10^{-5}$	$7.14 \cdot 10^{-5}$
3700	$8.58 \cdot 10^{-5}$	$7.39 \cdot 10^{-5}$
3800	$8.73 \cdot 10^{-5}$	$7.66 \cdot 10^{-5}$
3900	$8.80 \cdot 10^{-5}$	$7.86 \cdot 10^{-5}$
4000	$8.89 \cdot 10^{-5}$	$8.09 \cdot 10^{-5}$
4100	$8.83 \cdot 10^{-5}$	$8.18 \cdot 10^{-5}$
4200	$8.75 \cdot 10^{-5}$	$8.25 \cdot 10^{-5}$
4300	$8.90 \cdot 10^{-5}$	$8.53 \cdot 10^{-5}$
4400	$9.04 \cdot 10^{-5}$	$8.80 \cdot 10^{-5}$
4500	$9.18 \cdot 10^{-5}$	=
4600	$9.31 \cdot 10^{-5}$	=
4700	$9.41 \cdot 10^{-5}$	=
4800	$9.50 \cdot 10^{-5}$	=
4900	$9.56 \cdot 10^{-5}$	=
5000	$9.59 \cdot 10^{-5}$	=
5100	$9.64 \cdot 10^{-5}$	=
5200	$9.66 \cdot 10^{-5}$	=
5300	$9.64 \cdot 10^{-5}$	=
5400	$9.61 \cdot 10^{-5}$	=
5500	$9.56 \cdot 10^{-5}$	=
5600	$9.51 \cdot 10^{-5}$	=
5700	$9.44 \cdot 10^{-5}$	=
5800	$9.36 \cdot 10^{-5}$	=
5900	$9.28 \cdot 10^{-5}$	=
6000	$9.18 \cdot 10^{-5}$	=
6200	$8.99 \cdot 10^{-5}$	=
6400	$8.78 \cdot 10^{-5}$	=
6600	$8.55 \cdot 10^{-5}$	=
6800	$8.32 \cdot 10^{-5}$	=
7000	$8.12 \cdot 10^{-5}$	=
7200	$7.90 \cdot 10^{-5}$	=
7400	$7.66 \cdot 10^{-5}$	=
7600	$7.41 \cdot 10^{-5}$	=
7800	$7.17 \cdot 10^{-5}$	=
8000	$6.92 \cdot 10^{-5}$	=
8200	$6.66 \cdot 10^{-5}$	=
8400	$6.42 \cdot 10^{-5}$	=
8600	$6.15 \cdot 10^{-5}$	=
8800	$5.88 \cdot 10^{-5}$	=
9000	$5.61 \cdot 10^{-5}$	=
9200	$5.37 \cdot 10^{-5}$	=
9400	$5.12 \cdot 10^{-5}$	=
9600	$4.86 \cdot 10^{-5}$	=
9800	$4.63 \cdot 10^{-5}$	=
10000	$4.41 \cdot 10^{-5}$	=

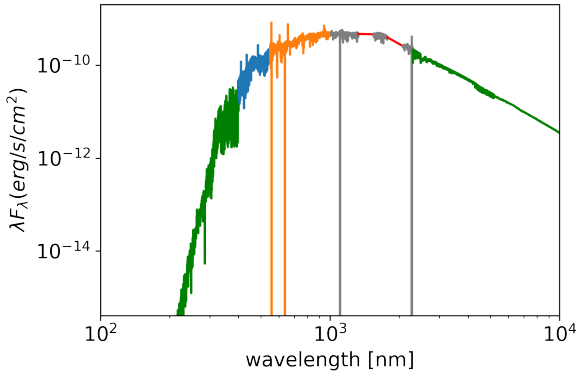

Figure 3.15: Example of a flux calibrated X-shooter spectrum extrapolated with a BT-Settl model spectrum. The model segments (dark green) are scaled at the blue and red edges of the X-shooter spectrum. The UVB, VIS, and NIR arms are plotted in blue orange and gray, respectively. The strong telluric bands in the NIR arm are replaced by a linear interpolation (red lines). In this figure, we show the example of RXJ1607.2-3839 which has been extended with a BT-Settl model of $T_{\rm eff} = 4000$ K. The BT-Settl model spectra have been convolved with a Gaussian kernel for clarity.

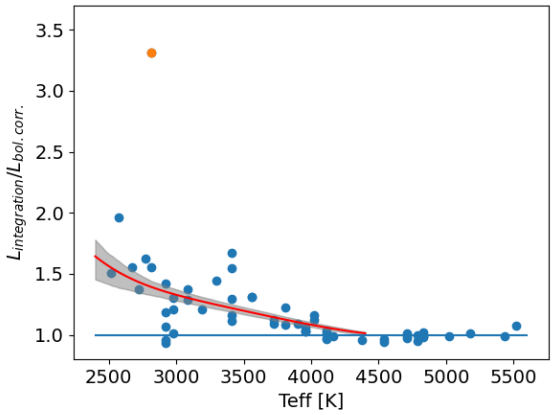

Figure 3.16: Ratio of the luminosities obtained from our spectral integration method and the value computed using the bolometric correction of (HH14). The blue dots indicate the values obtained for the spectra presented here aswell as in (MTR13) and (MFA17). The red line indicates the non-parametric fit, and the shaded area indicates the corresponding 1σ uncertainty interval obtained from bootstrapping the non-parametric fitting procedure. The orange point is Par-Lup3-1, which was excluded from this procedure.

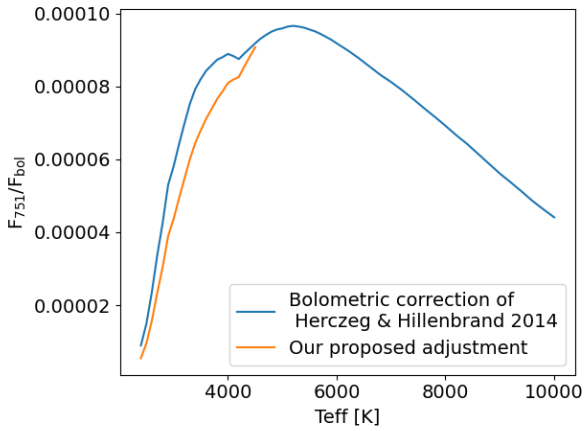

Figure 3.17: The bolometric correction (F_{751}/F_{Bol}) of HH14 and our suggested adjustment for the additional flux present in observations of class III YSOs.

3.D Notable results for the Chameleon I sample

WZ Cha: For WZ Cha our method obtains a SpT of M5 whereas the fit to the individual class III templates is degenerate with local solutions at M3 and M5. The local solution at SpT M3 appeared due to the CD -36 7429B template and since the solution appears to better reproduce the veiling in the Ca II line at $\sim$ 420nm. CD 36 7429B does however appear as an outlier among the M3 templates in that its TiO features around 710nm appear to be deeper than templates of the same SpT. When removing this template the degeneracy disappears. We therefore prefer the solution presented here.

CV Cha: The best fit of CV Cha displays a strong degeneracy in terms of SpT, stretching from $\sim$K4 to $\sim$G9. The solution found here results in a SpT of K3. This degeneracy is a likely consequence of the poor constraint on early spectral types in our model spectra.

VZ Cha: For VZ Cha we find an extinction that is $\Delta A_V = 0.5$ mag lower than obtained using the method of Manara et al. (2013a). This differing result appears to be a consequence of the stricter constraint imposed on the Paschen continuum by the best fit metric used in our method, resulting in a better fit of this region. Despite the large difference in obtained A_V, the accretion and stellar properties still agree within errors.

Sz 19: The luminosity of Sz19 appears large for its spectral type, resulting in a high mass estimate. Fig. 3.18 illustrates this by showing Sz19 and our class III templates on an HRD. The spectra of this target agree with the available photometry within < 2 mag. The results presented here agree with those found by Manara et al. (2014) (although the slightly later SpT results in a very different stellar mass). An analysis of the emission lines results in accretion luminosities that are in agreement with those found from our analysis of the UV excess. A detailed investigation into why this source appears as an outlier is beyond the scope of this paper.

3.E 2MASSJ16075888-3924347

The spectrum of 2MASSJ16075888-3924347 appears to have spectral features typical of an accreting T Tauri star rather than a non-accreting class III object. For example, the Hα line luminosity appears much larger than in the other class III templates of similar spectral type (M5.5). We measure an equivalent width of EW $= -3.914 \pm 0.093$nm. This would classify the target as a CTTS rather than a WTTS according to the classification scheme of Barrado y Navascués & Martín (2003); White & Basri (2003). Similarly, the Ca II IR triplet is detected for this target but not in comparable class III templates. This result is puzzling considering that the SED of this target presented by Lovell et al. (2021), does not show any excess emission at longer wavelengths and is consistent with that of other class III objects. Moreover, Lovell et al. (2021) did not detect any flux at 856 μm, giving an upper limit of < 0.11 mJy. No previous Hα equivalent widths are available in the literature for this target. A detailed analysis of this star is beyond the scope of this work and will be presented by Stelzer et al. in prep..

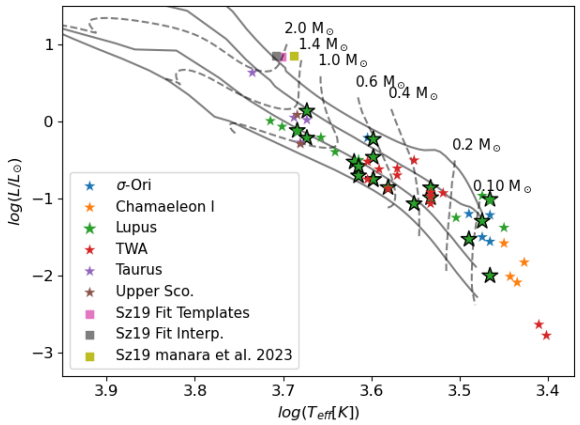

Figure 3.18: HRD Containing the different results obtained for Sz19 for comparison the objects analyzed here (highlighted with larger black outlined markers) and those analyzed by MTR13 and MFA17 are displayed. The model isochrones and evolutionary tracks by Feiden (2016) are also shown. The isochrones are the 1.2,3,10 and 30 Myrs ones

3.F The combined grid

Table 3.12: Final grid of spectral templates and their stellar properties.

Name	Region	SpT	T_{eff}[K]	distance [pc]	$\log(L/L_{\odot})$	reference
RXJ0445.8+1556	Taurus	G5	5430	$167.3^{+3.2}_{-3.8}$	0.64 ± 0.07	MFA17
RXJ1508.6-4423	Lupus	G8	5180	145.7 ± 0.4	0.01 ± 0.07	MFA17
RXJ1526.0-4501	Lupus	G9	5025	150.1 ± 0.3	-0.07 ± 0.06	MFA17
HBC407	Taurus	K0	4870	$249.1^{+43.5}_{-29.7}$	$0.05^{+0.17}_{-0.12}$	Manara et al. (2014)
PZ99J160843.4-260216	Upper Scorpius	K0.5	4830	$137.4^{+1.1}_{-1.0}$	0.09 ± 0.06	MFA17
CD-31_12522	Lupus	K0.5	4830	127.4 ± 0.5	-0.12 ± 0.06	This work
RXJ1515.8-3331	Lupus	K0.5	4830	115.4 ± 0.2	-0.14 ± 0.06	MFA17
PZ99J160550.5-253313	Upper Scorpius	K1	4790	105.1 ± 0.2	-0.29 ± 0.06	MFA17
RXJ0457.5+2014	Taurus	K1	4790	122.2 ± 0.3	-0.27 ± 0.06	MFA17
RXJ0438.6+1546	Taurus	K2	4710	139.1 ± 0.3	0.02 ± 0.06	This work
RXJ1608.9-3905	Lupus	K2	4710	156.0 ± 0.4	0.14 ± 0.06	This work
MV Lup	Lupus	K2	4710	137.1 ± 0.3	-0.21 ± 0.2	This work
RXJ1547.7-4018	Lupus	K3	4540	130.2 ± 0.3	-0.21 ± 0.06	MFA17
RXJ1538.6-3916	Lupus	K4	4375	122.5 ± 0.4	-0.40 ± 0.06	MFA17
MT Lup	Lupus	K5.5	4163	133.1 ± 0.3	-0.52 ± 0.2	This work
2MASSJ15552621-3338232	Lupus	K6	4115	119.0 ± 0.2	-0.70 ± 0.05	This work
RXJ1540.7-3756	Lupus	K6	4115	134.3 ± 0.3	-0.50 ± 0.05	MFA17
RXJ1543.1-3920	Lupus	K6	4115	$133.6^{+5.4}_{-6.2}$	$-0.50^{+0.06}_{-0.07}$	MFA17
MX Lup	Lupus	K6	4115	$128.8^{+0.3}_{-0.2}$	-0.58 ± 0.05	This work
SO879	σ Ori.	K7	4020	$395.6^{+3.4}_{-2.2}$	-0.21 ± 0.2	MTR13
TWA6	TW Hya	K7	4020	65.5 ± 0.1	-0.75 ± 0.2	MTR13
CD -36 7429A	TW Hya	K7	4020	76.3 ± 0.1	-0.52 ± 0.2	MTR13
RXJ1607.2-3839	Lupus	K7.5	3960	167.9 ± 2.7	-0.23 ± 0.05	This work
MWlup	Lupus	K7.5	3960	$129.6^{+0.2}_{-0.3}$	-0.75 ± 0.05	This work
NO Lup	Lupus	K7.5	3960	$132.8^{+0.3}_{-0.2}$	-0.46 ± 0.2	This work
THA15-43	Lupus	K7.5	3960	125.1 ± 0.3	-0.75 ± 0.05	This work
Tyc7760283_1	TW Hya	M0	3900	53.5 ± 0.1	-0.62 ± 0.2	MTR13
TWA14	TW Hya	M0.5	3810	$92.0^{+0.2}_{-0.1}$	-0.87 ± 0.2	MTR13
THA15-36A	Lupus	M0.5	3810	$145.6^{+0.9}_{-0.6}$	-0.86 ± 0.2	This work
RXJ1121.3-3447_app2	TW Hya	M1	3720	59.7 ± 0.1	-0.70 ± 0.2	MTR13
RXJ1121.3-3447_app1	TW Hya	M1	3720	59.7 ± 0.1	-0.61 ± 0.2	MTR13
THA15-36B	Lupus	M2	3560	$150.9^{+1.6}_{-1.5}$	-1.07 ± 0.2	This work
CD -29 8887A	TW Hya	M2	3560	$45.9^{+0.4}_{-0.5}$	-0.50 ± 0.2	MTR13
CD -36 7429B	TW Hya	M3	3410	76.1 ± 0.2	-1.06 ± 0.2	MTR13
TWA15_app2	TW Hya	M3	3410	114.7 ± 0.2	-0.92 ± 0.2	MTR13
TWA7	TW Hya	M3	3410	34.05 ± 0.03	-0.97 ± 0.2	MTR13
Sz67	LupusI	M3	3410	$103.2^{+1.0}_{-0.9}$	-0.86 ± 0.04	This work
RECX-6	LupusI	M3	3410	97.9 ± 0.1	-0.99 ± 0.04	This work
TWA15_app1	TW Hya	M3.5	3300	114.2 ± 0.2	-0.93 ± 0.2	MTR13
Sz94	Lupus	M4	3190	114.6 ± 0.3	-1.25 ± 0.2	MTR13
SO797	σ Ori.	M4.5	3085	$385.9^{+11.5}_{-10.6}$	-1.20 ± 0.2	MTR13
SO641	σ Ori.	M5	2980	$374.6^{+10.6}_{-14.8}$	-1.50 ± 0.2	MTR13
Par_Lup3_2	Lupus	M5	2980	157.2 ± 1.0	-0.96 ± 0.2	MTR13
2MASSJ16090850-3903430	LupusIII	M5	2980	$156.5^{+1.3}_{-0.9}$	$-1.29 \pm 0.$	This work
SO925	σ Ori.	M5.5	2920	$371.5^{+25.8}_{-19.4}$	-1.56 ± 0.2	MTR13
SO999	σ Ori.	M5.5	2920	$387.7^{+16.5}_{-15.7}$	-1.21 ± 0.2	MTR13
V1191Sco	LupusIII	M5.5	2920	$168.4^{+2.2}_{-2.4}$	-1.01 ± 0.04	This work
2MASSJ16091713-3927096	LupusIII	M5.5	2920	$133.7^{+2.6}_{-2.8}$	-2.00 ± 0.04	This work
Sz107	Lupus	M5.5	2920	$152.4^{+1.9}_{-1.8}$	-1.03 ± 0.2	MTR13
Par_Lup3_1	Lupus	M6.5	2815	$159.7^{+4.2}_{-4.1}$	-1.38 ± 0.2	MTR13
LM717	ChaI	M6.5	2815	$190.6^{+2.6}_{-2.5}$	-1.58 ± 0.04	MFA17
J11195652-7504529	ChaI	M7	2770	$189.2^{+4.7}_{-4.2}$	-2.01 ± 0.04	MFA17
LM601	ChaI	M7.5	2720	$186.1^{+4.8}_{-4.6}$	-2.09 ± 0.04	MFA17
CHSM17173	ChaI	M8	2670	$191.5^{+4.6}_{-4.2}$	-1.83 ± 0.04	MFA17
TWA26	TW Hya	M9	2570	46.6 ± 0.5	-2.63 ± 0.2	MTR13
DENIS1245	TW Hya	M9.5	2520	$83.1^{+2.3}_{-2.8}$	-2.78 ± 0.2	MTR13

4

Substructures through the lens of mass accretion

The work presented in this chapter is to be included in R. A. B. Claes, C. F. Manara, J. Campbell-White et al. to be submitted to A&A

Abstract

High angular resolution observations have revealed that protoplanetary disks display a variety of substructures. These substructures can take the form of spirals, inner cavities, annular rings/gaps, and asymmetries. A large number of mechanisms have been proposed, some of which should affect the accretion rate from the disk onto the central star. Here, we aim to characterize the accretion properties of sources with resolved substructures and relate the measured accretion rates to the type of substructures observed in each source. In particular, we investigate whether different classes of substructures have different accretion timescale distributions. We present the analysis of 29 X-Shooter spectra to derive stellar and accretion properties. These results are combined with accretion and disk properties obtained from literature to provide a sample of 61 disks with known substructures. This sample is divided into categories based on the observed morphology and the wavelength range of observation. The position in the $\dot{M}_{\rm acc}$ -$M_{\rm disk}$ of certain interesting sources is discussed with respect to the rest of the population. We perform a statistical comparison between the accretion timescale distributions of different disk morphology classes. Finally, we test whether the properties of hypothetical embedded planets, inferred from the observed substructures, relate to the measured accretion timescales. Our results hint at the fact that disks with resolved cavities display larger accretion timescales compared to the unknown-substructure population. We do not find the expected increase in accretion timescale in systems where massive planets have been hypothesized to exist. Instead, we find statistically insignificant anti-correlations between the accretion timescales and planet masses inferred from different methods. Larger samples or a better consideration of system age is needed to firmly conclude whether disks with inner cavities have larger accretion timescales. Larger samples and a homogeneous analysis of the observed substructures are also needed to quantify if there is a relationship between the accretion timescale and inferred planet properties in protoplanetary disks.

4.1 Introduction

In recent years, a large number of spatially resolved observations of protoplanetary disks have revealed a multitude of complex substructures. These include inner cavities (e.g., Pinilla et al. 2018b), spiral arms (e.g., Huang et al. 2018a,b; Long et al. 2018), concentric rings, and horseshoe-shaped asymmetries (See Andrews 2020; Benisty et al. 2023, for reviews). An even wider variety of mechanisms has been proposed in an attempt to explain these observations (See Bae et al. 2023, for a review).

Horseshoe-shaped asymmetries are the rarest type of substructure observed. For this type of substructure, two main causation mechanisms are being considered: lumps and vortices. Lumps are formed in eccentric disks because the particles will spend more time at the apogee of their orbit. Vortices, on the other hand, are caused by hydrodynamical instabilities such as convective overstability (Klahr & Hubbard 2014; Lyra 2014), vertical shear instability (Urpin & Brandenburg 1998; Nelson et al. 2013), zombie vortex instability (e.g., Barranco & Marcus 2005; Marcus et al. 2016) or inner binary (Ragusa et al. 2017). Due to their rotating motion, vortices can trap dust particles, resulting in horseshoe-shaped overdensities. Vortices and lumps can, therefore, be distinguished by the rotating motion of the gas around the brightness peak of the horseshoe.

The second rarest type of substructure consists of sources that display spiral arms. Spirals can be caused by a wide variety of different effects. The Rossby wave instability is a type of hydrodynamical instability that can cause weak spiral arms that are unlikely to be observed. We will therefore not discuss this source of spirals further and refer the interested reader to Bae et al. (2023). MRI-induced turbulence could be another potential origin (Heinemann & Papaloizou 2009a,b). Eccentric modes, that is, the coherent precession of gas on an eccentric orbit, could be another mechanism (Lin 2015). The influence of the environment, through the infall of material (e.g., Kuffmeier et al. 2020; Mesa et al. 2022) or stellar flybys (e.g., Cuello et al. 2020) can also induce spirals in the disk. Gravitational instability, that is, the collapse of the disk when its self-gravity overcomes the gas pressure, has also been shown to produce spiral arms in simulations (e.g., Rice et al. 2006). The presence of a protoplanet in the disk can also excite spiral waves (Bae & Zhu 2018; Miranda & Rafikov 2019). Both internal and external stellar companions can also excite spirals in the disk (e.g., Ragusa et al. 2017; Wagner et al. 2018).

The existence of inner cavities was hypothesized before we could spatially resolve disks. This is because disks with an inner cavity will show a lack of mid-infrared excess in their SED (e.g., Skrutskie et al. 1990; Calvet et al. 2002). Such cavities were first observed by Andrews et al. (2011), and have been observed repeatedly since (e.g., Pinilla et al. 2018b).

Several mechanisms have been proposed to explain the existence of an inner cavity in disks. Internal photoevaporation refers to the process in which high-energy photons (UV/X-ray) from the central star transfer enough energy to gas in the disk to eject it from the disk. This effect is expected to first create a gap separating the inner from the outer disk. After this, the inner disk will accrete onto the central star. During this stage, the disk will therefore display a cavity (Hardy et al. 2015). After the inner disk has been accreted, the outer disk will in turn be exposed to high-energy photons and dissipate. However, photoevaporation can not explain the properties of all disks with cavities (Alexander et al. 2014). A close stellar companion at the center of the

disk could tidally truncate the inner disk and, as a consequence, open a large cavity (Artymowicz & Lubow 1994, 1996). Similarly, one or multiple planets in the inner disk may clear the material in their orbit and create a cavity in the disk. The so-called "dead zones," that is, a region in the disk in which the MRI is ineffective in creating an effective viscosity, have also been proposed to explain inner cavities (Pinilla et al. 2016). In this scenario a gap is expected to form due to the lower accretion rate in the dead zone compared to inside its radius.

The mechanisms that can create rings in disks somewhat overlap. The earliest stage of internal photoevaporation results in an inner disk separated by a gap from an outer disk, therefore appearing as a gap/ring structure. The presence of massive protoplanets in the disk also has the potential to create gaps if they are situated on a wider orbit (Paardekooper & Mellema 2006; Zhu et al. 2012). Icelines are the radii at which different volatiles sublimate/condensate and can cause ring-like enhancements in the dust surface density in several different ways (See Bae et al. 2023, for an indepth discussion). It has been shown that the presence of a strong ambient magnetic field can launch a magnetocentrifugal wind from the disk in both ideal and non-ideal MHD simulations (Moll 2012). This type of wind can extract angular momentum from the disk and can form annular substructures. In simulations (e.g., Béthune et al. 2016; Riols et al. 2020) it has been shown that if the magnetic diffusivity is low enough, then the magnetic field is expected to concentrate in regions of lower density in the disk, thereby increasing the wind strength in these areas. This can then result in ring-like substructures forming if the viscous timescale is larger than the wind depletion timescale as dust concentrates near the pressure maxima around the formed gas gaps.

There still remains a great uncertainty as to which of these many mechanisms is responsible for the observed substructures in each disk. However, what has become evident is that the classical picture of a smooth disk is inappropriate (Huang et al. 2018a,b). The presence and origin of these substructures could complicate studies that attempt to constrain whether viscosity or MHD winds are the main mechanism responsible for the evolution of protoplanetary disks. One of the observables often used to try to distinguish between viscous and MHD-driven evolution is the mass accretion rate. Alexander et al. (2023), for example, find that a homogeneous sample of $\gtrsim 300$ measurements will allow us to distinguish between both paradigms by comparing the mass observed accretion rate distributions to those predicted by the models. Other works, such as, e.g., Lodato et al. (2017), Tabone et al. (2022b), and Somigliana et al. (2023) use the observed correlation between mass accretion rate and the disk mass instead. In the latter case, it is found that the MHD wind scenario is better able to reproduce the observed relationship between mass accretion rate and the disk mass. This is the case because the MHD wind scenario is better able to reproduce the large observed scatter in the correlation between mass accretion rate and disk mass, whereas the viscous scenario predicts a tighter correlation for more evolved disks.

A caveat to these studies is that a number of the various mechanisms that can create substructures are predicted to affect the mass accretion rate and are not considered in such studies. The presence of a snowline could decrease the mass accretion rate if the conditions are right for the dust to have a significant back reaction onto the gas. For this to occur, the viscous turbulence must be low ($\alpha \lesssim 10^{-3}$) the global dust-to-gas ratio needs to be high ($\gtrsim 0.03$) and the disk must be large enough ($\gtrsim 100$ au) and young ($\lesssim 1$ Myr) (Gárate et al. 2020). Using the Bern planet population synthesis models (Mordasini et al. 2009, 2012; Benz et al. 2014), Manara et al. (2019)

showed that disks with one or more embedded massive planets ($M_{planet} > M_J$) display lower mass accretion rates at comparable disk masses. Similarly, Lubow & D'Angelo (2006) found that the mass flow rate through a disk gap induced by a $\sim 1\,M_J$ to be lower by 10%-25% in viscous 2D hydrodynamical simulations. For a disk where MHD winds drive the accretion, 3D global non-ideal MHD simulations have shown that the presence of a massive planet has little effect on the accretion rate through the disk (Wafflard-Fernandez & Lesur 2023). As mentioned above, the presence of dead zones decreases the mass accretion rate in a region of a viscously evolving disk. As the disk inward of this region is cleared, one would also expect a lower accretion rate onto the central star. External influences on a protoplanetary disk, such as the late infall of material or perturbation of the disk, are expected to increase the mass accretion rate onto the central star (Kuffmeier et al. 2023). A perturbation of the disk induced by a stellar flyby is expected to increase the mass accretion rate. A stellar flyby has even been proposed to explain the extreme accretion outburst ($\dot{M}_{\rm acc} \sim 10^{-5}\,M_\odot/{\rm yr}$) observed in FU Ori (Vorobyov et al. 2021; Borchert et al. 2022). Zagaria et al. (2022a) showed both observationally and through the use of one-dimensional evolutionary models of tidally truncated disks that the presence of an external binary companion could have a similar effect.

Understanding the accretion properties of sources with known substructures can therefore significantly contribute to our understanding of the mechanisms responsible for creating the substructure in question. It is also vital for our understanding of disk evolution to constrain the influence of these substructure-creating mechanisms on the scatter observed in the $\dot{M}_{\rm acc}$-$M_{\rm disk}$ correlation.

Here, we conduct a pilot study investigating the accretion properties of sources with known substructures. In Section 4.2, we discuss our sample selection and classification of their substructures. We discuss the data we obtained from literature in section 4.3. In Section 4.4 we present the observations and data reduction. We present our analysis of the sample in Section 4.5. The position of the sources in the $\dot{M}_{\rm acc}$-$M_{\rm disk}$ relations is discussed in Section 4.6. In Section 4.7 we discuss the relationship between the properties of potential planets inferred from the observed substructures and the accretion timescale. Finally, we summarize our findings and conclusions in Section 4.8.

4.2 Sample selection

We selected sources that have been observed to display substructures in scattered light or millimeter-wavelength images. In this work, we limit ourselves to Classical T-Tauri stars. A complete overview of our sample and the substructures of each target is given in table 4.1. Our sample consists of targets that have been observed to display three main categories of substructure: cavities, rings, and spirals. In a previous work, Parker et al. (2022) compiled a list of 56 disks showing substructures. These sources were classified into four categories: rim, rings, spirals, and horseshoes. None of the disks classified as horseshoes by Parker et al. (2022) is present in our sample, as they are Herbig stars. Our classification corresponds well to that of Parker et al. (2022), with the exception that we include hybrid categories for targets that display both inner cavity and multiple outer rings or those that display both rings and spirals. This results in us

classifying AA Tau, DM Tau, WSB60, and LkCa15 as sources with multiple rings and an inner cavity, rather than just defining them by their cavity. We also choose to label GM Aur and Sz19 rings-cavity sources despite them being classified as ringed sources by Parker et al. (2022). Similarly, we choose to label Elias 2-27 and IM Lup as sources with both rings and spirals instead of only defining them by their rings. The rim classification of Parker et al. (2022) largely corresponds to our Cavity classification. The exceptions to this are DS Tau and J162556.1-242048 (EM * SR 4), which we classify as ringed sources despite being classified as rim sources by Parker et al. (2022), since both sources have a significant inner disk extending down to the central star. Finally, we note that J15583692-2257153 (HD 143006) displays an asymmetry in its ALMA observations, which does not resemble the typically observed horseshoe shape and is instead more localized. For J15583692-2257153, we adopt the same classifications as adopted by Parker et al. (2022), who ignored this asymmetry and classified both targets as sources displaying rings.

The category of targets with cavities is often associated with transition disks. Transition disks have historically been defined as targets whose SED displays a deficit of excess emission in the mid-infrared, whereas at longer wavelengths the excess emission is comparable to that of a full protoplanetary disk (Calvet et al. 2002). This lack of mid-infrared emission has been interpreted as a lack of dust in the inner disk. Here, however, we focus on targets in which a cavity has been resolved at either (sub)mm or NIR wavelengths. We, therefore, prefer the term Cavity.

Our sample can be further subdivided into two categories: those observed with millimeter observations and those observed in the NIR. This distinction is critical to our interpretation of the observed substructures, since different probes are sensitive to distinct physical conditions and materials. NIR observations trace scattered light reflected by small ($\sim \mu$m) dust grains suspended in the gaseous atmosphere of the protoplanetary disk (Benisty et al. 2023). (Sub)millimeter observations on the other hand, trace the thermal emission originating from large dust grains that settle near the midplane (Miotello et al. 2023).

4.2.1 Observational biases

In order to be able to detect substructures, a source needs to be observed with both sufficient angular resolution and sensitivity. Overall, these limitations bias the sample towards the more massive disk around brighter, more massive stars. This effect is illustrated in figure 4.1, where the stellar and disk mass of disks with and without detected substructures are compared. Different observations are color-coded by a measure of the *effective* angular resolution ($\theta_{\rm D}/\theta_{\rm res}$) of the observations. Here Bae et al. (2023) have chosen $\theta_{\rm D}/\theta_{\rm res}$ to be the ratio of the angular 90% flux radius ($\theta_{\rm D}$) and the angular resolution of the observation ($\theta_{\rm res}$). Figure 4.1 also contains histograms showing the detection of substructures as a function of stellar and disk mass. It can be seen that substructures are detected more often around more massive stars and disks. Figure 4.1 illustrates that this is probably an observational bias, as the disks that are more massive/orbit more massive stars tend to be observed at a higher effective resolution. For the 37 disks observed with an effective resolution $\theta_{\rm D}/\theta_{\rm res} > 10$, Bae et al. (2023) finds that only 2 disks lack detectable substructures. Meanwhile, for observations with an effective resolution $\theta_{\rm D}/\theta_{\rm res} < 3$, substructures are only detected in 5 out of 256 disks. The apparent lack of substructures in less massive

Table 4.1: Classical T Tauri stars observed to display substructures.

Name	2MASS	region	Sub. Type	Ref
J10563044-7711393	J10563044-7711393	ChamI	Cavity	PTP18
J16090141-3925119	J16090141-3925119	Lupus	Cavity	MWP20
Sz91*	J16071159-3903475	Lupus	Cavity	PTP18 *TMH14
RYLup	J15592838-4021513	Lupus	Cavity	PTP18
PDS 70	J14081015-4123525	uSco	Cavity	KTB19
SzCha	J10581677-7717170	ChamI	Cavity,Rings-IR	PTP18GGB24
CSCha**	J11022491-7733357	ChamI	Cavity	KPP22 **GGB24
RY_Tau	J04215740+2826355	Taurus	Cavity	LPH18
Sz123A	J16105158-3853137	Lupus	Cavity	PTP18
CIDA_1	J04141760+2806096	Taurus	Cavity	PKB18
Sz118	J16094864-3911169	Lupus	Cavity	PTP18
Sz111	J16085468-3937431	Lupus	Cavity	PTP18
Sz100	J16082576-3906011	Lupus	Cavity	PTP18
IPTau	J04245708+2711565	Taurus	Cavity,Cavity-IR	LPH18GGvH24
FTTau	J04233919+2456141	Taurus	Cavity	LPH18
J16083070-3828268	J16083070-3828268	Lupus	Cavity	PTP18
GGTau**	J04323034+1731406	Taurus	Cavity,Cavity-IR	BDF23PDD20**BD06
J16042165-2130284	J16042165-2130284	USco	Cavity,Cavity-IR	S23 BDF23
PDS 66	J13220753-6938121	uSco	NONE	RMW23
RX_J1615	J16152023-3255051	Lupus	Spiral, Cavity-Rings-IR	PWK2022(AQG18)
J162623.7-244314	J16262367-2443138	rOph	Rings	HAD18
J162556.1-242048	J16255615-2420481	rOph	Rings	HAD18
MYLup	J16004452-4155310	Lupus	Rings	HAD18
Sz114	J16090185-3905124	Lupus	Rings	HAD18
Sz98	J16082249-3904464	Lupus	Rings	MDD19
J15583692-2257153	J15583692-2257153	USco	Rings	HAD18
J10590699-7701404	J10590699-7701404	ChamI	Rings	K20!
Sz83	J15564230-3749154	Lupus	Rings	HAD18
Sz71	J15464473-3430354	Lupus	Rings	HAD18
DLTau	J04333906+2520382	Taurus	Rings	LPH18
RXJ1852.3-3700	J18521730-3700119	CrA	Cavity,Rings-IR	FVdM20VBD19
WWCha**	J11100010-7634578	ChamI	Rings,Spiral-IR	KHJ21 BDF23 **GGB24
HLTau	J04313843+1813576	Taurus	Rings	MDD19
DoAr33	J16273901-2358187	rOph	Rings	HAD18
CITau	J04335200+2250301	Taurus	Rings	LPH18

Table 4.2: Classical T Tauri stars observed to display substructures, continued.

IMLup	J15560921-3756057	Lupus	Rings-Spirals,Rings-IR	HAP18AQG18
v4046sgr**	J18141047-3247344	bPic	Rings-Cavity,Rings-IR	MCP18AQG18**PWK2022
AS209	J16491530-1422087	Ophiucus	Rings	HAD18MDD19
DM_Tau	J04334871+1810099	Taurus	Rings-Cavity	MDD19
Sz129	J15591647-4157102	Lupus	Rings-Cavity	AHP18
LkCa15	J04391779+2221034	Taurus	Rings-Cavity,Rings-IR	FBB20TJG16
GOTau	J04430309+2520187	Taurus	Rings	LPH18
CWTau	J04141700+2810578	Taurus	Rings	UKT22
ROX27	J16273942-2439155	rOph	Rings	HAD18
AA_Tau	J04345542+2428531	Taurus	Rings-Cavity	MDD19
DN_Tau	J04352737+2414589	Taurus	Rings	LPH18
BP_Tau	J04191583+2906269	Taurus	Rings	ZKL23
WSB60	J16281650-2436579	rOph	Rings-Cavity	CGH21
ATpyx	J08284070-3346222	GumNebula	Spiral-IR	BDF23
Sz75**	J15491210-3539051	Lupus	Spiral-IR	BDF23**AMD20
DR_Tau	J04470620+1658428	Taurus	Spiral-IR	BDF23
J16120668-3010270	J16120668-3010270	USco	Spiral-Cavity-IR	Ginski
DZCha	J11493184-7851011	eCha	Spiral-IR	BDF23
GMAur	J04551098+3021595	Taurus	Rings-Cavity,Spiral-IR	HAD20GGvH24
WaOph6	J16484562-1416359	rOph	Spirals	HAD18
TWHya	J11015191-3442170	TWhya	Rings,Rings-IR	MDD19BHM17
DS Tau**	J04474859+2925112	Taurus	Rings	LPH18**PWK2022
Elias 2-20	J16261886-2428196	rOph	Rings	HAD18
Elias 2-24	J16262407-2416134	rOph	Rings	HAD18
Elias 2-27	J16264502-2423077	rOph	Rings-Spirals	HAD18
V1094Sco	J16264502-2423077	rOph	Rings	MDD19

Notes: Circumbinary disks and stars that are part of a wide binary system are marked with * and ** respectively. References:Pinilla et al. (2018b):PTP18, van der Marel et al. (2022):MWP20, Long et al. (2018):LPH18, Pinilla et al. (2021):PKB18, Benisty et al. (2023) and references therein:BDF23, Andrews (2020) and references therin :A20, Huang et al. (2018a):HAD18, van der Marel et al. (2019):MDD19, Huang et al. (2018b):HAP18,Andrews et al. (2018):AHP18, Thalmann et al. (2016):TJG16, Facchini et al. (2020):FBB20, Cieza et al. (2021):CGH21, Ueda et al. (2022):UKT22, Zhang et al. (2023):ZKL23, Huang et al. (2020):HAD20, Keppler et al. (2018):KTB19, Kurtovic et al. (2022):KPP22, Ribas et al. (2023):RMW23, Phuong et al. (2020):PDD20,Avenhaus et al. (2018):AQG18, Martinez-Brunner et al. (2022):MCP18, Villenave et al. (2019):VBD19, Ginski et al. (2024):GGB24, Garufi et al. (2024):GGvH24, Stadler et al. (2023):S23, Kim et al. (2020):K20, Pascucci et al. (2016):P16 ,van Boekel et al. (2017):BHM17, Francis & van der Marel (2020):FVdM20, Garufi et al. (2024):GGvH24, Parker et al. (2022):PWK2022, Alcalá et al. (2020):AMD20, Beust & Dutrey (2006):BD06, Tsukagoshi et al. (2014):TMH14, Kanagawa et al. (2021):KHJ21

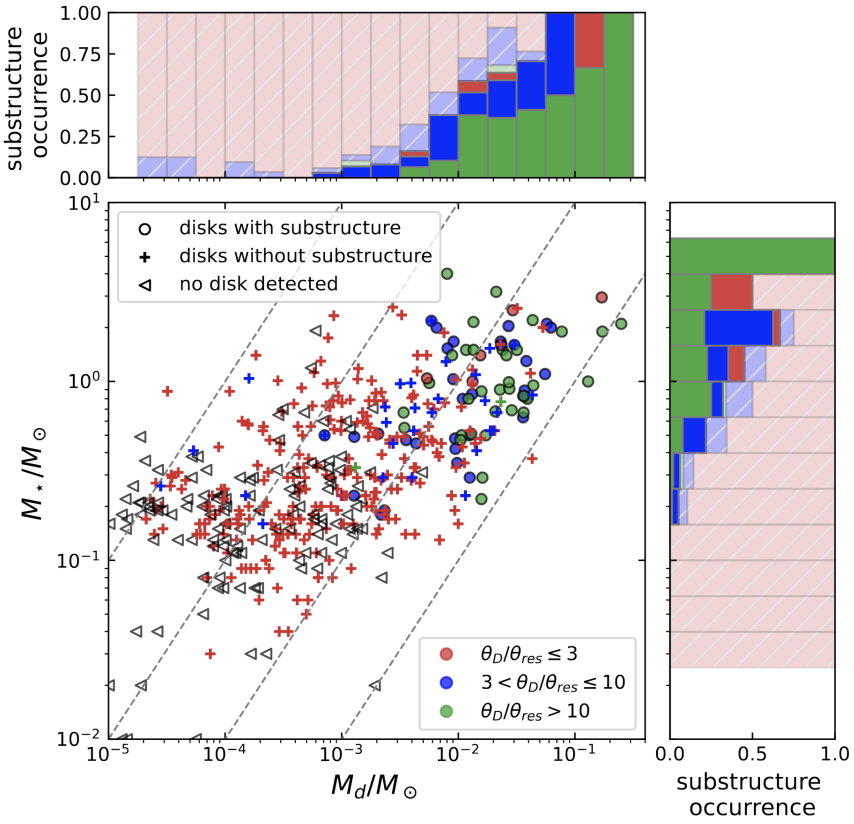

Figure 4.1: Mass of the host star vs. disk mass as obtained from the mm flux. $\theta_{\rm D}/\theta_{\rm res}$ is the ratio of the angular 90% flux radius $(\theta_{\rm D})$ and the angular resolution of the observation $\theta_{\rm res}$). The histograms are color-coded using the same colors as the points on the plot. The fraction of disks with substructures is marked with solid colors in the histogram, and those where none have been observed are marked with the hatched, faded colors. The four diagonal dashed lines on the plot display the stellar-to-disk mass ratio of $M_\star/M_{\rm d} = 10000, 1000, 100$, and 10 (from left to right). Source image: Bae et al. (2023)

disks or the disks around lower-mass stars is therefore likely an observational bias, and it remains plausible that the vast majority of disks display some form of substructures.

Within our sample, it can be seen that the targets in which rings are detected have a disk mass higher than $\sim 4 \cdot 10^{-3}\ M_\odot$. For the cavity category, this minimum disk mass is lower at $\sim 4 \cdot 10^{-4}\ M_\odot$. This is likely a consequence of the fact that cavities are easier to detect. This was shown by Parker et al. (2022), who found that all of the Ring substructures detected within their ALMA sample were detected with sensitivities below 60 μJy/Beam. Meanwhile, cavities in their sample are observed at sensitivities smaller than $\sim 140\,\mu$Jy/Beam. This is illustrated in Figure 4.2, where the angular resolution and sensitivity of the observations of the substructured disks in the sample of Parker et al. (2022) are shown. Here, it is important to note that figure 4.2 shows the observational angular resolution rather than an *effective* angular resolution of the observation as in figure 4.1. Therefore, while it appears in figure 4.2 that both rings and cavities are observed

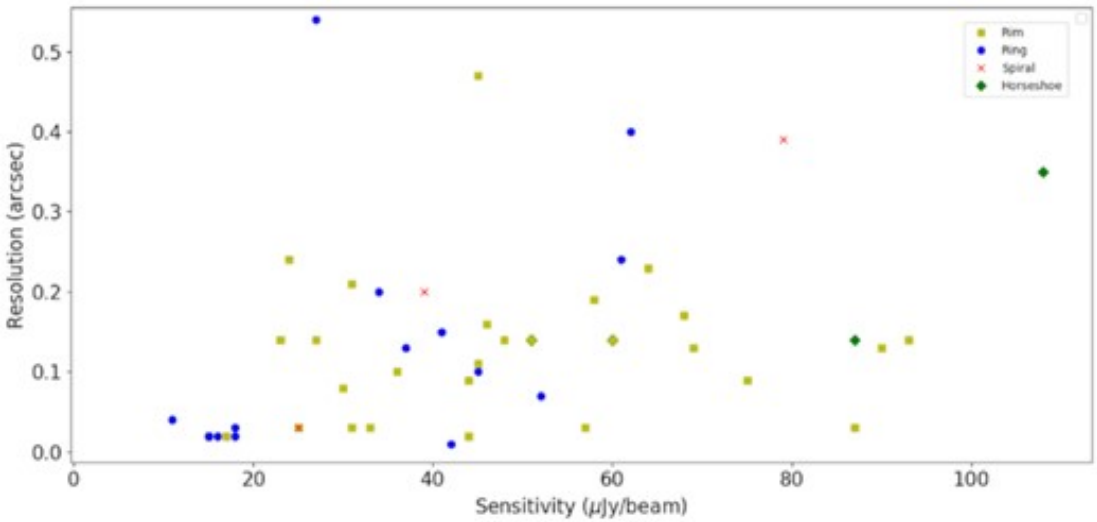

Figure 4.2: Angular resolution and sensitivity of the observations of substructured sources in the sample of Parker et al. (2022). Four protoplanetary disks observed at sensitivities smaller than $120\,\mu$Jy/Beam are not included in the figure. Source image: Parker et al. (2022)

in the entire range of resolutions, it may still be the case that rings are more likely to be detected at higher $\theta_{\rm D}/\theta_{\rm res}$. It could also be the case that disks labeled as cavities in our sample will display more complex substructures when observed at higher angular resolution and/or lower sensitivity.

For NIR observations with adaptive optics, the central star needs to be sufficiently bright. This prevents observations of targets below $\sim 0.4\ M_\odot$ in Taurus (Garufi et al. 2024) and $\sim 0.5\ M_\odot$ for Chamaeleon I (Ginski et al. 2024). The disk itself also needs sufficient polarized light contrast to observe the substructures. Indeed, Garufi et al. (2024) divided their VLT/SPHERE observations of Taurus sources into bright and faint sources based on their polarization contrast and found a near-perfect correspondence between the faint sources and those without detected substructures. The only exception was MWC480, which has a low polarized light contrast but has a high luminosity, which still allowed for the detection of rings. This leads Garufi et al. (2024) to conclude that the lack of detected substructures in faint sources is a likely consequence of sensitivity. Garufi et al. (2024) find no correlation between the scattered light brightness and the dust mass of the disk, implying that there is no direct bias towards the disk mass. Some bias towards higher disk masses may still exist since disk mass and stellar mass are known to be correlated (Manara et al. 2023).

4.3 Literature data

For 33 of the targets listed here, we use the results presented by Manara et al. (2023). The table of Manara et al. (2023) combines the results of various accretion rate surveys, the results of which are mainly based on the analysis of spectra obtained with the VLT/X-Shooter instrument. In particular, the stellar and accretion properties for the Chamaeleon I region are obtained from

Manara et al. (2016a, 2017a). For Lupus, the results were obtained from Alcalá et al. (2014, 2017). Upper Scorpius results were obtained from Manara et al. (2020), and the Chamaeleon II date was obtained from Villenave et al. (2021). For Corona Australis and Ophiuchus, the results were obtained from Testi et al. (2022), who obtained the accretion properties from the luminosities of a number of emission lines rather than a measurement of the UV continuum excess. The Taurus sample was obtained from a variety of works (e.g., Ingleby et al. 2013; Alcalá et al. 2021; Testi et al. 2022). The methods used to obtain the mass accretion rates in the Taurus region are therefore diverse. All of the accretion and stellar properties presented by Manara et al. (2023) have been recalculated using the individual target distances obtained from Gaia EDR3 (Gaia Collaboration et al. 2021). The values obtained from Manara et al. (2023) are listed in Table 4.3.

We decided not to use the results listed by Manara et al. (2023) that were obtained by fitting the X-Shooter Spectra to Class III templates that were omitted by Claes et al. (2024). Since IM Lup/Sz82 was fitted to the wrongly classified CD-36 7429A template, we reanalyze both here. Similarly, Sz Cha and CS Cha were fitted using the high extinction uncertainty template CrA 75. The table of Manara et al. (2023) also contains the results obtained with a low number of Class III templates available, namely the results adopted from Manara et al. (2014). Since this may result in higher uncertainties, we re-analyze the spectra of substructured sources presented by Manara et al. (2014). For GM Aur and RXJ1852.3-3700, we prefer to use the PENELLOPE observation over the spectrum of Manara et al. (2014), since it has been flux calibrated using broad-slit observations rather than by scaling to literature photometry.

We collect literature values for the disk masses of the sources analyzed here. The majority of these are obtained from Manara et al. (2023, and references therein), as is the case for all of the disk masses listed in table 4.3 and Bae et al. (2023, and references therein), with the exception of V4046sgr and PDS 66, where we obtained the disk mass from Martinez-Brunner et al. (2022) and Ribas et al. (2023), respectively. We ensured that all disk masses were computed using the same method and with the same assumptions. The disk masses were computed using the ALMA band 6 (1.3 mm) flux when available; otherwise, the band 7 flux was used instead, accounting for the different wavelengths. The millimeter flux is converted to disk mass using,

$$M_{dust} = \frac{d^2 F_\nu}{\kappa_\nu B(T)}, \tag{4.1}$$

where d is the distance to the object, F is the flux at frequency ν, and the opacity is given by $\kappa_\nu = 2.3(\nu/230\,\mathrm{GHz})\,\mathrm{cm}^2/\mathrm{g}$ (Beckwith et al. 1990). $B(T)$ is the Planck function, for which both Manara et al. (2023) and Bae et al. (2023) assume a temperature of $T = 20\,\mathrm{K}$. The dust mass is converted to a disk mass by assuming a gas-to-dust ratio of 100. This computation is based on some significant assumptions. The first is the assumption that the dust is optically thin at the wavelength of observation and that the flux, therefore, scales with the dust mass. In case this assumption does not hold, then our values should be interpreted as lower limits (e.g., Ballering & Eisner 2019; Ribas et al. 2020). The conversion is then also dependent on the assumed temperature and dust opacity. The dust opacity is, in turn, dependent on the assumed grain sizes, their chemical composition, and structure (Birnstiel et al. 2018).

Table 4.3: Stellar and accretion properties obtained from Manara et al. (2023)

Name	2MASS	$M_{\rm disk}$ $[M_\odot]$	SpT SpT	$L_{\rm star}$ $[L_\odot]$	$log(L_{\rm acc})$ $[L_\odot]$	$M_\star$ $[M_\odot]$	$log(\dot{M}_{\rm acc})$ $[M_\odot/{\rm yr}]$		dist. [pc]
AA_Tau	J04345542+2428531	1.076e-02	M0.6	0.754	-0.852	0.486	-7.635		137
BP_Tau	J04191583+2906269	7.473e-03	M0.5	0.978	-0.559	0.486	-7.290		129
CIDA_1	J04141760+2806096	2.065e-03	M4.5	0.210	-1.586	0.178	-8.033		135
DN_Tau	J04352737+2414589	1.237e-02	M0.3	0.695	-1.337	0.526	-8.185		128
DR_Tau	J04470620+1658428	2.105e-02	K6	1.902	0.029	0.600	-6.710		195
DS_Tau	J04474859+2925112	4.709e-03	M0.4	1.037	-0.573	0.497	-7.305		159
J10563044-7711393	J10563044-7711393	3.974e-04	K7	0.548	-2.131	0.670	-9.180		183
J10590699-7701404	J10590699-7701404	4.694e-02	K0	4.367	-1.290	1.530	-8.410	CN	187
J15583692-2257153	J15583692-2257153	1.486e-02	K0	2.608	-0.491	1.480	-7.710		166
J16042165-2130284	J16042165-2130284	1.401e-02	K3	0.843	-3.196	1.130	-10.480	CN	150
J16083070-3828268	J16083070-3828268	8.689e-03	K2	1.884	-2.009	1.270	-9.200	CN	156
J16090141-3925119	J16090141-3925119	1.258e-03	M4	0.093	-3.197	0.198	-9.893		164
J162556.1-242048	J16255615-2420481	1.149e-02	K6	1.824	-0.118	0.610	-6.880		134
J162618.9-242820	J16261886-2428196	1.639e-02	M0	2.537	-0.085	0.588	-6.711		138
J162623.7-244314	J16262367-2443138	4.147e-02	K6	1.490	-2.126	0.620	-8.940	CN	138
J162624.1-241613	J16262407-2416134	6.290e-02	K5.5	7.065	0.439	0.940	-6.225		136
J162645.0-242308	J16264502-2423077	3.401e-02	K8	0.943	-0.565	0.557	-7.383		139
MYLup	J16004452-4155310	1.504e-02	K0	0.860	-0.644	1.190	-8.000		157
RYLup	J15592838-4021513	1.930e-02	K2	1.844	-0.856	1.270	-8.050		159
RY_Tau	J04215740+2826355	3.482e-02	G0	23.400	-0.370	2.750	-7.550	CN	443
Sz100	J16082576-3906011	4.867e-03	M5.5	0.106	-3.205	0.130	-9.614		136
Sz111	J16085468-3937431	1.358e-02	M1	0.210	-2.399	0.520	-9.473		158
Sz114	J16090185-3905124	9.146e-03	M4.8	0.196	-2.709	0.160	-9.100		162
Sz118	J16094864-3911169	5.489e-03	K5	0.698	-1.983	0.830	-9.110	CN	163
Sz123A	J16105158-3853137	3.795e-03	M1	0.136	-1.980	0.557	-9.177		158
Sz129	J15591647-4157102	1.748e-02	K7	0.421	-1.138	0.730	-8.270		161
Sz71	J15464473-3430354	1.496e-02	M1.5	0.327	-2.173	0.414	-9.033		155
Sz75	J15491210-3539051	7.643e-03	K6	1.602	-0.655	0.610	-7.440		151
Sz83	J15564230-3749154	3.742e-02	K7	1.460	-0.258	0.550	-7.000		159
Sz91	J15464473-3430354	2.172e-03	M1	0.200	-1.998	0.520	-9.081		159
Sz98	J16082249-3904464	2.266e-02	K7	1.530	-0.709	0.550	-7.440		156
V1094Sco	J16083617-3923024	4.035e-02	K6	1.210	-1.007	0.640	-7.880		154

Notes: Results marked with CN fall below the chromospheric noise limit of Claes et al. (2024)

Lastly, the value assumed for the gas-to-dust ratio is that of typical ISM composition and may not be representative of protoplanetary disks. Various effects, such as dust growth and radial drift of the dust, have the potential to affect the dust-to-gas ratio (e.g., Franceschi et al. 2022).

4.4 Observations and data reduction

A complete list of the 11 X-Shooter Spectra was obtained specifically to constrain the accretion properties of sources with known substructures (PrID: 111.255B.001 & 112.25BZ.001 PI: Claes). We retrieved the X-Shooter spectra of 8 sources from the ESO archive (WaOph6, AS 209, V4046 Sgr, DZ Cha, IP Tau, PDS 66, and PDS 70). We include 4 spectra (GM Aur, RXJ1852.3-3700, TW Hya, and IM Lup) that were obtained as part of the PENELLOPE survey (Manara et al. 2021). We do not re-reduce the spectra presented by Manara et al. (2014) (WSB60, RXJ1615.3-3255, CS Cha, LkCa15,DM Tau, Sz Tau). All of the targets presented here have been observed in slit-nodding mode to obtain an ideal sky subtraction. X-shooter is divided into three arms, each covering a different wavelength range. These arms are the UVB arm ($\lambda\lambda \sim 300 - 550$ nm), the VIS arm ($\lambda\lambda \sim 500 - 1050$ nm), and the NIR arm ($\lambda\lambda \sim 1000 - 2500$ nm). Table 4.10 lists the width of the slits and the corresponding spectral resolutions for each arm, as well as the exposure times used for each observation analyzed here. Most of the targets listed here were observed using a broad-slit ($5.0 \times 11''$) immediately after the narrow-slit observations. Such broad-slit observations provide a lower spectral resolution but do not suffer from a loss of flux due to the slit. They are therefore used to correct the narrow-slit observations for slit losses, providing an absolute flux calibration. The flux standards observed for two of the archival observations (V4046sgr, PDS 66) lacked the signal-to-noise ratio in the NIR arm to obtain a good instrument response correction. We therefore excluded the NIR arm of these spectra from our analysis.

The reduction of the spectra presented by Manara et al. (2014) was performed using version 1.3.7 of the X-Shooter pipeline (Modigliani et al. 2010). The pipeline performs the standard reduction steps, including bias and dark frame subtraction, flat fielding, wavelength calibration, sky subtraction, and instrument response/fluxure corrections. The telluric removal of these spectra was achieved using the IRAF[1] task *telluric*. The steps followed to normalize the telluric lines in the VIS and prepare the response function in the NIR are described by Alcalá et al. (2014). Manara et al. (2014) used the standard telluric spectra provided as part of the X-Shooter calibration plan on each night of observations to perform the telluric correction. Manara et al. (2014) only had broad-slit observations for the spectra of Pr.Id. 090.005, of which we only use DM Tau. This spectrum was therefore corrected for slit losses by scaling it to the available broad-slit observations. The other spectra were corrected for slit losses by rescaling the reduced telluric-corrected spectra to the photometry available in the literature.

We reduced the spectra obtained from PrID: 111.255B.001 and 112.25BZ.001, as well as the archival spectra using version v.4.2.2 of the X-Shooter pipeline (Modigliani et al. 2010) in the Reflex workflow (Freudling et al. 2013). The pipeline performs the same reduction steps mentioned above. We corrected the narrow-slit spectra for tellurics using the MOLECFIT tool

[1]IRAF is distributed by National Optical Astronomy Observatories, which is operated by the Association of Universities for Research in Astronomy, Inc., under cooperative agreement with the National Science Foundation.

(Smette et al. 2015). Here we chose to fit the telluric features on the spectra themselves, rather than using the telluric standards observed during the same night. We corrected the spectra for slit losses by rescaling the telluric corrected narrow slit observations to the broad slit spectra using the method developed for the PENELLOPE program (see Manara et al. 2021). Both the VIS and NIR arms were flux corrected using a factor with a linear dependency on wavelength. For the UVB arm, the correction was done using a correction factor constant with wavelength. The spectra obtained from the PENELLOPE survey (PrID: 106.20Z8.008 PI: Manara) were reduced by the PENELLOPE collaboration following the same procedure outlined here Manara et al. (2021).

For the archival spectra of V4046sgr, AS209, WaOph6, and PDS 66, no wide-slit observations were available. Since these targets have ongoing accretion, they may exhibit variability. Therefore, we prefer not to rescale these spectra to archival photometry, which was taken at different times. We instead prefer to flux calibrate our spectra using the method of Sana et al. (2024). This method applies a slit loss correction, which takes into account the airmass (h) and seeing ($\sigma_{\rm obs}$) at the time of observation. For the seeing, we make use of the real-time measurements of real-time by a differential image motion monitor (DIMM) at Paranal. The DIMM seeing is defined at 500nm; therefore we need to correct this seeing for the wavelength dependence and the airmass of the observation. This is done using

$$\sigma_\lambda = \sigma_{\rm DIMM}\left(\frac{\lambda}{500nm}\right)^{-0.2} \cdot airmass^{0.6}. \tag{4.2}$$

The transmission fraction of the slit at a given wavelength is then given by

$$T_\lambda = erf\left(\sqrt{\ln(2)}\frac{w_{\rm slit}}{\sigma_\lambda}\right), \tag{4.3}$$

where $w_{\rm slith}$ erf is the errorfunction given by

$$erf(x) = \frac{2}{\sqrt{2\pi}}\int_x^0 e^{-t^2}dt. \tag{4.4}$$

The spectra are corrected by dividing the flux at a given wavelength by the corresponding T_λ. The corrected spectra typically agree within ~ 0.2 mag with the available SIMBAD photometry.

4.5 Analysis

4.5.1 UV excess fitting

The most direct way to constrain the accretion properties of young stars is by measuring the UV continuum excess emission. We use the method presented by Claes et al. (2024) to model the X-Shooter spectra. In this method, the spectra are fitted using an interpolated grid of class III templates to represent the stellar emission, and a slab model to represent the emission originating

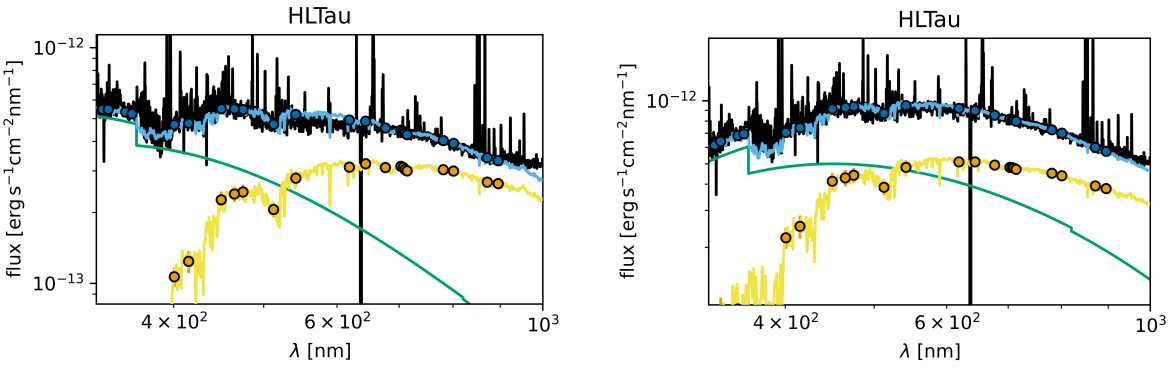

Figure 4.3: Right: The best fit result obtained for HL Tau when using $R_V = 3.1$. Left: The best fit result obtained for HL Tau when using $R_V = 5.0$. The observed spectra have been convolved with a Gaussian kernel with a standard deviation of 0.1 nm for clarity.

at the accretion shock while accounting for extinction.

The best-fit model is found by searching for the lowest value of a $\chi^2_{\rm like}$ function for a grid of parameters. The physics included in the used accretion slab models is detailed in Chapter 2 of Manara (2014). The parameters used for the slab model grid are described in Claes et al. (2024) and references therein. We account for extinction using the Cardelli et al. (1989) extinction law, where we let A_V vary in steps of 0.1 magnitude. We initially run all our fits with $R_V = 3.1$, which is the standard value for the diffuse interstellar medium.

For several highly extinct sources ($A_V \gtrsim 2$ mag), we observed that the observed spectra are poorly reproduced by the best-fit model in a broad region around 600 nm. The flux of the combined slab model and accretion template overpredicts that in the dereddened observed spectra. We find that these spectra are better reproduced when using $R_V = 5.0$ mag, a value more appropriate for dense clouds (Cardelli et al. 1989). An example of such a mismatch and the improvement obtained when using $R_V = 5.0$ can be seen in Figure 4.3.

Three of the targets for which this is the case are DL Tau, CW Tau, and HL Tau, which were previously studied by Herczeg & Hillenbrand (2014). Interestingly, Herczeg & Hillenbrand (2014) find that a higher R_V is only needed to fit the Taurus targets with extinction $A_V > 5$ mag in their analysis, and therefore it was not necessary to fit DL Tau, CW Tau, and HL Tau with $R_V > 3.1$. Here it is worth pointing out that the DoubleSpec/LRIS observations presented by Herczeg & Hillenbrand (2014) cover a wavelength range of 300-570 nm in the blue setup and 620-870 nm in the red setup. The spectra used by Herczeg & Hillenbrand (2014) therefore did not cover the wavelength region where we see the biggest difference due to the choice of R_V.

We fit the spectra to interpolated class III templates that have been created following the procedure of Claes et al. (2024). As in Claes et al. (2024), we do not fit the entire spectra and instead only compute $\chi^2_{\rm like}$ for a select number of wavelength ranges. We include wavelength ranges that constrain the Balmer jump, the Balmer continuum, the Paschen continuum, the TiO 710 nm band, and features used in the R515 index of Herczeg & Hillenbrand (2014). We extend upon the wavelength ranges used by Claes et al. (2024) by also including features at $\sim$ 780 nm

Table 4.4: Wavelength ranges included in the interpolated grid used in our fitting procedure.

Name	wavelength ranges [nm]
Balmer jump	359-362
	399-402
Balmer continuum	337.5-342.5
	352-358
Paschen continuum	414-415
	448-452
	474-476
TiO 710 nm	702.5-703.5
	706.5-707.5
	709.5-710.5
	713.5-714.5
R515	464-466
	510-515
	539-544
TiO 625 & 680 nm	617 - 620
	643 - 645
	675 - 678
TiO 770	780 - 782
	800 - 802
	870 - 872
	894 - 896

and $\sim$ 800 nm to constrain the TiO 770 band, at $\sim$ 620 nm, $\sim$ 645 nm, and $\sim$ 675 nm to constrain the TiO 625 and 680 nm bands, and finally, we include two ranges at $\sim$ 870 nm and $\sim$ 895 nm that help constrain the extinction. The precise wavelength ranges used in the best fit determination are listed in table 4.4. These wavelength ranges are comparable to the wavelength ranges proposed for a number of spectral indexes proposed by Herczeg & Hillenbrand (2014), although alterations have been made to avoid emission lines in the spectra of accretion targets and strong telluric features. Despite this, a poor telluric correction of the H_2O telluric lines from $\sim$ 900 to $\sim$ 1000 nm affected the best fit determination for the spectra of Manara et al. (2014). We, therefore, chose to fit the spectra of Manara et al. (2014) using the wavelength ranges used by Claes et al. (2024) instead. Plots comparing the best-fit models to the dereddened observations can be found in appendix 4.F.

To compute the luminosities, we use the Gaia DR3 distances (Gaia Collaboration et al. 2016, 2023). We calculate the stellar mass using the nonmagnetic isochrones of Feiden (2016). The effective temperature of the stars is obtained by using the SpT-$T_{\rm eff.}$ relation of Herczeg & Hillenbrand (2014). We apply the lower limit criterion for measurable mass accretion rates of Claes et al. (2024) to the results obtained here. Targets that have a $L_{\rm acc}/L_{\star}$smaller than the detectable limit are labeled with "CN" in table 4.5. Figure 4.4 shows our sample in a Hertzsprung-Russel

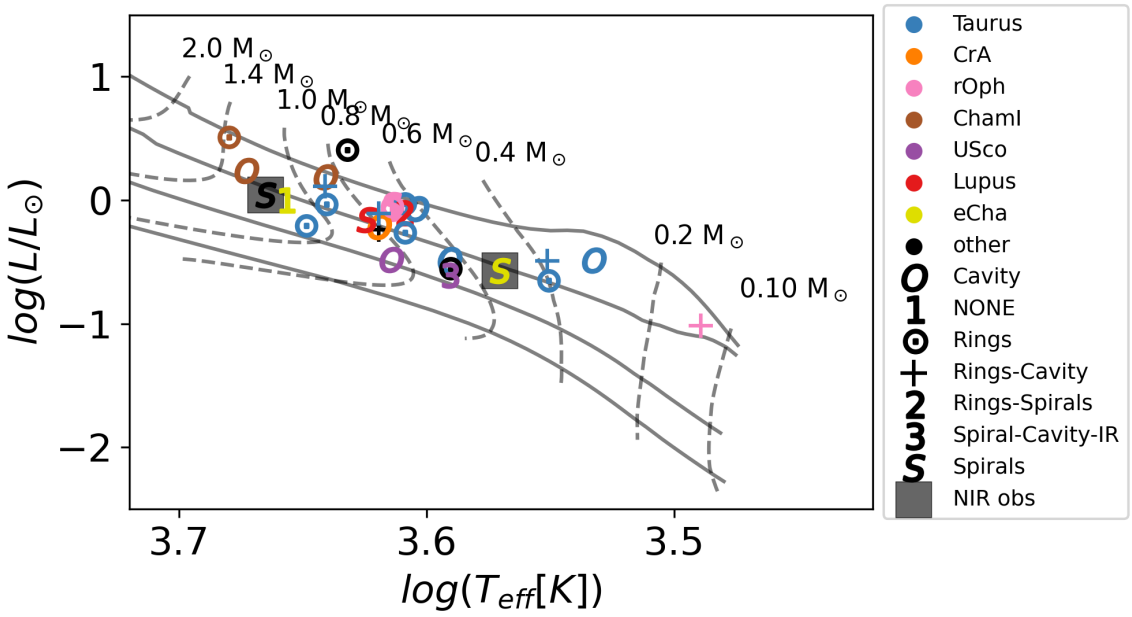

Figure 4.4: HRD of the objects analyzed here. The models' isochrones and evolutionary tracks of Feiden (2016) are also shown. The isochrones are those at 1.2,3,10 and 30 Myr.

Diagram (HRD) together with the nonmagnetic evolutionary tracks and isochrones of Feiden (2016). Here, it can be seen that all of our targets fall between the 1.2 and 10 Myr isochrones, with the exception of one star, which is AS 209. Given the young age of AS 209 (1-2 Myr (Andrews et al. 2009)) and the typical uncertainties on the luminosity of $\sim$ 0.2 dex, we do not believe AS 209 to be overluminous.

The signal-to-noise ratio of our spectra is listed in table 4.9. For two targets (WSB60 and ROX27), the spectra are too noisy (S/N $<$ 4) at short wavelengths to constrain the accretion properties from the slab model. In these cases we obtain the accretion properties from an analysis of the emission lines.

4.5.2 Analysis of emission lines

We analyze a number of emission lines present in our X-Shooter spectra to obtain an additional estimate of the accretion luminosity. In particular, we look at the Hα, Hβ, Hγ, Hδ, Ca K, He I 587 nm, He I 667 nm, Paβ, Paγ and Brγ lines. First, the line luminosities are computed. We first deredden the spectra using the best-fitting extinction law from our slab modeling. Then, we estimate the continuum in the region around the line of interest. This is achieved by iteratively fitting a second-order polynomial in the line region and removing the points of which the residual is 2 σ away from the mean residual from the fit. We then integrate the flux between the line and the continuum. We converted the line luminosities into accretion luminosities using the empirical

Table 4.5: Accretion properties of the sample analyzed here.

Name	2MASS	A_V [mag]	R_V [mag]	SpT SpT	$L_\star$ [$L_\odot$]	$\log(L_{\rm acc})$ [$L_\odot$]	$M_\star$ [$M_\odot$]	$\log(\dot{M}_{\rm acc})$ [$M_\odot$/yr]		dist. [pc]
J16120668	J16120668-3010270	0.10	3.10	M0.0	0.246	-2.332	0.699	-9.541		132.1
AS209	J16491530-1422087	1.40	3.10	K4.5	2.564	-0.963	0.732	-7.766		121.0
ATpyx	J08284070-3346222	1.50	3.10	K2.5	1.098	-1.171	1.197	-8.436		370.0
CITau	J04335200+2250301	1.80	3.10	K6.5	0.942	-0.866	0.638	-7.780		160.0
CSCha	J11022491-7733357	0.70	3.10	K4.0	1.548	-1.420	0.859	-8.419	CN	169.0
CWTau	J04141700+2810578	2.30	5.00	K4.0	0.924	-0.766	0.946	-7.918		131.0
DLTau	J04333906+2520382	2.70	5.00	K6.5	0.550	-0.404	0.732	-7.494		142.0
DMTau	J04334871+1810099	1.00	3.10	M2.0	0.323	-1.331	0.384	-8.141		144.0
DZCha	J11493184-7851011	0.00	3.10	M1.0	0.270	-2.950	0.501	-9.952	CN	101.0
DoAr33	J16273901-2358187	3.00	3.10	K6.0	0.831	-1.373	0.703	-8.366		142.0
FTTau	J04233919+2456141	2.20	3.10	M3.0	0.326	-1.209	0.300	-7.872		130.0
GGTau	J04323034+1731406	1.00	3.10	K7.0	0.852	-1.194	0.616	-8.104		116.0
GMAur	J04551098+3021595	1.00	3.10	K5.5	0.783	-0.570	0.763	-7.622		158.0
GOTau	J04430309+2520187	1.40	3.10	M2.0	0.223	-1.816	0.401	-8.726		142.0 [2]
HLTau	J04313843+1813576	3.40	5.00	K3.5	0.623	-0.410	1.064	-7.716		193.0
IMLup	J15560921-3756057	1.20	3.10	K6.5	0.789	-0.598	0.669	-7.571		155.0
IPTau	J04245708+2711565	0.80	3.10	M0.0	0.331	-1.454	0.652	-8.568		129.0
LkCa15	J04391779+2221034	1.00	3.10	K4.0	1.297	-1.830	0.883	-8.879	CN	157.0
PDS 66	J13220753-6938121	0.20	3.10	K3.0	1.004	-1.696	1.125	-8.938	CN	98.0
PDS 70	J14081015-4123525	0.50	3.10	K6.0	0.331	-2.899	0.853	-10.176	CN	112.0
ROX27	J16273942-2439155	6.70	5.00	K6.0	0.888	-0.948	0.683	-7.915		135.0
RXJ1852.3-3700	J18521730-3700119	0.10	3.10	K5.5	0.608	-2.036	0.807	-9.167	CN	147.0
RX_J1615	J16152023-3255051	0.30	3.10	K5.0	0.693	-2.880	0.830	-10.004	CN	155.0
SzCha	J10581677-7717170	1.50	3.10	K2.0	1.725	-1.676	1.274	-8.886	CN	169.0
TWHya	J11015191-3442170	0.30	3.10	M0.0	0.281	-1.099	0.674	-8.263		60.0
WSB60	J16281650-2436579	2.90	3.10	M4.5	0.097	-2.596	0.131	-9.075		135.0
WWCha	J11100010-7634578	4.10	5.00	K1.0	3.254	-0.473	1.375	-7.593		135.0
WaOph6	J16484562-1416359	2.30	3.10	K6.0	0.922	-0.914	0.683	-7.872		122.0
v4046sgr	J18141047-3247344	0.10	3.10	K5.5	0.579	-2.765	0.821	-9.914	CN	71.0

[2] Results marked with CN fall below the chromospheric noise limit of Claes et al. (2024)

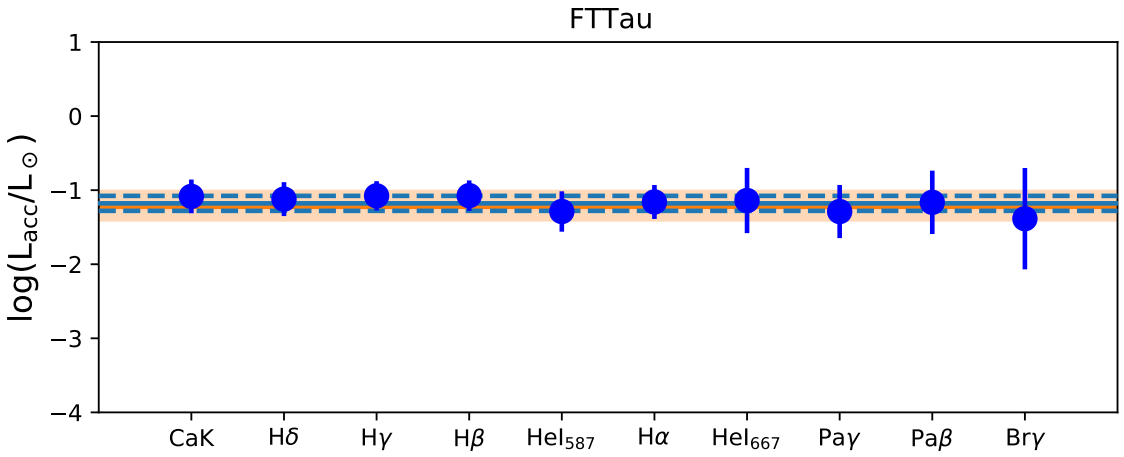

Figure 4.5: Accretion luminosities obtained from the line luminosities of different emission lines (blue dots). The solid blue line indicated the mean accretion luminosity obtained from the emission lines, and the dashed blue line the corresponding standard deviation. The orange solid line indicates the accretion luminosity obtained from the slab modeling, and the orange shaded area indicates the uncertainty thereon.

relationships of Alcalá et al. (2017). The resulting accretion luminosities can be found in Tables 4.11 and 4.12.

Figure 4.5 shows a comparison between the accretion luminosities obtained from the emission lines and the accretion slab modeling of FT Tau. We plotted the lines according to increasing wavelength. This allows us to verify the A_V obtained in our slab modeling. If A_V is underestimated, we expect the slope of the individual line accretion luminosities to increase with wavelength, since the line flux at shorter wavelengths will be increasingly underestimated. If A_V is overestimated, we expect to see the opposite trend. We do not see such trends in our sample. In figure 4.6 we plot a comparison between the mean accretion luminosities obtained from the lines and those obtained from the slab modeling, as well as $L_{\rm acc}/L_\star$. We find that both agree within uncertainties for all the targets in our sample with the exception of RXJ 1615, and V4046 Sgr. All of these targets were marked as dubious accretors by the criterion of Claes et al. (2024).

We converted the mean accretion luminosity measured from the lines into a mass accretion rate using the stellar mass obtained from the slab model fit using the nonmagnetic models of Feiden (2016). The mean derived accretion luminosities and the mass accretion rate computed are listed in table 4.6. For ROX 27 and WSB60, we adopt these mass accretion rates instead of those obtained from the slab model fitting. The disk mass, accretion rate, and stellar mass adopted for our comparison are listed in Table 4.7.

Table 4.6: Accretion luminosity and mass accretion rates obtained from our analysis of the emission lines.

Name	$\log(L_{\rm acc}[L_\odot])$	$\log(\dot{M}_{\rm acc}[M_\odot/{\rm yr}])$
2MASS-J16120668-3010270	-2.150 ± 0.260	-9.34
AS209	-1.150 ± 0.380	-7.96
ATpyx	-1.640 ± 0.410	-8.90
CITau	-0.880 ± 0.160	-7.79
CS-Cha	-1.440 ± 0.290	-8.44
CWTau	-0.690 ± 0.300	-7.84
DLTau	-0.330 ± 0.190	-7.43
DMTau	-1.850 ± 0.520	-8.66
DZCha	-2.920 ± 0.620	-9.92
DoAr33	-1.420 ± 0.190	-8.41
FTTau	-1.180 ± 0.100	-7.84
GGTau	-0.890 ± 0.150	-7.80
GMAur	-0.760 ± 0.240	-7.81
GOTau	-2.280 ± 0.800	-9.19
HLTau	-0.910 ± 0.690	-8.21
IPTau	-1.950 ± 0.590	-9.06
WSB60	-2.250 ± 0.270	-8.73
LkCa15	-1.490 ± 0.230	-8.54
PDS 66	-1.350 ± 0.210	-8.59
PDS 70	-3.100 ± 0.510	-10.38
ROX27	-0.780 ± 0.150	-7.74
RXJ1852.3-3700	-2.210 ± 0.570	-9.34
RX_J1615	-1.690 ± 0.180	-8.81
Sz-Cha	-1.470 ± 0.270	-8.68
Sz82	-1.060 ± 0.350	-8.04
TWHya	-1.120 ± 0.240	-8.28
WWcha	-0.350 ± 0.410	-7.47
WaOph6	-1.480 ± 0.390	-8.43
v4046sgr	-1.820 ± 0.310	-8.97

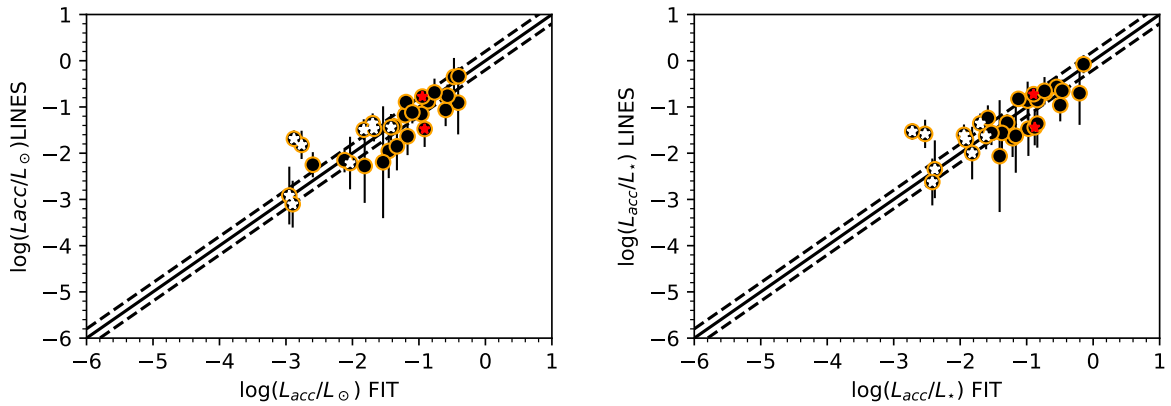

Figure 4.6: Right: Comparison between accretion luminosities obtained from the emission lines and those obtained from the slab model fitting. Left: Left comparison between $L_{\rm acc}/L_\star$ as obtained from the line luminosities and slab model fitting. Dubious accretors are highlighted with white stars, and sources with too low signal-to-noise at blue wavelengths are highlighted with red stars. The solid line indicates the one-to-one relationship, and the dashed lines are 0.2 dex (the typical uncertainty on $L_{\rm acc}$obtained from the slab models) above and below the one-to-one relation.

4.6 The position of different substructures in the $\dot{M}_{\rm acc}$ $M_\star$ and $M_{\rm disk}$ and diagrams

To discuss the relative accretion properties of the various substructured sources, we plot them in the $\dot{M}_{\rm acc}$ -$M_\star$ and $\dot{M}_{\rm acc}$ -$M_{\rm disk}$ planes. For clarity, we separate the categories of rings and cavities into different plots. The position of the ringed substructures in the $\dot{M}_{\rm acc}$ -$M_\star$ and $\dot{M}_{\rm acc}$ -$M_{\rm disk}$ diagrams can be seen in Figure 4.7, and the cavities can be seen in Figure 4.8. The sources displaying inner cavities can be seen in Figure 4.8. It is also important to note that the gray arrows are not upper limits but dubious accretors, for which the measurement of the accretion rate is dominated by uncertainties in the chromospheric contribution, as defined by the criterion of Claes et al. (2024). On the $\dot{M}_{\rm acc}$ -$M_{\rm disk}$ plots we also display the $t_{\rm acc} = \dot{M}_{\rm acc}/M_{\rm disk} = 10^6$ yr line as a visual aid. Meanwhile, on the $\dot{M}_{\rm acc}$ -$M_\star$ diagram, we plot the best-fit linear relation ($\log(\dot{M}_{\rm acc} = 2.17 \cdot \log(M_\star) - 7.97$) obtained by Betti et al. (2023) when fitting the stellar objects ($M_\star \geqslant 0.075$ $M_\odot$) in their CASPAR sample, as well as the $1\,\sigma$ dispersion of their sample around the best fit. CASPAR is the largest database of accretion properties, containing measurements of 658 stars, 130 brown dwarfs, and 210 planetary mass companions. The black line on the $\dot{M}_{\rm acc}$ -$M_\star$ plots therefore represents a fit to the overall observed population and not any of the samples displayed within the plots. In the background, we plot the Lupus, Taurus, and Upper Sco samples of Manara et al. (2023), for which we do not find substructure information in the literature. We will refer to these sources as unknown-substructure, although for some high enough angular resolution observations could be available to exclude/confirm large cavities/gaps. In these plots, we plot

Table 4.7: Adopted values for the sample analyzed here

Name	Substructure	$M_{\rm disk}$ $[0.01\,M_\odot]$	ref.	$\log(\dot{M}_{\rm acc})$ $[M_\odot/{\rm yr}]$	$M_\star$ $[M_\odot]$
J16120668-3010270	Cavity,Spiral-Cavity-IR	0.25	SPA24	-9.541	0.70
AS209	Rings	3.60	BIZ23	-7.766	0.73
ATpyx	Spirals-IR	...	...	-8.436	1.20
CITau	Rings	2.30	BIZ23	-7.780	0.64
CSCha	Cavity	2.40	BIZ23	< -8.419	0.86
CWTau	Rings	0.76	MAR23	-7.918	0.95
DLTau	Rings	3.70	BIZ23	-7.494	0.73
DMTau	Rings-Cavity	1.60	BIZ23	-8.141	0.38
DZCha	Spirals-IR	0.07	BIZ23	< -9.952	0.50
DoAr33	Rings	0.60	BIZ23	-8.366	0.70
FTTau	Cavity	1.30	BIZ23	-7.872	0.30
GGTau	Cavity,Cavity-IR	0.11	MAR23	-8.104	0.62
GMAur	Rings-Cavity,Spirals-IR	3.80	BIZ23	-7.622	0.76
GOTau	Rings	1.00	BIZ23	-8.726	0.40
HLTau	Rings	13.00	BIZ23	-7.716	1.06
IMLup	Rings-Spirals,Rings-IR	4.40	BIZ23	-7.571	0.67
IPTau	Cavity,Cavity-IR	0.10	BIZ23	-8.568	0.65
LkCa15	Rings-Cavity,Rings-IR	2.70	BIZ23	< -8.879	0.88
PDS 66	NONE	1.20	RMW23	< -8.938	1.12
PDS 70	Cavity,Cavity-IR	1.20	BIZ23	< -10.176	0.85
ROX27	Rings	1.10	BIZ23	-7.740	0.68
RXJ1852.3-3700	Cavity,Rings-IR	...	...	< -9.167	0.81
RX_J1615	Spirals,Cavity-Rings-IR	...	...	< -10.004	0.83
SzCha	Cavity,Rings-IR	3.50	MAR23	< -8.886	1.27
TWHya	Rings,Rings-IR	1.70	BIZ23	-8.263	0.67
WSB60	Rings-Cavity	1.60	BIZ23	-8.730	0.13
WWCha	Rings,Spirals-IR	17.20	BIZ23	-7.593	1.38
WaOph6	Spirals	2.08	BIZ23	-7.872	0.68
v4046sgr	Rings-Cavity,Rings-IR	1.40	MCP18	< -9.914	0.82

Notes: The disk mass is computed from the dust-mass as $M_{\rm disk} = 100\,M_{\rm dust}$ Ref. refers to the reference from which the disk mass was adopted. References: BIZ23: Bae et al. (2023), MAR23,SPA24: Sierra et al. (2024)

the substructures observed at millimeter wavelengths if both millimeter and NIR wavelength observations are available, since this provides the largest coherent sample. Similar plots where NIR substructures are prioritized can be found in Appendix 4.C.

In figure 4.7, it can be seen that the ringed sources can be found at both high disk and stellar

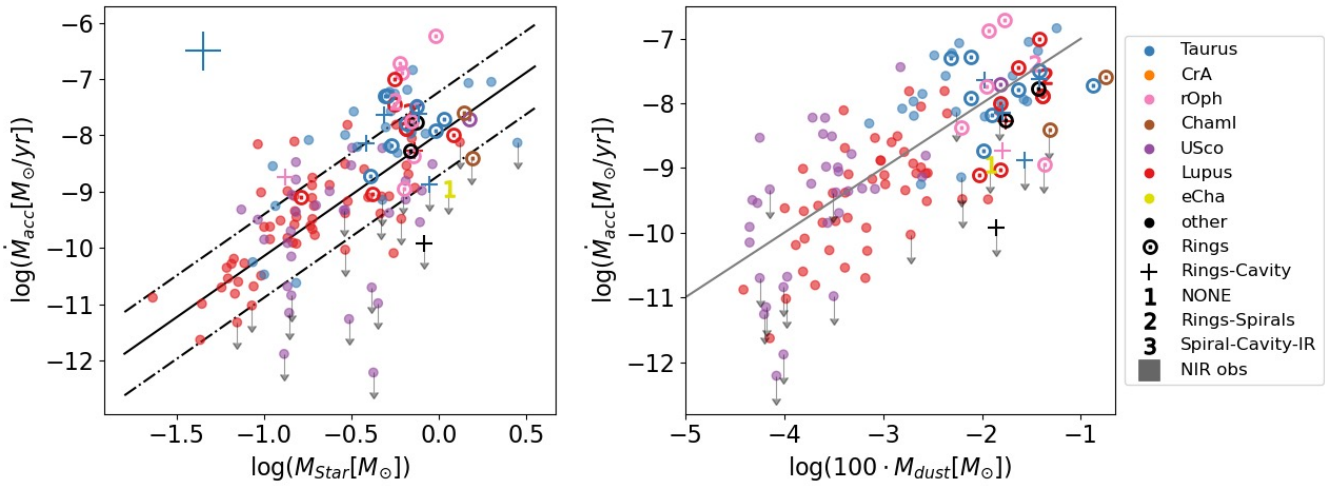

Figure 4.7: Left: $\dot{M}_{\rm acc}$ -$M_\star$ diagram containing the disks displaying cavities, spirals, and other less common types of substructures. The blue error-bars on the top left-hand side indicate the typical uncertainties in mass accretion rate and stellar mass. The solid black line indicates the best fit of Betti et al. (2023) to the stellar objects in their CASPAR sample; the dash-dotted lines indicate the 1σ dispersion of their sample around the best fit. Right: $\dot{M}_{\rm acc}$ -$M_{\rm disk}$ diagram containing the disks displaying cavities, spirals, and other less common types of substructures. The grey line indicates the $t_{\rm acc} = \dot{M}_{\rm acc}/M_{\rm disk} = 10^6$yr ratio.

mass. This is a consequence of observational bias. At the same time, massive disks are more likely to occur around more massive stars, causing an observational bias in terms of stellar mass (see Section 4.2.1). In the disk mass range where we have a sufficiently large sample ($\log(100 \cdot M_{\rm disk}) \gtrsim 2.35$ dex) of ringed sources, it can be seen that the ringed sources span a similar $\dot{M}_{\rm acc}$ range as the unknown-substructure sample. At the highest disk masses, some of the substructured sources appear to fall below the unknown-substructure sources, but since these display a similar scatter around the $\dot{M}_{\rm acc}/M_{\rm disk} = 10^6$ yr line, it seems likely that this is due to the lack of unknown-substructure sources in the plotted sample at these disk masses rather than due to any physical difference between both samples. Figure 4.7 also contains disks that have multiple rings and an inner cavity. Most sources within this category fall within the scatter of both the ringed and unknown-substructure targets. The only exception to this is V4046 Sgr, which is indicated with the black cross. v4046sgr is indicated as a dubious accretor, which means that the mass accretion rate we derived here is highly uncertain. Despite this, it is interesting to note that this source is an outlier compared to other dubious accretors at the same stellar/disk mass. V4046 Sgr is a very old ($\sim$18.5 Myr) circumbinary (Martinez-Brunner et al. 2022) disk and part of the much older β Pic moving group ($\sim$ 20 Myr (Miret-Roig et al. 2020)), which could potentially explain its low accretion rate. We also show PDS 66 (MP-MUS) in both diagrams, marked with the yellow 1. PDS 66 is notable because it does not show any significant substructures in millimeter wavelengths despite being resolved to scales of 4 au (Ribas et al. 2023). PDS

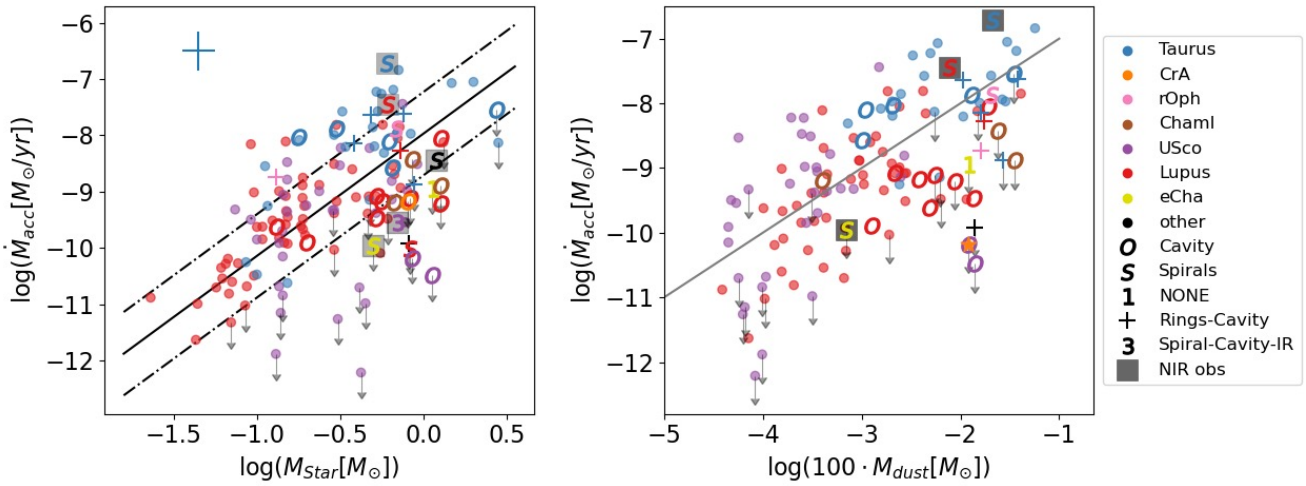

Figure 4.8: Left: $\dot{M}_{\rm acc}$ -$M_\star$ diagram containing the disks displaying cavities, spirals, and other less common types of substructures. The blue error-bars on the top left-hand side indicate the typical uncertainties in mass accretion rate and stellar mass. The solid black line indicates the best fit of Betti et al. (2023) to the stellar objects in their CASPAR sample; the dash-dotted lines indicate the 1σ dispersion of their sample around the best fit. Right: $\dot{M}_{\rm acc}$ -$M_{\rm disk}$ diagram containing the disks displaying cavities, spirals, and other less common types of substructures. The grey line indicates the $t_{\rm acc} = \dot{M}_{\rm acc}/M_{\rm disk} = 10^6$ yr ratio. The dot markers indicate sources for which we do not have any information about the presence of substructures.

66 is a dubious accretor and appears to fall at the lower edge of the scatter of both unknown-substructure and ringed sources. A potential explanation for the low position of PDS 66 in the diagrams could be its age, since it is part of the older ($\sim 5-10$ Myr (Pecaut & Mamajek 2016; Feiden 2016; David et al. 2019)) Upper Scorpius region. Figure 4.7 also displays two sources in which both rings and spirals are observed at millimeter wavelengths. These two sources are close to the $\dot{M}_{\rm acc}/M_{\rm disk} = 10^6$ yr line and therefore do not appear to be peculiar in terms of accretion properties.

In figure 4.8 it is clear that the sample of disks with inner cavities extends to lower disk masses than the sample of ringed sources. This is again likely an observational bias, since cavities are easier to detect than rings (see Section 4.2.1)(Parker et al. 2022). Three additional outliers with low accretion rates stand out: two with cavities and one with a cavity and rings. These sources are PDS 70, J16042165-2130284, and v4046sgr. Interestingly, PDS 70 is the only source in which protoplanets have been repeatedly observed directly (Keppler et al. 2018; Haffert et al. 2019). Similarly, for J16042165-2130284, Stadler et al. (2023) have kinematically detected a protoplanet candidate inside the cavity, making it a potential analog for PDS 70. Here, we need to point out two caveats. First, both are marked as dubious accretors, so the position of J16042165-2130284 may be coincidental due to the large uncertainties. For PDS 70 our accretion rate estimate agrees well within the uncertainty with the accretion rate that Thanathibodee et al.

(2020) obtained through detailed modeling of the Hα line profile, providing more confidence in our estimate. Secondly, both targets are members of the older ($\sim 5-10$ Myr (Pecaut & Mamajek 2016; Feiden 2016; David et al. 2019)) Upper Scorpius region. The older age of these targets with respect to the other sources with cavities and the Taurus and Lupus sample complicates the comparison, since the mass accretion rate is expected to decrease over time in both the viscous and evolutionary frameworks (e.g., Somigliana et al. 2023). In fact, such a decrease was observed by Betti et al. (2023). Comparison to the unknown-substructure Upper Scorpius sample in the figure is also not straightforward, since all other measurements are of lower disk/stellar mass targets and the sample of mass accretion rates in the Upper Scorpius is incomplete (Manara et al. 2020).

4.6.1 IR Spirals

Figure 4.8 also displays a number of sources observed at IR wavelengths. In figures 4.13 and 4.14, more sources with IR spirals can be seen. In total, our sample contains six sources in which spirals are observed at IR wavelengths. For one of these, AT Pyx, we do not have a disk mass available. Benisty et al. (2023) divides the spirals in their sample into different categories based on the appearance of the spiral arms. These categories are Doubelarm/symetric, Asymetric/Multiarm, Floculent, Environment, and Outer Companion. Here we discuss the categories of these sources in our sample and whether their relative accretion rates make sense with regard to our expectations.

One of the sources in our sample, GM Aur, was not classified by Benisty et al. (2023). Given the brightness of this disk and its substructure shape, Garufi et al. (2024) consider it likely that this disk was affected by late infall; therefore, we discuss it as falling into the Environment category, making it the largest subcategory, containing 3 targets. These 3 sources are GM Aur, WW Cha, and DR Tau. GM Aur falls only slightly below the $\dot{M}_{\rm acc}/M_{\rm disk} = 10^6$ yr line and at the lower edge of the Taurus sample in the $\dot{M}_{\rm acc}$ -$M_{\rm disk}$ diagram, while in the $\dot{M}_{\rm acc}$ -$M_{\rm disk}$ it falls near the upper 1 sigma dispersion of the sample. WW Cha appears as an outlier in the $\dot{M}_{\rm acc}$ -$M_{\rm disk}$ diagram due to its high disk mass; at the same time, its mass accretion rate appears low for its disk mass. In the $\dot{M}_{\rm acc}$ -$M_\star$ diagram, WW Cha falls on the best fit of Betti et al. (2023). However, for WW Cha, we need to note that its disk is circumbinary (Ginski et al. 2024), which may affect its measured accretion properties. Lastly, DR Tau appears to have a high relative mass accretion rate in terms of both stellar and disk mass. A larger sample is needed to make any statistically sound statements here. We therefore do not see a clear increase in mass accretion rates for disks with potential late infall, as expected (Kuffmeier et al. 2023).

Our sample also contains one target that was classified as being perturbed by an outer companion; this is Sz75. For Sz75 (GQ Lup), we indeed find that its mass accretion rate is on the higher side for its stellar and disk mass, as expected for disks perturbed by an external companion (Zagaria et al. 2022a).

The spirals in AT Pyx are classified by Benisty et al. (2023) as asymmetric/multi-arm, and its position in the $\dot{M}_{\rm acc}$ -$M_\star$ diagram appears to fall on the lower 1σ dispersion line; its relatively older age ($\sim$ 5 Myr (Ginski et al. 2022; Choudhury & Bhatt 2009)) could contribute to this. Another possible complication in its comparison could be the harsh UV radiation from nearby

stars to which it is exposed (Ginski et al. 2022), since Maucó et al. (2023) finds an apparent decrease in accretion timescale for sources exposed to a stronger FUV radiation field.

Finally, DZ Cha was classified as a symmetric/double-arm spiral. This type of spiral can be explained by a massive companion beyond the spiral arm (Dong et al. 2015) or a massive planet on an eccentric orbit in the inner disk (Calcino et al. 2020). In the case of an external perturber, an elevated mass accretion would be expected (Vorobyov et al. 2021; Borchert et al. 2022). In the case of an internal binary, the mass accretion rate could be highly variable (e.g., Lai & Muñoz 2023), which may be in better agreement with the relatively low accretion rate measured here.

Figure 4.8 contains 1 source labeled as Spiral-Cavity-IR; this is 2MASS-J16120668-3010270. This peculiar morphology was recently observed by Ginski et al. subm. to A&A, who hypothesize there to be a planet between 1 and 5 $M_{\rm jup}$ present in the cavity. The presence of such a planet could be a potential explanation for its low position in the $\dot{M}_{\rm acc}$ -$M_\star$ and $\dot{M}_{\rm acc}$ -$M_{\rm disk}$ diagrams. Its accretion rate is, however, still higher than that of PDS 70 and J16042165-2130284 despite the hypothesized massive planet and its lower disk mass.

4.6.2 Statistical comparison

At first sight the sources with resolved cavities appear skewed to lower mass accretion rates. To clarify this difference in distribution, we plot the cumulative distribution functions of the sample with cavities, that with rings and the unknown-substructure sample in both figures 4.9 respectively. Here the "unknown-substructure" population consists of the Lupus, Taurus, Chamaeleon I, Upper Scorpius, and Ophiuchus samples. We omitted hybrid substructure classifications from both the ring and cavity samples. On both figures we apply different cuts in disk mass to the unknown-substructure sample to ensure that we compare sources at a disk mass comparable to that of the observed substructure. The cut at $\log(M_{\rm disk}/M_\odot) > -2.35$ is chosen since this is only just below the lowest disk mass of the ringed sources, and that at $\log(M_{\rm disk}/M_\odot) > -3.1$ is chosen to span a comparable mass range to the disks with resolved cavities. In these plots we treated the dubious accretors the same way as the rest of the sample. Regardless of the used cut, it can be seen that the sample of sources with observed cavities differs the most from the unknown-substructure distribution, since it appears shifted to higher $t_{\rm acc}$ and therefore lower relative accretion rates. The distribution of the ringed sources, on the other hand, resembles that of the unknown-substructure sources well, particularly when only considering comparable disk masses. To test the hypothesis that disks with cavities have systematically lower accretion rates, regardless of the causative mechanism, we perform a set of Kolmogorov-Smirnov tests between the distributions shown in figure 4.9. The results of the KS test are summarized in table 4.8. We note that including a cut in stellar mass of $\log(M_{\rm disk}/M_\odot) > -0.5$ does not significantly change the results. Here it can be seen that we can only reject the null hypothesis of the KS-test at 95% confidence for the KS-test between the sample of sources with cavities and the unknown-substructure sources with a disk mass $\log(M_{\rm disk}/M_\odot) > -3.1$. There is, however, one caveat to this result: we compare the accretion timescale, which could be a function of age, of sources of different ages. Our sample contains two sources of the significantly older Upper Scorpius region ($\sim 5-10$ Myr (Pecaut & Mamajek 2016; Feiden 2016; David et al. 2019)). The Upper Scorpius region, meanwhile, is poorly represented at higher disk masses. We also only

Table 4.8: Results of the Kolmogorov-Smirnov test between the accretion timescale distributions of different subsamples.

Sample 1	Sample 2	Cuts	P - value
unknown-substructure	Cavities	$\log(M_{\rm disk}/M_\odot) > -2.35$	0.20
unknown-substructure	Rings	$\log(M_{\rm disk}/M_\odot) > -2.35$	0.88
unknown-substructure	Cavities	$\log(M_{\rm disk}/M_\odot) > -3.1$	0.007
unknown-substructure	Rings	$\log(M_{\rm disk}/M_\odot) > -3.1$	0.11
Rings	Cavities		0.17

have three sources with cavities in the ($\sim 1-2$ Myr (Galli et al. 2021)) Chameleon I region, while with 85 measurements, it is the largest sample in the unknown-substructure population. Similarly, the (L1688) Ophiuchus ($\sim 3-4$ Myr (Esplin & Luhman 2020)) sample contains 59 measurements, while our sample do not have any sources with resolved cavities in this region. The best represented regions in our sample of sources with cavities are Lupus ($\lesssim 3$ Myr (Luhman 2020)) with 8 sources and Taurus ($\sim 1-3$ Myr (Krolikowski et al. 2021)) with 5. With 71 and 31 measurements respectively, these regions are underrepresented in the combined sample. We therefore compare the samples within both of these regions. The results of this comparison can be found in appendix 4.D. The results in these cases are limited by low number statistics. Despite this, we still find a P-value of 0.01 for the KS-test between the unknown-substructure Lupus sources at $\log(M_{\rm disk}/M_\odot) > -3.1$ and the Lupus sources with resolved cavities. The accretion timescale distributions therefore indeed appear to be distinct. Another important caveat here is that our sample of disks with resolved cavities is poorly represented in the mass range between $\log(M_{\rm disk}/M_\odot) > -2.35$ and $\log(M_{disk}/M_\odot) > -3.1$, where the unknown-substructure Lupus sample is better represented. Indeed, increasing the disk mass cut to $\log(M_{\rm disk}/M_\odot) > -2.9$ (i.e., bigger than the lowest disk mass at which a cavity is resolved in Lupus) already results in a P-value of 0.08, so outside of the 95% confidence interval typically used. So while our results hint that the accretion timescales of sources with resolved cavities differ, ideally we need a larger sample with a better disk mass coverage as well a better understanding of the impact of the stellar mass and system ages to draw strong conclusions.

4.7 The influence of substructure properties on the accretion timescales.

Figure 4.10 shows several millimeter observations of disks within the rings substructure category. Here, it can be seen that this category comprises a varied number of different morphologies, including a varied number of gaps, different gap depths, sizes, and radial locations. It may therefore be an oversimplification to treat these sources as one simple category. Here we present a first look at the relationship between the detailed properties of the observed substructures and the accretion properties. In particular, we will look at the relationship between (proto)planetary system properties inferred from the observed substructures and the accretion properties of the

sources.

Ever since the first detection of the annular rings in HL Tau, a lot of theoretical research has been undertaken in attempts to explain such rings. One possibility that attracts a lot of attention is that the gaps in these ring-structured disks are carved by embedded protoplanets (Zhang et al. 2018; Rosotti et al. 2016; Dipierro et al. 2015). If such planets can indeed be confirmed by more direct methods of observation, then this would benefit our understanding of planet formation greatly, as it will provide us with the opportunity to study planet populations currently being formed. Doing so has, however, proven difficult. So far protoplanets have only been repeatedly directly detected in one system: PDS 70 (e.g., Keppler et al. 2018; Haffert et al. 2019; Benisty et al. 2021; Isella et al. 2019). On top of this, there are two direct detection candidates: AS209 (Bae et al. 2022) and AB Aur (Currie et al. 2022).

Several works have already tried to infer the properties of hypothetical embedded planets from the observed dust substructure morphology. Ideally, such studies are performed by comparing observations with numerical simulations of the dust and gas in the disk's response to the presence of embedded protoplanets. Such works have been performed by e.g., Dipierro et al. (2015); Zhang et al. (2018); Toci et al. (2020); Veronesi et al. (2020). The simulations used in such work come at large computational costs, which limit their applicability to large surveys (Andrews et al. 2018; Long et al. 2018). To this end, other works such as Lodato et al. (2019) and Wang et al. (2021) used an empirically determined scaling relation between the Hill radius R_H and the size of the dust gap carved by the planet in simulations. Since the hill radius is a function of the planet's mass, this can be expressed as

$$\Delta = CR_H = C\left(\frac{M_\mathrm{p}}{3M_\star}\right)^{1/3} R \tag{4.5}$$

where Δ is the dust gap size, R is the planet position, i.e., the gap minimum, and C is a disk property-dependent proportionality constant whose value ranges between 4 and 8 (Rosotti et al. 2016; Facchini et al. 2018; Fung & Chiang 2016; Pinilla et al. 2012). There are two main assumptions made in this picture. First and foremost, of course, the assumption that the gap is created by a planet. The second is that one gap is assumed to be created by one planet, whereas multiple planets could be responsible for a single gap (Zhu et al. 2011) or a single planet could create multiple gaps (Bae et al. 2017; Dong et al. 2017; Wafflard-Fernandez & Baruteau 2020).

The properties of hypothetical planets have not only been inferred from the disk morphology observed in gas tracers. This was done, for example, by Wang et al. (2021), who used the empirical relationship that derived from hydrodynamical simulations. This relationship is given by

$$M_\mathrm{p,gas} = 175 M_\oplus \left(\frac{M_\star}{M_\odot}\right)\left(\frac{\Delta_\mathrm{gap}}{0.5R_\mathrm{gap}}\right)^2\left(\frac{h_\mathrm{gap}}{0.05R_\mathrm{gap}}\right)^{3/2}\left(\frac{\alpha}{10^{-3}}\right)^{-1/4}, \tag{4.6}$$

where Δ_gap is the gas gap width, R_gap is the distance of the gap center to the central star, and h_gap is the gap depth. Dust gaps may be opened by planets of lower mass than gas gaps (e.g., Dipierro et al. 2016; Rosotti et al. 2016; Dipierro & Laibe 2017). This results in Wang et al. (2021) using

criteria dependent on the gap properties to decide whether to adopt the dust (using equation 4.5) and/or gas mass estimates.

Finally, Ruzza et al. (2024) proposed a convolutional neural network (named DBNets) trained on 2D hydrodynamical models to estimate the masses of hypothetical embedded planets. Using such an approach mitigates some of the assumptions used in the empirical formula and allows the presence of multiple gaps to be taken into account while limiting the computational cost.

This variety of methodology and dependence on assumed parameters leads to varied results for the obtained planet mass. This is well illustrated in figure 4.11, where the results obtained by Ruzza et al. (2024) with DBNets are compared with those of various other studies. It can be seen that while the inferred can differ over an order of magnitude between methods, different methods generally follow a similar trend in the estimated masses.

As discussed in section 4.1, embedded massive planets are expected to result in lower mass accretion rates at a given disk mass viscously evolving disks. Therefore, in order to test the hypothesis that embedded planets halt the accretion flow and contribute to the observed scatter in the $\dot{M}_{\rm acc}$ -$M_{\rm disk}$ relation, we compare the accretion timescales of disks in our sample with inferred planetary system properties. We use the properties of the inferred planets provided in the review of Bae et al. (2023). This comparison can be seen in Figure 4.12. If indeed massive planets are present and lower the accretion rate, then we would expect more massive planets to have a larger effect, or there to be a threshold mass below which planets are no longer effective at slowing the accretion flow. We therefore plot the $t_{\rm acc}$ as a function of the innermost planet's mass in case it is the innermost planet that dominates. We also plot $t_{\rm acc}$ as a function of the most massive planets and total planet mass, in case either dominates. Lastly, we plot $t_{\rm acc}$ as a function of the maximum planet mass over its orbital radius in case the distance to the central star also plays a role in the accretion properties. All of these plots appear rather similar; under our hypothesis, we expect to see an increase in $t_{\rm acc}$ for higher planet masses. No such correlation or jump in accretion can be seen. Instead, when ignoring PDS 70, for which the planets' masses are the result of direct detection, it appears that disks with high inferred planet masses have lower accretion timescales.

To test if there is a power law correlation between the accretion timescale and inferred planet masses, we compute between $\log(t_{\rm acc})$ and $\log(M_{\rm planet,max}/R_{\rm orb})$ or $\log(M_{\rm planet,max})$ for the planet properties. In this computation we excluded the planet masses of PDS 70 and AS 209 since they are the result of direct observation. Between $\log(t_{\rm acc})$ and $\log(M_{\rm planet,max}/R_{\rm orb})$ we find a correlation coefficient of -0.30 ± 0.65 (P-value = 0.11), and between $\log(t_{\rm acc})$ and $\log(M_{\rm planet,max})$ we find -0.28 ± 0.65 (P-Value = 0.13). The uncertainties here are obtained by bootstrapping the available data. We therefore find a weak statistically insignificant anticorrelation. However, the sample of Bae et al. (2023) is a compilation of results obtained with a variety of methods. To see if this homogeneity affects our results, we repeat this experiment with the smaller but homogeneously derived sample of Ruzza et al. (2024). The plots of this comparison can be seen in Appendix 4.E. Between $\log(t_{\rm acc})$ and $\log(M_{\rm planet,max}/R_{\rm orb})$ we find a Pearson correlation coefficient of -0.24 ± 0.63 (P-value = 0.18) whereas with $\log(M_{\rm planet,max})$ a correlation coefficient of -0.12 ± 0.58 (P-value = 0.51) is found. So once again we obtain weak, statistically insignificant anticorrelations.

Additional observations and a larger sample of homogeneously inferred planet masses are

needed to say if there is indeed an anticorrelation between the accretion timescale and the inferred planet mass or whether this is simply an effect of our limited sample.

4.8 Summary and conclusion

In this work, we present a pilot study of the accretion properties of CTTS. To achieve this, we presented the analysis of 11 newly obtained X-Shooter spectra as well as 18 spectra obtained from either the ESO archive or the previous works of Manara et al. (2014) and Manara et al. (2021). We obtained the stellar and accretion properties of this sample by modeling the UV excess in these spectra. We verified the obtained accretion luminosities by analyzing several emission lines in the spectra. The results were combined with literature data on stellar and accretion properties as well as disk masses. This allowed us to study the relative accretion properties of sources with distinct substructures. Our main conclusions are the following:

- By placing the sources with known substructures in the $\dot{M}_{\rm acc}$ -$M_{\rm disk}$ and $\dot{M}_{\rm acc}$ -$M_{\rm disk}$ we showed that the distributions of the sources with detected substructures occupy the same range as the unknown-substructure population, with some notable exceptions. These exceptions are PDS 70, the only TTS with confirmed embedded massive planets; 2MASSJ16042165-2130284, a source where massive planets have been inferred to exist within the cavity; and V4046 Sgr, a circumbinary disk in the much older β Pic moving group. All of these sources appear to have a lower mass accretion rate for their diskmass compared to the rest of the population. Here it is however, important to note that both PDS 70 and 2MASSJ16042165-2130284 are part of the older Upper Scorpius region, for which the currently available accretion rate surveys are highly incomplete and which is poorly sampled at the disk masses of PDS 70 and 2MASSJ16042165-2130284. A more complete sample in Upper Scorpius is therefore needed to conclude if both are significant outliers or whether this is an age evolution effect.

- We discussed the different types of spirals observed at NIR wavelengths. For the three sources (GM Aur, WW Cha, and DR Tau) where the spirals are caused by interactions with environmental material, we find no strong evidence of an elevated mass accretion rate. For the one source with evidence of being perturbed by an outer companion (Sz75), we do indeed find a relatively high accretion rate as expected. A larger sample is needed to verify whether environmental influences consistently affect the observed mass accretion rates.

- We compared the accretion timescale distributions of the disks with cavities, rings, and the unknown-substructure population. Here we found no statistically significant differences between the ringed and unknown-substructure populations. Indeed, the CDF of both appears to overlap well at the appropriate disk mass cut. This is not entirely unexpected, as it may be the case that the majority of unknown-substructure disks display similar substructures but have simply not yet been observed at sufficient angular resolution and sensitivity. We find that the distribution of the sources with cavities shows a statistically significant

difference from the unknown-substructure population. However, here we pointed out the caveats that both samples do not have the same contribution of targets at the same age and the resolved cavities are underrepresented at disk masses between $\log(M_{\rm disk}/M_{\odot}) > -2.35$ and $\log(M_{\rm disk}/M_{\odot}) > -3.1$. This prevents us from drawing a strong conclusion.

- We studied the relationship between the accretion timescales and the hypothetical planetary system properties inferred from the observed substructures. Here, one would expect either a correlation between the mass of the embedded planets and the accretion timescale or a jump to higher timescales at a given planetary mass (e.g., Mordasini et al. 2012; Benz et al. 2014). We do not find evidence for any such relationship between both quantities. Instead, we find a weak, statistically insignificant anti-correlation. A larger sample of preferably homogeneously studied disks is needed to confirm if this tenuous anti-correlation is a consequence of our small sample or indeed real. If indeed no correlation or an anti-correlation is found, this would imply that either these substructures are not formed by embedded planets, their mass estimates using current methods are systematically incorrect, or planet masses do not impact the accretion properties of protoplanetary disks as significantly or in a different way than predicted by the models presented in Manara et al. (2019). Different mechanisms, such as MHD-wind related zonal flows, may as of yet explain a lack of correlation or anti-correlation between the observed gap sizes (of which planet mass is essentially a proxy) and the accretion timescale. More theoretical work is needed to understand how embedded planets affect the accretion flow through MHD driven disks. Similarly, more theoretical works relating the morphology of substructures created by other mechanisms to the accretion flow through the disk could also be useful in understanding these substructures.

A more in-depth analysis, better taking into account the ages of each source, could strengthen the conclusions presented here. Future observations providing disk morphologies of additional sources at lower stellar and disk masses are needed to constrain the relationships between morphologies and accretion properties. These efforts should be supported by observations that allow the accretion properties to be constrained of both these resolved sources and the unknown-substructure population. Particularly in Upper Scorpius, additional observations are needed. Ideally, the samples of available disk morphologies and accretion properties should be analyzed uniformly.

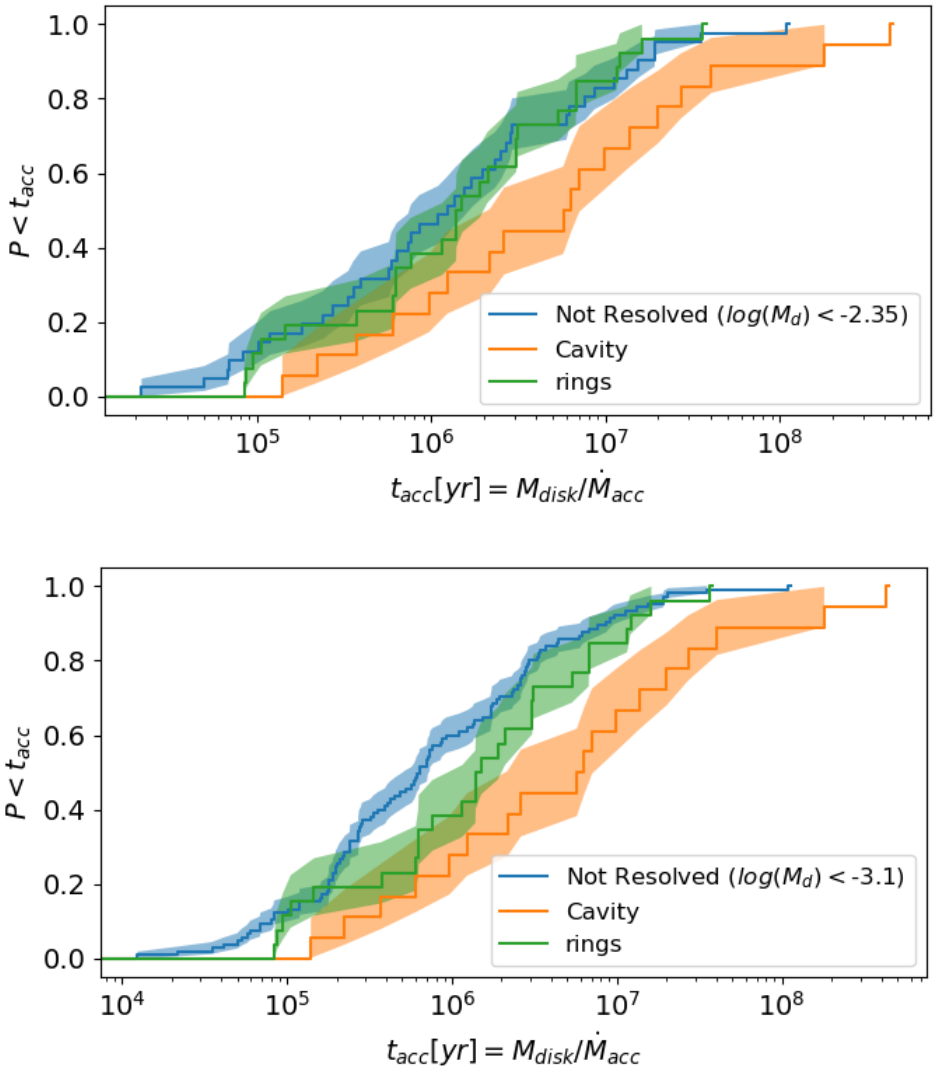

Figure 4.9: Cumulative distribution functions of the unknown-substructure targets compared to the targets observed to have cavities and rings. Top: The CDF obtained when excluding the unknown-substructure sources at $\log(M_{\rm disk}/M_\odot) > -2.35$ Bottom: The CDF obtained when excluding the unknown-substructure sources at $\log(M_{\rm disk}/M_\odot) > -3.1$ The shaded areas indicate the 1σ uncertainty interval on the curve of the corresponding colors.

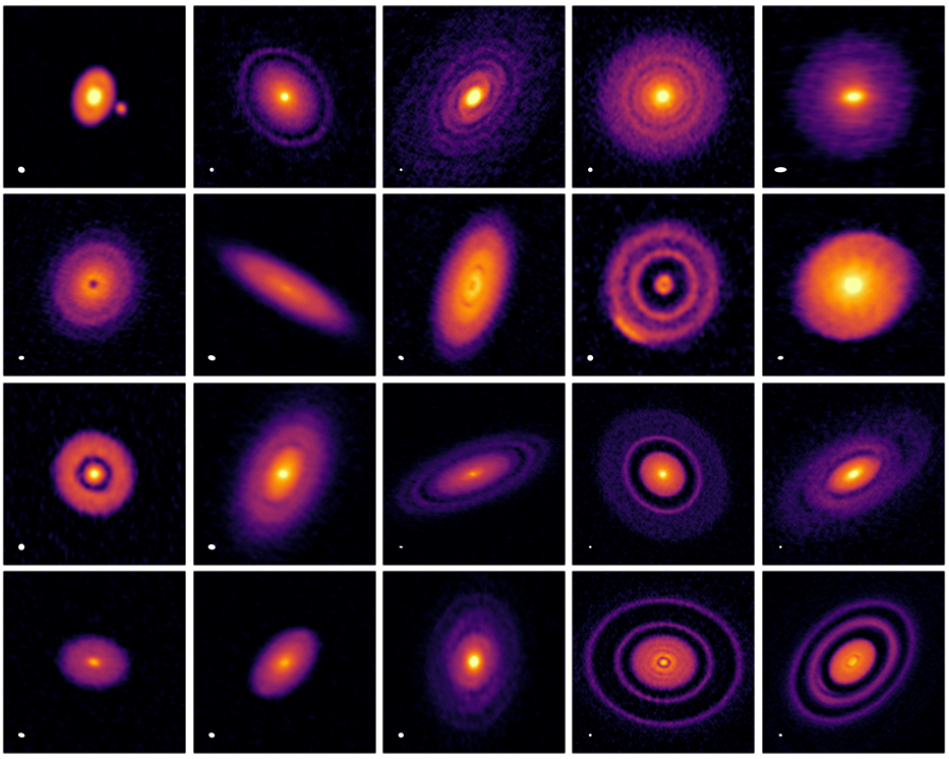

Figure 4.10: A number of disks observed to have annular substructures with the ALMA band 6 Cycle 4 Large Program Disk Substructures at High Angular Resolution Project (DSHARP). source image: `https://almascience.eso.org/almadata/lp/DSHARP/`, credit: (Andrews et al. 2018)

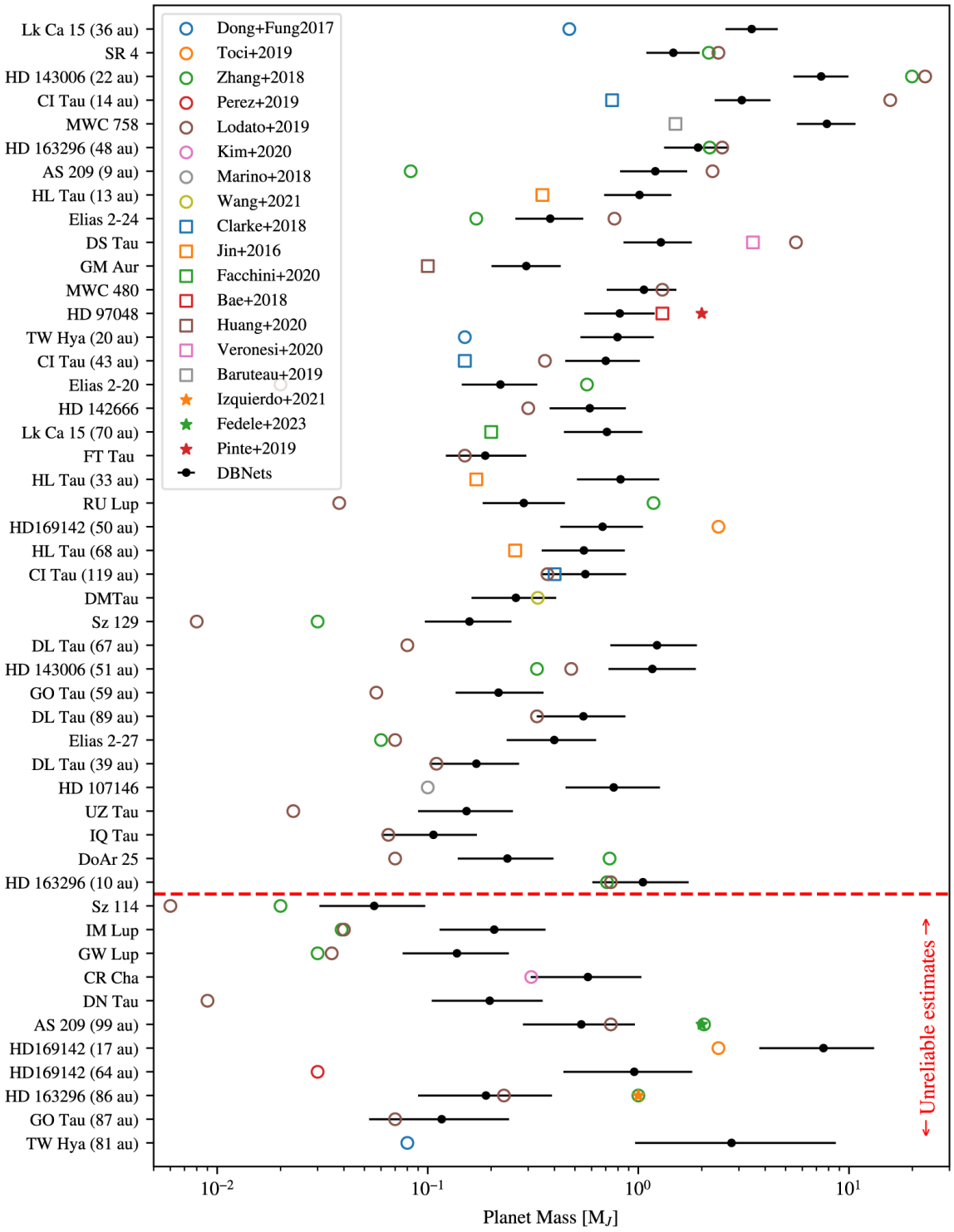

Figure 4.11: Comparison between the planet masses inferred by Ruzza et al. (2024) and various works in literature. Masses inferred from dust substructures are indicated with circles and squares, while stars indicate kinematic detections. The red dashed line indicates the uncertainty threshold of 0.25 dex. Source figure: Ruzza et al. (2024)

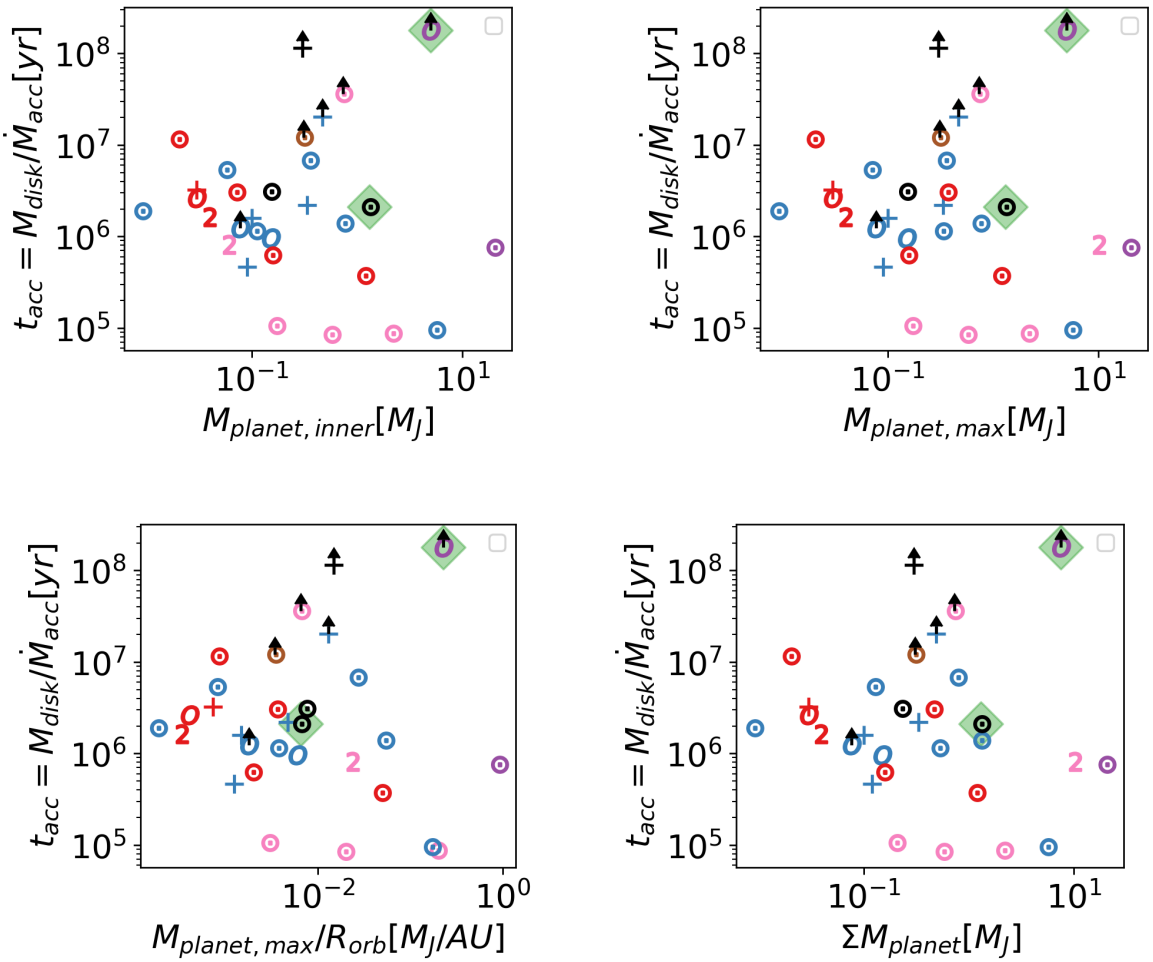

Figure 4.12: Inferred planet properties in the sample of Bae et al. (2023) vs. accretion timescale. Top left: Mass of the innermost planet vs. $t_{\rm acc}$. Top left: Mass of the innermost inferred planet vs. $t_{\rm acc}$ Top right: Mass of the most massive inferred planet vs. $t_{\rm acc}$. Bottom left: Mass of the most massive planet over its orbital radius vs. $t_{\rm acc}$. Bottom right: Total mass of all the inferred planets vs. $t_{\rm acc}$. The markers and colors have the same meaning as in figures 4.7 and 4.8. Planetary system properties obtained from direct observations are highlighted with the green diamonds. For AS 209, we plot the properties of the directly observed planet rather than the inferred system properties.

4.A Observations

Table 4.9: Signal to noise measured at different wavelengths in the spectra analyzed here.

name	416nm	448nm	490nm	701nm	750nm	801nm	1217.5nm	1600nm	2214nm
J16120668	10.79	6.02	9.65	17.37	19.65	85.27	138.18	18.72	282.52
AS209	7.19	6.37	7.45	21.37	18.95	84.20	190.76	18.53	282.78
ATpyx	8.54	8.98	8.58	24.07	22.93	55.73	107.24	35.56	353.99
CITau	13.25	6.53	11.60	24.21	21.78	84.39	135.17	20.56	277.86
CS-Cha	7.58	6.96	7.39	17.27	17.56	70.27	97.60	16.06	85.15
CWTau	9.31	8.18	8.89	26.65	25.19	124.17	153.58	36.23	382.22
DLTau	12.88	4.00	53.76	43.30	40.74	67.02	162.31	29.20	379.48
DMTau	33.20	3.16	28.44	9.88	16.53	23.21	35.48	17.31	44.18
DZCha	9.52	8.44	9.88	15.16	19.40	65.19	79.82	22.11	192.32
DoAr33	5.81	6.05	9.09	19.92	19.03	74.20	156.72	21.71	504.91
FTTau	32.39	2.12	41.72	18.07	29.82	38.50	122.39	39.98	168.19
GGTau	9.19	7.06	10.10	21.12	20.23	76.80	163.71	20.36	249.88
GMAur	17.43	5.75	12.08	25.84	23.14	79.01	33.64	14.58	19.16
GOTau	21.40	3.04	22.68	16.42	24.99	63.73	138.59	26.00	248.46
HLTau	12.47	13.07	15.16	34.41	32.54	61.74	192.03	36.45	508.77
IPTau	17.93	5.31	15.57	21.05	23.14	36.40	110.19	34.53	158.10
WSB60	0.46	0.92	1.37	8.75	19.09	22.32	27.72	2.40	7.55
LkCa15	7.31	6.74	7.22	20.74	18.67	75.90	87.59	16.76	24.78
PDS 66	5.93	6.42	6.73	19.58	17.71	81.28	NaN	NaN	NaN
PDS 70	7.05	6.81	7.30	20.26	18.50	75.05	68.53	17.56	137.62
ROX27	2.16	2.77	9.09	34.59	28.06	70.12	169.22	33.86	527.45
RXJ1852.3-3700	6.43	6.33	6.65	18.90	16.77	73.08	147.58	14.93	202.34
RX_J1615	6.17	5.96	6.66	18.20	17.90	50.17	52.08	13.69	44.74
Sz-Cha	7.90	9.72	8.66	15.30	22.49	40.94	25.17	9.76	8.18
Sz82	19.41	5.14	13.14	24.06	24.93	60.38	133.65	29.40	377.91
TWHya	22.40	3.78	15.83	20.40	23.56	58.78	136.28	25.42	190.07
WWcha	10.84	13.61	11.68	39.09	38.30	85.83	162.95	35.95	720.64
WaOph6	8.97	6.21	8.65	24.52	24.00	85.22	170.96	21.52	328.81
v4046sgr	7.02	6.88	7.32	29.57	21.26	140.04	NaN	NaN	NaN

Table 4.10: Observing log

Name	Date [UT]	Slit width [″ × 11″] UVB	VIS	NIR	Exp. Time[$N_{\rm exp}$ × s] UVB	VIS	Exp. time NIR [$N_{\rm exp}$ × $NDIT$ s]	Prop. ID.
J16120668-3010270	2023-05-18	1.0	0.4	0.4	4 × 200.0	4 × 160.0	4 × 3 × 80.0	111.255B.001
AS209	2011-05-01	0.5	0.4	0.4	10 × 60.0	10 × 60.0	2 × 5 × 60.0	087.C-0531(A)
ATpyx	2023-10-30	1.0	0.4	0.4	4 × 250.0	4 × 160.0	4 × 5 × 50.0	112.25BZ.001
CITau	2023-08-19	1.0	0.4	0.4	4 × 800.0	4 × 700.0	4 × 4 × 200.0	111.255B.001
CS-Cha	2010-01-19	1.0	0.4	0.4	1 × 55.0	1 × 60.0	1 × 1 × 60.0	084.C-1095(A)
CWTau	2023-08-31	1.0	0.4	0.4	4 × 225.0	4 × 135.0	4 × 3 × 80.0	111.255B.001
DLTau	2023-09-13	1.0	0.4	0.4	4 × 255.0	4 × 165.0	4 × 3 × 60.0	111.255B.001
DMTau	2012-11-13	0.5	0.4	0.4	1 × 300.0	1 × 10.0	1 × 2 × 150.0	090.C-0050(A)
DZCha	2018-06-11	1.0	0.4	0.4	4 × 330.0	4 × 240.0	4 × 10 × 8.0	0101.C-0527(A)
DoAr33	2023-06-26	1.0	0.4	0.4	4 × 900.0	4 × 850.0	4 × 3 × 300.0	111.255B.001
FTTau	2023-09-23	1.0	0.4	0.4	4 × 940.0	4 × 850.0	4 × 3 × 300.0	111.255B.001
GGTau	2023-09-16	1.0	0.4	0.4	4 × 315.0	4 × 225.0	4 × 2 × 175.0	111.255B.001
GMAur	2021-12-08	1.0	0.4	0.4	2 × 390.0	2 × 300.0	2 × 4 × 100.0	106.20Z8.006
GOTau	2023-09-26	1.0	0.4	0.4	4 × 940.0	4 × 850.0	4 × 3 × 300.0	111.255B.001 [3]
HLTau	2023-09-26	1.0	0.4	0.4	4 × 940.0	4 × 850.0	4 × 3 × 300.0	111.255B.001
IM Lup	2022-06-23	1.0	0.4	0.4	2 × 140.0	2 × 50.0	2 × 3 × 50.0	106.20Z8.008
IPTau	2024-03-01	1.0	0.4	0.4	2 × 380.0	2 × 290.0	2 × 4 × 100.0	112.25DB.001
LkCa15	2011-12-02	0.8	0.7	0.9	1 × 200.0	1 × 220.0	1 × 1 × 200.0	288.C-5013(A)
PDS 66	2010-05-04	0.5	0.4	0.4	4 × 150.0	8 × 60.0	12 × 1 × 100.0	085.C-0764(A)
PDS 70	2020-12-24	1.0	0.4	0.4	4 × 150.0	4 × 80.0	4 × 3 × 50.0	105.205R.001
ROX27	2023-04-21	1.0	0.4	0.4	4 × 940.0	4 × 850.0	4 × 3 × 300.0	111.255B.001
RXJ1852.3-3700	2022-07-02	1.0	0.4	0.4	2 × 150.0	2 × 60.0	2 × 4 × 50.0	106.20Z8.008
RX1615	2012-05-22	0.5	0.4	0.4	1 × 300.0	1 × 300.0	1 × 2 × 150.0	089.C-0840(A)
Sz-Cha	2010-01-19	1.0	0.4	0.4	1 × 140.0	1 × 150.0	1 × 10 × 15.0	084.C-1095(A)
TWHya	2021-04-02	0.5	0.4	0.4	2 × 140.0	2 × 50.0	2 × 3 × 40.0	106.20Z8.002
ISO-Oph196/WSB60	2010-07-29	1.0	0.9	0.9	1 × 750.0	1 × 750.0	1 × 3 × 250.0	085.C-0876(A)
WWcha	2023-04-14	1.0	0.4	0.4	4 × 800.0	4 × 700.0	4 × 4 × 200.0	111.255B.001
WaOph6	2011-05-04	0.5	0.4	0.4	10 × 60.0	10 × 60.0	2 × 5 × 60.0	087.C-0531(A)
v4046sgr	2010-05-04	0.5	0.4	0.4	4 × 150.0	8 × 60.0	12 × 1 × 100.0	085.C-0764(A)

[3] The typical spectral resolutions in the UVB arm are R≈ 9700 for a slit width of 0.5”, R≈6700 for a slit width of 0.8”, and R≈5400 for a slit width of 0.5”. Those in the VIS arm are R≈8900 for a slit width of 0.9”, R≈11400 for a slit width of 0.7”, and R≈18400 for a slit width of 0.4”. In the NIR arm they are R≈5600 for a slit width of 0.9” and R≈11600 for a slit width of 0.4”

4.B Results analysis

Table 4.11: Line accretion luminosities obtained for the Hα, Hβ,Hγ, Hδ, and Ca K lines.

Name	A_V [mag]	R_V	$\log(L_{\rm acc,H_\alpha})$ [$L_\odot$]	$\log(L_{acc,{\rm H}_\beta})$ [$L_\odot$]	$\log(L_{\rm acc,H_\gamma})$ [$L_\odot$]	$\log(L_{\rm acc,H_\delta})$ [$L_\odot$]	$\log(L_{\rm acc,CaK})$ [$L_\odot$]
2MASS-J16120668-3010270	0.1	3.1	-1.860 ± 0.248	-1.900 ± 0.226	-1.960 ± 0.213	-1.950 ± 0.253	-2.120 ± 0.255
AS209	1.4	3.1	-0.975 ± 0.225	-0.944 ± 0.222	-1.050 ± 0.233	-0.974 ± 0.273	-0.871 ± 0.224
ATpyx	1.5	3.1	-0.857 ± 0.222	-1.390 ± 0.233	-2.110 ± 0.359	-2.200 ± 0.702	-1.380 ± 0.244
CITau	1.8	3.1	-0.843 ± 0.222	-0.808 ± 0.200	-1.020 ± 0.200	-1.080 ± 0.235	-0.510 ± 0.215
CS-Cha	0.7	3.1	-0.938 ± 0.224	-1.420 ± 0.238	-1.450 ± 0.258	-1.390 ± 0.311	-1.360 ± 0.238
CWTau	2.3	5.0	-0.401 ± 0.212	-0.721 ± 0.200	-1.160 ± 0.221	-1.320 ± 0.310	-0.739 ± 0.220
DLTau	2.7	5.0	-0.604 ± 0.216	-0.345 ± 0.190	-0.464 ± 0.191	-0.536 ± 0.217	-0.090 ± 0.206
DMTau	1.0	3.1	-1.160 ± 0.229	-1.600 ± 0.218	-1.530 ± 0.206	-1.530 ± 0.239	-2.040 ± 0.252
DZCha	0.0	3.1	-2.950 ± 0.283	-2.640 ± 0.249	-2.670 ± 0.237	-2.610 ± 0.279	-2.210 ± 0.257
DoAr33	3.0	3.1	-1.730 ± 0.244	-1.360 ± 0.217	-1.300 ± 0.211	-1.190 ± 0.235	-1.500 ± 0.239
FTTau	2.2	3.1	-1.160 ± 0.229	-1.070 ± 0.205	-1.080 ± 0.198	-1.120 ± 0.229	-1.080 ± 0.228
GGTau	1.0	3.1	-0.995 ± 0.225	-0.767 ± 0.199	-0.914 ± 0.197	-0.997 ± 0.228	-0.604 ± 0.217
GMAur	1.0	3.1	-0.619 ± 0.217	-0.747 ± 0.200	-0.811 ± 0.201	-0.875 ± 0.235	-1.320 ± 0.235
GOTau	1.4	3.1	-1.900 ± 0.249	-1.840 ± 0.224	-1.700 ± 0.208	-1.720 ± 0.243	-2.180 ± 0.256
HLTau	3.4	5.0	-0.853 ± 0.222	-1.160 ± 0.214	-1.990 ± 0.532	-2.290 ± 1.540	-0.170 ± 0.208
IPTau	0.8	3.1	-2.080 ± 0.255	-1.680 ± 0.220	-1.510 ± 0.206	-1.470 ± 0.238	-1.690 ± 0.243
WSB60	2.9	3.1	-2.460 ± 0.266	-2.360 ± 0.241	-2.130 ± 0.228	-2.110 ± 0.279	-1.780 ± 0.252
LkCa15	1.0	3.1	-1.330 ± 0.234	-1.590 ± 0.274	-1.690 ± 0.306	-1.420 ± 0.278	-1.210 ± 0.233
PDS 66	0.2	3.1	-1.040 ± 0.226	-1.180 ± 0.219	-1.510 ± 0.295	-1.640 ± 0.382	-1.510 ± 0.250
PDS 70	0.5	3.1	-3.130 ± 0.289	-3.350 ± 0.485	-3.870 ± 1.920	-3.100 ± 0.550	-2.170 ± 0.259
ROX27	6.7	5.0	-0.890 ± 0.223	-0.827 ± 0.202	-0.867 ± 0.212	-0.899 ± 0.273	-0.892 ± 0.257
RXJ1852.3-3700	0.1	3.1	-1.440 ± 0.236	-1.940 ± 0.241	-2.160 ± 0.300	-2.200 ± 0.367	-1.870 ± 0.251
RX_J1615	0.3	3.1	-1.290 ± 0.233	-1.550 ± 0.230	-1.870 ± 0.243	-1.840 ± 0.323	-1.790 ± 0.248
Sz-Cha	1.5	3.1	-1.180 ± 0.230	$nan \pm nan$	$nan \pm nan$	$nan \pm nan$	-1.910 ± 0.373
Sz82	1.2	3.1	-0.907 ± 0.223	-0.879 ± 0.202	-0.765 ± 0.198	-0.737 ± 0.222	-1.320 ± 0.235
TWHya	0.3	3.1	-0.827 ± 0.221	-0.945 ± 0.203	-1.030 ± 0.198	-1.140 ± 0.230	-1.660 ± 0.243
WWcha	4.1	5.0	-0.212 ± 0.209	-0.443 ± 0.197	-0.991 ± 0.275	-1.210 ± 0.682	-0.122 ± 0.208
WaOph6	2.3	3.1	-1.400 ± 0.235	-1.230 ± 0.217	-1.230 ± 0.218	-1.200 ± 0.253	-1.290 ± 0.235
v4046sgr	0.1	3.1	-1.230 ± 0.231	-1.620 ± 0.224	-2.010 ± 0.257	-2.030 ± 0.331	-2.100 ± 0.258

Table 4.12: Line accretion luminosities obtained for the He 587 nm, He 667 nm lines.

Name	A_V [mag]	R_V	$\log(L_{\mathrm{acc,\,He\,587\,nm}})$ $[L_\odot]$	$\log(L_{\mathrm{acc,\,He\,667\,nm}})$ $[L_\odot]$	$\log(L_{\mathrm{acc,\,Pa}_\beta})$ $[L_\odot]$	$\log(L_{\mathrm{acc,\,Pa}_\gamma})$ $[L_\odot]$	$\log(L_{\mathrm{acc,\,Br}_\gamma})$ $[L_\odot]$
2MASS-J16120668-3010270	0.1	3.1	-1.990 ± 0.306	-2.550 ± 0.727	-2.260 ± 0.477	-2.270 ± 0.411	-2.660 ± 0.761
AS209	1.4	3.1	-0.792 ± 0.284	-2.020 ± 1.150	-1.150 ± 0.428	-1.000 ± 0.355	-1.750 ± 0.744
ATpyx	1.5	3.1	-1.620 ± 0.424	*nan* $\pm$ *nan*	-1.690 ± 0.455	-1.840 ± 0.410	*nan* $\pm$ *nan*
CITau	1.8	3.1	-0.805 ± 0.268	-0.742 ± 0.427	-0.985 ± 0.421	-1.020 ± 0.353	-0.939 ± 0.660
CS-Cha	0.7	3.1	-1.350 ± 0.302	*nan* $\pm$ *nan*	-1.470 ± 0.443	-1.450 ± 0.379	-2.120 ± 0.738
CWTau	2.3	5.0	-0.435 ± 0.260	-0.481 ± 0.418	-0.534 ± 0.404	-0.511 ± 0.335	-0.552 ± 0.639
DLTau	2.7	5.0	-0.108 ± 0.249	-0.007 ± 0.402	-0.509 ± 0.403	-0.334 ± 0.330	-0.351 ± 0.629
DMTau	1.0	3.1	-1.460 ± 0.305	-1.510 ± 0.503	-2.470 ± 0.516	-2.860 ± 0.536	-2.360 ± 0.789
DZCha	0.0	3.1	-2.490 ± 0.348	-4.300 ± 8.950	*nan* $\pm$ *nan*	-3.470 ± 0.641	*nan* $\pm$ *nan*
DoAr33	3.0	3.1	-1.170 ± 0.279	-1.510 ± 0.481	*nan* $\pm$ *nan*	-1.600 ± 0.385	*nan* $\pm$ *nan*
FTTau	2.2	3.1	-1.290 ± 0.272	-1.140 ± 0.440	-1.160 ± 0.428	-1.290 ± 0.359	-1.380 ± 0.684
GGTau	1.0	3.1	-0.695 ± 0.278	-1.110 ± 0.464	-0.985 ± 0.421	-0.891 ± 0.347	-0.986 ± 0.662
GMAur	1.0	3.1	-0.781 ± 0.269	-0.897 ± 0.431	-0.479 ± 0.402	-0.436 ± 0.334	-0.595 ± 0.641
GOTau	1.4	3.1	-1.860 ± 0.289	-1.670 ± 0.462	-3.050 ± 0.610	-2.520 ± 0.433	-4.330 ± 2.820
HLTau	3.4	5.0	-0.548 ± 0.264	-0.719 ± 0.438	-0.647 ± 0.408	-0.592 ± 0.338	-0.095 ± 0.616
IPTau	0.8	3.1	-1.580 ± 0.289	-1.760 ± 0.464	*nan* $\pm$ *nan*	-2.340 ± 0.425	-3.440 ± 0.916
WSB60	2.9	3.1	-2.470 ± 0.304	-2.380 ± 0.484	-2.020 ± 0.466	-2.760 ± 0.441	-2.020 ± 0.858
LkCa15	1.0	3.1	-1.140 ± 0.297	*nan* $\pm$ *nan*	-1.820 ± 0.478	-1.480 ± 0.392	-1.750 ± 0.713
PDS 66	0.2	3.1	-1.240 ± 0.299	*nan* $\pm$ *nan*	*nan* $\pm$ *nan*	*nan* $\pm$ *nan*	*nan* $\pm$ *nan*
PDS 70	0.5	3.1	-3.000 ± 0.639	*nan* $\pm$ *nan*	*nan* $\pm$ *nan*	*nan* $\pm$ *nan*	*nan* $\pm$ *nan*
ROX27	6.7	5.0	-0.574 ± 0.272	-0.420 ± 0.419	-0.801 ± 0.413	-0.782 ± 0.344	-0.802 ± 0.652
RXJ1852.3-3700	0.1	3.1	-2.100 ± 0.389	*nan* $\pm$ *nan*	-2.230 ± 0.477	-2.330 ± 0.425	-3.660 ± 1.160
RX_J1615	0.3	3.1	-1.810 ± 0.342	*nan* $\pm$ *nan*	-1.690 ± 0.453	-1.650 ± 0.386	*nan* $\pm$ *nan*
Sz-Cha	1.5	3.1	*nan* $\pm$ *nan*	*nan* $\pm$ *nan*	-1.330 ± 0.437	-1.470 ± 0.380	*nan* $\pm$ *nan*
Sz82	1.2	3.1	-0.824 ± 0.268	-0.855 ± 0.436	-1.710 ± 0.455	-1.580 ± 0.390	*nan* $\pm$ *nan*
TWHya	0.3	3.1	-0.882 ± 0.269	-0.979 ± 0.439	-1.110 ± 0.425	-1.250 ± 0.359	-1.360 ± 0.682
WWcha	4.1	5.0	-0.010 ± 0.255	-0.456 ± 0.425	-0.082 ± 0.388	0.013 ± 0.322	0.006 ± 0.612
WaOph6	2.3	3.1	-1.120 ± 0.283	-1.480 ± 0.495	-2.060 ± 0.500	-2.290 ± 0.516	*nan* $\pm$ *nan*
v4046sgr	0.1	3.1	-1.930 ± 0.344	*nan* $\pm$ *nan*	*nan* $\pm$ *nan*	*nan* $\pm$ *nan*	*nan* $\pm$ *nan*

4.C Additional $\dot{M}_{\rm acc}$ -$M_{\star}$ and $\dot{M}_{\rm acc}$ -$M_{\rm disk}$ diagrams

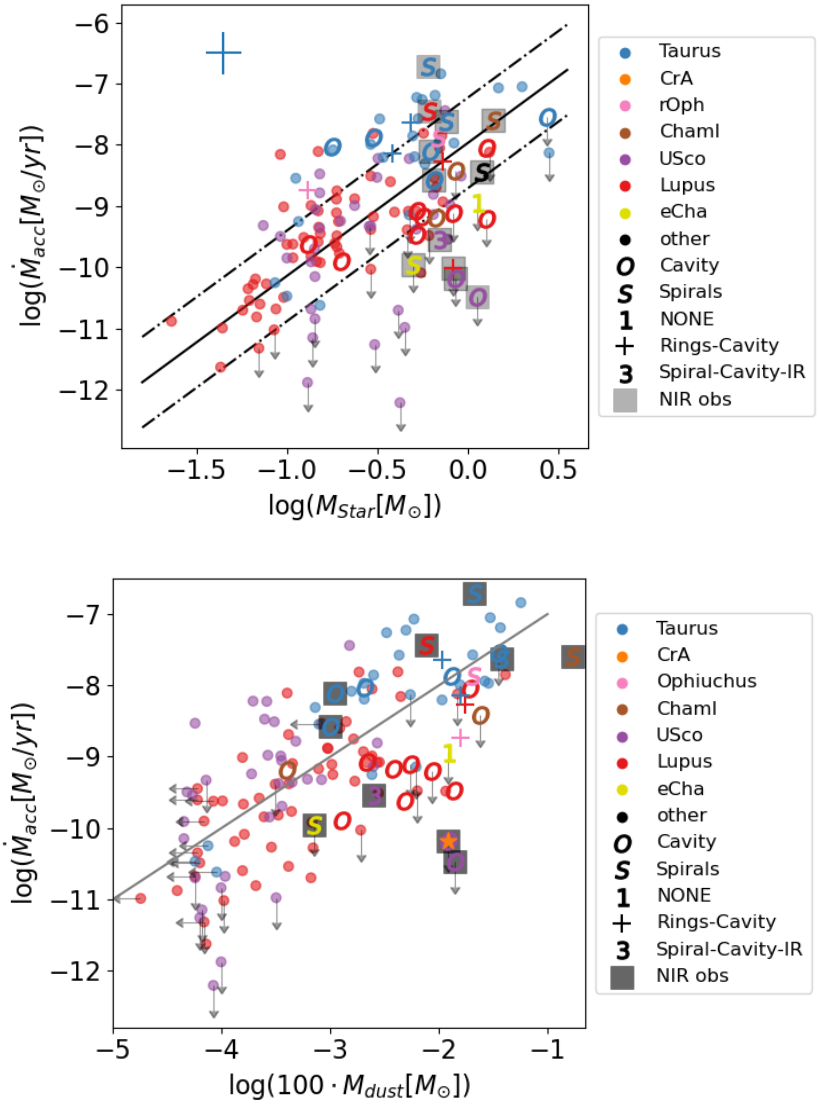

Figure 4.13: Top: $\dot{M}_{\rm acc}$ -$M_\star$ diagram containing the disks displaying cavities, spirals, and other less common types of substructures. The blue error-bars on the top left-hand side indicate the typical uncertainties in mass accretion rate and stellar mass. The solid black line indicates the best fit of Betti et al. (2023) to the stellar objects in their CASPAR sample; the dash-dotted lines indicate the 1σ dispersion of their sample around the best fit. Bottom: $\dot{M}_{\rm acc}$ -$M_\star$ diagram containing the disks displaying cavities, spirals, and other less common types of substructures. The grey line indicates the $t_{\rm acc} = \dot{M}_{\rm acc}/M_{\rm disk} = 10^6$yr ratio. The dots indicate sources for which we do not have any information about the presence of substructures. The substructures observed at IR wavelengths are prioritized over those observed at mm wavelengths in both figures.

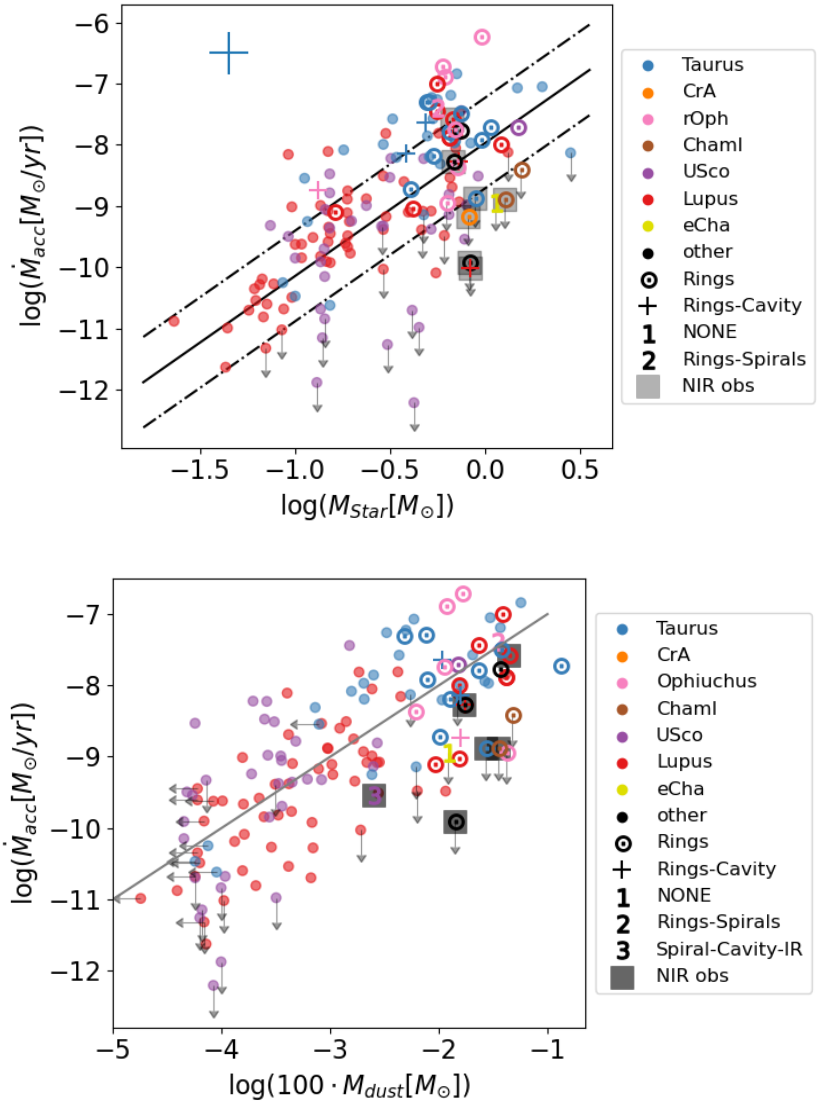

Figure 4.14: Top: $\dot{M}_{\rm acc}$ -$M_\star$ diagram containing the disks displaying Rings, Spirals, and other less common types of substructures. The blue error-bars on the top left-hand side indicate the typical uncertainties in mass accretion rate and stellar mass. The solid black line indicates the best fit of Betti et al. (2023) to the stellar objects in their CASPAR sample; the dash-dotted lines indicate the 1σ dispersion of their sample around the best fit. Bottom: $\dot{M}_{\rm acc}$ -$M_\star$ diagram containing the disks displaying Rings, Spirals, and other less common types of substructures. The grey line indicates the $t_{\rm acc} = \dot{M}_{\rm acc}/M_{\rm disk} = 10^6$ yr ratio. The dots indicate sources for which we do not have any information about the presence of substructures. The substructures observed at IR wavelengths are prioritised over those observed at mm wavelengths in both figures.

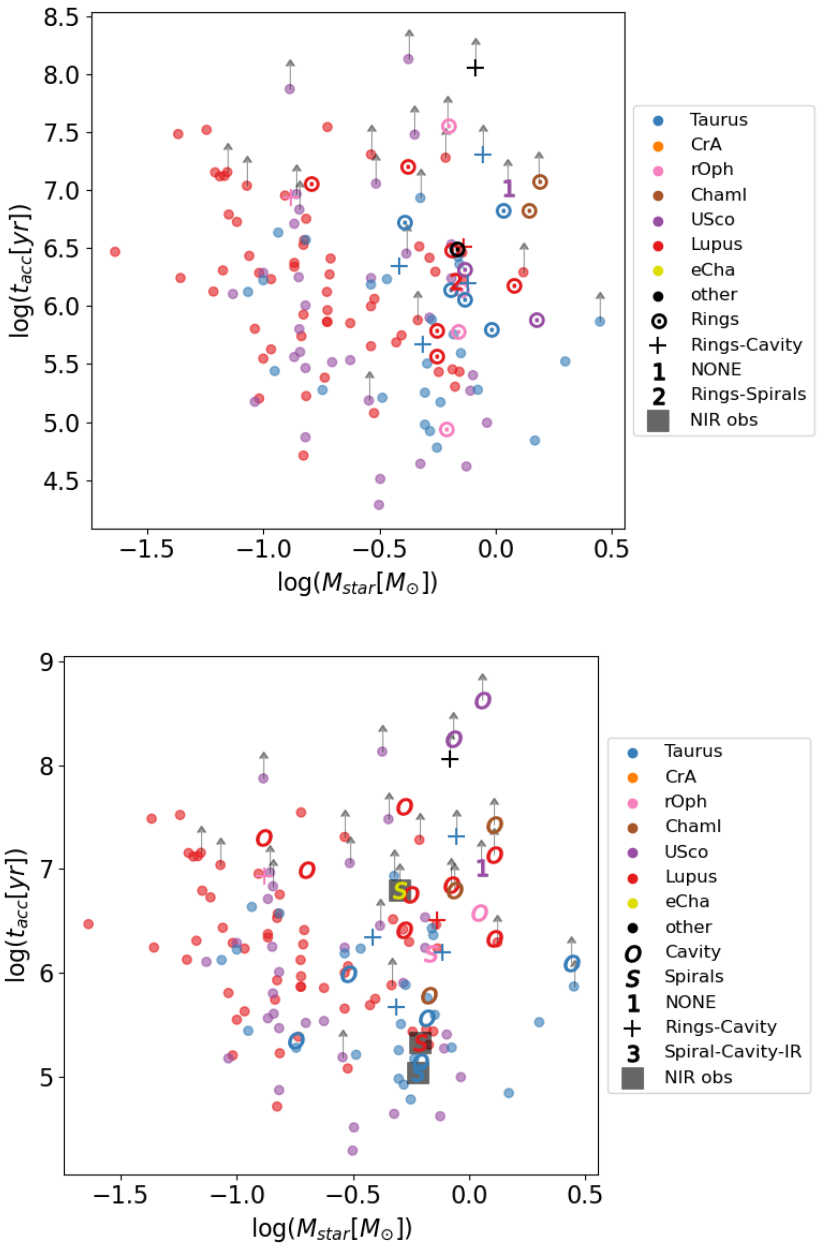

Figure 4.15: Top: $t_{\rm acc}$ as a function of $M_\star$ diagram containing the disks displaying rings, spirals, and other less common types of substructures. Bottom: $t_{\rm acc}$ as a function of $M_\star$ diagram containing the disks displaying rings, spirals, and other less common types of substructures. The dots indicate sources for which we do not have any information about the presence of substructures. The substructures observed at mm wavelengths are prioritized over those observed at IR wavelengths in both figures.

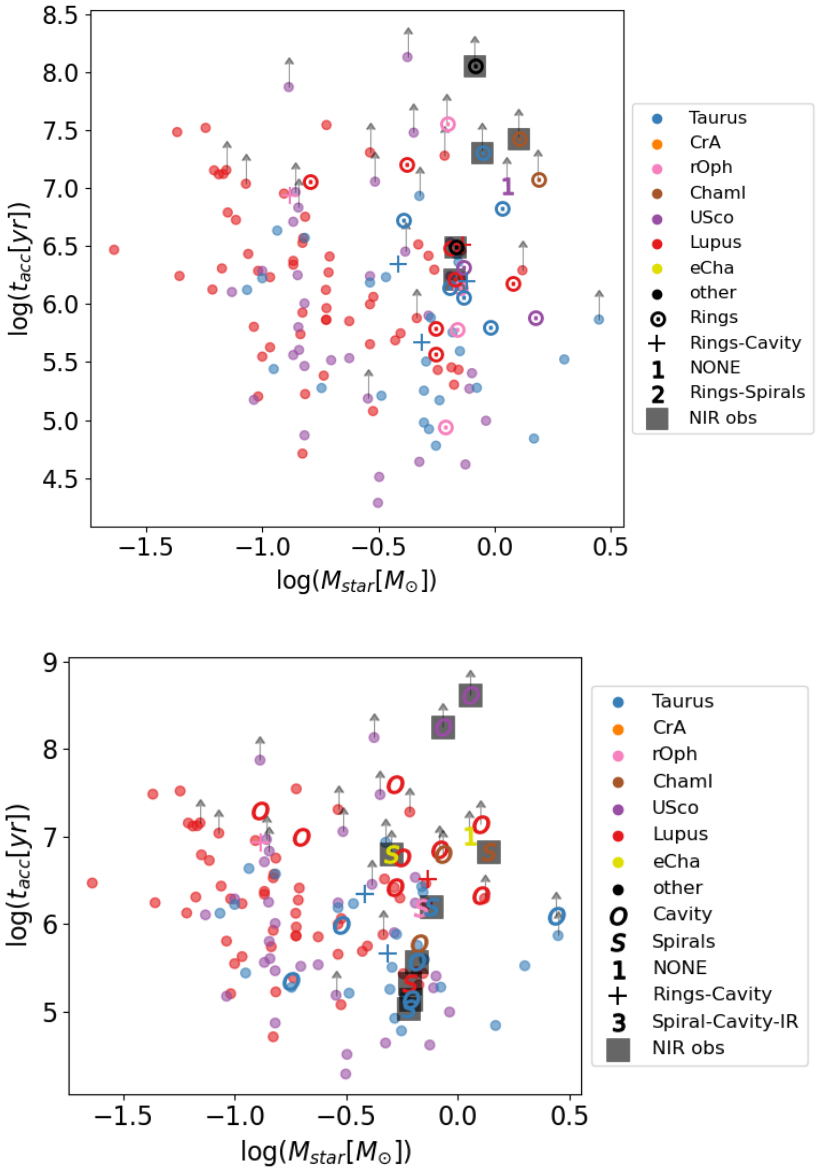

Figure 4.16: Top: $t_{\rm acc}$ as a function of $M_\star$ diagram containing the disks displaying rings, spirals, and other less common types of substructures. Bottom: $t_{\rm acc}$ as a function of $M_\star$ diagram containing the disks displaying rings, spirals, and other less common types of substructures. The dots indicate sources for which we do not have any information about the presence of substructures. The substructures observed at IR wavelengths are prioritized over those observed at mm wavelengths in both figures.

4.D Statistical comparison of individual regions

Table 4.13: Results of the KS-tests obtained for the samples in Lupus and Taurus

	Sample 1	Sample 2	Cut	P - value
Lupus	unknown-substructure	Cavities	$\log(M_{\rm disk}/M_{\odot}) > -2.35$	0.71
	unknown-substructure	Rings	$\log(M_{\rm disk}/M_{\odot}) > -2.35$	0.25
	unknown-substructure	Cavities	$\log(M_{\rm disk}/M_{\odot}) > -3.1$	0.01
	unknown-substructure	Rings	$\log(M_{\rm disk}/M_{\odot}) > -3.1$	0.73
	unknown-substructure	Cavities	$\log(M_{\rm disk}/M_{\odot}) > -2.9$	0.08
	Rings	Cavities		0.31
Taurus	unknown-substructure	Cavities	$\log(M_{\rm disk}/M_{\odot}) > -2.35$	0.46
	unknown-substructure	Rings	$\log(M_{\rm disk}/M_{\odot}) > -2.35$	0.97
	unknown-substructure	Cavities	$\log(M_{\rm disk}/M_{\odot}) > -3.1$	0.47
	unknown-substructure	Rings	$\log(M_{\rm disk}/M_{\odot}) > -3.1$	0.68
	Rings	Cavities		0.31

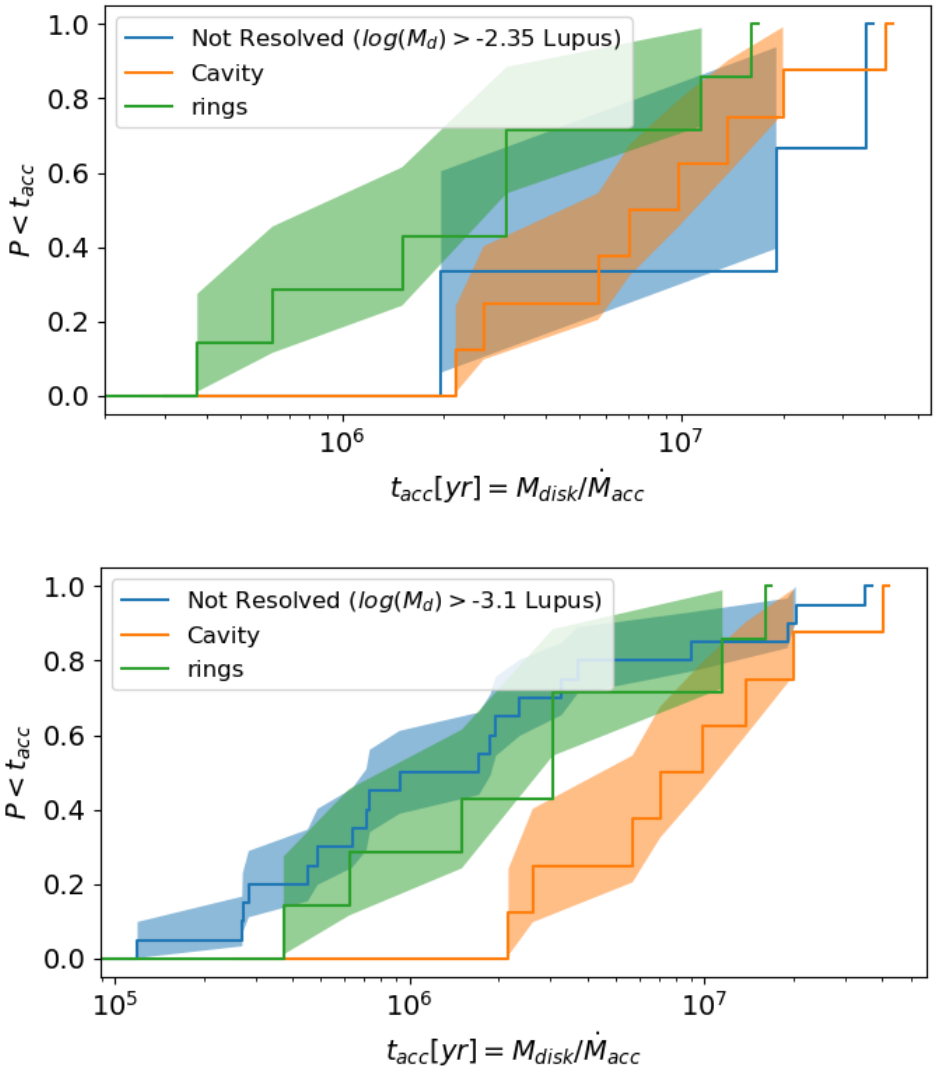

Figure 4.17: Cumulative distribution functions of the unknown-substructure targets compared to the targets observed to have cavities and rings. Top: The CDF obtained for the Lupus samples when excluding the unknown-substructure sources at $\log(M_{\rm disk}/M_{\odot}) > -2.35$. Bottom: The CDF obtained for the Lupus when excluding the unknown-substructure sources at $\log(M_{\rm disk}/M_{\odot}) > -3.1$ The shaded areas indicate the 1σ uncertainty interval on the curve of the corresponding colors.

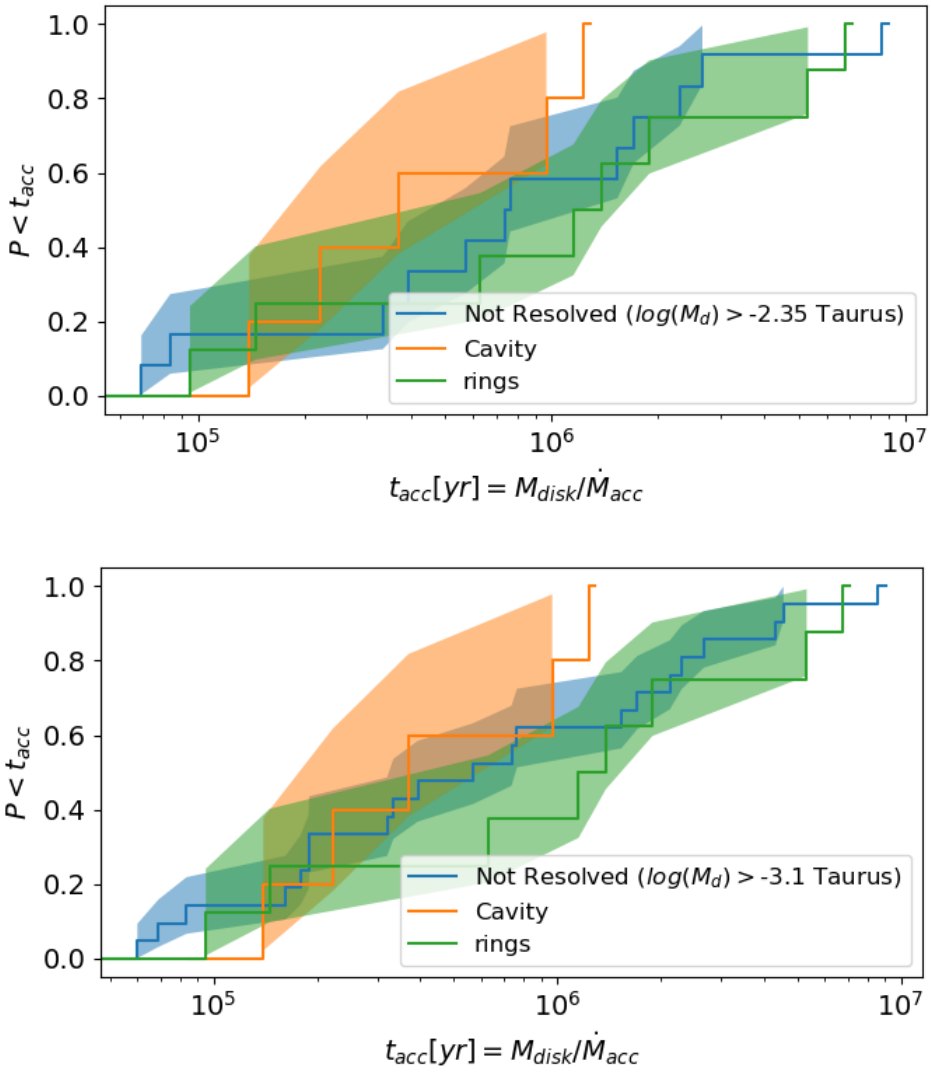

Figure 4.18: Cumulative distribution functions of the unknown-substructure targets compared to the targets observed to have cavities and rings. Top: The CDF obtained for the Taurus samples when excluding the unknown-substructure sources at $\log(M_{\rm disk}/M_{\odot}) > -2.35$. Bottom: The CDF obtained for the Taurus when excluding the unknown-substructure sources at $\log(M_{\rm disk}/M_{\odot}) > -3.1$ The shaded areas indicate the 1σ uncertainty interval on the curve of the corresponding colors.

4.E Hypothetical embedded planet mass v.s. accretion timescale

4.E Hypothetical embedded planet mass v.s. accretion timescale

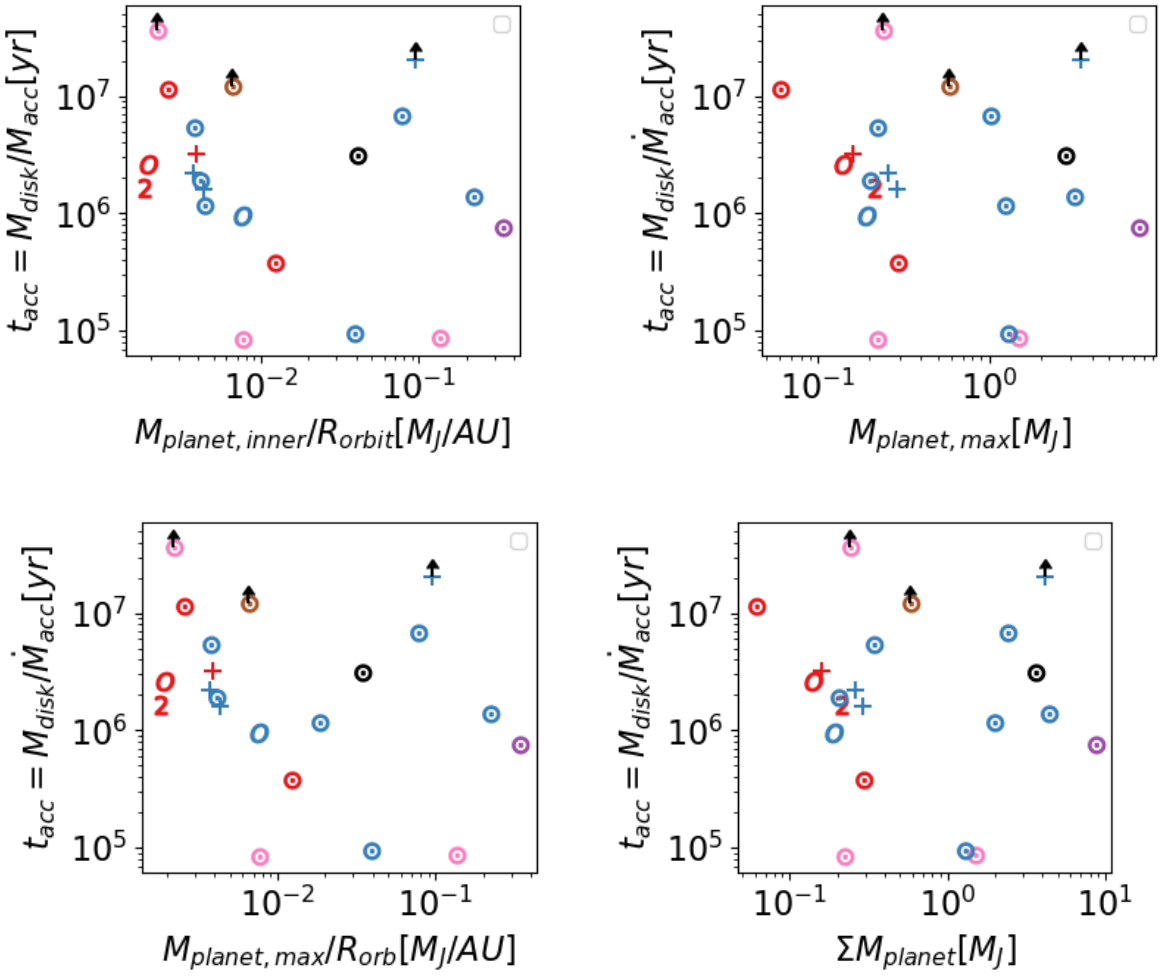

Figure 4.19: Inferred planet properties in the sample of Ruzza et al. (2024) vs. accretion timescale. Top left: Mass of the inner-most planet vs. $t_{\rm acc}$. Top left: Mass of the inner-most inferred planet vs. t_{acc} Top right: Mass of the most massive inferred planet vs. $t_{\rm acc}$. Bottom left: Mass of the most massive planet over its orbital radius vs. t_{acc}. Bottom right: Total mass of all the inferred planets vs. $t_{\rm acc}$. The markers and colors have the same meaning as in figures 4.7 and 4.8. For AS 209, we plot the properties of the directly observed planet rather than the inferred system properties.

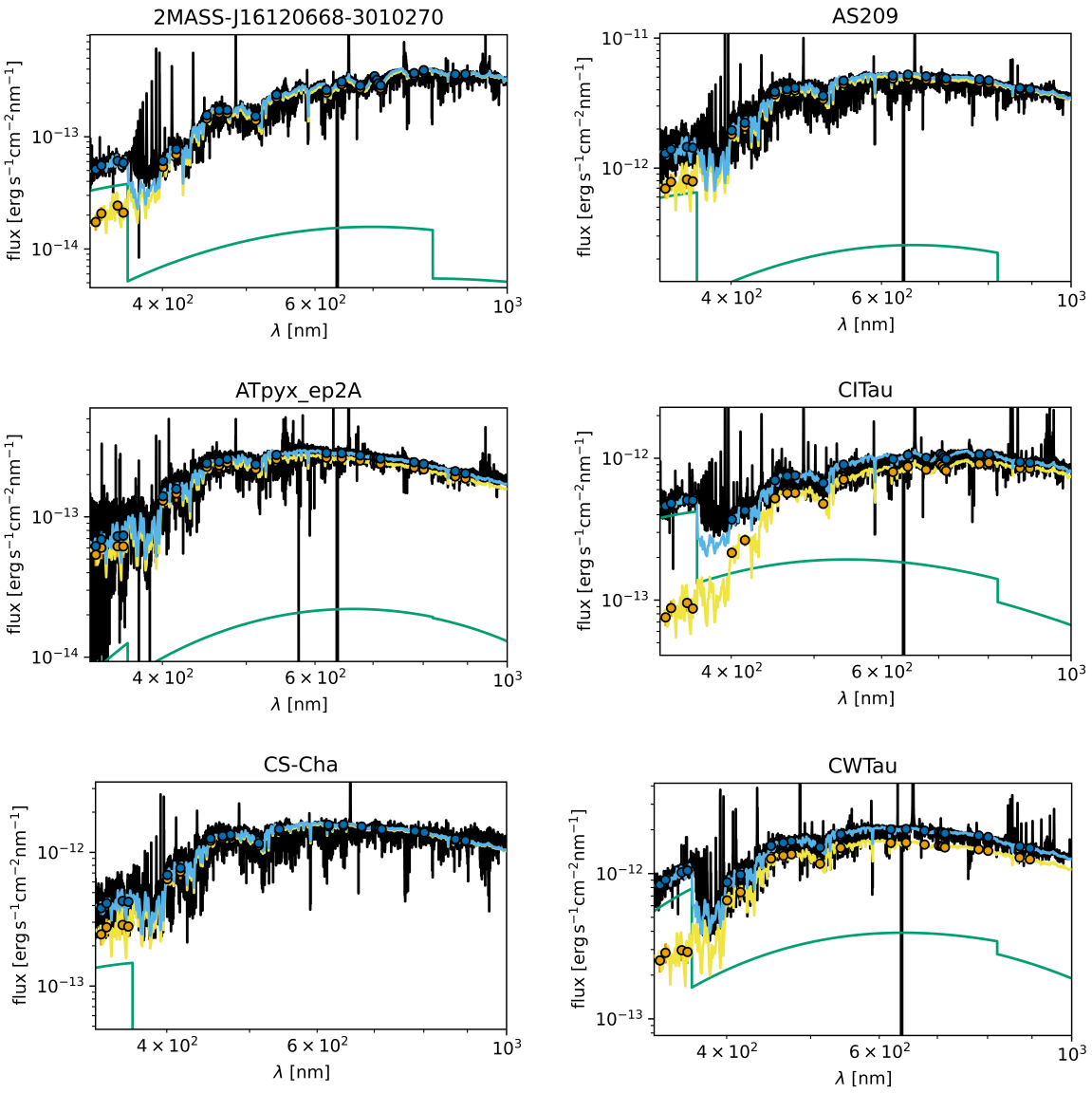

Figure 4.20: Best-fit of spectra analyzed in this work. The extinction-corrected observed spectrum is shown in black. The continuum excess emission of the slab model is shown in green. The adopted Class III template is shown in yellow. The best-fit is shown in blue. The points mark the wavelength ranges used in the best-fit determination.

4.F Accretion rate determination

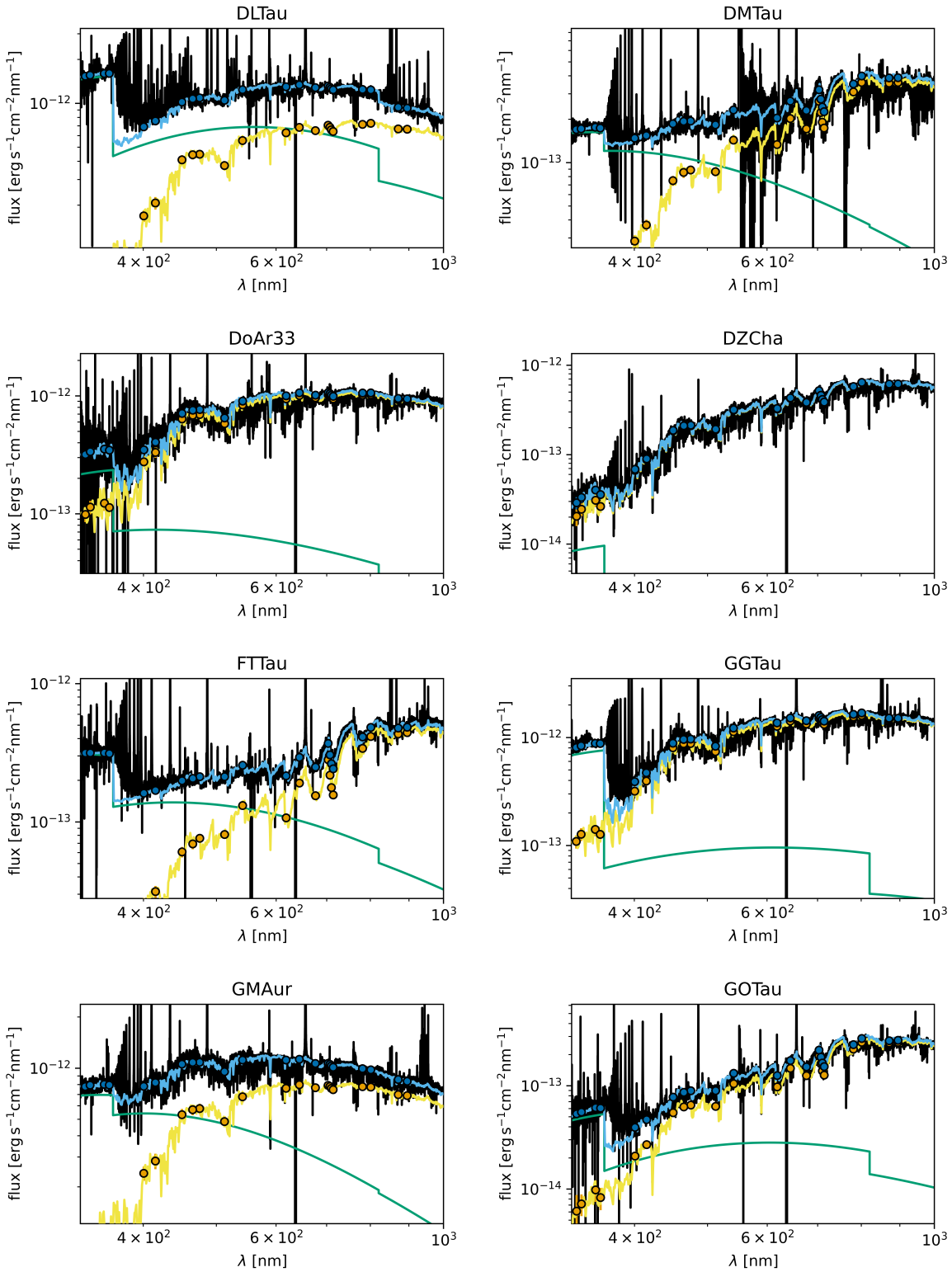

Figure 4.21: Best-fit of spectra analyzed in this work. Same as Fig. 4.20

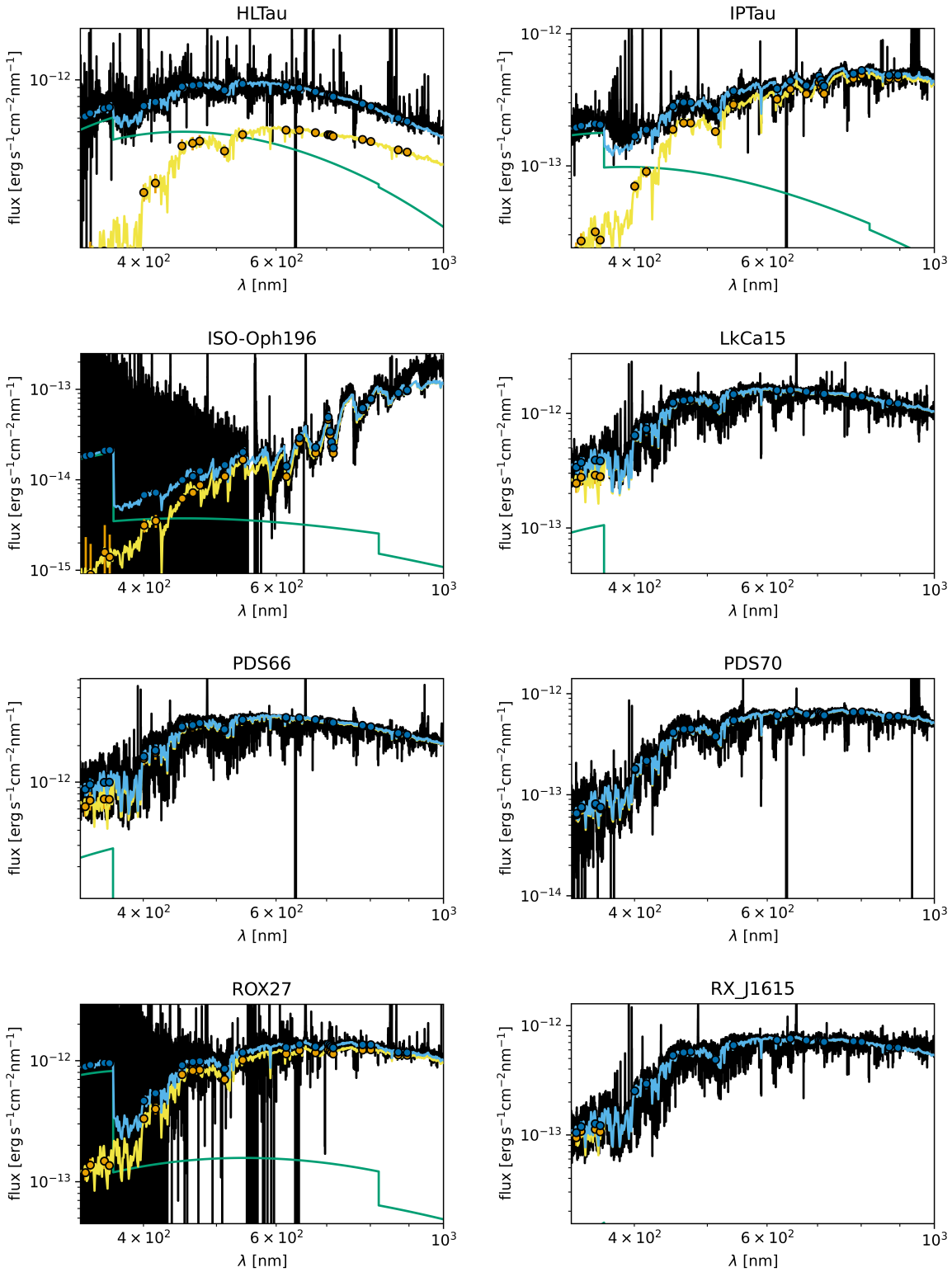

Figure 4.22: Best-fit of spectra analyzed in this work. Same as Fig. 4.20

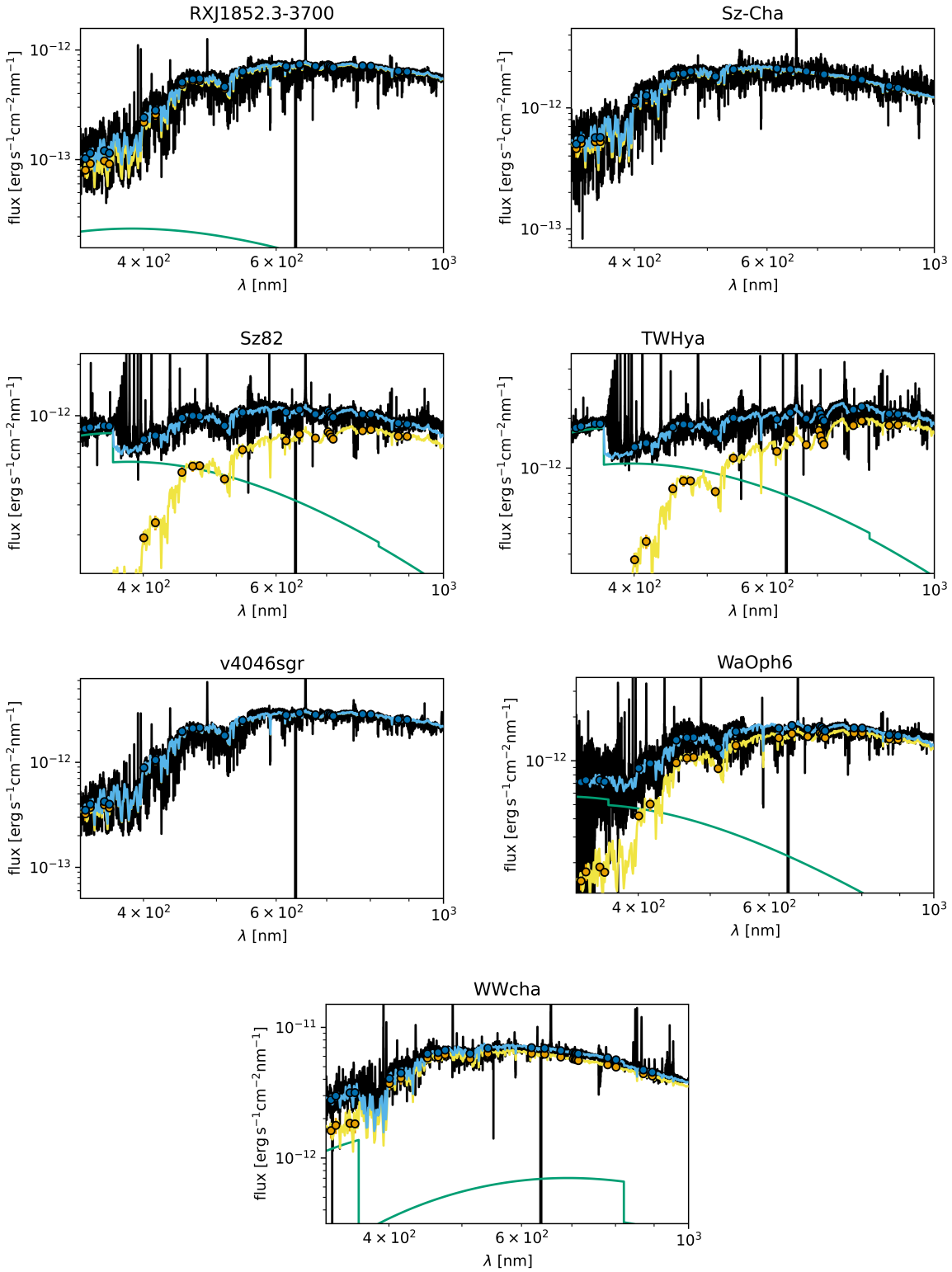

Figure 4.23: Best-fit of spectra analyzed in this work. Same as Fig. 4.20

4.F Accretion rate determination

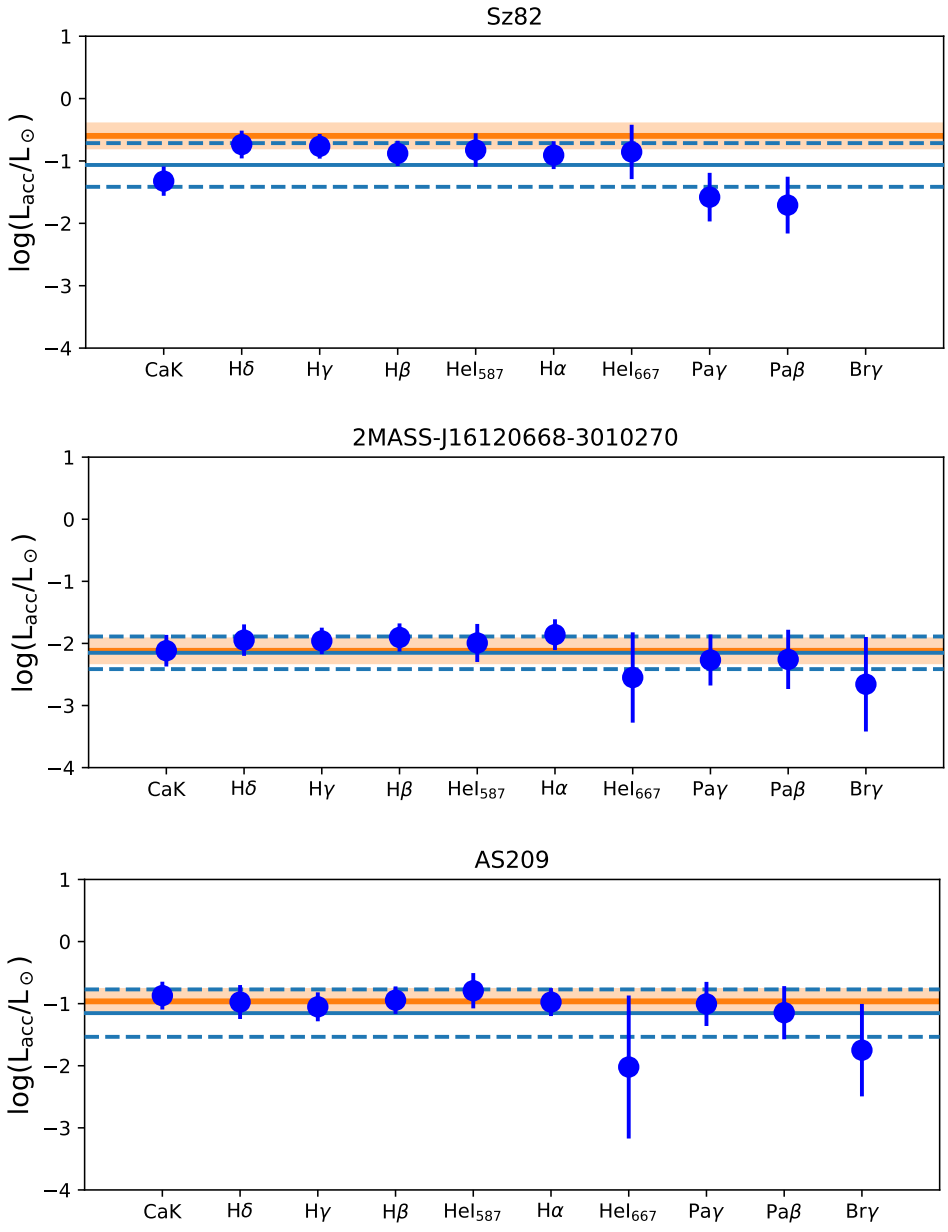

Figure 4.24: Accretion luminosities obtained from the line luminosities of different emission lines (blue dots). The solid blue line indicated the mean accretion luminosity obtained from the emission lines, and the dashed blue line the corresponding standard deviation. The orange solid line indicates the accretion luminosity obtained from the slab modeling, and the orange shaded area indicates the uncertainty therein.

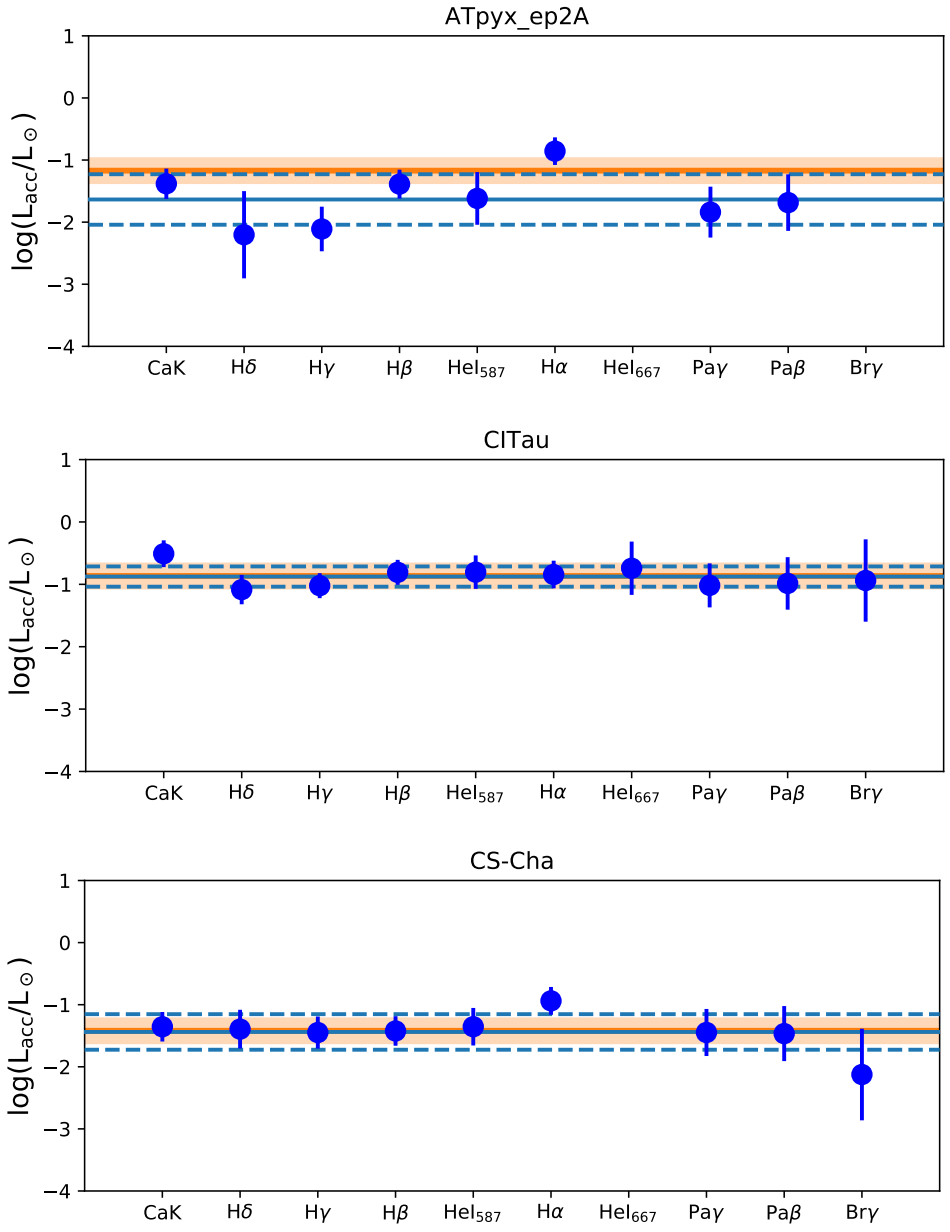

Figure 4.25: Same as figure 4.24.

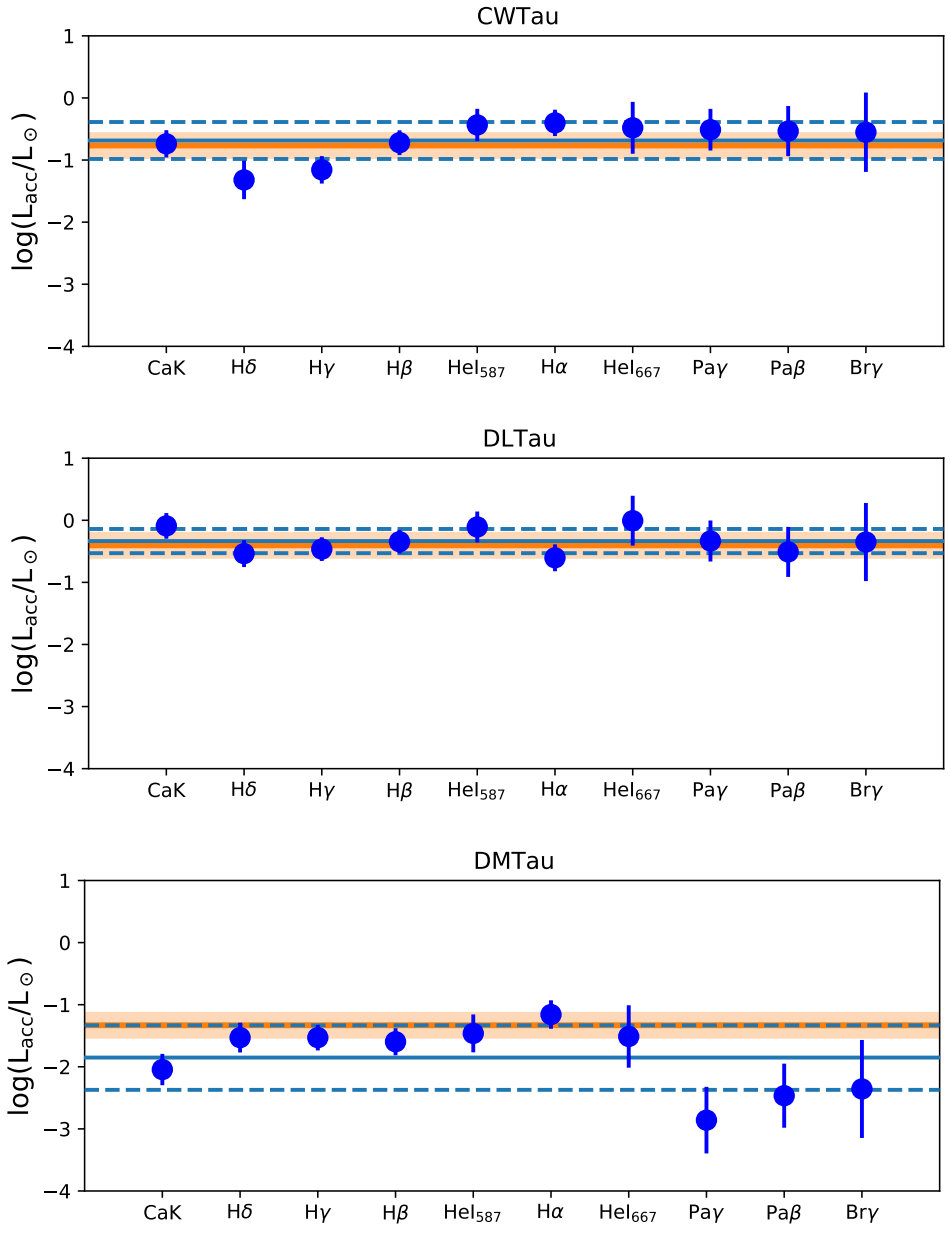

Figure 4.26: Same as figure 4.24.

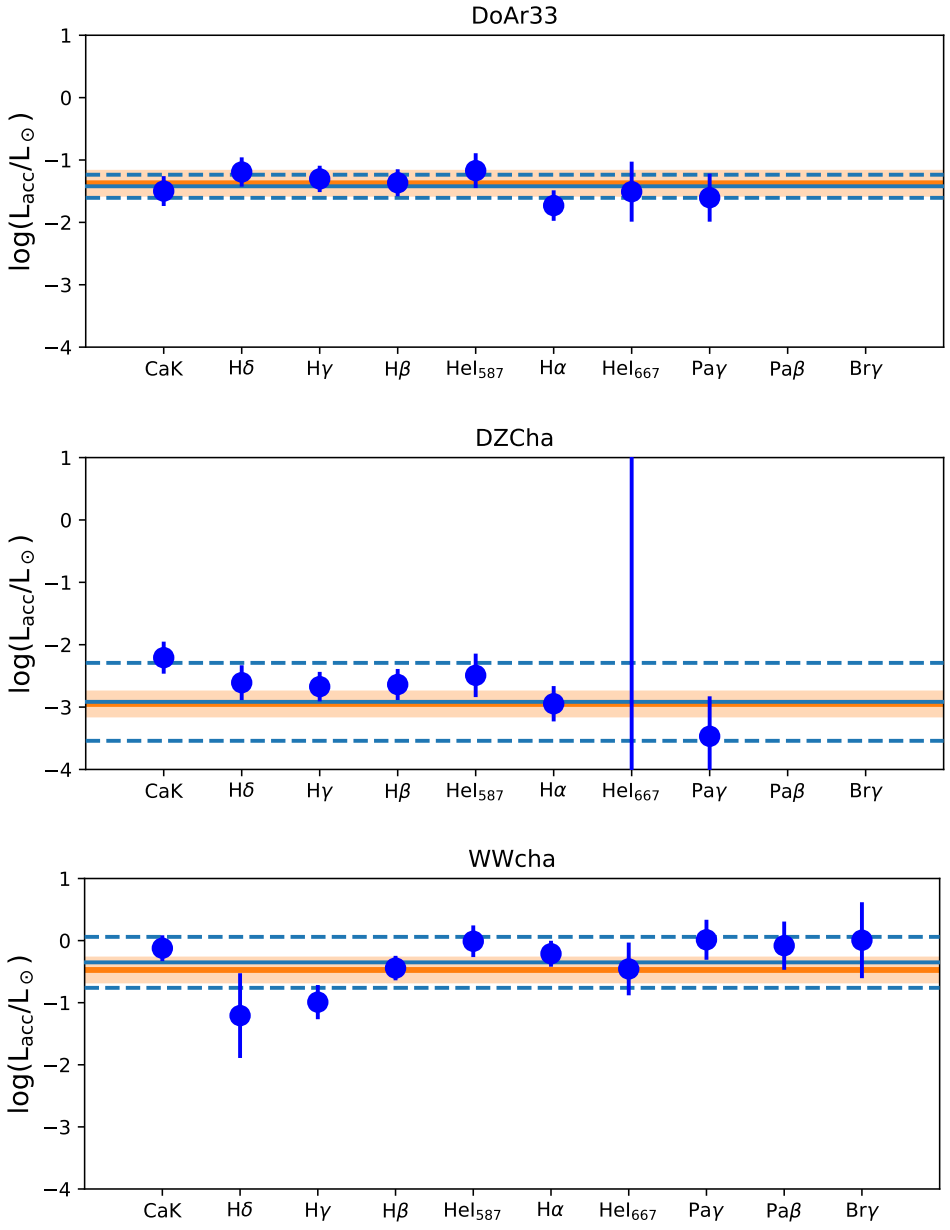

Figure 4.27: Same as figure 4.24.

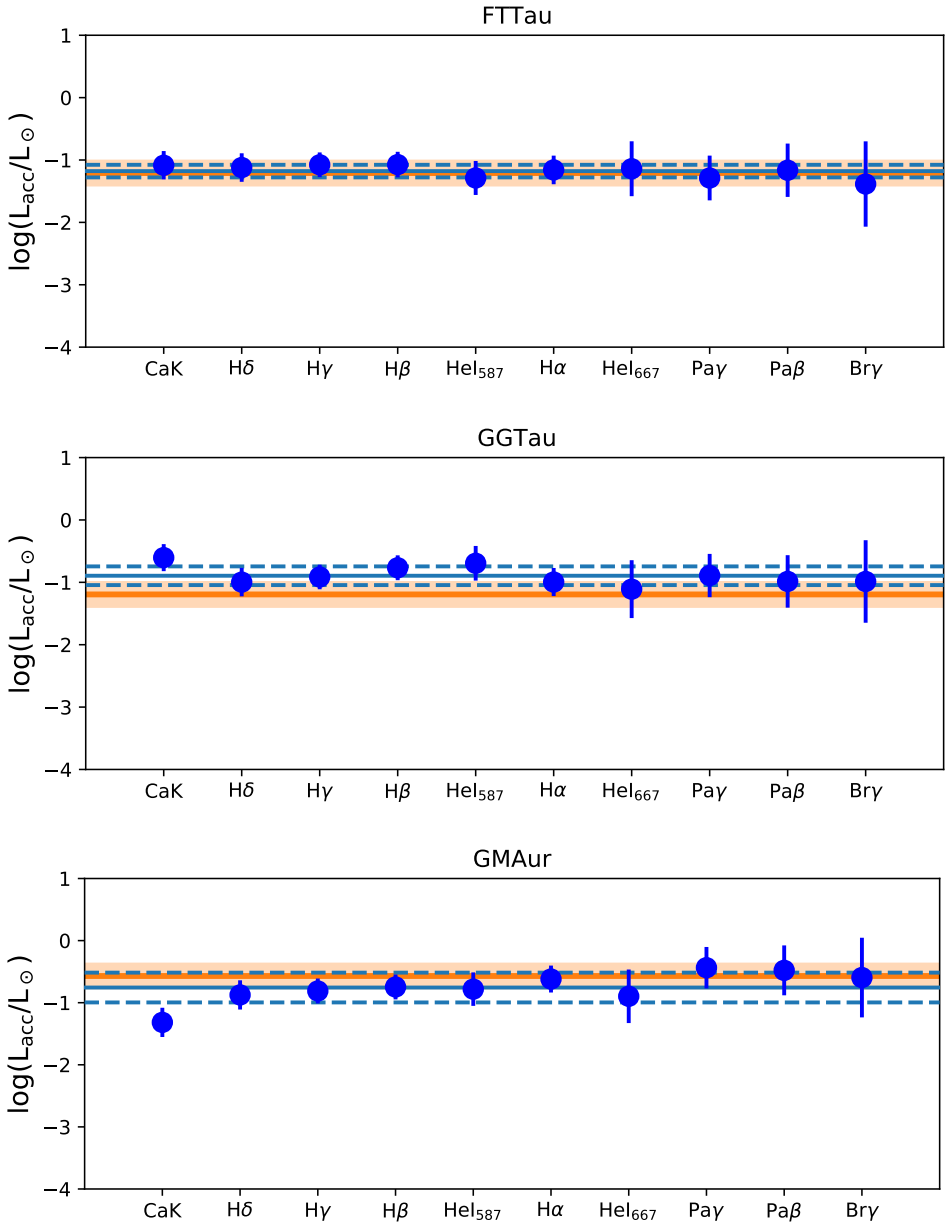

Figure 4.28: Same as figure 4.24.

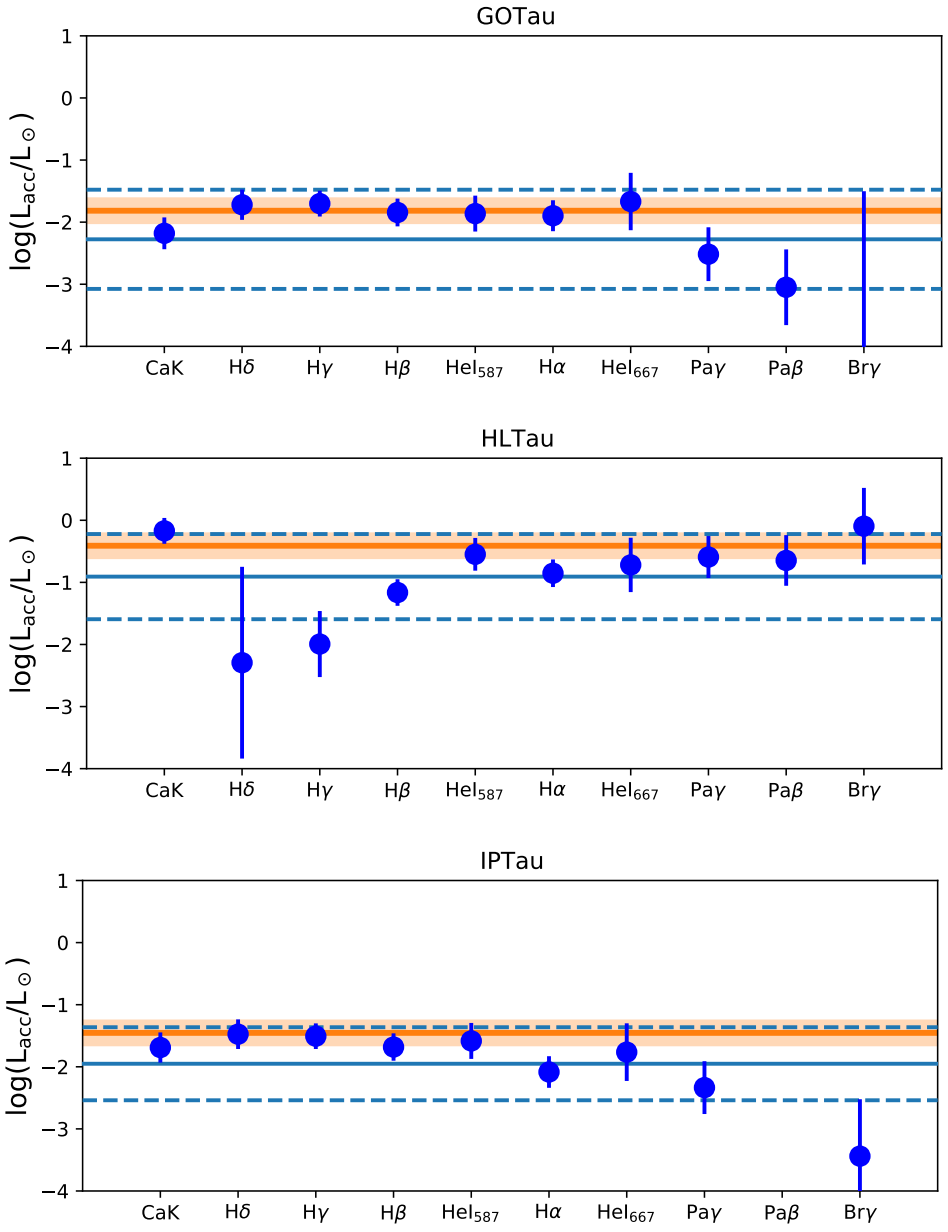

Figure 4.29: Same as figure 4.24.

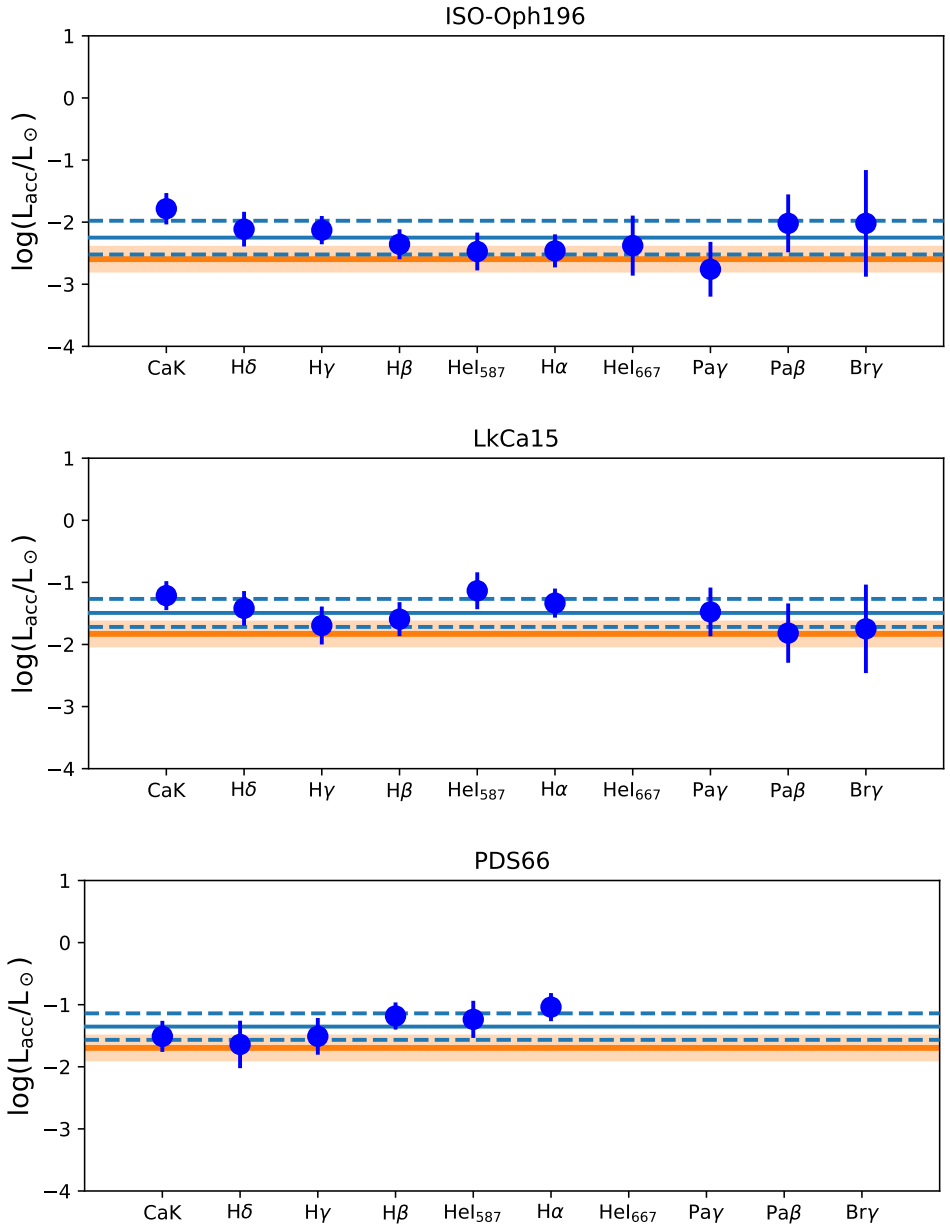

Figure 4.30: Same as figure 4.24

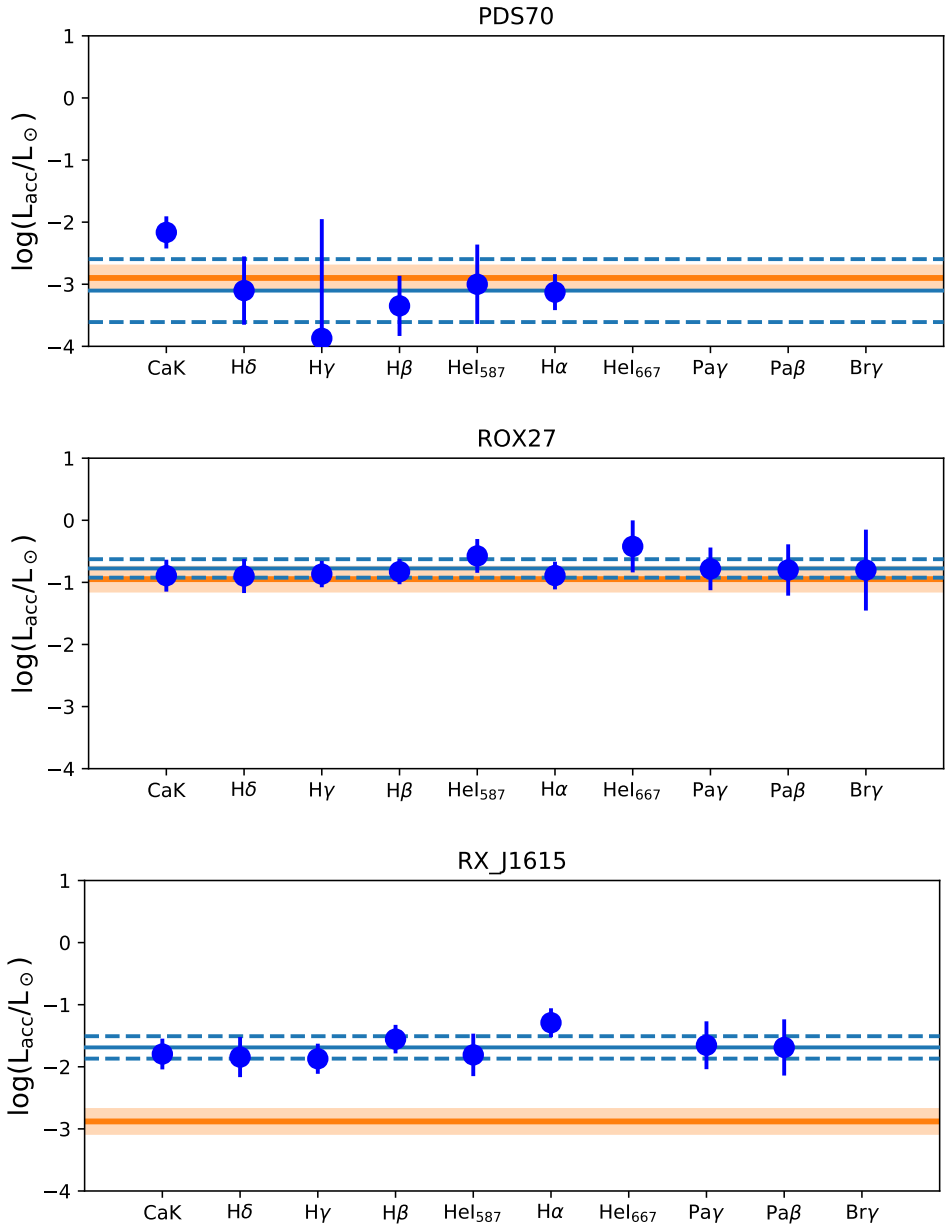

Figure 4.31: Same as figure 4.24

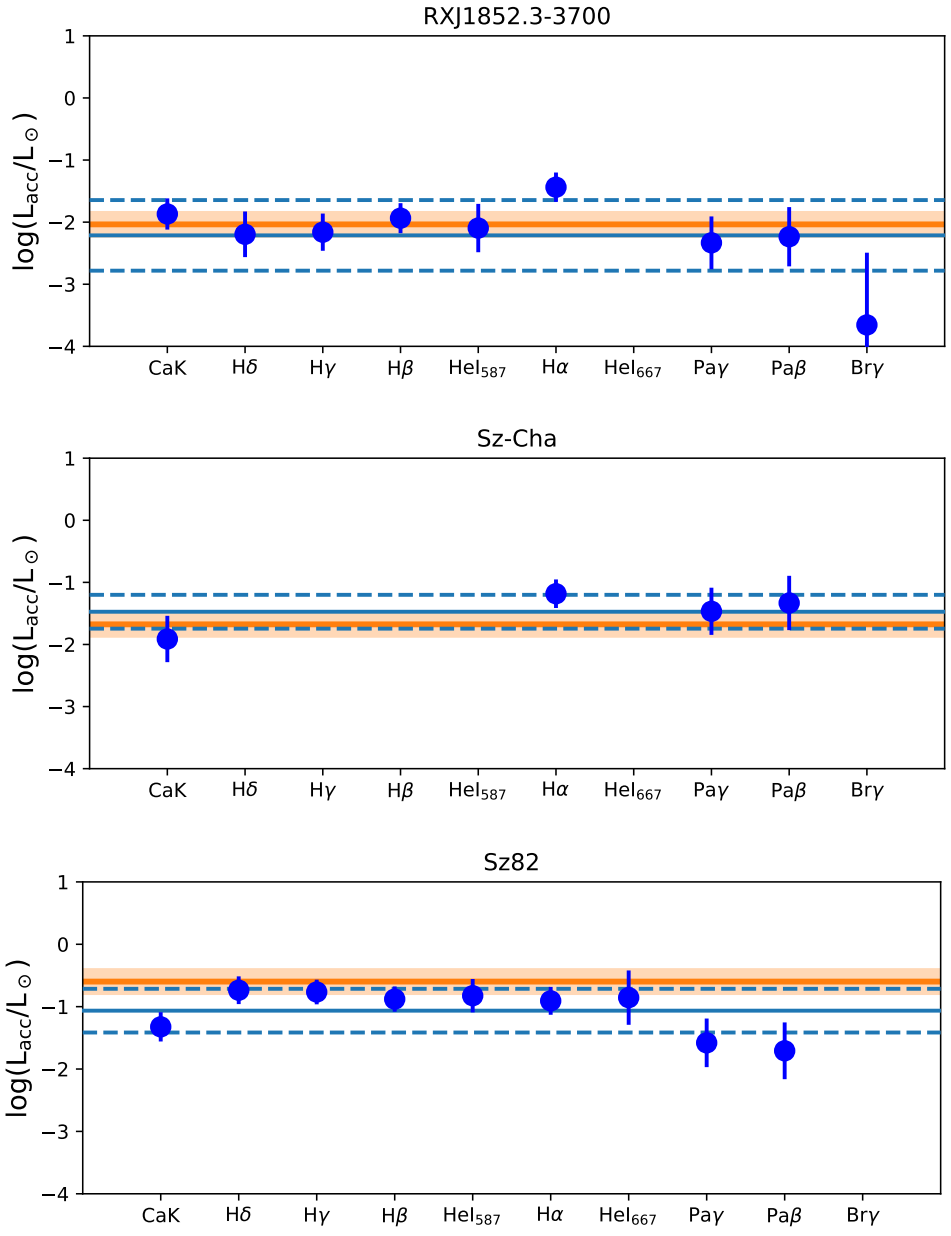

Figure 4.32: Same as figure 4.24

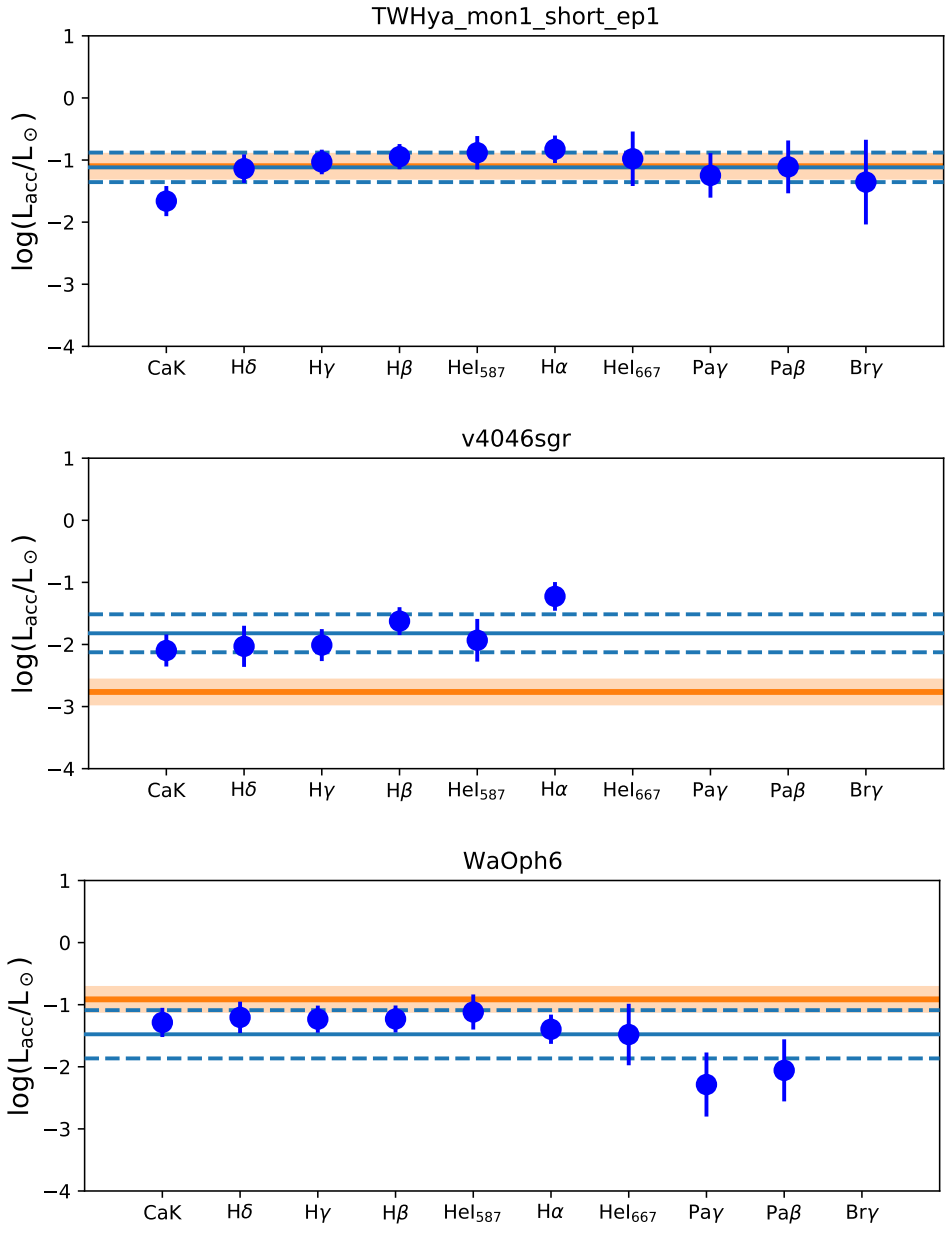

Figure 4.33: Same as figure 4.24

5

Conclusion

5.1 Summary and conclusions

In this thesis I studied the mass accretion rates of various CTTS and improved upon the methodology used to measure both mass accretion rates and stellar properties. The motivation for this thesis was to improve our understanding of the observed correlations between mass accretion rates and disk or stellar mass, since these relationships provide important constraints for our understanding of disk evolution. In particular, the large spread in mass accretion rates at a given disk mass has proved hard to explain using disk evolution models. Therefore, I considered which other mechanisms may contribute to this observed spread.

In this thesis I reported on the peculiarly large accretion variability of XX Cha. Extinction was excluded as the cause of the variability observed between the two X-Shooter observations obtained $\sim$ 10 years apart. XX Cha was found to show an accretion variability of $\gtrsim 1.4$ dex. The impact of such variability on the observed correlation between $\dot{M}_{\rm acc}$and $M_{\rm disk}$or $M_{\star}$was evaluated. Here, it was found that the impact of such variability is likely minor and that the spread in these relations is related to the mechanisms driving disk evolution.

I then presented my work on improving the method of Manara et al. (2013a), which self-consistently models X-Shooter spectra of classical T Tauri stars in order to derive the accretion and stellar properties. I achieved this by changing the way the stellar emission is represented. To do this, I first extended the grid of Class III templates that can be used for this by 18 templates. I then used a nonparametric fitting method to create an interpolated grid of Class III templates as a function of spectral type and implemented it in a method to obtain the stellar and accretion properties of CTTS. This interpolated grid mitigates the degeneracies associated with the use of individual Class III templates and reduces the influence of the uncertainties on the observed Class III temples themselves on the obtained best-fit parameters. The uncertainties on the interpolated grid of templates also allowed me to estimate the lowest accretion luminosity that can be confidently measured with this method. The limit found here suggests that the emission lines present in the spectra of young stars may provide a better constraint on the accretion rates of low accretors. The uncertainties associated with the use of Class III templates were found to not significantly affect the observed correlation between $\dot{M}_{\rm acc}$ and $M_{\star}$. Overall, good agreement was also found between the accretion properties derived using the interpolated grid and those derived using the class III templates themselves. Uncertainties introduced through the use of these empirical templates are therefore unlikely to contribute to the observed spread in mass accretion rates.

Finally, I presented a pilot study on the accretion properties of CTTS with resolved disk

substructures. This provided stellar and accretion properties that may be useful for future studies that try to constrain the mechanism responsible for the observed substructures. I discussed the position of several sources in the $\dot{M}_{\rm acc}$ - $M_{\rm disk}$ and $\dot{M}_{\rm acc}$ - $\dot{M}_{\rm acc}$ diagrams in the context of their observed substructures. The accretion properties of the two biggest categories of substructures (rings and cavities) as a whole were also analyzed. Here, hints were found that disks with inner cavities have lower accretion rates for their disk mass than the unresolved population. The disks with annular rings, on the other hand, appear to follow a distribution similar to the unresolved disks, suggesting that these may not be distinct populations and that most of the unresolved disks may have similar substructures. I presented a first study relating the properties of hypothetical planetary systems inferred from the observed substructures to the accretion properties of the system. Here I did not find any evidence of an increase in the accretion time scale ($M_{\rm disk}/\dot{M}_{\rm acc}$) for systems with more massive hypothetical planets. Instead, I found an apparent decrease in the accretion timescale for the systems where more massive planets have been inferred. However, this anti-correlation is statistically insignificant, and further observations are therefore needed to validate if this trend is indeed real. In conclusion, disks with inner cavities may contribute to the observed scatter in mass accretion rates but cannot explain it fully. No evidence was found that hypothetical embedded protoplanets affect the accretion properties of CTTS; it is therefore not possible to conclude that such protoplanets are the cause of the observed dispersion in mass accretion rates. Further studies are needed to explain the observed spreads in mass accretion rates.

5.2 Perspective

5.2.1 The variability of XX Cha

To understand how common the accretion variability in XX Cha may be, it is important to understand the driving mechanisms behind it. How this mechanism may be constrained depends on its nature. Promising methods may include spectroscopic monitoring, which may simultaneously allow for the study of emission lines, providing better constraints on the accretion properties of the system, and may be used to infer whether or not XX Cha is a binary. Another approach could be to observe XX Cha with a NIR interferometer such as VLTI/Gravity. This would allow us to look for warps in the inner disk or to constrain the stability of the magnetospheric accretion process in XX Cha (Gravity Collaboration et al. 2023). However, it remains to be seen whether current interferometers can resolve the inner regions of XX Cha.

Although the type of variability observed in XX Cha appears rare, it may prove to be an ideal testbed for studying the influence of large accretion bursts on the disk. The additional UV radiation released during a large accretion outburst affects the snow lines within the disks, moving them outward. This results in the sublimation of the ice mantles of the dust grains that suddenly find themselves inside the snowline. Houge et al. (2024) showed that dust grains indeed survive the sublimation of their ice mantles in an FU Ori-type outburst of V883 Ori. Since V883 Ori is currently still undergoing its outburst, it is impossible to study how the dust will evolve once the snowline moves back in after the outburst. The short timescale of the accretion variability

of XX Cha, implied by the lightcurve, may allow such studies. The snow lines are not the only disk property affected by accretion variability. The molecular content of the inner disk is also affected by the UV radiation released at the accretion shock (e.g., Banzatti et al. 2015). Once again, the short timescale and high amplitude of XX Cha's variability would facilitate studies of the response of the molecular content to accretion variability.

5.2.2 Determination of mass accretion rates

Several improvements can still be made to the method for obtaining stellar and accretion properties presented here. A more complete utilization of the information present in the X-Shooter spectra would drastically improve the constraints on the obtained best-fit. This would be particularly useful when fitting early K- and late G-type spectra, since these have less pronounced molecular bands and therefore tend to have more degenerate solutions.

a) Emission line luminosities. In chapter 4, I used a number of accretion tracing emission lines to confirm the accretion luminosities and extinction (A_V) obtained from the fitting procedure. However, the measured line luminosities could be used to further constrain the best-fit determination itself. To do so, two terms could be included in the $\chi^2_{\rm like}$ metric used to find the best-fit. A first term would put constraints on the accretion luminosity obtained from the slab model fit at each position in the probed parameter space. By requiring its value to be similar to the mean value obtained from the emission lines at the corresponding A_V. Implementing such a term in a statistically correct way is not straightforward, as both luminosity measurements are dependent on the A_V value, making them highly correlated. To appropriately implement such a term, one needs to measure this correlation, which will be specific to each analyzed spectrum, as, for example, in some spectra certain emission lines may not be detected due to a higher SNR or lower mass accretion rate. The second term would impose the slope of the emission line accretion luminosities as a function of wavelength to be close to zero in the best-fit solution. Such a term may be easier to implement. Measuring line luminosities is computationally expensive. It would therefore be best to measure the line luminosities before starting the best-fit determination and correct these measurements for the A_V being considered during the best-fit determination.

b) Veiling Emission line luminosities are not the only information present in the spectra that is not fully utilized. Many photospheric absorption lines are also present. These absorption lines are affected by veiling. That is, their equivalent width is reduced by the continuum emission originating from the accretion shock. In our current implementation, we only use this information to confirm the obtained best-fit by a visual comparison between the lines in the observed spectra and a class III template of the nearest SpT veiled with the best-fit slab model. Ideally, this information should be included in the best-fit determination. This could be done by including a term in $\chi^2_{\rm like}$ that imposes the equivalent of the model to be similar to the equivalent width in the observed spectrum. This can be achieved in a computationally efficient way by measuring the equivalent width of absorption lines before the best-fit optimization. During the best-fit determination, this equivalent width can then be compared to the equivalent width of the model.

The latter can be computed by correcting the equivalent widths of the lines corresponding to the spectral type being considered by the ratio between the photospheric continuum flux and accretion continuum flux for the considered parameters. This is the case as

$$r_\lambda = \frac{EW(phot., Line_\lambda)}{EW(model, Line_\lambda)} - 1 = \frac{F_{acc.,\lambda}}{F_{phot.,\lambda}}, \tag{5.1}$$

and therefore

$$EW(model, Line_\lambda) = EW(phot., Line_\lambda)\left(\frac{F_{phot.,\lambda}}{F_{acc.,\lambda} + F_{phot.,\lambda}}\right). \tag{5.2}$$

This procedure would require a grid of equivalent widths as a function of spectral type for absorption line(s) that are not strongly dependent on other stellar parameters such as surface gravity. To obtain such a grid, ideally one would measure the equivalent width of such lines in Class III template spectra and interpolate these as a function of SpT using a similar non-parametric fitting method as used in chapter 3.

c) Slab model As mentioned in Section 1.4.2, Pittman et al. (2022) found that the modeling of X-Shooter spectra with the slab models used here systematically underpredicted the values they obtained by fitting spectra extending to shorter wavelengths with complicated shock models by a factor of $\sim$ 1.5 to 5. Fiorellino in prep. are studying a larger sample with both methods and finds a large scatter between the results obtained in both cases. It therefore remains to be seen which improvements, if any, need to be made to the slab models used in this thesis. However, one improvement in the way they are used can be made by obtaining computationally cheap accretion emission models that are continuous in their parameters. A neural network could provide such an interpolation.

d) Best-fit The final potential improvement I will mention consists in replacing the current method for determining the best-fit. In our current scheme, the best-fit is obtained by evaluating a grid of parameters and selecting the parameters that minimize the $\chi^2_{\rm like}$ function. This does not provide sufficient information about the posterior distribution, which is essential for understanding the uncertainties of each fit. Implementing our models into a Monte Carlo Markov Chain (MCMC) chain would provide such insights. Doing so requires an accretion emission model that is continuous in its parameters. An MCMC chain is more computationally expensive, given the larger number of iterations it requires. This may necessitate a GPU-based implementation. Implementing these changes in a computationally efficient way would facilitate an easier analysis of large samples since less post-fit validation would be required. The implementation of an MCMC chain would also provide uncertainties for each target, which can improve the use of mass accretion rates as a constraint on disk evolution.

5.2.3 Accretion rates and substructure

The study of the relationship between accretion properties and substructures presented here was limited by several factors. The observational bias towards higher disk and stellar masses. While more disks can certainly be resolved with existing infrastructure, new or updated facilities will be needed to provide large enough samples at lower disk and stellar masses. One study, which tried to image the disks around earlier stars than used in this thesis, can be found in Shi et al. (2024). Incorporating these targets into our study could strengthen it. To do this, additional X-Shooter spectra are needed.

An additional uncertainty in this study comes in the form of the influence of disk age on its accretion properties. Additional analysis, which better takes into account the various ages of the disks in the sample, may strengthen the conclusion. Perhaps this could already be achieved by better taking into account the ages of each region. However, it is important to note that the ages of young stars and star-forming regions are highly uncertain. A more complete sample in the older Upper Scorpius region would also strengthen this work. PDS70 and 2MASS J16042165-2130284, a disk with confirmed massive planets and one with massive planets inferred from the disk kinematics, respectively, are both in Upper Scorpius and appear outliers in terms of their accretion properties compared to the younger population. A complete sample in Upper Scorpius is therefore essential to determine if these sources are indeed also outliers with respect to a population of the same age. A proposal to provide a complete accretion rate survey in Upper Scorpius has been accepted (PrID: 113.26NN PI: Manara), and the data will be analyzed with FRAPPE.

The study of the relationship between hypothetical planet properties and accretion timescale presented in this thesis was severely limited by the homogeneous nature in which the observed substructures have been analyzed. A homogeneous analysis of observed disk properties could drastically increase the power of population studies that try to constrain the effects of these substructures on disk evolution.

Bibliography

Acosta-Pulido, J. A., Kun, M., Ábrahám, P., et al. 2007, AJ, 133, 2020

Alcalá, J. M., Gangi, M., Biazzo, K., et al. 2021, A&A, 652, A72

Alcalá, J. M., Majidi, F. Z., Desidera, S., et al. 2020, A&A, 635, L1

Alcalá, J. M., Manara, C. F., Natta, A., et al. 2017, A&A, 600, A20

Alcalá, J. M., Natta, A., Manara, C. F., et al. 2014, A&A, 561, A2

Alencar, S. H. P., Bouvier, J., Walter, F. M., et al. 2012a, A&A, 541, A116

Alencar, S. H. P., Bouvier, J., Walter, F. M., et al. 2012b, A&A, 541, A116

Alexander, R., Pascucci, I., Andrews, S., Armitage, P., & Cieza, L. 2014, Protostars and Planets VI, 475

Alexander, R., Rosotti, G., Armitage, P. J., et al. 2023, MNRAS, 524, 3948

Alexander, R. D., Clarke, C. J., & Pringle, J. E. 2006, MNRAS, 369, 229

Alibert, Y., Mordasini, C., Benz, W., & Winisdoerffer, C. 2005, A&A, 434, 343

Allard, F., Homeier, D., & Freytag, B. 2011, in Astronomical Society of the Pacific Conference Series, Vol. 448, 16th Cambridge Workshop on Cool Stars, Stellar Systems, and the Sun, ed. C. Johns-Krull, M. K. Browning, & A. A. West, 91

ALMA Partnership, Brogan, C. L., Pérez, L. M., et al. 2015, ApJ, 808, L3

Almendros-Abad, V., Manara, C. F., Testi, L., et al. 2024, A&A, 685, A118

André, P. 2002, in EAS Publications Series, Vol. 3, EAS Publications Series, ed. J. Bouvier & J.-P. Zahn, 1–38

André, P. 2015, in Encyclopedia of Astrobiology, ed. M. Gargaud, W. M. Irvine, R. Amils, I. Cleaves, Henderson James (Jim), D. L. Pinti, J. C. Quintanilla, D. Rouan, T. Spohn, S. Tirard, & M. Viso, 2308–2313

André, P., Men'shchikov, A., Bontemps, S., et al. 2010, A&A, 518, L102

Andre, P., Ward-Thompson, D., & Barsony, M. 1993, ApJ, 406, 122

Andrews, S. M. 2020, ARA&A, 58, 483

Andrews, S. M., Huang, J., Pérez, L. M., et al. 2018, ApJ, 869, L41

Andrews, S. M., Wilner, D. J., Espaillat, C., et al. 2011, ApJ, 732, 42

Andrews, S. M., Wilner, D. J., Hughes, A. M., Qi, C., & Dullemond, C. P. 2009, ApJ, 700, 1502

Andrews, S. M., Wilner, D. J., Zhu, Z., et al. 2016, ApJ, 820, L40

Ansdell, M., Williams, J. P., Trapman, L., et al. 2018, ApJ, 859, 21

Ansdell, M., Williams, J. P., van der Marel, N., et al. 2016, ApJ, 828, 46

Antoniucci, S., García López, R., Nisini, B., et al. 2011, A&A, 534, A32

Appenzeller, I., Reitermann, A., & Stahl, O. 1988, PASP, 100, 815

Armitage, P. J., Simon, J. B., & Martin, R. G. 2013, ApJ, 778, L14

Artymowicz, P. 1993, ApJ, 419, 155

Artymowicz, P. & Lubow, S. H. 1994, ApJ, 421, 651

Artymowicz, P. & Lubow, S. H. 1996, ApJ, 467, L77

Aspin, C., Reipurth, B., Herczeg, G. J., & Capak, P. 2010, ApJ, 719, L50

Audard, M., Ábrahám, P., Dunham, M. M., et al. 2014, in Protostars and Planets VI, ed. H. Beuther, R. S. Klessen, C. P. Dullemond, & T. Henning, 387

Avenhaus, H., Quanz, S. P., Garufi, A., et al. 2018, ApJ, 863, 44

Avenhaus, H., Quanz, S. P., Schmid, H. M., et al. 2017, AJ, 154, 33

Bae, J., Isella, A., Zhu, Z., et al. 2023, in Astronomical Society of the Pacific Conference Series, Vol. 534, Protostars and Planets VII, ed. S. Inutsuka, Y. Aikawa, T. Muto, K. Tomida, & M. Tamura, 423

Bae, J., Teague, R., Andrews, S. M., et al. 2022, ApJ, 934, L20

Bae, J. & Zhu, Z. 2018, ApJ, 859, 118

Bae, J., Zhu, Z., & Hartmann, L. 2017, ApJ, 850, 201

Bai, X.-N. 2016, ApJ, 821, 80

Bailer-Jones, C. A. L., Rybizki, J., Fouesneau, M., Demleitner, M., & Andrae, R. 2021, AJ, 161, 147

Balbus, S. A. & Hawley, J. F. 1991, ApJ, 376, 214

Ballering, N. P. & Eisner, J. A. 2019, AJ, 157, 144

Bans, A. & Königl, A. 2012, ApJ, 758, 100

Banzatti, A., Pontoppidan, K. M., Bruderer, S., Muzerolle, J., & Meyer, M. R. 2015, ApJ, 798, L16

BIBLIOGRAPHY

Baraffe, I., Elbakyan, V. G., Vorobyov, E. I., & Chabrier, G. 2017, A&A, 597, A19

Baraffe, I., Homeier, D., Allard, F., & Chabrier, G. 2015, A&A, 577, A42

Barenfeld, S. A., Carpenter, J. M., Sargent, A. I., Isella, A., & Ricci, L. 2017, ApJ, 851, 85

Barrado y Navascués, D. & Martín, E. L. 2003, AJ, 126, 2997

Barranco, J. A. & Marcus, P. S. 2005, ApJ, 623, 1157

Bastian, U., Finkenzeller, U., Jaschek, C., & Jaschek, M. 1983, A&A, 126, 438

Beccari, G., De Marchi, G., Panagia, N., et al. 2015, A&A, 574, A44

Beckwith, S. V. W., Sargent, A. I., Chini, R. S., & Guesten, R. 1990, AJ, 99, 924

Bell, C. P. M., Rees, J. M., Naylor, T., et al. 2014, MNRAS, 445, 3496

Benisty, M., Bae, J., Facchini, S., et al. 2021, ApJ, 916, L2

Benisty, M., Dominik, C., Follette, K., et al. 2023, in Astronomical Society of the Pacific Conference Series, Vol. 534, Protostars and Planets VII, ed. S. Inutsuka, Y. Aikawa, T. Muto, K. Tomida, & M. Tamura, 605

Benisty, M., Juhász, A., Facchini, S., et al. 2018, A&A, 619, A171

Benz, W., Ida, S., Alibert, Y., Lin, D., & Mordasini, C. 2014, Protostars and Planets VI, 691

Béthune, W., Lesur, G., & Ferreira, J. 2016, A&A, 589, A87

Betti, S. K., Follette, K. B., Ward-Duong, K., et al. 2023, AJ, 166, 262

Beust, H. & Dutrey, A. 2006, A&A, 446, 137

Biazzo, K., Alcalá, J. M., Covino, E., et al. 2012, A&A, 547, A104

Biazzo, K., Alcalá, J. M., Frasca, A., et al. 2014, A&A, 572, A84

Biazzo, K., Frasca, A., Alcalá, J. M., et al. 2017, A&A, 605, A66

Birnstiel, T., Dullemond, C. P., Zhu, Z., et al. 2018, ApJ, 869, L45

Birnstiel, T., Klahr, H., & Ercolano, B. 2012, A&A, 539, A148

Blandford, R. D. & Payne, D. G. 1982a, MNRAS, 199, 883

Blandford, R. D. & Payne, D. G. 1982b, MNRAS, 199, 883

Blinova, A. A., Romanova, M. M., & Lovelace, R. V. E. 2016, MNRAS, 459, 2354

Blum, J. 2018, Space Sci. Rev., 214, 52

Blum, J., Gundlach, B., Krause, M., et al. 2017, MNRAS, 469, S755

Boccaletti, A., Pantin, E., Ménard, F., et al. 2021, A&A, 652, L8

Bonnell, I. A., Smith, K. W., Meyer, M. R., et al. 1998, MNRAS, 299, 1013

Booth, A. S., Walsh, C., Ilee, J. D., et al. 2019, ApJ, 882, L31

Booth, R. A. & Clarke, C. J. 2016, MNRAS, 458, 2676

Booth, R. A., Meru, F., Lee, M. H., & Clarke, C. J. 2018, MNRAS, 475, 167

Borchert, E. M. A., Price, D. J., Pinte, C., & Cuello, N. 2022, MNRAS, 517, 4436

Bouvier, J., Alencar, S. H. P., Harries, T. J., Johns-Krull, C. M., & Romanova, M. M. 2007, in Protostars and Planets V, ed. B. Reipurth, D. Jewitt, & K. Keil, 479

Bouvier, J., Grankin, K., Ellerbroek, L. E., Bouy, H., & Barrado, D. 2013, A&A, 557, A77

Briceño, C., Vivas, A. K., Hernández, J., et al. 2004, ApJ, 606, L123

Bryden, G., Chen, X., Lin, D. N. C., Nelson, R. P., & Papaloizou, J. C. B. 1999, ApJ, 514, 344

Calcino, J., Christiaens, V., Price, D. J., et al. 2020, MNRAS, 498, 639

Calvet, N., D'Alessio, P., Hartmann, L., et al. 2002, ApJ, 568, 1008

Calvet, N., D'Alessio, P., Watson, D. M., et al. 2005, ApJ, 630, L185

Calvet, N. & Gullbring, E. 1998, ApJ, 509, 802

Calvet, N., Muzerolle, J., Briceño, C., et al. 2004, AJ, 128, 1294

Campbell-White, J., Sicilia-Aguilar, A., Manara, C. F., et al. 2021, MNRAS, 507, 3331

Canovas, H., Ménard, F., Hales, A., et al. 2013, A&A, 556, A123

Canovas, H., Rodenhuis, M., Jeffers, S. V., Min, M., & Keller, C. U. 2011, A&A, 531, A102

Cardelli, J. A., Clayton, G. C., & Mathis, J. S. 1989, ApJ, 345, 245

Carrera, D., Gorti, U., Johansen, A., & Davies, M. B. 2017, ApJ, 839, 16

Carrera, D., Simon, J. B., Li, R., Kretke, K. A., & Klahr, H. 2021, AJ, 161, 96

Chambers, J. 2019, ApJ, 879, 98

Chen, K. & Lin, M.-K. 2020, ApJ, 891, 132

Chiang, E. & Youdin, A. N. 2010, Annual Review of Earth and Planetary Sciences, 38, 493

Choudhury, R. & Bhatt, H. C. 2009, MNRAS, 393, 959

Cieza, L., Padgett, D. L., Stapelfeldt, K. R., et al. 2007, ApJ, 667, 308

Cieza, L. A., González-Ruilova, C., Hales, A. S., et al. 2021, MNRAS, 501, 2934

Claes, R. A. B., Campbell-White, J., Manara, C. F., et al. 2024, A&A, 690, A122

Clarke, C. J., Gendrin, A., & Sotomayor, M. 2001, MNRAS, 328, 485

Clarke, C. J. & Pringle, J. E. 2006, MNRAS, 370, L10

Cleveland, W. S. 1979, Journal of the American statistical association, 74, 829

Cody, A. M., Hillenbrand, L. A., David, T. J., et al. 2017, ApJ, 836, 41

Connelley, M. S. & Reipurth, B. 2018, ApJ, 861, 145

Costigan, G., Scholz, A., Stelzer, B., et al. 2012, MNRAS, 427, 1344

Costigan, G., Vink, J. S., Scholz, A., Ray, T., & Testi, L. 2014, MNRAS, 440, 3444

Cuello, N., Louvet, F., Mentiplay, D., et al. 2020, MNRAS, 491, 504

Cui, C. & Bai, X.-N. 2022, MNRAS, 516, 4660

Currie, T., Lawson, K., Schneider, G., et al. 2022, Nature Astronomy, 6, 751

Cutri, R. M., Skrutskie, M. F., van Dyk, S., et al. 2003, VizieR Online Data Catalog: 2MASS All-Sky Catalog of Point Sources (Cutri+ 2003), VizieR On-line Data Catalog: II/246. Originally published in: 2003yCat.2246....0C

Cuzzi, J. N., Hogan, R. C., Paque, J. M., & Dobrovolskis, A. R. 2001, ApJ, 546, 496

D'Angelo, C. R. & Spruit, H. C. 2010, MNRAS, 406, 1208

D'Angelo, C. R. & Spruit, H. C. 2012, MNRAS, 420, 416

David, T. J., Hillenbrand, L. A., Gillen, E., et al. 2019, ApJ, 872, 161

De Marchi, G., Beccari, G., & Panagia, N. 2013, ApJ, 775, 68

Dipierro, G. & Laibe, G. 2017, MNRAS, 469, 1932

Dipierro, G., Laibe, G., Price, D. J., & Lodato, G. 2016, MNRAS, 459, L1

Dipierro, G., Price, D., Laibe, G., et al. 2015, MNRAS, 453, L73

Donati, J. F., Morin, J., Petit, P., et al. 2008, MNRAS, 390, 545

Dong, R., Li, S., Chiang, E., & Li, H. 2017, ApJ, 843, 127

Dong, R., Zhu, Z., & Whitney, B. 2015, ApJ, 809, 93

Drążkowska, J., Bitsch, B., Lambrechts, M., et al. 2023, in Astronomical Society of the Pacific Conference Series, Vol. 534, Protostars and Planets VII, ed. S. Inutsuka, Y. Aikawa, T. Muto, K. Tomida, & M. Tamura, 717

Dullemond, C. P., Küffmeier, M., Goicovic, F., et al. 2019, A&A, 628, A20

Dullemond, C. P. & Monnier, J. D. 2010, ARA&A, 48, 205

Dullemond, C. P., Natta, A., & Testi, L. 2006, ApJ, 645, L69

Dunham, M. M., Evans, Neal J., I., Terebey, S., Dullemond, C. P., & Young, C. H. 2010, ApJ, 710, 470

Edwards, S., Hartigan, P., Ghandour, L., & Andrulis, C. 1994, AJ, 108, 1056

Eisenhauer, F., Monnier, J. D., & Pfuhl, O. 2023, ARA&A, 61, 237

Emsenhuber, A., Burn, R., Weder, J., et al. 2023, A&A, 673, A78

Ercolano, B., Mayr, D., Owen, J. E., Rosotti, G., & Manara, C. F. 2014, MNRAS, 439, 256

Ercolano, B. & Pascucci, I. 2017, Royal Society Open Science, 4, 170114

Ercolano, B. & Picogna, G. 2022, European Physical Journal Plus, 137, 1357

Ercolano, B., Picogna, G., & Monsch, K. 2023, MNRAS, 526, L105

Espaillat, C., Muzerolle, J., Najita, J., et al. 2014, in Protostars and Planets VI, ed. H. Beuther, R. S. Klessen, C. P. Dullemond, & T. Henning, 497–520

Espaillat, C. C., Herczeg, G. J., Thanathibodee, T., et al. 2022, AJ, 163, 114

Espaillat, C. C., Robinson, C. E., Romanova, M. M., et al. 2021, Nature, 597, 41

Esplin, T. L. & Luhman, K. L. 2020, AJ, 159, 282

Evans, Neal J., I., Dunham, M. M., Jørgensen, J. K., et al. 2009, ApJS, 181, 321

Facchini, S., Benisty, M., Bae, J., et al. 2020, A&A, 639, A121

Facchini, S., Manara, C. F., Schneider, P. C., et al. 2016, A&A, 596, A38

Facchini, S., Pinilla, P., van Dishoeck, E. F., & de Juan Ovelar, M. 2018, A&A, 612, A104

Fang, M., Kim, J. S., Pascucci, I., & Apai, D. 2021, ApJ, 908, 49

Fang, M., Kim, J. S., Pascucci, I., et al. 2017, AJ, 153, 188

Fang, M., Kim, J. S., van Boekel, R., et al. 2013, ApJS, 207, 5

Fedele, D., van den Ancker, M. E., Henning, T., Jayawardhana, R., & Oliveira, J. M. 2010, A&A, 510, A72

Feiden, G. A. 2016, A&A, 593, A99

Field, G. B., Somerville, W. B., & Dressler, K. 1966, ARA&A, 4, 207

Fiorellino, E., Tychoniec, Ł., Cruz-Sáenz de Miera, F., et al. 2023, ApJ, 944, 135

Fischer, W. J., Hillenbrand, L. A., Herczeg, G. J., et al. 2023, in Astronomical Society of the Pacific Conference Series, Vol. 534, Protostars and Planets VII, ed. S. Inutsuka, Y. Aikawa, T. Muto, K. Tomida, & M. Tamura, 355

Folha, D., Emerson, J., & Calvet, N. 1997, in IAU Symposium, Vol. 182, Herbig-Haro Flows and the Birth of Stars, ed. B. Reipurth & C. Bertout, 272

Franceschi, R., Birnstiel, T., Henning, T., et al. 2022, A&A, 657, A74

Franchini, M., Morossi, C., & Malagnini, M. L. 1998, ApJ, 508, 370

Francis, L. & van der Marel, N. 2020, ApJ, 892, 111

Frasca, A., Biazzo, K., Alcalá, J. M., et al. 2017, A&A, 602, A33

Frasca, A., Biazzo, K., Lanzafame, A. C., et al. 2015, A&A, 575, A4

Freudling, W., Romaniello, M., Bramich, D. M., et al. 2013, A&A, 559, A96

Fung, J. & Chiang, E. 2016, ApJ, 832, 105

Gaia Collaboration, Brown, A. G. A., Vallenari, A., et al. 2021, A&A, 649, A1

Gaia Collaboration, Prusti, T., de Bruijne, J. H. J., et al. 2016, A&A, 595, A1

Gaia Collaboration, Vallenari, A., Brown, A. G. A., et al. 2023, A&A, 674, A1

Galli, P. A. B., Bertout, C., Teixeira, R., & Ducourant, C. 2015, VizieR Online Data Catalog: T Tauri star population in Lupus (Galli+, 2015), VizieR On-line Data Catalog: J/A+A/580/A26. Originally published in: 2015A&A...580A..26G

Galli, P. A. B., Bouy, H., Olivares, J., et al. 2021, A&A, 646, A46

Gangi, M., Antoniucci, S., Biazzo, K., et al. 2022, A&A, 667, A124

Gárate, M., Birnstiel, T., Drążkowska, J., & Stammler, S. M. 2020, A&A, 635, A149

Garaud, P., Meru, F., Galvagni, M., & Olczak, C. 2013, ApJ, 764, 146

Garufi, A., Ginski, C., van Holstein, R. G., et al. 2024, A&A, 685, A53

Ginski, C., Facchini, S., Huang, J., et al. 2021, ApJ, 908, L25

Ginski, C., Garufi, A., Benisty, M., et al. 2024, A&A, 685, A52

Ginski, C., Gratton, R., Bohn, A., et al. 2022, A&A, 662, A74

Ginski, C., Stolker, T., Pinilla, P., et al. 2016, A&A, 595, A112

Goldreich, P. & Tremaine, S. 1980, ApJ, 241, 425

Goldreich, P. & Ward, W. R. 1973, ApJ, 183, 1051

Gómez, G. C., Vázquez-Semadeni, E., & Palau, A. 2021, MNRAS, 502, 4963

GRAVITY Collaboration, Garcia Lopez, R., Natta, A., et al. 2024, A&A, 684, A43

Gravity Collaboration, Soulain, A., Perraut, K., et al. 2023, A&A, 674, A203

Greene, T. P., Wilking, B. A., Andre, P., Young, E. T., & Lada, C. J. 1994, ApJ, 434, 614

Gregorio-Hetem, J. & Hetem, A. 2002, MNRAS, 336, 197

Guenther, E. W., Esposito, M., Mundt, R., et al. 2007, A&A, 467, 1147

Gullbring, E., Hartmann, L., Briceño, C., & Calvet, N. 1998, ApJ, 492, 323

Gully-Santiago, M. A., Herczeg, G. J., Czekala, I., et al. 2017, ApJ, 836, 200

Guo, Z., Lucas, P. W., Contreras Peña, C., et al. 2020, MNRAS, 492, 294

Gupta, A., Miotello, A., Manara, C. F., et al. 2023, A&A, 670, L8

Gupta, A., Miotello, A., Williams, J. P., et al. 2024, A&A, 683, A133

Haffert, S. Y., Bohn, A. J., de Boer, J., et al. 2019, Nature Astronomy, 3, 749

Hardy, A., Caceres, C., Schreiber, M. R., et al. 2015, A&A, 583, A66

Hartmann, L., Calvet, N., Gullbring, E., & D'Alessio, P. 1998, ApJ, 495, 385

Hartmann, L., D'Alessio, P., Calvet, N., & Muzerolle, J. 2006, ApJ, 648, 484

Hartmann, L., Herczeg, G., & Calvet, N. 2016, ARA&A, 54, 135

Hartmann, L., Hewett, R., & Calvet, N. 1994, ApJ, 426, 669

Hartmann, L. & Kenyon, S. J. 1996, ARA&A, 34, 207

Heinemann, T. & Papaloizou, J. C. B. 2009a, MNRAS, 397, 52

Heinemann, T. & Papaloizou, J. C. B. 2009b, MNRAS, 397, 64

Hendler, N., Pascucci, I., Pinilla, P., et al. 2020, ApJ, 895, 126

Herczeg, G. J. & Hillenbrand, L. A. 2008, ApJ, 681, 594

Herczeg, G. J. & Hillenbrand, L. A. 2014, ApJ, 786, 97

Herczeg, G. J. & Hillenbrand, L. A. 2015, ApJ, 808, 23

Hernández, J., Hartmann, L., Megeath, T., et al. 2007, ApJ, 662, 1067

Hildebrand, R. H. 1983, QJRAS, 24, 267

Hillenbrand, L. A. & Findeisen, K. P. 2015, ApJ, 808, 68

Hillenbrand, L. A., Strom, S. E., Vrba, F. J., & Keene, J. 1992, ApJ, 397, 613

Høg, E., Fabricius, C., Makarov, V. V., et al. 2000, A&A, 355, L27

Houdebine, E. R., Mathioudakis, M., Doyle, J. G., & Foing, B. H. 1996, A&A, 305, 209

Houge, A., Macías, E., & Krijt, S. 2024, MNRAS, 527, 9668

Huang, J., Andrews, S. M., Dullemond, C. P., et al. 2018a, ApJ, 869, L42

Huang, J., Andrews, S. M., Dullemond, C. P., et al. 2020, ApJ, 891, 48

Huang, J., Andrews, S. M., Pérez, L. M., et al. 2018b, ApJ, 869, L43

Hughes, A. M., Duchêne, G., & Matthews, B. C. 2018, ARA&A, 56, 541

Ingleby, L., Calvet, N., Bergin, E., et al. 2011, ApJ, 743, 105

Ingleby, L., Calvet, N., Herczeg, G., et al. 2013, ApJ, 767, 112

Isella, A., Benisty, M., Teague, R., et al. 2019, ApJ, 879, L25

Isella, A., Guidi, G., Testi, L., et al. 2016, Phys. Rev. Lett., 117, 251101

Izquierdo, A. F., Facchini, S., Rosotti, G. P., van Dishoeck, E. F., & Testi, L. 2022, ApJ, 928, 2

Jeffries, R. D., Oliveira, J. M., Naylor, T., Mayne, N. J., & Littlefair, S. P. 2007, MNRAS, 376, 580

Johansen, A., Oishi, J. S., Mac Low, M.-M., et al. 2007, Nature, 448, 1022

Johnstone, D., Hollenbach, D., & Bally, J. 1998, ApJ, 499, 758

Jones, M. G., Pringle, J. E., & Alexander, R. D. 2012, MNRAS, 419, 925

Kafka, S. 2020, in European Planetary Science Congress, EPSC2020–314

Kama, M., Bruderer, S., van Dishoeck, E. F., et al. 2016, A&A, 592, A83

Kamp, I., Tilling, I., Woitke, P., Thi, W. F., & Hogerheijde, M. 2010, A&A, 510, A18

Kamp, I., Woitke, P., Pinte, C., et al. 2011, A&A, 532, A85

Kanagawa, K. D., Hashimoto, J., Muto, T., et al. 2021, ApJ, 909, 212

Kennicutt, R. C. & Evans, N. J. 2012, ARA&A, 50, 531

Kenyon, S. J., Calvet, N., & Hartmann, L. 1993, ApJ, 414, 676

Kenyon, S. J. & Hartmann, L. 1995, ApJS, 101, 117

Keppler, M., Benisty, M., Müller, A., et al. 2018, A&A, 617, A44

Keppler, M., Teague, R., Bae, J., et al. 2019, A&A, 625, A118

Kim, S., Takahashi, S., Nomura, H., et al. 2020, ApJ, 888, 72

Kimmig, C. N., Dullemond, C. P., & Kley, W. 2020, A&A, 633, A4

Kiraga, M. 2012, Acta Astron., 62, 67

Klahr, H. & Hubbard, A. 2014, ApJ, 788, 21

Kley, W. 1999, MNRAS, 303, 696

Kluska, J., Berger, J. P., Malbet, F., et al. 2020, A&A, 636, A116

Köhler, R., Kunkel, M., Leinert, C., & Zinnecker, H. 2000, A&A, 356, 541

Kóspál, Á. 2011, A&A, 535, A125

Kóspál, Á., Ábrahám, P., Acosta-Pulido, J. A., et al. 2012, ApJS, 201, 11

Kóspál, Á., Ábrahám, P., Goto, M., et al. 2011, ApJ, 736, 72

Koumpia, E., Ababakr, K. M., de Wit, W. J., et al. 2019, A&A, 623, L5

Koutoulaki, M., Facchini, S., Manara, C. F., et al. 2019, A&A, 625, A49

Kratter, K. & Lodato, G. 2016, ARA&A, 54, 271

Kraus, A. L. & Hillenbrand, L. A. 2007, ApJ, 662, 413

Krautter, J., Wichmann, R., Schmitt, J. H. M. M., et al. 1997, A&AS, 123, 329

Krolikowski, D. M., Kraus, A. L., & Rizzuto, A. C. 2021, AJ, 162, 110

Kuffmeier, M., Goicovic, F. G., & Dullemond, C. P. 2020, A&A, 633, A3

Kuffmeier, M., Jensen, S. S., & Haugbølle, T. 2023, European Physical Journal Plus, 138, 272

Kuhn, J. R., Potter, D., & Parise, B. 2001, ApJ, 553, L189

Kurtovic, N. T., Pinilla, P., Penzlin, A. B. T., et al. 2022, A&A, 664, A151

Labdon, A., Kraus, S., Davies, C. L., et al. 2019, A&A, 627, A36

Lada, C. J. 1987, in Star Forming Regions, ed. M. Peimbert & J. Jugaku, Vol. 115, 1

Lada, C. J., Muench, A. A., Luhman, K. L., et al. 2006, AJ, 131, 1574

Lagage, P.-O., Doucet, C., Pantin, E., et al. 2006, Science, 314, 621

Lai, D. & Muñoz, D. J. 2023, ARA&A, 61, 517

Laibe, G., Gonzalez, J. F., & Maddison, S. T. 2012, A&A, 537, A61

Lambrechts, M. & Johansen, A. 2012, A&A, 544, A32

Law, C. J., Loomis, R. A., Teague, R., et al. 2021, ApJS, 257, 3

Lee, Y.-N., Charnoz, S., & Hennebelle, P. 2021, A&A, 648, A101

Lesur, G. 2021a, Journal of Plasma Physics, 87, 205870101

Lesur, G., Flock, M., Ercolano, B., et al. 2023, in Astronomical Society of the Pacific Conference Series, Vol. 534, Protostars and Planets VII, ed. S. Inutsuka, Y. Aikawa, T. Muto, K. Tomida, & M. Tamura, 465

Lesur, G. R. J. 2021b, A&A, 650, A35

Lin, D. N. C. & Papaloizou, J. 1986, ApJ, 309, 846

Lin, M.-K. 2015, MNRAS, 448, 3806

Lissauer, J. J. 1993, ARA&A, 31, 129

Liu, B., Ormel, C. W., & Johansen, A. 2019, A&A, 624, A114

Lodato, G., Dipierro, G., Ragusa, E., et al. 2019, MNRAS, 486, 453

Lodato, G., Scardoni, C. E., Manara, C. F., & Testi, L. 2017, MNRAS, 472, 4700

Long, F., Herczeg, G. J., Pascucci, I., et al. 2017, ApJ, 844, 99

Long, F., Pinilla, P., Herczeg, G. J., et al. 2018, ApJ, 869, 17

Lorenzetti, D., Larionov, V. M., Giannini, T., et al. 2009, ApJ, 693, 1056

Lovell, J. B., Wyatt, M. C., Ansdell, M., et al. 2021, MNRAS, 500, 4878

Lubow, S. H. & D'Angelo, G. 2006, ApJ, 641, 526

Lubow, S. H. & Ida, S. 2010, in Exoplanets, ed. S. Seager, 347–371

Luhman, K. L. 2020, AJ, 160, 186

Luhman, K. L., Stauffer, J. R., Muench, A. A., et al. 2003, ApJ, 593, 1093

Lynden-Bell, D. & Pringle, J. E. 1974, MNRAS, 168, 603

Lyra, W. 2014, ApJ, 789, 77

Lyra, W., Johansen, A., Cañas, M. H., & Yang, C.-C. 2023, ApJ, 946, 60

Macías, E., Guerra-Alvarado, O., Carrasco-González, C., et al. 2021, A&A, 648, A33

Makarov, V. V. 2007, ApJ, 658, 480

Mamajek, E. E. 2009, in American Institute of Physics Conference Series, Vol. 1158, Exoplanets and Disks: Their Formation and Diversity, ed. T. Usuda, M. Tamura, & M. Ishii (AIP), 3–10

Manara, C. F. 2014, PhD thesis, Ludwig-Maximilans-Universitat Munchen

Manara, C. F. 2017, arXiv e-prints, arXiv:1712.09570

Manara, C. F., Ansdell, M., Rosotti, G. P., et al. 2023, in Astronomical Society of the Pacific Conference Series, Vol. 534, Protostars and Planets VII, ed. S. Inutsuka, Y. Aikawa, T. Muto, K. Tomida, & M. Tamura, 539

Manara, C. F., Beccari, G., Da Rio, N., et al. 2013a, A&A, 558, A114

Manara, C. F., Fedele, D., Herczeg, G. J., & Teixeira, P. S. 2016a, A&A, 585, A136

Manara, C. F., Frasca, A., Alcalá, J. M., et al. 2017a, A&A, 605, A86

Manara, C. F., Frasca, A., Venuti, L., et al. 2021, A&A, 650, A196

Manara, C. F., Morbidelli, A., & Guillot, T. 2018, A&A, 618, L3

Manara, C. F., Mordasini, C., Testi, L., et al. 2019, A&A, 631, L2

Manara, C. F., Natta, A., Rosotti, G. P., et al. 2020, A&A, 639, A58

Manara, C. F., Rosotti, G., Testi, L., et al. 2016b, A&A, 591, L3

Manara, C. F., Testi, L., Herczeg, G. J., et al. 2017b, A&A, 604, A127

Manara, C. F., Testi, L., Natta, A., et al. 2014, A&A, 568, A18

Manara, C. F., Testi, L., Rigliaco, E., et al. 2013b, A&A, 551, A107

Marcus, P. S., Pei, S., Jiang, C.-H., & Barranco, J. A. 2016, ApJ, 833, 148

Marino, S., Perez, S., & Casassus, S. 2015, ApJ, 798, L44

Martinez-Brunner, R., Casassus, S., Pérez, S., et al. 2022, MNRAS, 510, 1248

Masset, F. & Snellgrove, M. 2001, MNRAS, 320, L55

Masset, F. S. 2001, ApJ, 558, 453

Masset, F. S. & Casoli, J. 2009, ApJ, 703, 857

Masset, F. S. & Papaloizou, J. C. B. 2003, ApJ, 588, 494

Maucó, K., Manara, C. F., Ansdell, M., et al. 2023, A&A, 679, A82

McNally, C. P., Nelson, R. P., Paardekooper, S.-J., Benítez-Llambay, P., & Gressel, O. 2020, MNRAS, 493, 4382

Melo, C. H. F., Covino, E., Alcalá, J. M., & Torres, G. 2001, A&A, 378, 898

Mendigutía, I., Brittain, S., Eiroa, C., et al. 2013, ApJ, 776, 44

Mendigutía, I., Oudmaijer, R. D., Rigliaco, E., et al. 2015, MNRAS, 452, 2837

Merín, B., Jørgensen, J., Spezzi, L., et al. 2008, ApJS, 177, 551

Mesa, D., Ginski, C., Gratton, R., et al. 2022, A&A, 658, A63

Mesa, D., Keppler, M., Cantalloube, F., et al. 2019, A&A, 632, A25

Michel, A., van der Marel, N., & Matthews, B. C. 2021, ApJ, 921, 72

Milli, J., Mouillet, D., Lagrange, A. M., et al. 2012, A&A, 545, A111

Millour, F. 2014, in EAS Publications Series, Vol. 69-70, EAS Publications Series, 17–52

Miotello, A., Kamp, I., Birnstiel, T., Cleeves, L. C., & Kataoka, A. 2023, in Astronomical Society of the Pacific Conference Series, Vol. 534, Protostars and Planets VII, ed. S. Inutsuka, Y. Aikawa, T. Muto, K. Tomida, & M. Tamura, 501

Miotello, A., van Dishoeck, E. F., Kama, M., & Bruderer, S. 2016, A&A, 594, A85

Miranda, R. & Rafikov, R. R. 2019, ApJ, 875, 37

Miret-Roig, N., Galli, P. A. B., Brandner, W., et al. 2020, A&A, 642, A179

Modigliani, A., Goldoni, P., Royer, F., et al. 2010, in Society of Photo-Optical Instrumentation Engineers (SPIE) Conference Series, Vol. 7737, Observatory Operations: Strategies, Processes, and Systems III, ed. D. R. Silva, A. B. Peck, & B. T. Soifer, 773728

Moll, R. 2012, A&A, 548, A76

Monnier, J. D. & Millan-Gabet, R. 2002, ApJ, 579, 694

Morbidelli, A. & Raymond, S. N. 2016, JGR, 121, 1962

Mordasini, C., Alibert, Y., & Benz, W. 2009, A&A, 501, 1139

Mordasini, C., Alibert, Y., Klahr, H., & Henning, T. 2012, A&A, 547, A111

Mulders, G. D., Pascucci, I., Ciesla, F. J., & Fernandes, R. B. 2021, ApJ, 920, 66

Mulders, G. D., Pascucci, I., Manara, C. F., et al. 2017, ApJ, 847, 31

Müller, A., Keppler, M., Henning, T., et al. 2018, A&A, 617, L2

Muzerolle, J., Calvet, N., & Hartmann, L. 1998, ApJ, 492, 743

Muzerolle, J., Calvet, N., & Hartmann, L. 2001, ApJ, 550, 944

Muzerolle, J., Hillenbrand, L., Calvet, N., Briceño, C., & Hartmann, L. 2003, ApJ, 592, 266

Najita, J. R., Andrews, S. M., & Muzerolle, J. 2015, MNRAS, 450, 3559

Najita, J. R. & Bergin, E. A. 2018, ApJ, 864, 168

Najita, J. R. & Kenyon, S. J. 2014, MNRAS, 445, 3315

Nelson, R. P., Gressel, O., & Umurhan, O. M. 2013, MNRAS, 435, 2610

Nesvorný, D., Li, R., Youdin, A. N., Simon, J. B., & Grundy, W. M. 2019, Nature Astronomy, 3, 808

O'Dell, C. R. & Wen, Z. 1994, ApJ, 436, 194

O'Dell, C. R., Wen, Z., & Hu, X. 1993, ApJ, 410, 696

Ohashi, N., Tobin, J. J., Jørgensen, J. K., et al. 2023, ApJ, 951, 8

Owen, J. E., Clarke, C. J., & Ercolano, B. 2012, MNRAS, 422, 1880

Owen, J. E. & Menou, K. 2016, ApJ, 819, L14

Paardekooper, S., Dong, R., Duffell, P., et al. 2023, in Astronomical Society of the Pacific Conference Series, Vol. 534, Protostars and Planets VII, ed. S. Inutsuka, Y. Aikawa, T. Muto, K. Tomida, & M. Tamura, 685

Paardekooper, S. J., Baruteau, C., Crida, A., & Kley, W. 2010, MNRAS, 401, 1950

Paardekooper, S. J., Baruteau, C., & Kley, W. 2011, MNRAS, 410, 293

Paardekooper, S. J. & Mellema, G. 2006, A&A, 453, 1129

Padgett, D. L., Cieza, L., Stapelfeldt, K. R., et al. 2006, ApJ, 645, 1283

Parker, R., Ward-Thompson, D., & Kirk, J. 2022, MNRAS, 511, 2453

Pascucci, I., Testi, L., Herczeg, G. J., et al. 2016, ApJ, 831, 125

Pecaut, M. J. 2016, in Young Stars & Planets Near the Sun, ed. J. H. Kastner, B. Stelzer, & S. A. Metchev, Vol. 314, 85–90

Pecaut, M. J. & Mamajek, E. E. 2013, ApJS, 208, 9

Pecaut, M. J. & Mamajek, E. E. 2016, MNRAS, 461, 794

Pepliński, A., Artymowicz, P., & Mellema, G. 2008, MNRAS, 387, 1063

Pérez Paolino, F., Bary, J. S., Hillenbrand, L. A., & Markham, M. 2024, ApJ, 967, 45

Persson, M. V. 2014, SEDs of the different protostellar evolutionary stages, https://figshare.com/articles/figure/SEDs_of_the_different_protostellar_evolutionary_stages/1121574

Phuong, N. T., Dutrey, A., Diep, P. N., et al. 2020, A&A, 635, A12

Pinilla, P., Benisty, M., & Birnstiel, T. 2012, A&A, 545, A81

Pinilla, P., Benisty, M., de Boer, J., et al. 2018a, ApJ, 868, 85

Pinilla, P., de Boer, J., Benisty, M., et al. 2015, A&A, 584, L4

Pinilla, P., Flock, M., Ovelar, M. d. J., & Birnstiel, T. 2016, A&A, 596, A81

Pinilla, P., Kurtovic, N. T., Benisty, M., et al. 2021, A&A, 649, A122

Pinilla, P., Tazzari, M., Pascucci, I., et al. 2018b, ApJ, 859, 32

Pinte, C., Price, D. J., Ménard, F., et al. 2018, ApJ, 860, L13

Pinte, C., van der Plas, G., Ménard, F., et al. 2019, Nature Astronomy, 3, 1109

Pittman, C. V., Espaillat, C. C., Robinson, C. E., et al. 2022, AJ, 164, 201

Potapov, A., Jäger, C., & Henning, T. 2020, Phys. Rev. Lett., 124, 221103

Puranen, E. J., Finer, E., Helling, C., & Smith, V. A. 2024, arXiv e-prints, arXiv:2405.00684

Ragusa, E., Dipierro, G., Lodato, G., Laibe, G., & Price, D. J. 2017, MNRAS, 464, 1449

Reipurth, B., Lindgren, H., Mayor, M., Mermilliod, J.-C., & Cramer, N. 2002, AJ, 124, 2813

Renard, S., Thiébaut, E., & Malbet, F. 2011, A&A, 533, A64

Ribas, Á., Bouy, H., & Merín, B. 2015, A&A, 576, A52

Ribas, Á., Espaillat, C. C., Macías, E., & Sarro, L. M. 2020, A&A, 642, A171

Ribas, Á., Macías, E., Weber, P., et al. 2023, A&A, 673, A77

Rice, W. K. M., Lodato, G., Pringle, J. E., Armitage, P. J., & Bonnell, I. A. 2006, MNRAS, 372, L9

Riddick, F. C., Roche, P. F., & Lucas, P. W. 2007, MNRAS, 381, 1067

Rigliaco, E., Gratton, R., Kóspál, Á., et al. 2020, A&A, 641, A33

Rigliaco, E., Natta, A., Randich, S., Testi, L., & Biazzo, K. 2011, A&A, 525, A47

Rigliaco, E., Natta, A., Testi, L., et al. 2012, A&A, 548, A56

Riols, A., Lesur, G., & Menard, F. 2020, A&A, 639, A95

Robinson, C. E., Espaillat, C. C., & Owen, J. E. 2021, ApJ, 908, 16

Robinson, C. E., Espaillat, C. C., & Rodriguez, J. E. 2022, ApJ, 935, 54

Roman-Duval, J., Proffitt, C. R., Taylor, J. M., et al. 2020, Research Notes of the American Astronomical Society, 4, 205

Romanova, M. M., Kulkarni, A. K., & Lovelace, R. V. E. 2008, ApJ, 673, L171

Romanova, M. M., Ustyugova, G. V., Koldoba, A. V., & Lovelace, R. V. E. 2012, MNRAS, 421, 63

Rosotti, G. P., Clarke, C. J., Manara, C. F., & Facchini, S. 2017, MNRAS, 468, 1631

Rosotti, G. P., Juhasz, A., Booth, R. A., & Clarke, C. J. 2016, MNRAS, 459, 2790

Rosotti, G. P., Tazzari, M., Booth, R. A., et al. 2019, MNRAS, 486, 4829

Ruaud, M., Gorti, U., & Hollenbach, D. J. 2022, ApJ, 925, 49

Rugel, M., Fedele, D., & Herczeg, G. 2018, A&A, 609, A70

Ruzza, A., Lodato, G., & Rosotti, G. P. 2024, A&A, 685, A65

Sana, H., Tramper, F., Abdul-Masih, M., et al. 2024, A&A, 688, A104

Schisano, E., Covino, E., Alcalá, J. M., et al. 2009, A&A, 501, 1013

Schneider, P. C., France, K., Günther, H. M., et al. 2015, A&A, 584, A51

Schneider, P. C., Manara, C. F., Facchini, S., et al. 2018, A&A, 614, A108

Schräpler, R., Blum, J., Krijt, S., & Raabe, J.-H. 2018, ApJ, 853, 74

Sellek, A. D., Booth, R. A., & Clarke, C. J. 2020, MNRAS, 498, 2845

Shadmehri, M. & Ghoreyshi, S. M. 2019, MNRAS, 488, 4623

Shakura, N. I. & Sunyaev, R. A. 1973, A&A, 24, 337

Sheehan, W. & Dobbins, T. 2003, Journal for the History of Astronomy, 34, 53

Shi, Y., Long, F., Herczeg, G. J., et al. 2024, ApJ, 966, 59

Shu, F., Najita, J., Ostriker, E., et al. 1994, ApJ, 429, 781

Sicilia-Aguilar, A., Bouwman, J., Juhász, A., et al. 2009, ApJ, 701, 1188

Sicilia-Aguilar, A., Oprandi, A., Froebrich, D., et al. 2017, A&A, 607, A127

Sierra, A., Pérez, L. M., Agurto-Gangas, C., et al. 2024, ApJ, 974, 102

Siess, L., Dufour, E., & Forestini, M. 2000, A&A, 358, 593

Singh, K., Ninan, J. P., Romanova, M. M., et al. 2024, ApJ, 968, 88

Skrutskie, M. F., Dutkevitch, D., Strom, S. E., et al. 1990, AJ, 99, 1187

Smette, A., Sana, H., Noll, S., et al. 2015, A&A, 576, A77

Somers, G., Cao, L., & Pinsonneault, M. H. 2020, ApJ, 891, 29

Somers, G. & Pinsonneault, M. H. 2015, ApJ, 807, 174

Somigliana, A., Testi, L., Rosotti, G., et al. 2023, ApJ, 954, L13

Somigliana, A., Toci, C., Lodato, G., Rosotti, G., & Manara, C. F. 2020, MNRAS, 492, 1120

Somigliana, A., Toci, C., Rosotti, G., et al. 2022, MNRAS, 514, 5927

Stadler, J., Benisty, M., Izquierdo, A., et al. 2023, A&A, 670, L1

Stammler, S. M., Lichtenberg, T., Drążkowska, J., & Birnstiel, T. 2023, A&A, 670, L5

Stauffer, J., Cody, A. M., Baglin, A., et al. 2014, AJ, 147, 83

Stauffer, J. R., Jones, B. F., Backman, D., et al. 2003, AJ, 126, 833

Stelzer, B., Frasca, A., Alcalá, J. M., et al. 2013, A&A, 558, A141

Strom, K. M., Strom, S. E., Edwards, S., Cabrit, S., & Skrutskie, M. F. 1989, AJ, 97, 1451

Suzuki, T. K., Ogihara, M., Morbidelli, A., Crida, A., & Guillot, T. 2016, A&A, 596, A74

Tabone, B., Rosotti, G. P., Cridland, A. J., Armitage, P. J., & Lodato, G. 2022a, MNRAS, 512, 2290

Tabone, B., Rosotti, G. P., Lodato, G., et al. 2022b, MNRAS, 512, L74

Tacconi, L. J., Genzel, R., & Sternberg, A. 2020, ARA&A, 58, 157

Takahashi, S. Z. & Muto, T. 2018, ApJ, 865, 102

Tazzari, M., Testi, L., Natta, A., et al. 2017, A&A, 606, A88

Tazzari, M., Testi, L., Natta, A., et al. 2021, MNRAS, 506, 5117

Testi, L., Birnstiel, T., Ricci, L., et al. 2014, in Protostars and Planets VI, ed. H. Beuther, R. S. Klessen, C. P. Dullemond, & T. Henning, 339–361

Testi, L., Natta, A., Manara, C. F., et al. 2022, A&A, 663, A98

Thalmann, C., Janson, M., Garufi, A., et al. 2016, ApJ, 828, L17

Thanathibodee, T., Calvet, N., Hernández, J., Maucó, K., & Briceño, C. 2022, AJ, 163, 74

Thanathibodee, T., Molina, B., Calvet, N., et al. 2020, ApJ, 892, 81

Thanathibodee, T., Molina, B., Serna, J., et al. 2023, ApJ, 944, 90

Thiébaut, É. & Young, J. 2017, Journal of the Optical Society of America A, 34, 904

Thompson, A. R., Moran, J. M., & Swenson, George W., J. 2017, Interferometry and Synthesis in Radio Astronomy, 3rd Edition

Tilling, I., Clarke, C. J., Pringle, J. E., & Tout, C. A. 2008, MNRAS, 385, 1530

Toci, C., Lodato, G., Fedele, D., Testi, L., & Pinte, C. 2020, ApJ, 888, L4

Torres, C. A. O., Quast, G. R., da Silva, L., et al. 2006, A&A, 460, 695

Trapman, L., Bosman, A. D., Rosotti, G., Hogerheijde, M. R., & van Dishoeck, E. F. 2021, A&A, 649, A95

Trapman, L., Miotello, A., Kama, M., van Dishoeck, E. F., & Bruderer, S. 2017, A&A, 605, A69

Trapman, L., Rosotti, G., Bosman, A. D., Hogerheijde, M. R., & van Dishoeck, E. F. 2020, A&A, 640, A5

Trapman, L., Tabone, B., Rosotti, G., & Zhang, K. 2022, ApJ, 926, 61

Tsukagoshi, T., Momose, M., Hashimoto, J., et al. 2014, ApJ, 783, 90

Tychoniec, Ł., Manara, C. F., Rosotti, G. P., et al. 2020, A&A, 640, A19

Ueda, T., Flock, M., & Okuzumi, S. 2019, ApJ, 871, 10

Ueda, T., Kataoka, A., & Tsukagoshi, T. 2022, ApJ, 930, 56

Urpin, V. & Brandenburg, A. 1998, MNRAS, 294, 399

Vacca, W. D. & Sandell, G. 2011, ApJ, 732, 8

Valenti, J. A., Basri, G., & Johns, C. M. 1993, AJ, 106, 2024

van Boekel, R., Henning, T., Menu, J., et al. 2017, ApJ, 837, 132

van der Marel, N. 2023, European Physical Journal Plus, 138, 225

van der Marel, N., Dong, R., di Francesco, J., Williams, J. P., & Tobin, J. 2019, ApJ, 872, 112

van der Marel, N., Williams, J. P., Picogna, G., et al. 2022, arXiv e-prints, arXiv:2204.08225

Varga, J., Hogerheijde, M., van Boekel, R., et al. 2021, A&A, 647, A56

Venuti, L., Bouvier, J., Flaccomio, E., et al. 2014, A&A, 570, A82

Venuti, L., Bouvier, J., Irwin, J., et al. 2015, A&A, 581, A66

Venuti, L., Cody, A. M., Beccari, G., et al. 2024, AJ, 167, 120

Vericel, A. & Gonzalez, J.-F. 2020, MNRAS, 492, 210

Vernet, J., Dekker, H., D'Odorico, S., et al. 2011, A&A, 536, A105

Veronesi, B., Ragusa, E., Lodato, G., et al. 2020, MNRAS, 495, 1913

Villenave, M., Benisty, M., Dent, W. R. F., et al. 2019, A&A, 624, A7

Villenave, M., Ménard, F., Dent, W. R. F., et al. 2021, A&A, 653, A46

Vorobyov, E. I., Elbakyan, V. G., Liu, H. B., & Takami, M. 2021, A&A, 647, A44

Wafflard-Fernandez, G. & Baruteau, C. 2020, MNRAS, 493, 5892

Wafflard-Fernandez, G. & Lesur, G. 2023, A&A, 677, A70

Wagner, K., Dong, R., Sheehan, P., et al. 2018, ApJ, 854, 130

Wang, S., Kanagawa, K. D., & Suto, Y. 2021, ApJ, 923, 165

Ward, W. R. 1997, Icarus, 126, 261

Ward, W. R. 2007, in 38th Annual Lunar and Planetary Science Conference, Lunar and Planetary Science Conference, 2289

Wetherill, G. W. & Stewart, G. R. 1989, Icarus, 77, 330

White, R. & Basri, G. 2003, in Brown Dwarfs, ed. E. Martín, Vol. 211, 143

White, R. J. & Hillenbrand, L. A. 2004, ApJ, 616, 998

Wichittanakom, C., Oudmaijer, R. D., Fairlamb, J. R., et al. 2020, MNRAS, 493, 234

Williams, J. P. & Cieza, L. A. 2011, ARA&A, 49, 67

Windmark, F., Birnstiel, T., Ormel, C. W., & Dullemond, C. P. 2012, A&A, 544, L16

Winter, A. J., Clarke, C. J., Rosotti, G., et al. 2018, MNRAS, 478, 2700

Winter, A. J. & Haworth, T. J. 2022, European Physical Journal Plus, 137, 1132

Wyatt, M. C. 2008, ARA&A, 46, 339

Yap, T. E. & Batygin, K. 2024, Icarus, 417, 116085

Youdin, A. N. & Shu, F. H. 2002, ApJ, 580, 494

Zacharias, N., Finch, C. T., Girard, T. M., et al. 2012, VizieR Online Data Catalog: UCAC4 Catalogue (Zacharias+, 2012), VizieR On-line Data Catalog: I/322A. Originally published in: 2012yCat.1322....0Z; 2013AJ....145...44Z

Zagaria, F., Clarke, C. J., Rosotti, G. P., & Manara, C. F. 2022a, MNRAS, 512, 3538

Zagaria, F., Facchini, S., Miotello, A., et al. 2023, A&A, 672, L15

Zagaria, F., Rosotti, G. P., Clarke, C. J., & Tabone, B. 2022b, MNRAS, 514, 1088

Zhang, K., Crockett, N., Salyk, C., et al. 2015, ApJ, 805, 55

Zhang, S., Kalscheur, M., Long, F., et al. 2023, ApJ, 952, 108

Zhang, S., Zhu, Z., Huang, J., et al. 2018, ApJ, 869, L47

Zhu, W. & Dong, S. 2021, ARA&A, 59, 291

Zhu, Z., Nelson, R. P., Dong, R., Espaillat, C., & Hartmann, L. 2012, ApJ, 755, 6

Zhu, Z., Nelson, R. P., Hartmann, L., Espaillat, C., & Calvet, N. 2011, ApJ, 729, 47

Zsidi, G., Manara, C. F., Kóspál, Á., et al. 2022, A&A, 660, A108

Zurlo, A., Cieza, L. A., Ansdell, M., et al. 2021, MNRAS, 501, 2305

Acknowledgements

This thesis concludes what will most likely be on eof the most interesting periods of my life. Over the past three years I got to experience something a younger me would have never even imagined. The many amazing interactions with people form all over the world really taught me a lot.

I would like to thank my Supervisor Carlo Manara for his guidance and commitment throughout the past years. I would also like to thank Justyn Campbell-White for his support, be it scientific or non scientific. I also want to acknowledge the suggestions and comments of all the co-authors with whom I worked throughout these years. Beyond this I would like to thank all the students at ESO for creating such a wonderfull and welcoming community. I would also like to thank my parents for their support throughout the years. I really could not have done it without their encouragement. Lastly, I would like to thank Stephenie for all her encouragement aswell as the beatifull figures she made for this thesis.